# Magnetic memory optimized for cryoelectronics operation

Pedro Brandao Veiga

## To cite this version:

Pedro Brandao Veiga. Magnetic memory optimized for cryoelectronics operation. Micro and nanotechnologies/Microelectronics. Université Grenoble Alpes [2020-..], 2023. English. NNT : 2023GRALT077 . tel-04503963

THÈSE

Pour obtenir le grade de

## DOCTEUR DE L'UNIVERSITÉ GRENOBLE ALPES

École doctorale : EEATS - Electronique, Electrotechnique, Automatique, Traitement du Signal (EEATS)
Spécialité : Nano électronique et Nano technologies
Unité de recherche : Spintronique et Technologie des Composants

# Mémoires magnétiques optimisées pour un fonctionnement en cryoélectronique

# Magnetic memory optimized for cryoelectronics operation

Présentée par :

**Pedro BRANDAO VEIGA**

Direction de thèse :

| | |
|---|---|
| **Ricardo SOUSA**<br>Directeur de Recherche, CEA | Directeur de thèse |

Rapporteurs :

**Daniel LACOUR**
DIRECTEUR DE RECHERCHE, CNRS DELEGATION CENTRE-EST
**Julie GROLLIER**
DIRECTRICE DE RECHERCHE, CNRS DELEGATION ILE-DE-FRANCE SUD

Thèse soutenue publiquement le **4 décembre 2023**, devant le jury composé de :

| | |
|---|---|
| **Ricardo SOUSA**<br>DIRECTEUR DE RECHERCHE, CEA CEA CENTRE DE GRENOBLE | Directeur de thèse |
| **Daniel LACOUR**<br>DIRECTEUR DE RECHERCHE, CNRS DELEGATION CENTRE-EST | Président |
| **Diana LEITAO**<br>ASSISTANT PROFESSOR, Technische Universiteit Eindhoven | Examinatrice |
| **Julie GROLLIER**<br>DIRECTRICE DE RECHERCHE, CNRS DELEGATION ILE-DE-FRANCE SUD | Rapporteure |
| **Matias URDAMPILLETA**<br>CHARGE DE RECHERCHE, CNRS DELEGATION ALPES | Examinateur |
| **Martin KOGELSCHATZ**<br>MAITRE DE CONFERENCES HDR, Université Grenoble Alpes | Examinateur |

# Abstract

Magnetic Random Access Memories (MRAM) arise as the second main industrial application of spintronics after hard disk drives. They harbor a number of assets to outperform the current state-of-the-art devices used in electronics, such as eFLASH and possibly SRAM and DRAM. They still hold many interesting facets that have yet to be fully explored with the advances in Spin Transfer Torque (STT), Spin Orbit Torque and Voltage Controlled Anisotropy (VCMA) driven magnetization reversal. It is a thriving field, and the progress in High Performance Computing and advent of quantum processors are attracting more and more attention, motivating the interest on the subject of this work. To engineer new magnetic memory devices for cryoelectronics, we focused on two different writing mechanisms: STT and VCMA. We studied them under the framework of macrospin numerical simulations to better understand the switching dynamics of our system. For cryo-STT-MRAM, we demonstrated that it is highly beneficial in terms of switching speed and energy consumption to consider a storage layer exhibiting higher order anisotropy terms, resulting in a canted magnetization state called "easy-cone". Switching simulations revealed that this approach enables very low temperature switching without thermal activation and reduces the switching energy necessary to write the bit.We also demonstrated that the VCMA effect, under certain optimized conditions, yields a novel non-precessional switching regime for temperatures below 50K, enabling deterministic switching of magnetization independently of write pulse duration. Next, with a micromagnetic approach, we corroborated the results for VCMA switching. In systems switched by STT, a deviation was found from the macrospin model within the easy-cone system. The dependence of its switching voltage with temperature and its magnetic hysteresis provided guidelines to interpret some of our experimental observations. To take advantage of the low thermal activation energy at cryogenic temperatures, we fabricated MRAM cells with much lower anisotropy compared to conventional devices. The approach used was to modify the storage layer structure of the magnetic tunnel junctions to either reduce its anisotropy at the interface with the tunnel barrier or increase its demagnetizing energy. The purpose was to lower the energy barrier between the two writeable states. For that, we introduced embedded magnetic layers, such as Co or Permalloy, onto the FeCoB layer and conducted magnetic and electrical characterization at room temperature down to 4K. Using a storage layer containing Permalloy, they showed improvement in the figure of merit over conventional MTJs and those using either Co, Mg, or Ru as an embedded layer. Further analysis and MFM imaging of the Permalloy stack at thin-film and device level indicate the presence of the easy-cone anisotropy discussed in the numerical simulation results. For the VCMA samples, over 1000 devices were characterized at room temperature and the VCMA coefficient was extracted for each one. The method described allows for a large amount of data to be acquired in a short period of time, enabling us to quantify impact of layer stack variations on the VCMA effect without the need for switching experiments, and to select devices for low temperature characterization.

# Resumé

Les Magnetic Random Access Memories (MRAM) se présentent comme la deuxième application industrielle principale de la spintronique après les disques durs. Ils offrent plusieurs avantages pour surpasser les dispositifs actuels de pointe utilisés en électronique, tels que l'eFLASH et éventuellement les SRAM et DRAM. Ils conservent encore de nombreuses facettes intéressantes qui restent à explorer pleinement avec les avancées en matière de Transfert de Spin par Effet Tunnel (STT), de Transfert de Spin par Effet Orbitale et d'Anisotropie Contrôlée par Tension (VCMA). Pour concevoir de nouveaux dispositifs de mémoire magnétique pour la cryoélectronique, nous nous sommes concentrés sur deux mécanismes d'écriture différents : le STT et le VCMA. En les étudiant dans le cadre de simulations numériques de macrospin, nous avons cherché à mieux comprendre la dynamique de commutation de notre système. Pour les cryo-STT-MRAM, nous avons démontré qu'il est hautement bénéfique en termes de vitesse de commutation et de consommation d'énergie de considérer une couche de stockage présentant des termes d'anisotropie d'ordre supérieur, résultant en un état de magnétisation incliné appelé "easy-cone". Les simulations de commutation ont révélé que cette approche permet une commutation à très basse température sans activation thermique et réduit l'énergie de commutation nécessaire pour écrire le bit. Nous avons démontré que l'effet VCMA permet un régime de commutation non précessionnel novateur pour des températures inférieures à 50K, permettant une commutation déterministe de la magnétisation indépendamment de la durée de l'impulsion d'écriture. Ensuite, en utilisant une approche micromagnétique, nous avons corroboré les résultats de la commutation VCMA. Dans les systèmes commutés par le STT, une déviation par rapport au modèle de macrospin a été trouvée dans le système du easy-cone. Nous avons décidé de fabriquer nos MRAM avec une anisotropie beaucoup plus faible par rapport aux dispositifs conventionnels. L'approche utilisée consistait à modifier la structure de la couche de stockage des jonctions tunnel magnétiques pour réduire son anisotropie à l'interface avec la barrière tunnel ou augmenter son énergie de désaimantation. Le but était de réduire la barrière d'énergie entre les deux états inscriptibles. Pour ce faire, nous avons introduit des couches magnétiques intégrées, telles que le Co ou le Permalloy, sur la couche FeCoB et avons effectué une caractérisation magnétique et électrique à température ambiante jusqu'à 4 K. En utilisant une couche de stockage contenant du Permalloy, les échantillons analysés ont montré une amélioration du facteur de mérite par rapport aux jonctions tunnel magnétiques conventionnelles et à celles utilisant du Co, du Mg ou du Ru comme couche intégrée. Des analyses magnétiques supplémentaires et des images MFM de la pile Permalloy au niveau des films et des dispositifs indiquent la présence de l'anisotropie du easy-cone discutée dans les résultats de la simulation numérique. Pour le VCMA, un ensemble de plus de 1000 dispositifs a été caractérisé à température ambiante et son coefficient a été extrait pour chacun d'entre eux. La méthode décrite permet d'acquérir de grandes quantités de données en peu de temps, ce qui nous permet de quantifier l'effet VCMA sans effectuer d'expériences de commutation.

# Contents

# List of Figures

# List of Tables

# Chapter 1

# Introduction

Goals

In this first chapter, we initially explore the state-of-the-art context for low temperature technologies and how it matured with the development of novel magnetic memories and computer architectures that enabled the birth of supercomputation. The main fundamental physics behind the workings of an MRAM are dissected for room temperature and a the most important mechanisms for bit writing is explained in detail. Afterwards, we delve into the intricacies of applying current MRAMs into cryoelectronics and how it can impact the design and engineering of the device elements of the memory.

## Contents

# 1 MRAM in cryoelectronics for quantum technologies and high performance computing (HPC)

Research and development related to magnetic thin films and multilayers started about 60 years ago [3]. Over the years, the scientific community has discovered a plethora of new phenomena in these materials that stimulated interest from both a fundamental and commercial point of view. In particular, the phenomena that contributed greatly to the research and technological advancement of magnetic memories were the giant magnetoresistance of metallic multilayers (GMR) [4], perpendicular magnetic anisotropy (PMA) [5], tunnel magnetoresistance of magnetic tunnel junctions (TMR) [6], spin transfer torque in magnetic structures (STT) [7] and giant TMR in MgO-based magnetic tunnel junctions (MTJ) [8]. In its maturing over the decades, the technology eventually led the industry to introduce new electrical devices into the market, such as hard disk drives (HDD) [9], magnetic random access memory (MRAM) [10] and magnetic field sensors [11].

All the innovative components for these devices were designed to ultimately reduce the power consumption in conventional processors. The status quo of the memory hierarchy used in electronic circuits is highly dependent on volatile memory (VM), which must be electrically powered to retain information. In 2001 a new system was proposed to replace it with a revised, fully nonvolatile hierarchy (NVM), with the ability to keep information without being electrically powered [12]. Fig.1.1 exemplifies each component at its hierarchy level.

As with any new device in development, these technologies had to be improved from the early prototypes to overcome the challenges imposed by a trilemma [13], which is a balance of power consumption in information writing, retention of information and a reliable readability of the bit. These three topics are discussed in more detail in the following chapters.

The status of MRAM implementation in electronics is limited due to its higher manufacturing cost and lower density currently at the sub-20nm node compared to volatile memories such as the dynamic random access memory (DRAM) that are at the 10nm node for cell feature sizes. The 1x node, as it is called, has seen a large barrier for breaking through to sub-10 cells, for VM components and, as it currently stands, novel architectures must be devised if they are to compete with the fast progress of NVMs. This is due to the inherent current leakage VMs face when scaled down to extremely small sizes, as current tunneling becomes more probable and consequentially a larger amount of energy must be expended to refresh the bits that undergo this information loss.

Researchers, therefore, are increasingly studying new iterations of MRAM devices as lithography techniques are improved and novel material concepts are developed. The first mechanism proposed for functioning devices was based on magnetic field switching, which faced scalability limitations, and was discontinued in research. A thermally assisted MRAM (TA-MRAM) structure was devised in the 2000s to alleviate the required energy necessary to write very small bits [14], though with the implementation of the already known STT mechanism in 2006 most efforts were diverted to focus on this new technology [15, 16].

The introduction of the STT-MRAM as a substitute for VMs is a big achievement for this generation of spintronics. It has the potential to perform better than its counterparts, with low power consumption and GHz operation frequency [17]. Additionally, its variant pSTT-MRAM has an in-

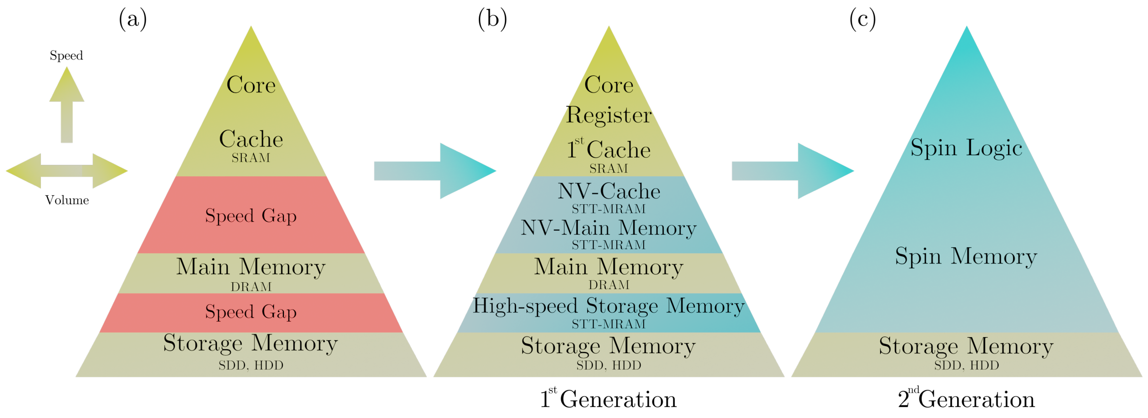

Figure 1.1: Restructuring of computer hierarchy: (a) conventional hierarchy, (b) NV computer in 1st generation, (c) NV computer in 2nd generation, adapted from [1]

trinsically lower write current compared to established in-plane configurations [18] and another novel property that will be further discussed in the following chapter, the easy-cone regime, allows for more reliable writing [19, 20]. Concomitantly with these developments, the fabrication of faster processors allowed the design of supercomputers with extremely high performance, which follows the well-known Moore's Law [21]. This is possible because of the investment of many companies in new architectures that can accommodate a denser integrated circuit, increasing its storage capacity by decreasing the size of the transistors. In 2006, the Korean Advanced Institute of Science and Technology reported the 5nm node transistor [22], which brought the technology close to the limits of physics. It is intrinsically tied to the nature of quantum mechanics by Heisenberg's uncertainty principle ($\Delta E \Delta t \geq \hbar$) and the Shannon-von Neumann-Landauer expression ($E_{bit} \geq k_B T ln2$). From these two uncertainties, the limit for an operable conventional device is in the 1.5nm node [23]. Therefore, a fundamental constraint is set to conventional electronics/spintronics in terms of data storage density, driving research to look for alternative methods of data manipulation. One in particular, quantum computation, is not bound by these limitations; rather, it uses them to our advantage.

In the framework of supercomputers, also called High Performance Computing (HPC), the implementation of Josephson junctions as a quantum bit (qbit) logic element has enabled the development of a competing technology to conventional computation. This is important because recent projections for global energy consumption present some challenges to overcome in terms of energy efficiency of current technology [24]. The energy demands may increase up to 15x by 2030 through the expansion of data centers that can now scale up to hundreds of thousands of servers. As the necessity of higher computational capabilities and higher power consumption place a considerable strain on electrical grids, the viability of conventional CMOS technology is put into question, making the industry consider whether the increase in their performance and its potential to keep up with computational demands are worth the investment in light of the advantages superconducting computing has to offer. Qubits have a much shorter writing time and energy per switch of $\approx 1ps$ and smaller than $0.1aJ$, with current pulses traveling at relativistic speeds of 0.3c and very low losses in the transmission lines. And in 1999 these devices were already shown to be operable with 770GHz [25], almost 100x faster than conventional SRAM for L1 cache memory levels, which have speeds of a few GHz. The gain in performance will be even more attractive once refrigeration systems become more efficient and are capable of high-power cooling with a net gain over room temperature architectures, as most of HPC computation is done below 10K.

This culminated with the microelectronics industry looking to develop components specifically optimized for low temperature operation to reduce the electrical consumption of electronic circuits and to mitigate the weak points of the current superconducting devices. Their limitations, which have dampened the competitiveness of the technology, are the lack of compatible memory elements, the issues with interconnecting the cryogenic circuitry with room temperature instrumentation, its fabrication scaling capabilities and bit density. The solutions for the first two obstacles have been approached by redesigning existing cryogenic memories, integrating MRAM elements into its architecture [26, 27, 28]. And the data density problem is easily solved as current lithography techniques are capable of manufacturing bits in the sub-20nm node, while HPC memory bits have yet to break the micron node [29].

Quantum computing is also an area of cryoelectronics that has gained notoriety in recent years with the promise of quantum supremacy, an algorithm capable of computing tasks faster than any supercomputer could within a reasonable time frame (e.g. seconds or hours instead of millions of years). However, the technology is still in its early stages of development, and there are significant challenges that must be overcome before it can be fully implemented and adopted in the industrial sector. It requires very specialized component parts that are compatible with quantum circuitry and isolating the qbits to avoid decoherence is increasingly difficult for denser arrays, although much effort is being invested in improving its scalability. Initial iterations of quantum computers were limited to only a few dozen bits, such as the Sycamore with 53 bits from Google in 2018, and now the 100-bit node has been truly broken, with the development of the Osprey processor by IBM in 2022 with 433 bits. While the consensus within the field states that a 1Mbit processor is the critical threshold for a veritably useful quantum computer capable of solving real-world practical problems, smaller chips can be integrated with conventional super-computing to aid in calculation tasks not feasible by classical computation. Additionally, by using classical electrical components suitable for quantum circuitry, we can expand its uses and capabilities.

In this context, MRAM can play a considerable role in reducing power consumption and dissipation as a stand-alone component due to their combination of non-volatility, speed in write/read in the GHz range, areal density and writing endurance. Their nonvolatility greatly reduces the static consumption of the circuits. The ability to integrate them over logic circuits also reduces dynamic power consumption by reducing data transfer distances between memory and logic, which is an important factor in quantum circuits with the added benefit of reducing the heating of the devices that can introduce noise to the system.

Spin transfer torque perpendicular anisotropy magnetic tunnel junctions (STT-pMTJ) are of particular interest for low-temperature application due to their scalability, non-volatility, and the possibility of adjusting the stability of the cell to a given operating temperature [30, 31]. In the context of HPC [32], it can be envisioned that STT-pMTJ is capable of cryogenic operation at 77K and 4K [33, 34, 35, 36], which would provide a memory solution adapted for more energy efficient computing in these cryogenic environments.

# 2 MRAM operating at room temperature

A strong focus of MRAM research has been to improve the quality of the devices to reduce its energy consumption and its resistance to temperature variation for automotive and industrial applications, requiring strong reliability in a wide range of temperatures, from $-40^oC$ to $125^oC$. With the context for cryoelectronics in place, we open the discussion on the fundamental aspects of this technology at room temperature before delving into the specific requirements to implement it at ranges outside the purview of conventional MRAM research.

At its core, we have the magnetic tunnel junction (MTJ), a trilayer structure comprised of an insulating ultrathin and nonmagnetic layer deposited or grown sandwiched by two ferromagnetic layers with uniaxial anisotropy. And the relative configuration between their magnetizations will define the only two possible stable states in which the MTJ can be in either parallel (P) or antiparallel (AP) states. The conductance of electrons through the barrier will strongly depend on whether we have either P or AP, creating an observable change on the resistance measured for this structure, which will then define the single bit of information for an MRAM. A fully functional bit will also require other magnetic components to its structure to couple and pin one of the ferromagnets, which is called the polarizer or reference layer. In this manner, only one ferromagnet, the storage or free layer, is capable of changing orientation.

There are two main types of magnetic memories, defined by the orientation of the magnetization vectors $\vec{m}$ of the ferromagnets: the in-plane (iMTJ), in which $\vec{m}$ lies on the plane of the film and the perpendicular (pMTJ), with $\vec{m}$ aligned perpendicularly with the film plane. Before the research on perpendicular magnetic anisotropy (PMA) took the field in stride, the development of iMTJs had reached a major bottleneck for increasing its array density. Its state-of-the-art was based on CoFeB/MgO junctions that had magnetostatic field curling issues when their lateral size went below 60nm, inducing vortex magnetization [37]. It could be avoided by fabricating the devices with an aspect ratio of 2 or higher [38], but these elliptical structures are not trivial to manufacture and occupy a larger area that limits its density.

## 2.1 Interfacial perpendicular magnetic anisotropy

We focus our discussion on pMTJs, as they have certain advantages over their IP counterpart in regards to scalability and energy consumption, as will be discussed in the following section. The first commercial product to use PMA was in perpendicular magnetic recording for HDDs in 2005 [39], and since then has expanded extensively into spintronics applications such as MRAMs. The total contribution for the anisotropy of a thin-film material is given by the effective anisotropy:

$$K_{eff} = K_V + K_D + \frac{K_S}{t} \tag{1.1}$$

where we have the bulk magneto-crystalline $K_V$, the demagnetizing $K_D < 0$ and the interfacial $K_S$ contributions to the total anisotropy of the layer, with $t$ being the its thickness. For the dimensions considered in MTJs (sub-5nm films), $K_V$ is usually regarded as negligible, while $K_D$ is the result of dipole-dipole interactions that favors in-plane magnetization. It is present in every finite structure and is the source of shape anisotropy in iMTJs.

This material property has been explored for various material systems, such as Co/Pt and Fe(Co)/MgO. It arises from the interface of ferromagnets with either non-magnetic or insulating/oxide materials, when their thicknesses are limited to just a few monolayers. Currently, the extensive use of FeCoB as the storage layer for pMTJs in part due to its role in iMTJs, when it was discovered that it showed PMA characteristics at below 1.5nm [40]. This effect arises from the spin-orbit coupling between the atoms of the two materials which causes orbital hybridization that is strongly dependent on the crystalline structure of the layers and stoichiometry of the oxide formed at the interface. For example, in Co/Pt multilayers, PMA is only present if the crystal lattice is textured as (111), while for FeCo/MgO, a (001) configuration is needed. For this specific case, it can be achieved by depositing amorphous FeCoB and MgO with a Ta or W buffer layer. During an annealing process, the B atoms are drawn out of the interface and allows the compound to crystallize into the desired texture. Additionally, in over-oxidized interfaces, the hybridization of in-plane orbitals essentially kills the PMA, with only a small reduction for under-oxidized samples [41].

## 2.2 Tunneling magneto-resistance

The ratio between the aforementioned difference of the parallel resistance ($R_P$) and the anti-parallel resistance ($R_{AP}$) of an MTJ is what is defined as the tunneling magneto-resistance (TMR).

$$TMR = \frac{R_{AP} - R_P}{R_P} \tag{1.2}$$

In its infancy, this effect was first demonstrated by Jullière in 1975 [6] at low temperatures using a Fe/Ge/Fe thin-film, showing $TMR = 14\%$ at 4.2K. The observed change in conductance was attributed to the tunneling of electrons through the oxidized semiconductor, whose interfaces with the ferromagnets exhibited Fermi levels with different density of states for majority and minority spins. In parallel, majority/minority spins can tunnel through to majority/minority states, while in anti-parallel, the majority/minority spins tunnel to minority/majority states.

An important step was made in 1995 for alumina (AlOx) tunnel barriers, showing TMR of 11.8% at room temperature [42]. But not until 2004 was the 100% mark broken through with the implementation of crystalline MgO as the tunnel barrier [43], albeit still a far cry from the theoretical prediction value of 1000% from 2001 [44]. In these systems, the simplified density of states model for explaining the TMR was no longer sufficient and a revision was proposed by Butler in 2001. It introduces orbital symmetry tunneling dependence that comes into play with the presence of crystalline structures such as MgO(001) [45]. In Fig.1.2, a schematic representation of the alumina incoherent tunneling is shown in (a), in which all electrons have the same probability of tunneling, while in (b) the crystalline structure of MgO filters out higher order symmetries $\Delta_2$ and $\Delta_5$ of the electrons only $\Delta_1$ has a significant contribution to tunneling. Then in (c) we see a magnetic hysteresis loop for an MRAM bit with a visible TMR signal between the low resistance state P and high resistance state AP. The vectors $\vec{m}$ and $\vec{p}$ are the magnetization vectors for the ferromagnetic layers of the MTJ.

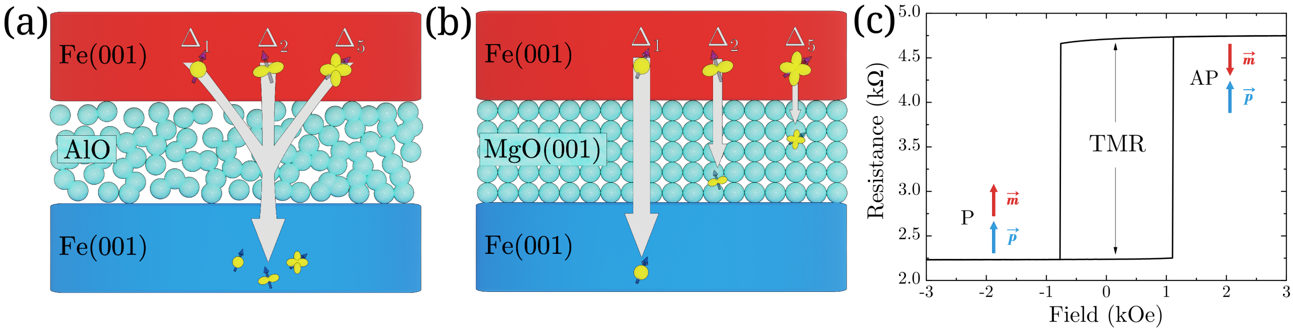

Figure 1.2: Schematic of orbital symmetry tunneling characteristics in a tri-layer using a)Amorphous AlOx compound and b)Crystalline MgO with lattice [001]. c)Example of a magnetic hysteresis loop showing the TMR signal and the distinction between the two stable states P and AP.

TMR is a critical device parameter for technological application as it controls the gap between the read measurement signal from the P and AP states, which is important due to variability in the fabrication process of processor chips. In an array of memory bits, each one may have a slightly different resistance and if the TMR value is too low, this can induce errors in the data storage manipulation if among the resistances we have a condition such as $R_{AP}^{min} < R_{P}^{max}$. Avoiding this overlap of the states is crucial for the level of reliability required in industrial production.

Since its inception, development of higher quality devices has come a long way, from the first reported value of 14%, to improvements with alumina oxides up to 80% [46] and more recently with highly optimized interfaces of FeCo/MgO/FeCo exceeding 600% at RT and over 1000% at 4K [47, 48].

## 2.3 Bit thermal Stability

Another one of the most important properties of a memory cell is the thermal stability Δ, also called the retention factor, which is used as a quality factor for the timescale for which the stored bit will remain unchanged. It was first approached by Néel's theory of relaxation in magnetic nanoparticles [49] and it is derived from Arrhenius' law for the speed of chemical reactions. In an anisotropic magnetic system, much like a reaction, an energy barrier normally separates only two existing stable states, which in our case are the P and AP states of the MTJ. Due to the presence of thermal energy in the environment in the form of $k_BT$, there is a finite possibility that the system will overcome the barrier and stabilize in its alternative state, which in this case is the parallel or antiparallel magnetization configuration. The Néel-Arrhenius equation for the mean transition time between states is expressed as:

$$\tau = \tau_0 exp\left(\frac{\varepsilon_B V_{ol}}{k_B T}\right) \tag{1.3}$$

where $\tau_0$ is the attempt frequency and $\varepsilon_B$ is the energy barrier density. This prefactor describes the time-length scale of the system and is highly dependent on its material properties. Its extraction involves computationally heavy calculations by solving the Fokker-Planck equation for probability diffusion [50], and methods such as Monte Carlo operations are only affordable to be implemented in small systems [51]. Therefore, in experiments, it is usually taken as $10^{-9}s$ as a good approximation for MTJs, and the transition time is spoken of in terms of the exponent factor in the form of:

$$\Delta = \frac{\varepsilon_B V_{ol}}{k_B T} \tag{1.4}$$

Most technologies that use non-volatile memories require extended periods of data retention, up to decades long, while CPU usage for web applications may tolerate cache storage of only a few minutes. This would translate to retentions of $\Delta = 40$ for 10 years and $\Delta = 27$ for 5 minutes for a single bit. To calculate the level of retention for memory arrays, we use a modified version of Eq.1.3 at room temperature of 300K [52]:

$$\Delta = -ln\left(-\frac{\tau_0}{\tau} ln\left(1 - \frac{FIT}{N}\right)\right) \tag{1.5}$$

where $FIT$ is the number of failures in time of the array and $N$ is the size of the array, the probability of failure for N bits is given by:

$$F = 1 - exp\left(-N\frac{\tau}{\tau_0} exp\left(-\Delta\right)\right) \tag{1.6}$$

Depending on the processor density and the architecture requirements for Read/Write Error Rates and the operating temperatures of its cores, the retention can vary substantially, with system-specific optimizations. As an example, for 10-year storage of a 1Mb array at $80^oC$ with 1000 failures, we have $\Delta = 57$, while for 1Gb it scales to $\Delta = 65$.

## 3 Bit writing mechanisms

In this section, three mechanisms for bit writing will be discussed: spin-transfer-torque, voltage-controlled magnetic anisotropy, and spin-orbit-torque. The first two are the focus of the present discussion, and the latter is an honorable mention as it has become increasingly important in the field of MRAM research in recent years. In Fig.1.3, we have a basic circuit schematic for the three mechanisms in order, showing their differences in which direction the writing $I_W$ and read $I_R$ currents are applied and how the bit (BL), write (WL), read (RL) and source (SL) lines are connected to each other.

To understand how the magnetization is susceptible to current manipulation, we look into the dynamics of its precession under these forces through the Landau-Lifshitz-Gilbert equation, which governs the dynamics of a ferromagnet in the presence of magnetic fields:

$$\frac{\partial \vec{m}}{\partial t} = -\gamma(\vec{m} \times \mu_o \vec{H_{eff}}) + \alpha\left(\vec{m} \times \frac{\partial \vec{m}}{\partial t}\right) \tag{1.7}$$

Where $\vec{m}$ is the magnetization of the layer, $\gamma$ is the reduced gyromagnetic ratio, $\mu_0$ is the vacuum permeability, $\vec{H_{eff}}$ is the effective field, $\alpha$ is the Gilbert damping. The first term is responsible for a precessional movement around the $\vec{H_{eff}}$ axis, while the second is the damping term, which controls the rate in which the magnetization relaxes to its equilibrium state. It is important to engineer materials with optimized $\alpha$, as it has two major impacts on an MRAM: the writing speed increases for high damping, while the critical switching current for STT also increases. Therefore, most research focuses

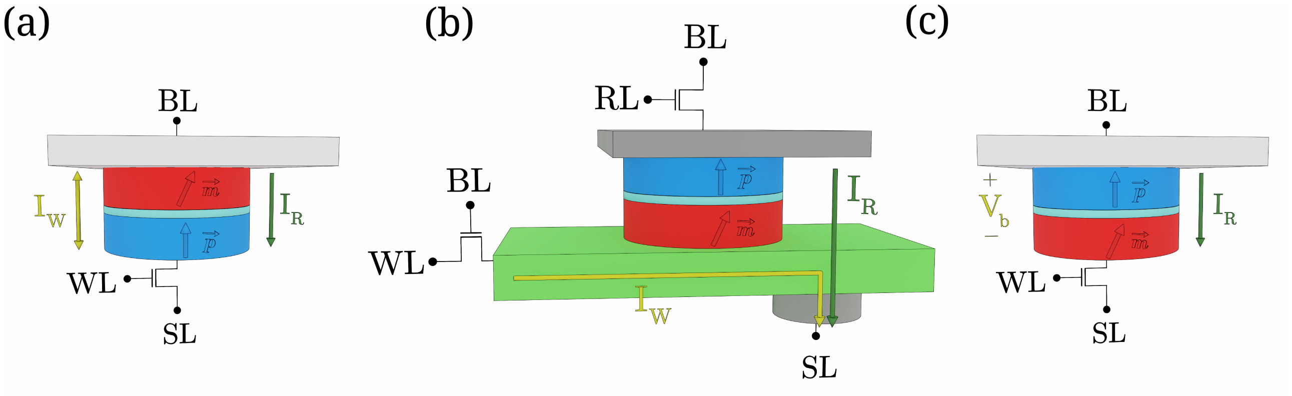

Figure 1.3: Schematics of the circuit connections for bit, write, read and source lines using a)STT, b)SOT and c)VCMA writing mechanisms.

on materials with the lowest damping possible since at the current stage of the technology, reducing the energy consumption takes priority over achieving larger writing speeds.

## 3.1 STT-MRAM

The spin-transfer effect is a phenomenon that occurs at the interface of a FM/NM/FM, in which the non-magnetic layer may be either paramagnetic or an insulating barrier in the case of an MTJ, with the multilayer R/I/F, where R is the reference/polarizer layer, I is the MgO insulator, and F is the free layer. The passage of an electron flux through a ferromagnetic layer will induce an exchange interaction between the incident particles and the local magnetization, which by conservation of angular momentum will absorb some of the incident momentum and vice versa [53]. Thus, considering a current flowing from P to I for our system in question, due to the pinning of our polarizer, the injected current will undergo spin polarization to align itself with the local magnetization $\vec{p}$. Subsequently, the tunneling through the barrier conserves the spin state, which will scatter at the interface with the ferromagnets and act on the free layer that absorbs the angular momentum and initiate a precessional motion with a transverse and parallel component. This current polarity is used to write the P states and, by reversing it, the AP state can be written. The difference is that in the reverse direction, the backscattered electrons going from F to R will act upon the free layer, which are the minority spin components of the electron flux. The imbalance on the occupancy of states will then create an asymmetry on the currents for STT when comparing P-to-AP and AP-to-P writing.

To describe the effect mathematically, the LLG equation that governs single-spin dynamics can be modified by adding the Slonczewski term for spin-transfer (or current-driven) torque, given by [53]:

$$\Gamma_{STT} = -\gamma a_{\|}(\vec{m} \times (\vec{m} \times \vec{p})) + \gamma a_{\perp}(\vec{m} \times \vec{p}) \tag{1.8}$$

The spin torque, given by the parallel term $\vec{m} \times (\vec{m} \times \vec{p})$, is sometimes referred to as a damping-like term where $\dot{\vec{m}}$ is the time derivative of the magnetization. And the precessional transverse torque $(\vec{m} \times \vec{p})$ is called field-like because of its mathematical similarities with the LLG contributions [54]. Under currents below the critical threshold for switching $I < I_C$, the magnetization will precess around the easy axis from the effects of the field-like torque and its angle $\theta$, given by $\vec{m} \times \hat{n}$, will increase to

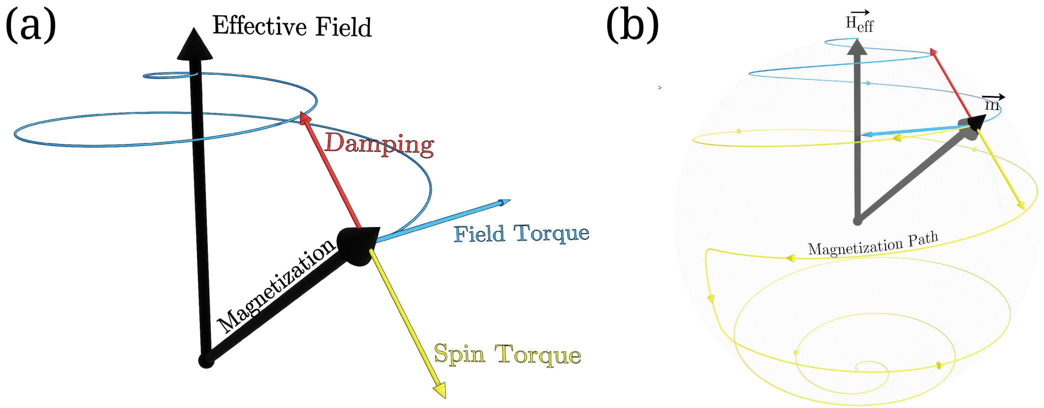

Figure 1.4: a)Schematic representation of the forces upon the magnetization of a ferromagnetic layer being driven by an STT current and the pathway in blue in the condition $I_b < I_C$. b)Switching pathway representation if $I_b > I_C$.

compensate the energy dissipation coming from the Gilbert damping. Here, $\hat{n}$ is the normal vector of the plane of the ferromagnetic layer. In Fig.1.4a we have a representation of the forces involved, with the directions in which each pulls the magnetization; with the line in blue is the relaxation path after the current is removed. If the condition $I > I_C$ is reached, the spin-torque effect is strong enough to overcome the energy dissipation and cross the in-plane hard axis, changing the rotation chirality and stabilizing in the opposite stable state, shown in Fig.1.4b.

As previously mentioned, the in-plane configuration for STT-MRAM had limitations on the scalability due to the anisotropy magnitude that was capped by the geometry of the cell. This also meant that the switching itself had an extra barrier to overcome to reach criticality, expressed by the current density necessary for writing.

$$J_C^{IP} = \frac{4e}{\hbar}\frac{\alpha k_B T}{\eta A}\left(\Delta + \frac{\pi M_S^2 V_{ol}}{k_B T}\right) \tag{1.9}$$

where $\eta$ is the STT polarization and $A$ is the surface area of the device. The second term in parentheses is the extra energy that iMTJ needs to switch. Compared to the perpendicular critical current density, it is clear that this configuration brings advantages that cannot be surmounted.

$$J_C^{\perp} = \frac{4e}{\hbar}\frac{\alpha k_B T}{\eta A}\Delta \tag{1.10}$$

The expression of the critical current density assumes that the switching pulse $\tau$ injected into the layers has an infinite duration and it is an important distinction to make, as it can have a drastic influence on the necessary energy required to write a bit. In literature work, two writing regimes can be distinguished: thermally assisted or thermally activated, which is derived from the Néel-Brown model [55], and ballistic, which arises from an over-driving current [56]. The first one is defined as:

$$I_C = I_C(0)\left(1 - \frac{k_B T}{\varepsilon_B V_{ol}} ln\left(\frac{\tau}{\tau_0}\right)\right) \tag{1.11}$$

And the ballistic regime can be described as [57]:

$$\frac{1}{\tau} = A(I - I_C(0)) \tag{1.12}$$

with $A$ being a dynamic parameter that controls the switching rate. The gap between the two modes arises from the speed at which the misalignment angle between the two ferromagnets fluctuates due to thermal energy. If the writing pulse is faster than the given temperature can influence $\vec{m}$, then the current needed to switch it will have a much larger dependence on its pulse width, going with $1/\tau$ instead of a logarithmic function.

## 3.2 SOT-MRAM

Spin orbit torque (SOT) is often referred to as the next step in the MRAM development timeline and was first proposed in 2011 [58]. It is a mechanism that relies on the spin-orbit coupling of an injected electron flux with the crystal lattice of a heavy metal material that generates a spin-hall effect (SHE-SOT), accumulating polarized electrons on the surface of the heavy metal that can be interfaced with a ferromagnet, which will absorb the spins in an analogous form as if an STT current was injected [59]. The illustration of such a writing scheme is shown in Fig.1.5, where an in-plane writing current is used to switch a three-terminal MTJ bit. It has the potential to outperform STT switching in terms of switching speeds down to sub-ns [60] with lower power dissipation, high endurance and a much lower read disturbance rate due to the splitting of the Read-Write pathways into two separate lines. Additionally, due to the spin-hall effect, the SOT writing is symmetric in regards to PAP and APP switching, with a spin current density absorbed by the storage layer given by

$$j_{SOT}^{SHE} = \frac{\hbar}{2e}\eta\theta_{sh}\sigma_N E \tag{1.13}$$

where $\eta$ here is the spin injection efficiency (or transparency) across the NM/FM interface, $\theta_{sh}$ is the spin hall angle of the non-magnetic material with conductivity $\sigma_N$ and $E$ is the orthogonal applied in-plane electric field. The write path, not passing through the tunnel barrier, also allows for over-driving currents to operate the bit at much faster switching speeds without incurring in dielectric breakdown of the junction.

These new features of SOT have generated much research for its ability to substitute DRAM and SRAM and L1-level cache, although there are still obstacles to tackle for its industrial applicability, such as a reduced density capacity of the three-terminal configuration and the external field requirements to create the SHE [61].

Solutions for these challenges have been proposed in the form of field-free switching [62], STT-assisted devices [63] and its architecture studies shed light on the limitations of both STT and SOT and the advantages of each one [64] .

## 3.3 VCMA-MRAM

Unlike the previous two writing mechanisms, voltage-controlled magnetic anisotropy is an effect that relies, as the name implies, on the modulation of the anisotropy with an applied voltage bias $V_b$ across the tunnel barrier. It has been determined to have a linear effect on the surface anisotropy of the form [65]

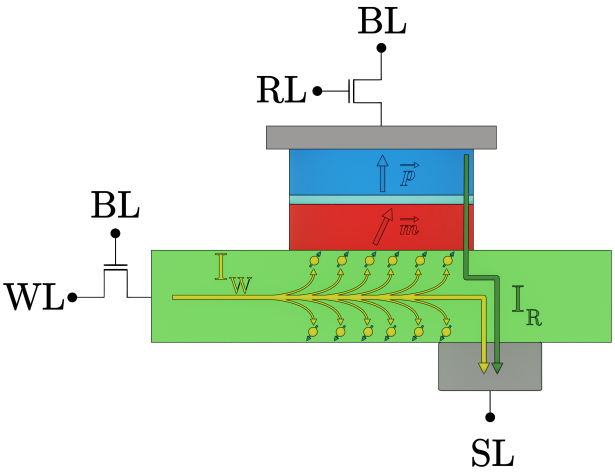

Figure 1.5: SOT bit scheme, showing the spin polarized flow of electrons of the SOT track in green, created by the writing current $I_W$.

$$K_S(V) = K_{S_0} + \xi \frac{V}{t_{MgO}} \tag{1.14}$$

In this expression, $\xi$ is the VCMA coefficient, $t_{MgO}$ is the thickness of the tunnel barrier, and $K_{S_0}$ is the surface anisotropy at zero bias. In Fig.1.6a, we see the effects that different applied voltages have on the energy density of a pMTJ free layer, with negative bias increasing the barrier between states and it reducing to zero at $V_b = 0.23V$. Above this critical threshold, the two stable states merge into a single state at $\theta = \pi$, which correspond to the in-plane position. As we have seen, the magnetic properties of a thin ferromagnetic layer exhibiting PMA are strongly dependent on surface effects that arise from electron occupancy of hybrid orbitals. The application of an electric field across the MTJ by supplying voltage to the circuit will modify the band structure of the interface and the density of states of these orbitals will change accordingly, altering the magnitude of the surface anisotropy by means of a spin-dependent screening effect [66, 67]. This effect has been observed to have a linear dependence, although other literature discussions on its nature also suggest a second-order dependence via Rashba spin-orbit coupling [68]. To define the critical switching voltage of a VCMA device, we can use the expression for the stability factor in Eq.1.4 and Eq.1.14. By equating $\Delta(V_b) = 0$, we have [69]:

$$V_C = \Delta(0) k_B T \frac{t_{MgO}}{\xi A} \tag{1.15}$$

The tunnel barrier for this type of device usually has much higher resistance, going from $\approx 1-10k\Omega$ for STT to $> 100k\Omega$ for VCMA, suppressing most of any possible STT effect on the bit and, for that, drastically reducing its energy dissipation. However, one of the disadvantages is that it necessarily requires a break in the symmetry of its azimuthal angle by means of an in-plane applied field or other methods, such as using magnetostriction [70] or elliptical junctions [71]. As a voltage is applied, the energy barrier that separates its P and AP states reduces until it eventually vanishes for $V_b > V_C$. At this stage, if the effective field of the system has a preferred direction that is not collinear with the

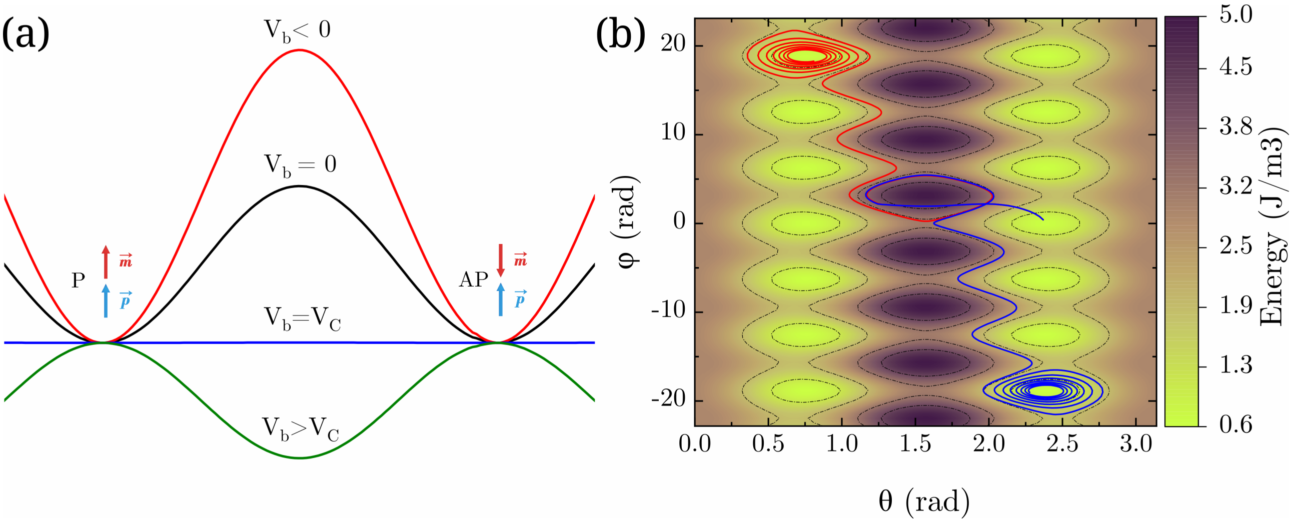

Figure 1.6: a)Energy density dependence with magnetization angle for different applied biases. b)2D representation of the magnetization motion under applied bias for two different pulse lengths. The red switches from AP to P while the blue back-switches to AP. The angles $\phi$ and $\theta$ are relative to the plane rotation and the vertical axis, respectively.

magnetization, it will start precessing around $\vec{H_{eff}}$, continuously passing through both states until it either relaxes into the field direction or the voltage is turned off. If the field is not present, the system will appear static, as exemplified in Fig.1.6b.

Another particularity of this mechanism is its precessional nature. It requires a writing scheme that uses monopolar currents, classifying it as a toggle-switch system, meaning that a single current pulse can write either P or AP states. This presents some difficulty in integrating it with the conventional CMOS architecture, as the pulse widths used must be very narrow and with low losses along the connection lines to avoid writing errors. The frequency of the motion depends on the external magnetic field and can have a short time window $t_{sw}$ to complete a single half-precession to switch, around 500ps [72]:

$$t_{sw} \approx \frac{\pi(1-\alpha^2)}{\gamma\mu_0 H_{IP}} \tag{1.16}$$

These characteristics can have favorable roles, however, depending on its application due to its high-speed switching, separation of current polarity for Read/Write operations, and the very low currents used, which allow transistor down-scalability and much lower energy consumption.

## 4 From room temperature to cryogenic operations

In a memory, an optimal trade-off imposed by the previously mentioned trilemma has to be achieved between stability of the written information (retention of the memory) and energy necessary to change its state. Compared to conventional memories, at our operating temperatures for these circuits (for example, 1K to 4K), the available thermal energy $k_B T$ is reduced by 1-2 orders of magnitude compared to the ambient temperature of 300K, which considerably increases the thermal stability of the magnetization of the storage layer in MRAM cells and allows us to reduce the magnetic anisotropy of our devices by the same factor of 10-100 while maintaining a reasonable memory retention. For example, a bit with an energy barrier of $E_B = 15000k_B$ would have a stability $\Delta^{300K} = 50$ at room temperature, while one with $E_B = 150k_B$ would have $\Delta^{3K} = 50$, and since the critical switching currents necessary to write with STT are proportional to $E_B$, the energy pumped into the system will be reduced accordingly.

The total write energy will consist of the dissipative $E_D$ losses, which can be derived by Ohm's Law $V = RI$ and $E = \int Pdt$, where $P$ is power:

$$E_D = \int_0^\tau \frac{V_C^2}{R_P} dt \tag{1.17}$$

and the capacitive $E_C$ losses, derived by the integration of the work done to charge a capacitor:

$$E_C = \frac{CV_C^2}{2} \tag{1.18}$$

where $C$ is the capacitance of the tunnel junction. As a result of the smaller $E_B$, the write current of the memory can be decreased compared to conventional memories operating at ambient temperatures. However, to achieve this, it requires us to completely re-optimize its structure (composition of the stacks, shape of magnetic pillars) and take into account possible obstacles for high performance in the form of writing latency due to reduced thermal activation and the increase of the switching currents at low temperatures, which can influence the duration of the writing pulses and stochasticity of the switching from local heating of the cell.

In the context of quantum technologies, cryoelectronic components are needed to control qubits. For these applications, including possible direct interfacing, the first obstacle for integration is the power dissipation of the memory. For STT and SOT, Joule heating is inevitable, becoming a source of noise and decoherence for the qubits. Therefore, it is necessary to optimize the whole system, as the available typical dilution refrigerators have a cooling power in the range of a few dozen $\mu W$ to a few hundred $\mu W$, operating from 20 to 120 mK [73, 74]. Current MRAM development must achieve higher electrical efficiency of the writing process to become compatible with the expected refrigeration cooling powers of these ultra deep cryogenic systems. The requirements for interfacing with HPC components in 4K operation are less strict, with state-of-the-art refrigeration achieving almost 1000W of available power [75]. Compared to non-volatile memory technology such as Phase Change RAM (PCRAM) or Resistive oxide RAM (RRAM), MRAM has the advantage of not relying on a local heating of the cells during write, which would be detrimental for low temperature operation.

## 4.1 Impact on the design of STT-MRAM

Implementation of STT-MRAMs into quantum circuits is feasible due to our approach based on the easy-cone regime for storage layers. It is an intermediate MTJ configuration that has characteristics from both perpendicular and in-plane junctions, with its magnetization in a stable canted state relative to the film plane, rather than completely out-of-plane. This is an important point to tackle in designing devices for very low temperatures because even though the mechanism for STT is not technically thermally assisted, by the nature of the torque from Eq.1.8, the vectorial product between the storage layer and the polarizer means that, unequivocally, a misalignment must exist for the switching to be initiated. Normally, this small angle is provided by $k_B T$, which in cryogenic environments is strongly reduced. Therefore, rather than using conventional pMTJs, this regime waives the necessity for thermal fluctuations to trigger the spin-torque switching by having a permanent and ideally constant angle that can potentially decrease the stochasticity of the logic operations and avoid a large writing latency. The easy-cone state will be discussed in greater detail in the following chapters.

In Chapter 3 we will also explore methods to reduce the total anisotropy of the storage layer, which will ideally balance its stability with the much lower $k_B T$ and retain an adequate value for $\Delta$ with respect to its intended application.

### 4.2 Integration of VCMA-MRAM in cryoelectronics

VCMA is one of the most promising MRAM variants to be integrated with HPCs. It has very low or negligible Joule heating and can switch in the GHz range. The high pulse precision required for low BER is also mitigated by the fact that Josephson junctions also operate at very high speeds, meaning that the superconducting electronics are already adapted to be used with it.

MRAM functionality should also be concerned with parasitic fields coming from quantum processors. Certain categories of qbits function under an applied magnetic field to split the energy level degeneracy [76], which would normally act on an MRAM to decrease its thermal stability, but it can be a considerable advantage to VCMA systems. Instead of isolating the memory element, it can potentially be integrated at the same hierarchy level of the qbit and use its uniform field to set the precessional effective field axis. By engineering the bit to require the same field magnitude, this major disadvantage of VCMA-MRAM can be resolved.

## 5 Thesis objectives

The first objective is to analyze a toy model of an MTJ by performing numerical simulations using a macrospin and micromagnetic approach. From it we can acquire a better understanding of the STT and VCMA mechanisms and develop a better insight to optimal MRAM cell parameters (composition, operating voltage, write pulse duration, etc.). Additionally, a comparison with systems at absolute zero and room temperature will be valuable for pointing out the main advantages and disadvantages when working in a cryogenic environment.

The second objective is to conceptualize and fabricate new stack structures for our MTJs to achieve very low energy barriers and, consequentially, low switching energies. These studies are initially conducted at room temperature and are followed by their magnetic and electrical characterization at low temperatures to assess the next steps that can be taken to refine our ideas for device optimization.

From the presented methods and available technologies for faster computing, this project has the potential to be a step towards cryogenic computing with reliable memory storage.

# Chapter 2

# Macrospin and Micromagnetic Numerical Simulations

Goals

In numerical simulations of magnetic systems, there are two available approaches, the macrospin or micromagnetic approximations. The macrospin approximates the system into a single cell, where the magnetization behaves as a single spin. The second considers a division of the system into separate cells with their own magnetization, allowing for the distinction of domain-wall motion. Thus, macrospin has a much simpler analytical model and requires less computational time. Both approaches will be investigated in the following sections using the model described previously. Data analysis will be done looking at the switching dynamics for both STT and VCMA cases.

## Contents

# 1 Macrospin Model

To investigate the switching and relaxation dynamics of STT and VCMA systems, macrospin numerical simulations were performed on a trilayer system defining a magnetic tunnel junction. The construction of the model was based on the stack design explored in the previous chapter, and its basic schematics are depicted in Fig.2.1, in which the bottom layer is the pinned reference layer and the top is the storage layer, separated by a tunnel barrier with a parametrically defined resistance.

The macrospin model assumes that the total magnetization $\vec{M}$ of a layer, or the total sum of individual spins of a magnetic system, can be approximated by a single spin. This means that $\vec{M}$ behaves coherently with no domain formation, i.e., with a uniform magnetization. Additionally, for our purposes, the following assumptions were made to construct the numerical model.

1. The polarizer/reference layer has much higher stability than the storage layer, therefore, any STT effect will be negligible acting upon it.
2. The storage layer has a second-order anisotropy contribution $K_2$.
3. The VCMA effect is present and acts linearly on the first order anisotropy $K_1$.
4. The tunnel junction has finite dimensions and a non-trivial demagnetization tensor $\bar{N}$.
5. Heating effects are present and are taken into account in the material parameters.

This initial setup is used to customize the parameters of the Landau-Lifshitz-Gilbert equation, which we reiterate here from Chapter 1:

$$\frac{\partial \vec{m}}{\partial t} = -\gamma(\vec{m} \times \mu_o \vec{H_{eff}}) + \alpha\left(\vec{m} \times \frac{\partial \vec{m}}{\partial t}\right) + \left(\frac{\partial \vec{m}}{\partial t}\right)_{STT} \tag{2.1}$$

Where $\vec{m}$ is the magnetization of the layer, $\gamma$ is the reduced gyromagnetic ratio, $\mu_0$ is the vacuum permeability, $\vec{H_{eff}}$ is the effective field, $\alpha$ is the Gilbert damping and the last term of the equation is the Slonczewski term for spin-transfer torque, given by [53]:

$$\left(\frac{\partial \vec{m}}{\partial t}\right)_{STT} = -\gamma a_{\|}(T, V_b)[\vec{m} \times (\vec{m} \times \vec{p})] + \gamma a_{\perp}(T, V_b)(\vec{m} \times \vec{p}) \tag{2.2}$$

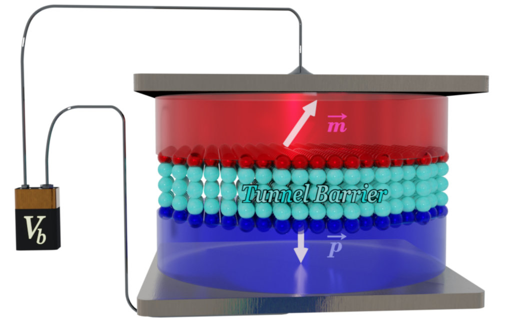

Figure 2.1: Illustration of simulation system, with a free storage layer $\vec{m}$ and a fixed polarizer $\vec{p}$ with a tunnel barrier subjected to bias voltage $V_b$.

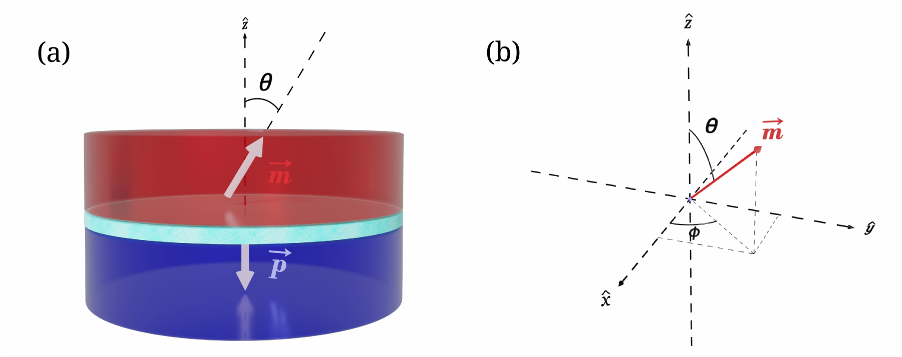

Figure 2.2: a) Cartesian coordinates of the system. b) Definition of the angles of $\vec{m}$ in spherical coordinates.

in which the first and second terms are the damping-like and field-like torque, respectively, and $\vec{p}$ is the magnetization of the polarizer. The factors $a_{\parallel}$ and $a_{\perp}$ are dependent on temperature $T$ and voltage bias $V_b$, here expressed as:

$$a(T, V_b) = a_0(T) + a_1(T)V_b + a_2(T)V_b^2 + \cdots \tag{2.3}$$

In perpendicular MTJs, the field-like torque $a_{\perp}$ has a negligible contribution to STT, therefore it is not taken into account in the model[77]. The reference axis for the denomination of each component of the magnetization and the angles involved are shown in figure 2.2.

To calculate the solution for a given system, the energy density $\varepsilon$ must be expressed in its entirety, for which then we can obtain the effective magnetic field, defined generally by

$$\vec{H} = -\frac{1}{\mu_0 M_S}\frac{\partial \varepsilon}{\partial \vec{m}} \tag{2.4}$$

Each contribution to the system can be treated separately, with consideration to the energy expressions for the anisotropy, demagnetization, thermal energy, external applied field, VCMA effect and magnetoelastic energy:

$$\vec{H_{eff}} = \vec{H_{PMA}} + \vec{H_{demag}} + \vec{H_{th}} + \vec{H_{zeeman}} + \vec{H_{VCMA}}(V_b) + \vec{H_{me}}(V_{PZT}) \tag{2.5}$$

In the following subsections we delve into each term in more details and expand on their contributions.

## 1.1 Exchange energy

The exchange interaction is a purely quantum mechanical effect that, for electrons, stems from the Pauli exclusion principle. The indistinguishability of fermions gives rise to an exchange integral $J_{ex}$ in the Heisenberg model that dictates whether a material is ferro- or anti-ferromagnetic [78] depending whether $J_{ex}$ is either positive or negative, respectively. Its Hamiltonian is given by:

$$\hat{H_{ex}} = -\sum_{i,j} J_{i,j} < \vec{S_i} \cdot \vec{S_j} > \tag{2.6}$$

Where $< \vec{S_i} \cdot \vec{S_j} >$ is the scalar product between adjacent spins and $J_{i,j}$ is the exchange constant. For conductive solids, its metallicity demands the use of an alternative model that treats electrons as being delocalized. The Stoner model has seen some success in estimating $J_{ex}$ for ferromagnets, whose energy can be expressed as:

$$E_{ex} = \int_V A_{ex}\{(\nabla m_x(\vec{r})^2 + (\nabla m_y(\vec{r})^2 + (\nabla m_z(\vec{r})^2\}\, dr \tag{2.7}$$

Where $A_{ex}$ is the exchange stiffness and dependent on the crystal's lattice parameter of its unit cell. In materials that show an intermediate behavior between localized/delocalized orbitals, the established model was developed by Ruderman–Kittel–Kasuya–Yosida (RKKY). It is a constant term for the macrospin model, since the magnetization is supposed to be uniform, becoming an important contribution to the overall energy in micromagnetic simulations.

### 1.2 Zeeman energy

In the presence of an external applied field $\vec{H_{app}}$, the magnetization vector $\vec{m}$ of the storage layer will favor alignment in the field direction to minimize energy and can be expressed as [79]:

$$E_{zeeman} = -\mu_0 M_S \int_V \vec{m} \cdot \vec{H_{app}} dV \tag{2.8}$$

For the macrospin approximation, this expression is reduced to $-\mu_0 M_S \left(\vec{m} \cdot \vec{H_{app}}\right)$, as a single domain is taken into account.

### 1.3 Demagnetization energy

Each spin in a ferromagnet can be approximated to a magnetic dipole, which "sees" its neighbors through magnetostatic interactions. If only this contribution is taken into account, the energy of two spins would be minimized in an antiparallel configuration, but in a large system such as a thin-film a single spin is under the influence of virtual charges created by the magnetic volume of the layer through dipole-dipole interactions. This virtual charge distribution will strongly depend on the geometry of the system, which is why it is also called "shape anisotropy", and is non-uniform due to surface effects. The overall field created this way is called the demagnetization field and it interacts with the magnetization state of the layer. The demagnetization energy density is defined in a magnetic system as:

$$\varepsilon_{demag} = -M_S \sum_{i,j} \vec{m_i} N_{ij} \vec{m_j} \tag{2.9}$$

The demagnetization tensor $\bar{N}$ is a 3x3 matrix and is directly related to the geometry of the system, with its diagonal terms imposing the preferred axial orientation for the crystalline anisotropy. For thin films, $\bar{N}$ is a diagonal matrix with $N_{xx} = N_{yy} = 0$ and $N_{zz} = 1$. For the case of a circular MTJ, we must calculate $\bar{N}$ for its finite dimensions.

$$\bar{N} = \begin{pmatrix} N_{xx} & N_{xy} & N_{xz} \\ N_{yx} & N_{yy} & N_{yz} \\ N_{zx} & N_{zy} & N_{zz} \end{pmatrix} \tag{2.10}$$

And since we have azimuthal symmetry in our system, we only need to compute the diagonal terms of $\bar{N}$ as the cross terms are negligible, reducing the demagnetizing energy to:

$$\varepsilon_{demag} = -\frac{1}{2}\mu_0 M_S^2 \vec{m} N \vec{m} \tag{2.11}$$

## 1.4 Interfacial magnetic anisotropy energy

The perpendicular magnetic anisotropy energy density can be expanded into higher-order terms and is generally defined as:

$$\varepsilon_{PMA} = -\sum \frac{K_{i,s}}{t_{SL}}(\hat{n}\cdot\vec{m})^{2i} \tag{2.12}$$

Where $t_S L$ is the thickness of the storage layer, $\hat{n}$ is the normal vector to the surface plane and $K_{i,s}$ is the surface anisotropy term of $i$th order. $\varepsilon_{PMA}$ can contain high-order terms such as $K_2$ and $K_3$ with each higher-order term having decreasingly smaller contributions to the total energy. As such, the $3^{rd}$ order term and beyond are usually neglected in calculations. The total PMA field will then be given by:

$$\mathbf{H}_{PMA_i} = -N_{ii} M_S \vec{m}_i + \frac{2K_1(\vec{u}_k \cdot \vec{u}_i)}{\mu_0 M_S} + \frac{4K_2(\vec{u}_k^3 \cdot \vec{u}_i)}{\mu_0 M_S} \tag{2.13}$$

The nature of the second-order anisotropy can be attributed to existing inhomogeneous properties of the thin film layer, which leads to spatial fluctuations of the first-order anisotropy. It can be described by a single constant $K_2$ [80] [81].

## 1.5 Magnetoelastic energy

For the magnetoelastic contribution to be significant, the system would have to be grown on a PZT substrate, on which we can apply a transverse voltage $V_{PZT}$ and induce strain on the magnetic material, creating an effective axial in-plane field [82] [83][84].

$$\vec{H_{me}} = \frac{3\lambda_{100}}{\mu_o M_S}[\sigma_x(V_{PZT})\vec{m_x} + \sigma_y(V_{PZT})\vec{m_y}] \tag{2.14}$$

In $\vec{H_{me}}$, $\lambda_{100}$ is the magnetostriction coefficient along the 100 lattice direction and $\sigma_i$ is the stress along the $i$ axis. It is presented here as a possibility of application and will not be considered in this work.

## 1.6 Model including VCMA effect

To include the voltage modulation to the model, we treat the VCMA contribution as a separate field that will be included in the total effective field.

$$\vec{H_{VCMA}} = -\frac{1}{\mu_0 M_S}\frac{2\xi}{t_{SL}t_{MgO}}V_b\vec{m_z} \tag{2.15}$$

However, it can also be more intuitively seen as a modulation of the surface anisotropy of the magnetic material in the storage layer, as discussed in the previous chapter. There are two possible ways of defining this modulation, either as a second order, or as a first order parameter. Previous work on the origins of the effect has pointed out that a Rashba Spin-Orbit anisotropy mechanism is directly modulating the anisotropy of the system [85], which is proportional to $V_b^2$, but most experimental literature reports a linear dependence of $\vec{H_{VCMA}}$ [65], so Rashba-induced effects will not be considered in simulations.

As discussed previously, the VCMA effect modulates the anisotropy of the storage layer, adding a linear term to the first-order anisotropy constant:

$$K_1(V_b) = K_1(0) - 2\xi\frac{V_b}{t_{SL}t_{MgO}} \tag{2.16}$$

Due to the inclusion of second-order anisotropy $K_2$, it could be assumed that it also depends on voltage, but it has been measured to induce only a negligible modulation [65], so it is not taken into account in the total $\vec{H_{eff}}$.

Gilbert damping can also depend on voltage bias and thickness of the storage layer, which, for device optimization purposes, will be set at higher values than the threshold for $\partial\alpha/\partial E \approx 0V/nm$ ($t_{th} = 1.5nm$) [86], so it is also not taken into account in the simulations.

## 2 The role of temperature in the model

The inclusion of temperature in this study is important in understanding the evolution of the switching dynamics of pMTJs. It is especially interesting how it may diverge from the expected behavior of conventional room-temperature devices. We highlight three effects: the thermal field/thermal noise, the temperature dependence of material parameters, and self-heating from applied current.

### 2.1 The stochastic LLGS equation

To account for stochasticity in the system, we introduce a random thermal field into $H_{eff}$ of the form [87]:

$$< H_{th} > \approx 0 \tag{2.17}$$

$$< H_{th}^2 > = f\sqrt{\frac{\alpha}{1+\alpha^2}\frac{2k_BT}{\gamma V_{ol}dtM_S}} \tag{2.18}$$

where $f$ is a random Gaussian function without correlation with standard deviation equal to 1, $V_{ol}$ is the volume of the storage layer and $dt$ is the time integration step. The model utilized to compute $dt$ is taken from [88]. This field has a mean of zero with temperature, inducing a fluctuating total effective field that will act on the angle of magnetization. The mean value of $\vec{m}$ will remain static, while its position with time changes according to the intensity of the temperature setpoint.

## 2.2 Material parameter variation with temperature

Due to the presence of thermal energy, any given magnetic parameter of a material, such as saturation magnetization $M_S$ will be measured as the mean value of a disordered system of spins not at absolute zero. This disorder is proportional to temperature, due to Eq.2.18, and becomes increasingly chaotic as it approaches the Curie temperature where $M_S = 0$. Fortunately, we can model our system analytically using the Curie-Bloch equation to describe the profile of the magnetization saturation dependence with temperature $M_S(T)$ [89] [90]:

$$M_S(T) = M_S(0)\left[1 - (\frac{T}{T_C})^a\right]^b \tag{2.19}$$

Here $M_S(0)$ is the magnetization at absolute zero and $T_C$ is the Curie temperature. In bulk ferromagnetic materials it is well established that $M_S$ varies under a $T^{3/2}$ power [91], but for materials such as nanoparticles and thin films there is a measurable deviation that we can fit through the exponents $a$ and $b$ [92][93]. We assume the same characteristics for the dependence of the damping-like STT factor:

$$a_\parallel(T) = a_\parallel(0)\left[1 - (\frac{T}{T_C})^a\right]^b \tag{2.20}$$

The Curie temperature, defined as the temperature in which the magnetization of a material loses its spontaneous ferromagnetic properties and becomes paramagnetic, has been shown to be voltage dependent in 2D systems [94]. This effect originates from the energy dependent $T_C$ that depends on the charge carrier concentration of the valence bands in the metal structure when the spin-orbit coupling is included in the calculation of its density of states. The total effect measured was reported to be a change of 10% under the gate voltage applied at 125V. Since simulations are calculated at temperatures and voltages much lower, we consider this effect to be negligible.

For the dependence on magnetic anisotropy, we use the general derivation of the $l(l+1)/2$ law of ferromagnetic molecular field theory [95, 96]

$$K_1(T) = K_1(0)\left[\frac{M_S(T)}{M_S(0)}\right]^{l(l+1)/2} \tag{2.21}$$

where the exponent $l$ has previously been determined in W / CoFeB / MgO thin film materials [97]. Although atomistic calculations have found that the scaling exponent is reduced when a dead magnetic layer is considered or if the magnetic layer has surface imperfections at the MgO/Fe interface [98]. An inclusion of higher-order terms like $K_2$ would a-priori follow the same general theory as $K_1$ and in fact it has been reported that spatial fluctuations $\delta K_1$ follow $K_1$, leading to $K_2(T) \propto (\delta K_1(T))^2$ [99], meaning $l_{K_2} = 3$.

It can be further corroborated by numerical analysis of the angle of the easy cone and using material parameters from the same work: $M_S = 1.17MA/m$, $K_S = 2.3mJ/m$, and $t_{SL} = 2.8nm$. We also assume a dead layer thickness of 0.5nm based on experimental evidence, from measurements in

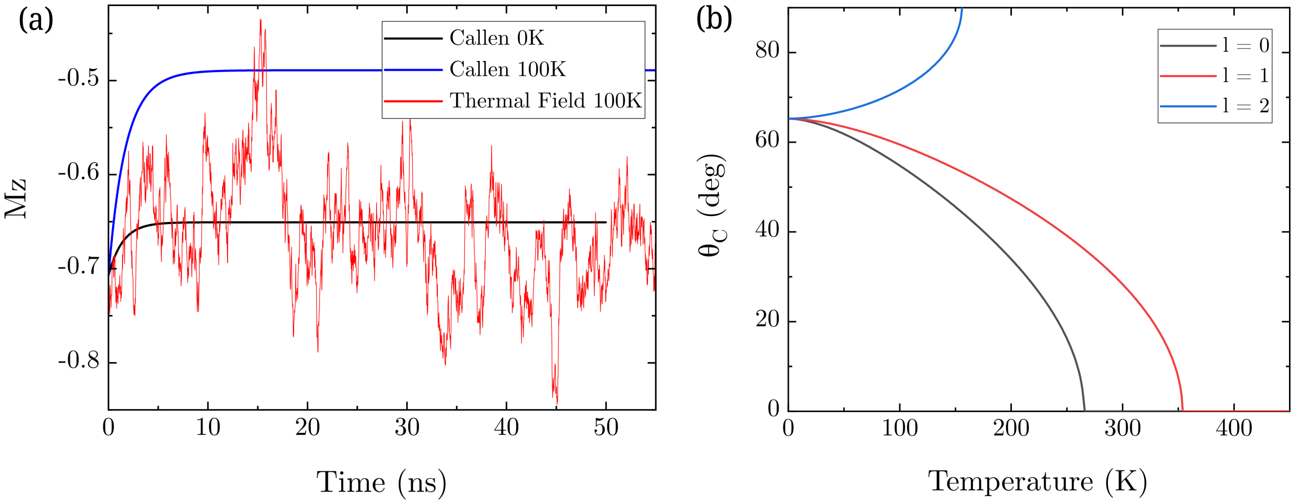

Figure 2.3: a) Relaxation of $m_z$ at 0K and 100K with thermal fluctuations in red and using the Callen-Callen law in blue, showing the distinction between the two models. b) Easy cone angle dependence with temperature for $l = 0, 1, 2$ of the Callen-Callen exponent from equation 2.21.

Chapter 3, and calculate the dependence of $\theta_C$ with $T$ for thin films with $l = 0, 1, 2$, as shown in Fig. 2.3b[1].

From the three curves presented, only the one with $l = 2$ has the expected behavior from the experimental data [99], in which the easy cone angle increases with increasing temperature. For values lower than 2, the equilibrium state of $\vec{m_Z}$ at higher temperatures is out of plane, resulting in a system that has higher anisotropy, in conflict with Eq.2.12 since $K_2 < 0$. Fig. 2.3a[2] shows the comparison between the application of the power law and the random thermal field on magnetization, showing the effects on the relaxation of $m_z$ for 0K and 100K.

The random fluctuating field, often introduced using Langevin dynamics, simulates the thermal fluctuations that arise due to the system's finite temperature. This component accounts for the stochastic nature of thermal fluctuations and is essential for modeling the stochastic dynamic behavior of the magnetic system at finite temperature. However, using random fluctuating field alone to describe the temperature dependence of magnetization or anisotropy often requires introducing unrealistically high value of effective temperature. For this reason, we also introduced in our simulations a temperature dependence of magnetization and anisotropy. These temperature-dependent parameters describe how the material's magnetic properties change as a function of temperature. When both of these components are included in the simulation, one may seem to double-count the effect of thermal fluctuations. However, by doing so, we can model the impact of thermal fluctuations on the device properties beyond what is captured by the temperature-dependent parameters and in particular the stochastic nature of magnetization switching.

Another important parameter to consider is the exchange stiffness $A_{ex}$ in Eq.2.22, which plays a role in the reversal dynamics of the magnetization as it controls the exchange interactions between

---

[1] Simulation parameters for Fig.2.3b: $Diameter = 64nm$, $t_{SL} = 1nm$, $R_P = 5k\Omega$, $T = 0K$, $K_1 = 0.6MJ/m^3$, $K_2 = -0.05MJ/m^3$, $M_S = 1MA/m$, $\xi = 0fJ/Vm$, $H_{app} = 0mT$, $\alpha = 0$

[2] Simulation parameters for Fig.2.3a: $Diameter = 64nm$, $t_{SL} = nm$, $R_P = k\Omega$, $T = 0 - 100K$, $K_1 = 0.6MJ/m^3$, $K_2 = -0.0207MJ/m^3$, $M_S = 1MA/m$, $\xi = 0fJ/Vm$, $H_{app} = 0mT$, $\alpha = 0$

spins. The model used here has been reported to fit well for a wide range of temperatures, with a higher degree of reliability for temperatures much lower than $T_C$, which is the range we are concerned with [100]. There is a general discussion in the literature as to the correct formalism to model this dependence, where we adopted the following variation of the exchange stiffness constant $A_{ex}(T)$ [101] :

$$A_{ex} = A_{ex}(0)\left(\frac{M_S}{M_{S_0}}\right)^{1.8} \tag{2.22}$$

## 2.3 Joule Heating or current heat dissipation

As a current is applied through the barrier, which is an insulator, the model is set to raise the temperature of the system accordingly. The heating equation used takes into account the shape of the current pulse to create a dynamic temperature profile with time. It is derived from the first law of thermodynamics as a simple one-dimensional differential equation [102]:

$$\frac{dT}{d\tau} + \frac{Q}{C}(T - T_0) = \frac{[V(\tau)]^2}{CR} \tag{2.23}$$

where $Q$ is the heat transfer coefficient, $C$ is the heat capacity, $T_0$ is the temperature at time $\tau$, at temperature $T$ and at time $\tau + d\tau$, $V(t)$ is the voltage pulse dependent on time and $R$ is the resistance of the tunnel barrier. We then have the time profiles for heating and cooling during the pulse application:

$$\begin{align}
T(t) &= (T_i - T_0)e^{-(\frac{k}{c_p\rho_m t})\tau} + T_0 && \mathit{Cooling} \tag{2.24}\\
T(t) &= (T_f - T_0) + (1 - e^{-(\frac{k}{c_p\rho_m t})\tau}) + T_0 && \mathit{Heating} \tag{2.25}
\end{align}$$

giving us the temperature as a function of time $\tau$, with $(T_f - T_0) = k_V V^2$. And $k_V = t/kRA$, where the four material parameters: thermal conductivity $k$, specific heat capacity $c_p$, thickness $t$, and mass density $\rho_m$ take into account the properties of the multiple layers of the MTJ.

This is an important effect to consider because, at very low T, the electron specific heat of Fe decreases considerably [103] and the heat capacity of MgO rapidly decreases for $T < 100K$ [2]. Increased Joule heating impacts the device and reduces its memory retention during write/read, while also hindering the performance of adjacent electronic components due to increased heat dissipation. Recent estimates show that the heating experienced by an MTJ during writing is around $100^oC$ at a bath temperature of 4K and only $15^oC$ at room temperature [?]. Knowing that the temperature difference is $\Delta T \propto V^2/k$, we find that the thermal conductivity of the stack decreases by at least a factor of 2 if we consider a critical switching voltage increase of 75% within this temperature range. Fig.2.4a[3] shows the stability variation with the temperature increase for a low anisotropy operating at 4K and, in the inset image, a conventional device at 300K. As they experience different Joule heating, the stability for the first device can be significantly affected, but remains highly stable with

---

[3] Simulation parameters for Fig.2.4: $Diameter = 64nm$, $\tau_{Read} = 20\mu s$, T = 300K, $t_{SL} = 1nm$, $M_S = 1.255MA/m$, $K_1 = 1.115MJ/m^3$ for $\Delta = 60$ and $K_1 = 1.044MJ/m^3$ for $\Delta = 20$.

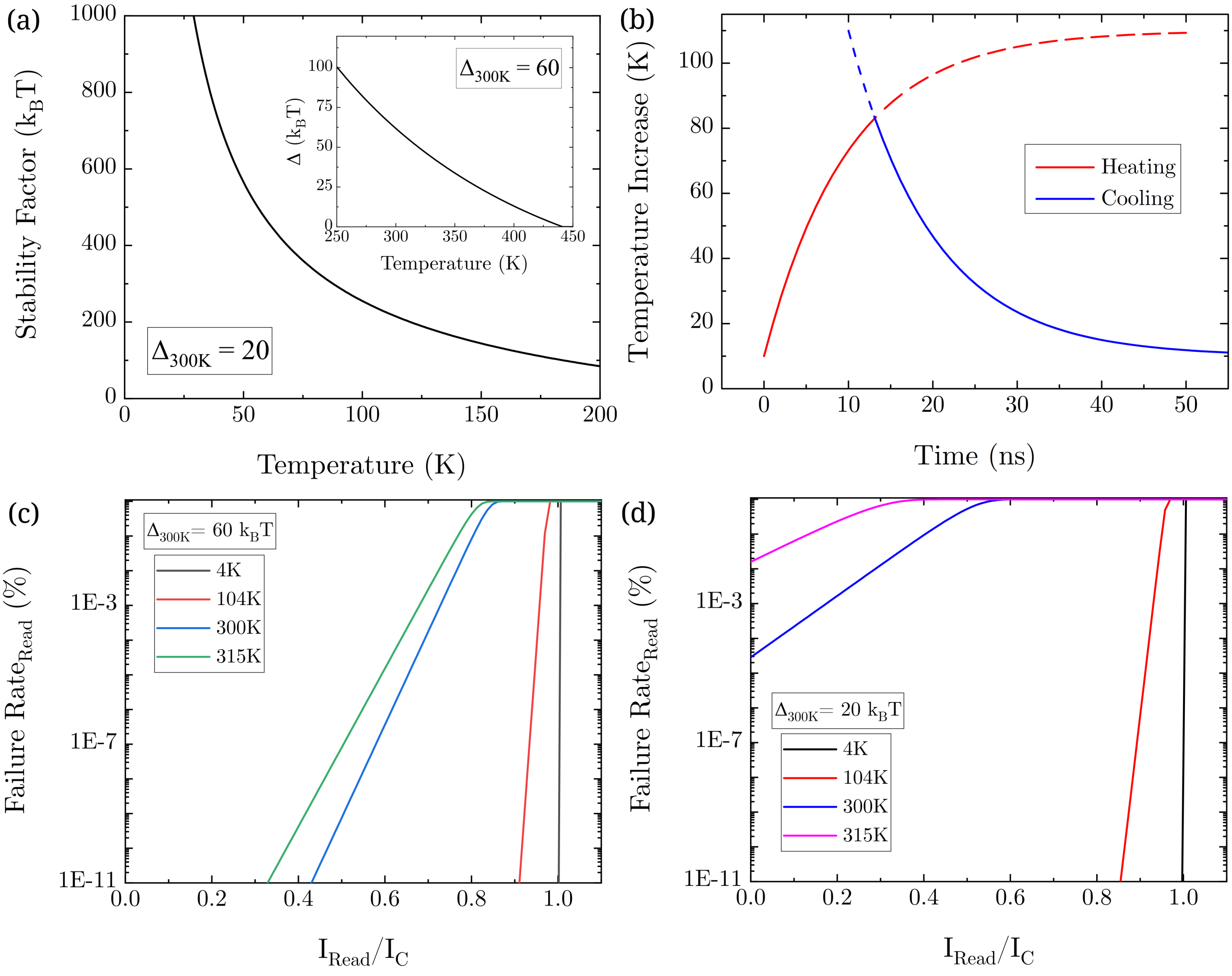

Figure 2.4: a)Retention factor $\Delta$ dependence with absolute temperature for a system with weak anisotropy ($\Delta_{300K} = 20$); Inset) the same dependence for a system with a stability of $\Delta_{300K} = 60$. b)Temperature profile during heating (in red) and cooling (in blue) for a pulse of $\tau = 13ns$ for an MTJ operating at 4K. The dashed lines represent its behavior for longer pulses, with a maximum heating reached at $\tau = 50ns$. c)Failure rate for a device with $\Delta_{300K} = 60$ and d)Failure rate for a device with $\Delta_{300K} = 20$

$\Delta(104K) = 242$. The second device at room temperature has a reduction to $\Delta(315K) = 52$. If it was under the same 100K heating, its stability would drop to $\Delta(400K) = 12$, which is excessively low for applications that require a retention longer than one year. The drop in $\Delta$ considers that a long pulse is applied to allow the junction to reach thermalization, but if shorter pulses are used, Fig.2.4b shows that the temperature variation can be limited.

There are two main advantages in this context to use a cryogenic memory instead of a conventional device: first, the larger temperature variation during writing will decrease the energy necessary to write the bit and second, it can reach ultra-low failure rates smaller than $10^{-11}$. In Figs.2.4 (c) and (d), the rate for low operating temperatures has a much steeper slope, meaning that to achieve better error rates, a conventional device must use a circuit line with a narrow distribution band for read currents, while the cryogenic bit has less strict requirements and much higher reliability on write/reading operations.

We exclude from our model the effects of tunnel heating asymmetry [104]. In a real MTJ, the heat dissipation takes place on the receiving electrode, assuming that the tunneling process occurs without scattering. The tunneling hot electrons lose their excess energy in the receiving electrode within the inelastic relaxation length on the order of 1nm. This yields a slight gradient in the heating of the tunnel junction between the two sides of the oxide, which would create an asymmetry between positive and negative currents that is neglected. We examine the dependence of $\Delta$ on pulse length in Fig.2.4.

# 3 Introducing easy-cone anisotropy in the model

Memory concepts utilizing a second-order $K_2$ term have not yet been investigated to great extent in the literature, and existing models usually simplify the anisotropy energy to exhibit an ideal case of only a first-order $K_1$ term. In this section, we will explore the details of the easy-cone anisotropy and try to obtain analytical expressions for its properties.

## 3.1 Macrospin model versus analytical calculation

To verify that the simulation performs as expected by our model, we can analyze the static equation for the energy density to find the equilibrium angle $\theta_{eq}$ of the magnetization $\vec{m}$ under the applied field.

$$\varepsilon = -K_1 m_z^2 - K_2 m_z^4 - \mu_0 M_S \sum N_{ii} \vec{m_i}^2 - \mu_0 M_S H_{IP} m_x \tag{2.26}$$

Where in spherical coordinates, taking the orientation defined in figure 2.2, and knowing from the azimuthal symmetry of the system that $N_{xx} = N_{yy}$, can be represented as:

$$\varepsilon = -K_{eff} \cos\theta^2 - K_2 \cos\theta^4 - \mu_0 M_S H_{IP} \sin\theta \cos\phi \tag{2.27}$$

where the effective anisotropy is given by

$$K_{eff} = K_1 - \frac{\mu_0 M_S^2}{2}(N_{zz} - N_{xx}) \tag{2.28}$$

In a static configuration, $\vec{m}$ will relax in the direction of the applied field with a tilt $\theta eq$ when $\frac{\partial E(\theta eq, \phi = 0^o)}{\partial \theta} = 0$. With this approach, we must assume that there is no damping $\alpha \to 0$. Then we have the following.

$$\sin\theta_{eq}{}^3 - \left(1 + \frac{K_{eff}}{2K_2}\right)\sin\theta_{eq} + \frac{\mu_0 M_S H_{IP}}{4K_2} = 0 \tag{2.29}$$

Solving this third-order equation, the following real solution can be found [105]:

$$\sin\theta_{eq} = \frac{2 * 3^{\frac{1}{3}} a + 2^{\frac{1}{3}} (-9b + \sqrt{-12a^3 + 81b^2})^{\frac{2}{3}}}{6^{\frac{2}{3}} (-9b + \sqrt{-12a^2 + 81b^2})^{\frac{1}{3}}} = \frac{\mu_0 M_S H_{IP}}{2K_{1eff}} \tag{2.30}$$

where

$$a = 1 + \frac{K_{1eff}}{2K_2}; \quad b = \frac{\mu_0 M_S H_{IP}}{4K_2} \tag{2.31}$$

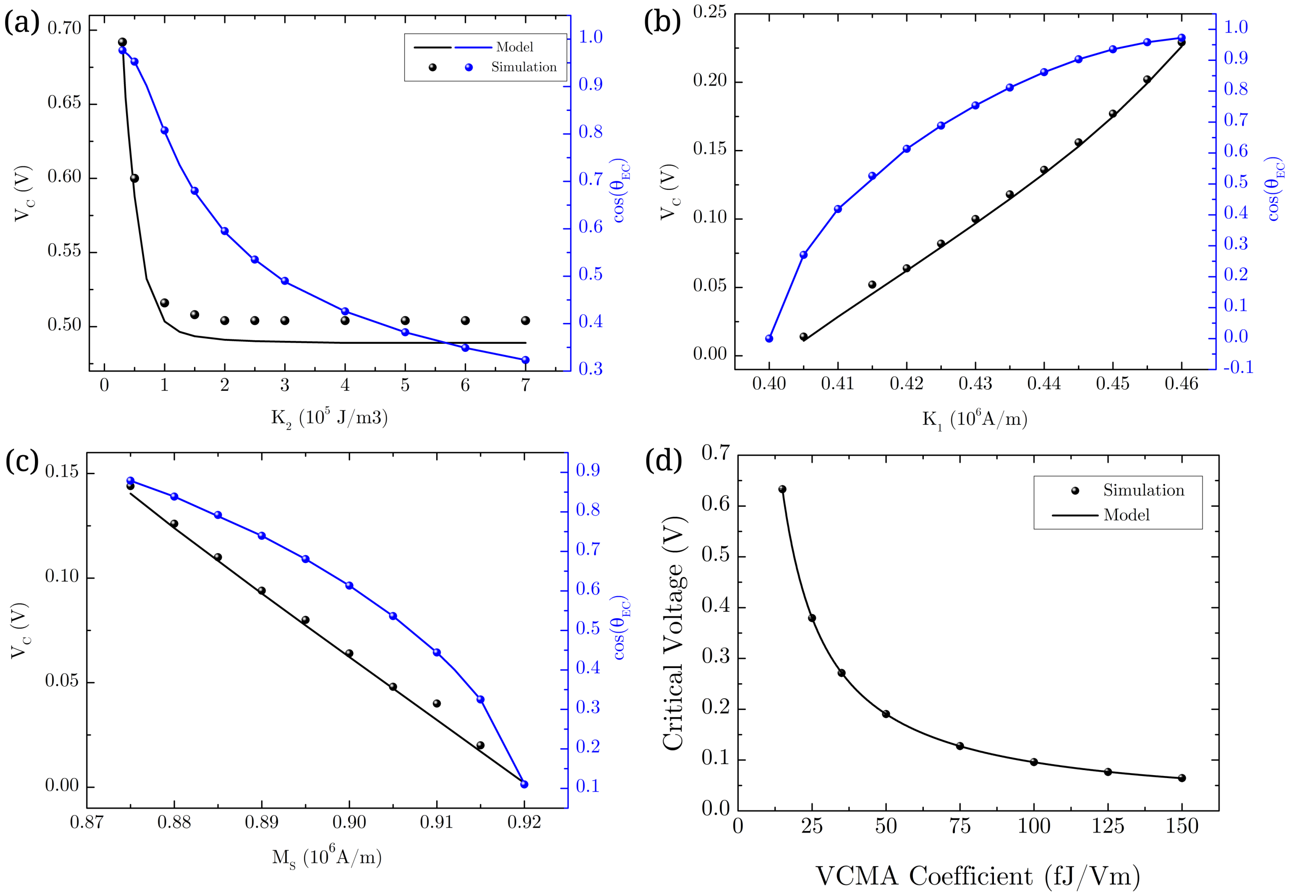

Figure 2.5: Dependence of the critical switching voltage $V_C$ and the z-component of $\vec{m}$, shown as $\cos\theta_{eq}$ for simulation data and analytical model prediction with varying $M_S$, $K_1$, $H_{IP}$ and $\xi$.

Once the voltage is applied to the state $\vec{m}(\theta,\phi) = (\theta_{eq}, 0^o)$, reversal will begin when the system reaches a threshold of energy that is equivalent to the state $(90^o, 0^o)$, allowing us to calculate the critical switching voltage $V_C$. Its full expression is given by

$$-\left(K_{eff} + \xi\frac{V_C}{t_{SL}t_{MgO}}\right)\cos\theta_{eq}{}^2 - K_2\cos\theta_{eq}{}^4 - \mu_0 M_S H_{IP}\sin\theta_{eq} = -\mu_0 M_S H_{IP} \tag{2.32}$$

$$V_C = \frac{t_{SL}t_{MgO}}{\xi}\left[\frac{\mu_0 M_S H_{IP}(1-\sin\theta_{eq})}{\cos\theta_{eq}{}^2} - K_2\cos\theta_{eq}{}^2 - K_{1eff}\right] \tag{2.33}$$

Now, to verify that our model agrees with numerical simulation results, we define the system parameters for a generic MTJ. For a Gilbert damping of $\alpha = 0.01$ and $t_{SL} = 2nm$, the parameters $K_1$, $K_2$, $M_S$ and $\xi$ are varied through a wide range of values and the corresponding $V_C$ and $\theta_{eq}$ are plotted in figure 2.5[4].

The values obtained for $\theta_{eq}$ with Eq.2.30 fit the simulation, while the values obtained for $V_C$ deviate slightly due to a finite damping, as it does not return meaningful results if $\alpha = 0$.

---

[4] System parameters for Fig.2.5: $Diameter = 30nm$, $t_{SL} = 2nm$, $R_P = 300k\Omega$, $T = 0K$, $K_1 = 0.42MJ/m^3$, $K_2 = -0.02304MJ/m^3$, $M_S = MA/m$, $\xi = 100fJ/Vm$, $H_{app} = 10mT$, $\alpha = 0.1$

## 3.2 Stability factor $\Delta$ and easy-cone angle

When choosing material parameters, we will be focusing on combinations of anisotropy constants and magnetization to bring the equilibrium state of the system into an easy-cone state that has a specific range of values for which it is stable. For its derivation, we do not take into account the in-plane applied field required for VCMA for simplification of the analytical solution. We can use the total energy density $\varepsilon$ of the system and analyze its first and second derivatives with respect to the angle $\theta$, depicted in Fig. 2.2:

$$\frac{\partial\varepsilon}{\partial\theta} = K_{1eff}\sin 2\theta + 2K_2\cos^2\theta\sin 2\theta \tag{2.34}$$

$$\frac{\partial^2\varepsilon}{\partial\theta^2} = 2K_{1eff}\cos 2\theta - 2K_2\sin^2 2\theta + 4K_2\cos^2\theta\cos 2\theta \tag{2.35}$$

The equilibrium state of the system is given by $\frac{\partial\varepsilon}{\partial\theta} = 0$.

$$(K_{eff} + 2K_2\cos\theta^2)\sin 2\theta = 0 \tag{2.36}$$

There are two cases to analyze:

1. Easy-plane regime

$$\sin 2\theta = 0 \rightarrow \theta = 0, \pi/2, \pi \tag{2.37}$$

$$\frac{\partial^2\varepsilon}{\partial\theta^2}(\theta = 0^\circ, 180^\circ) = 2K_{1eff} + 4K_2 \rightarrow \varepsilon(\theta = 0^\circ, 180^\circ) \quad \text{minimum if} \quad K_{1eff} > -2K_2 \tag{2.38}$$

2. Easy-cone regime

$$K_{1eff} + 2K_2\cos^2\theta = 0 \rightarrow \cos^2\theta = -\frac{K_{1eff}}{2K_2} \rightarrow \varepsilon(\theta) \quad \text{minimum if} \quad 0 < \cos^2\theta = -\frac{K_{1eff}}{2K_2} < 1 \tag{2.39}$$

At equilibrium, the magnetization is tilted from the normal to the layer plane by an angle $\theta_C$, given by

$$K_2 = -\frac{K_{1eff}}{2\cos^2\theta_C} \tag{2.40}$$

The easy-cone regime has two energy barriers to overcome:

1. The maximum corresponding to the in-plane direction.

$$\Delta E = E(90^\circ) - E(\theta_C) \rightarrow \Delta E = \frac{K_{1eff}^2}{4K_2}V_{ol} \tag{2.41}$$

2. The maximum corresponding to the in-plane direction:

$$\Delta E = E(0°) - E(\theta_C) \rightarrow \Delta E = -\left(K_{eff} + K_2 + \frac{K_{eff}^2}{4K_2}\right) V_{ol} \tag{2.42}$$

where $V$ is the volume of the storage layer. Only the first one has a physical meaning and thus allows us to define the retention factor for this regime as:

$$\Delta = \frac{\Delta E}{k_B T} V_{ol} = -\frac{K_{eff}^2 V_{ol}}{4K_2 k_B T} \tag{2.43}$$

To calculate the stability for cases where there is a $H_{IP}$ present, we would have to use equation 2.30 and isolate $K_{eff}$ or $K_2$, but its analytical solution is fairly convoluted. Rather than an analytical solution, we can simply calculate it numerically.

$$\Delta = \frac{E(0°) - E(\theta_C)}{k_B T} V_{ol} \tag{2.44}$$

The stability will heavily influence the choice of parameters, and the additional constraint from Eq.2.40 gives us a range of possible combinations for the three main variables of $K_1$, $K_2$ and $M_S$, shown in Fig.2.6[5]. In (a) we have a fixed $K_1 = 1.115 MJ/m^3$ and in (b) a fixed $M_S = 1.24 MA/m$. In (c) and (d), we have $K_2 = -0.1 MJ/m^3$ and $K_2 = -0.5 MJ/m^3$, respectively. These four stability diagrams define the easy-cone stability region within the hashed area, with a boundary delimited by $K_{eff} < -2K_2$ in black and an upper limit of $\Delta = 40$ in magenta. For a defined value of either $K_1$ or $M_S$, there is a very small window of anisotropy and magnetization for which an easy cone can exist, indicated by the red circles. This is one of the reasons why obtaining it experimentally is challenging, as will be discussed in later chapters. By having a fixed $K_2$ in (c) and (d), there is a visibly larger stable zone, although most of its area falls into $\Delta < 10$, which is interesting for only some applications that have less retention time constraints.

An interesting way to visualize "what" an easy-cone "is" is by plotting its energy density in a 3D plot. First, looking at a conventional pMTJ with $K_2 = 0$, there will be only two stable states, either parallel or antiparallel, as shown in Fig.2.7[6]. In (a), we plot the magnitude of the energy, which is a sphere with pinched poles (a topology with zero holes). In (b) we plot the energy on a unitary sphere, facilitating the identification of low-/high-energy zones. Evidently, pMTJs are stable in both pole directions.

When $K_2$ is present, in Fig.2.8[7], it is easy to see why it is referred to as the easy cone (EC) state. The shape of the energy magnitude has a valley in between the poles and the equator, delimiting the ring of stability that defines the direction of the two stable directions that will no longer be exactly the P and AP states. The magnetization is free to rotate around the azimuthal axis of the sphere

---

[5] System parameters for Fig.2.6: D = 64nm, T = 300K, $t_{SL} = 1nm$, $M_S = 1.24MA/m$, $K_1 = 1.115MJ/m^3$ and $K_2 = -0.1MJ/m^3$ or $K_2 = -0.5MJ/m^3$.

[6] System parameters for Fig.2.7: $Diameter = 30nm$, $t_{SL} = 1nm$, $R_P = 5k\Omega$, $T = 0K$, $K_1 = 0.42MJ/m^3$, $K_2 = 0MJ/m^3$, $M_S = 0.9MA/m$, $\xi = 0fJ/Vm$, $H_{app} = 0mT$, $\alpha = 0$

[7] System parameters for Fig.2.8: $Diameter = 30nm$, $t_{SL} = 1nm$, $R_P = 5k\Omega$, $T = 0K$, $K_1 = 0.42MJ/m^3$, $K_2 = -0.02304MJ/m^3$, $M_S = 0.9MA/m$, $\xi = 0fJ/Vm$, $H_{app} = 0mT$, $\alpha = 0$

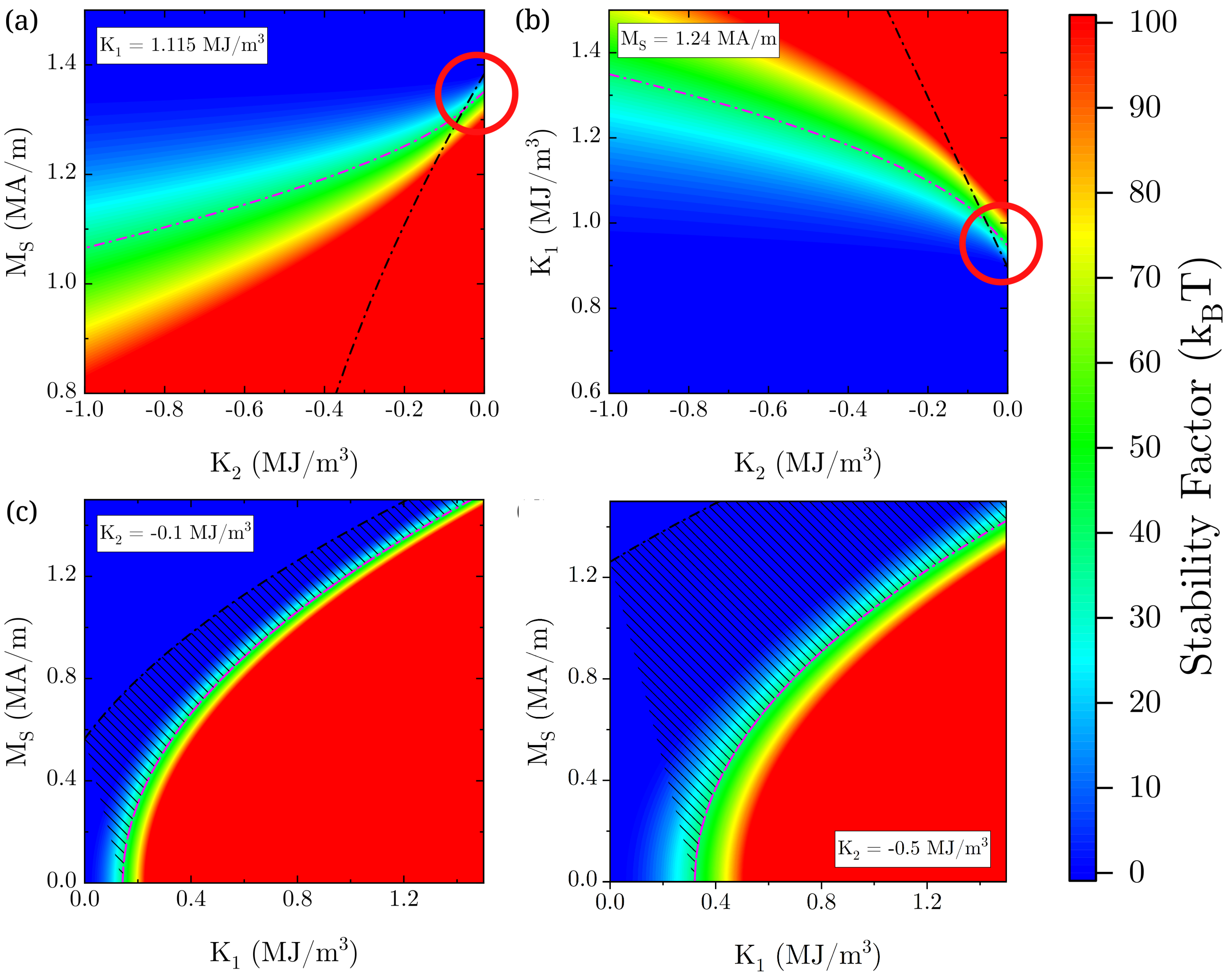

Figure 2.6: Dependence of Δ with magnetic material parameters with fixed a) $K_1 = 1.115MJ/m^3$, b) $M_S = 1.24MA/m3$, c) $K_2 = -0.1MJ/m^3$ and d) $K_1 = -0.5MJ/m^3$. The easy-cone stable region limit is bounded by the black curve defined by $K_{eff} < -2K_2$ and the boundary for $\Delta(300K) = 40$ in magenta. The two red circles in (a) and (b) explicitly indicate the small region where these conditions are met.

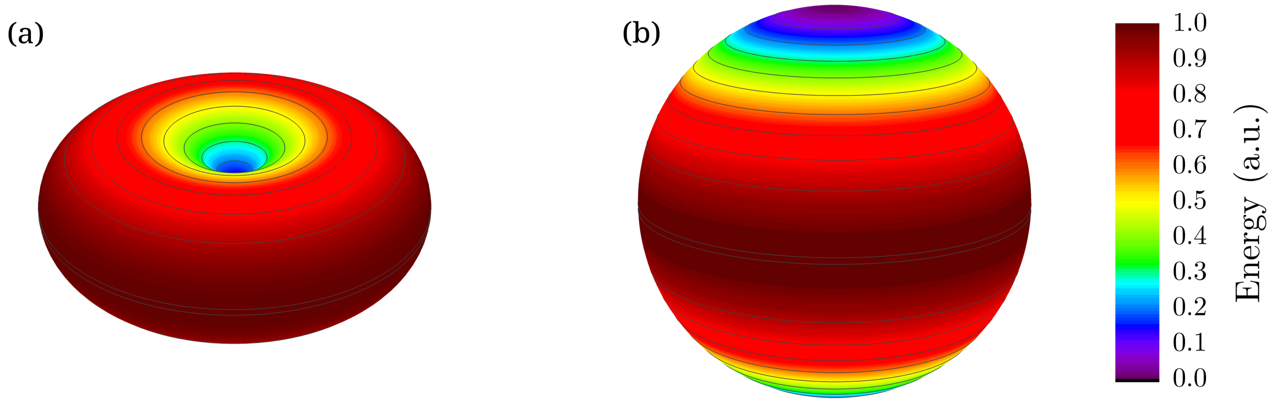

Figure 2.7: A 3D energy density landscape of a pMTJ, plotted in magnitude (left) and its representation on a unitary sphere (right) for a system with only a first order anisotropy term.

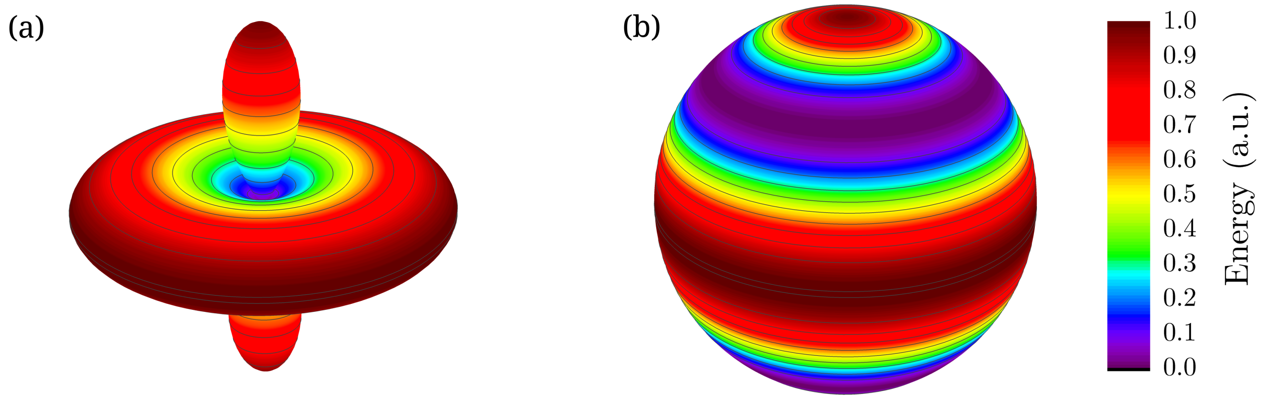

Figure 2.8: A 3D energy density landscape of a pMTJ, plotted in magnitude (left) and its representation on a unitary sphere (right) for a system with a second order anisotropy term, forming an easy-cone state.

and the absolute value of $K_2$ will then modulate the angle of aperture of the cone. For smaller values of $K_2$, the cone closes into a pMTJ configuration, while a larger value will open it until it eventually crosses the threshold indicated in Fig.2.6 and transitions into an in-plane magnetized system.

For VCMA switching, as an in-plane field $H_{IP}$ is applied, it can drastically modulate the energy states, breaking the easy-cone symmetry and favoring a relaxed directional state, as seen in Fig.2.9[8] by modulating the lowest energy states into two distinct degenerate levels.

In this scenario, the IP field will slightly shift the angle of the tilted stable states. The $45^o$ easy cone will open to $52^o$, representing a small shift $7^o$. In another configuration, with the application of a small out-of-plane (OOP) field, it will lift the degeneracy of the stable states, favoring alignment with the field and splitting $\Delta$ into $\Delta_{AP}$ and $\Delta_P$, representing the two transitions with different energy gaps.

## 3.3 Magnetic hysteresis of a free layer with easy cone anisotropy

To better understand what the inclusion of $K_2$ to the PMA energy does to its magnetic properties, we simulate hysteresis loops and extract the dependence of the MTJ resistance with field by applying a conductance model [106] and using arbitrary values for the parallel resistance state $R_P$ and TMR.

$$G_P = \frac{1}{R_P}; \quad G_{AP} = \frac{G_P}{1 + TMR} \tag{2.45}$$

$$R_{12} = \frac{2}{(G_P + G_{AP}) + (G_P - G_{AP}) * (\vec{m_{RL}} \cdot \vec{m_{SL}})} \tag{2.46}$$

We can then analyze the behavior of the reference and storage layer magnetizations through $\vec{m_{RL}}$

---

[8] System parameters for Fig.2.9: $Diameter = 30nm$, $t_{SL} = 2nm$, $R_P = 5k\Omega$, $T = 0K$, $K_1 = 0.42MJ/m^3$, $K_2 = -0.02304MJ/m^3$, $M_S = 0.9MA/m$, $\xi = 0fJ/Vm$, $H_{app} = 10mT$, $H_{IP} = 2mT$ $\alpha = 0$

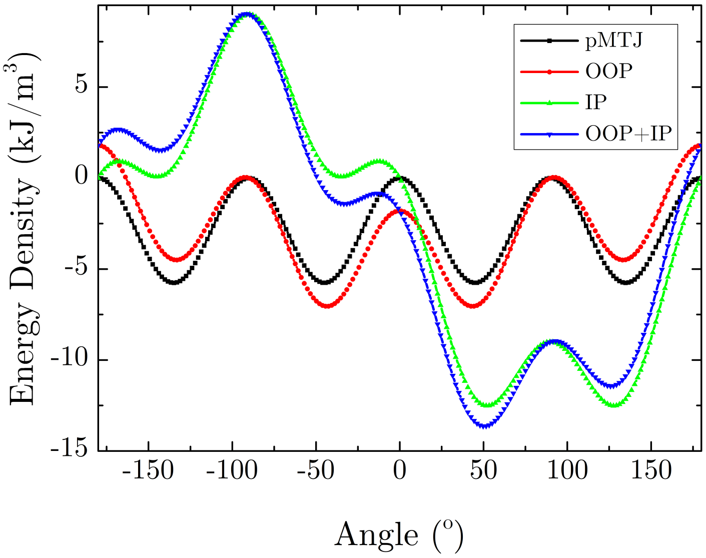

Figure 2.9: 2D representation of the energy density at $\phi = 0^o$ for: pMTJ with no applied field in black, an easy-cone MTJ without external field in orange and its modulation with 10mT of applied in-plane field in green; The shift of the easy-cone stable energy states when a 2mT out-of-plane field is applied

and $\vec{m_{SL}}$, respectively, and the total barrier resistance $R_{12}$ at each field point, shown in Fig.2.10[9].

In conventional MTJs, the hysteresis loop is essentially a square loop, with full remanence at zero field. The S-shaped loop of $\vec{m_{SL}}$ comes from the easy-cone state, which lies in a transition region between the out-of-plane and in-plane, resulting in finite coercivity and lower remanence than a fully out-of-plane layer. In other words, the magnetization at saturation begins to rotate towards the equilibrium angle $\theta_{EC}$ as the field decreases. When the coercive field is reached, the system flips and starts to rotate again, forming a symmetric loop. However, in Fig.2.10b, we see that the resistance profile is asymmetric. This is a direct effect of the TMR on the antiparallel conductance, which reduces the remanence of the AP state compared to the P state for larger TMR. We can easily see the increased asymmetry in Fig.2.11, where the $R_{50\%}$ threshold becomes biased towards larger negative values of $\vec{m_{RL}} \cdot \vec{m_{SL}}$, defining the antiparallel state of the memory.

## 3.4 Magnetic domain size calculation

Due to the nature of the macrospin model, we do not account here for the formation of magnetic domains, which will be explored in the dedicated micromagnetic MuMax3 simulation section. We can still identify critical dimensions for the lateral size of an MTJ pillar, how they change with temperature, to verify the applicability of the macrospin model to the system dimensions. In a pMTJ we have the critical diameter, defined as the threshold for coherent reversal, that can be calculated as [107]:

$$d_C = \frac{16}{\pi}\sqrt{\frac{A_{ex}}{K_{eff}}} \tag{2.47}$$

---

[9] System parameters for Fig.2.10: $Diameter = 30nm$, $t_{SL} = 1nm$, $t_{RL} = 1nm$ $R_P = 5k\Omega$, $T = 10K$, $K_1 = 0.572MJ/m^3$, $K_2 = -0.06MJ/m^3$, $M_S = 0.94MA/m$, $\xi = 0fJ/Vm$, $H_{app} = 0mT$, $\alpha = 0.1$

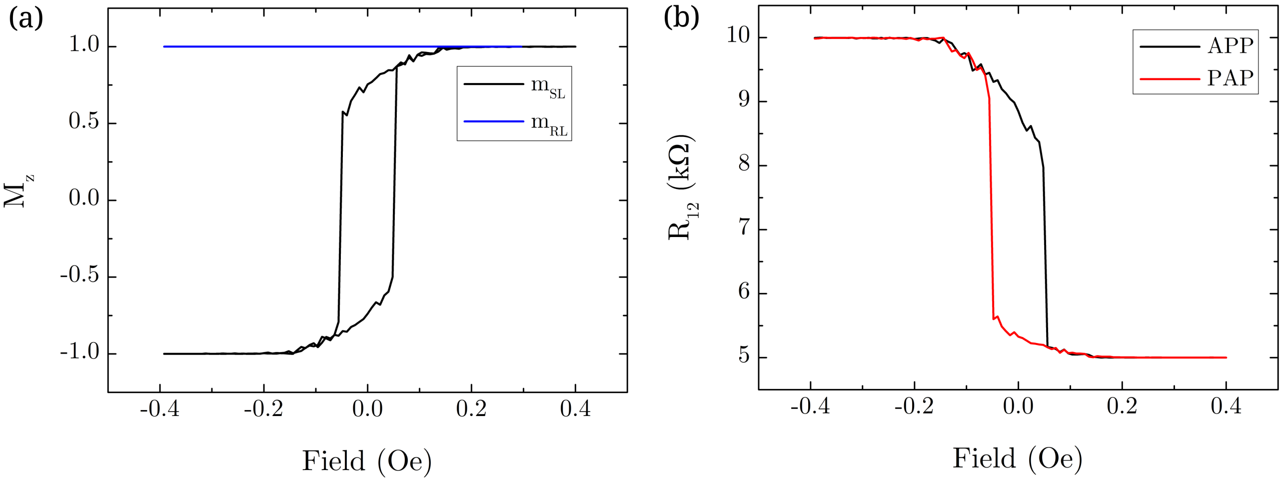

Figure 2.10: Macrospin simulation at 10K. a)Magnetic hysteresis loop of the reference and storage layers in red and blue, respectively. b)Calculated resistance state for the system assuming $R_P = 5k\Omega$ and $TMR = 100\%$. Notice that the $\vec{m}$ curve is symmetric, while the asymmetry in resistance loop and the larger rotation of the APP branch compared to PAP is due to the conductance $G_{AP}$.

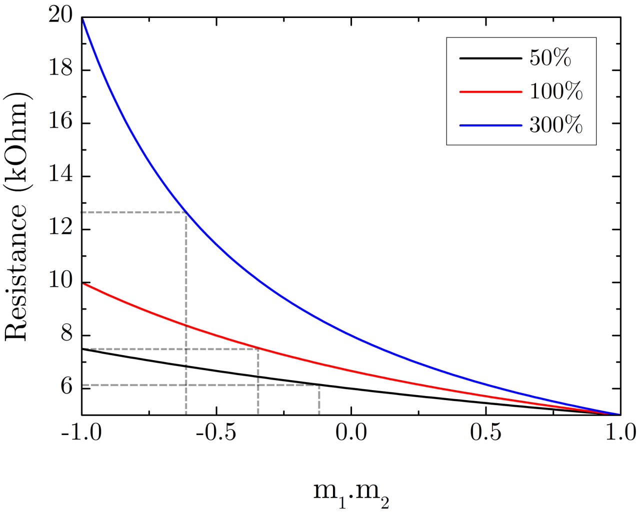

Figure 2.11: Resistance calculated for $R_P = 5kOhm$ and $TMR = 50$, 100 and 300%, showing the increasing asymmetry for larger TMR at lower values for $(\vec{m_{RL}} \cdot \vec{m_{SL}})$. The dotted gray lines indicate the threshold for half of the TMR signal and how the angular variation of resistance becomes more biased towards '-1'.

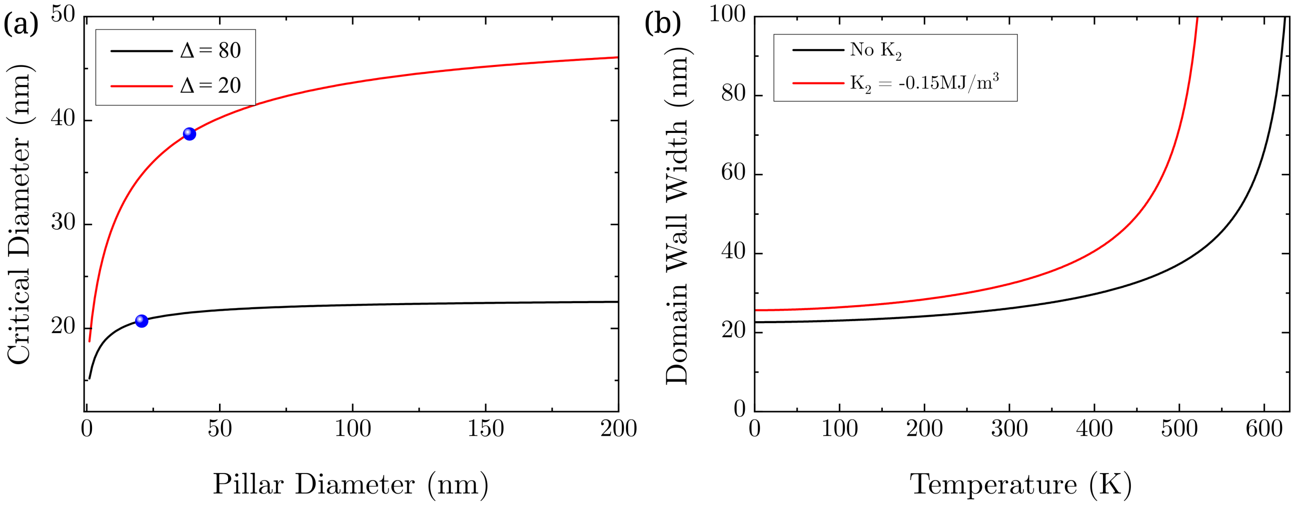

Figure 2.12: a) Domain wall critical diameter dependence for coherent STT switching for devices with $\Delta = 80$ in black and $\Delta = 20$ in red. The blue data-points indicate the critical size for domain formation at $t_{80} = 21nm$ and $t_{20} = 39nm$. b) Temperature dependence of domain wall width for a first order anisotropy in black and a higher order anisotropy system with a $K_2$ term in red, both with a stability of $\Delta = 20$

Since the demagnetizing tensor $\bar{N}$ changes with varying size, we can calculate the dependence $d_c$ with the diameter of the pillar for different devices. This allows us to better understand the differences between conventional MTJs designed for room-temperature operation and those optimized with low anisotropy for cryogenic operation. Fig.2.12a[10] shows $d_c$ for devices with retentions of $\Delta = 80$ and $\Delta = 20$ at 300K with a transition diameter of $d_c^{80} = 21nm$ and $d_c^{20} = 39nm$, respectively. That means that a storage layer with weak PMA will have a higher size threshold before it loses its macrospin behavior.

This is because as $K_{1eff}$ decreases, the diameter increases due to the demagnetization energy while the exchange stiffness remains constant. When going to low temperatures, the anisotropy will increase faster than the exchange energy, reducing the domain wall width, as shown in Fig.2.12b[11]. The calculation of the width for higher-order anisotropy is given by the more general equation Eq.2.49 [108]:

$$\delta_W = \pi\sqrt{A_{ex}/K_{1eff}}/\sqrt{1+\kappa} \quad for \quad \kappa > -0.5 \tag{2.48}$$

$$= 2\left\{[\pi - 2arctan(\sqrt{-1-2\kappa})]\sqrt{-\kappa} + arctanh\left(\sqrt{\frac{1+2\kappa}{\kappa}}\right)\right\}\sqrt{\frac{A_{ex}}{K_{1eff}}} \quad for \quad \kappa < -0.5 \tag{2.49}$$

In which $\kappa = K_2/K_{1eff}$, a ratio that will control how many inflection points the rotation of the wall has in its structure, with a discontinuity at $\kappa = -1$. As $\kappa$ increases, the total PMA energy decreases, which in turn increases the width of the domain wall compared to a system without a term $K_2$. As

---

[10] Simulation parameters for Fig.2.12a: Diameter=30nm, $t_{SL} = 1nm$, $R_P = 5k\Omega$, $T = 0K$, $K_1 = 1.35MJ/m^3$, $K_2 = 0MJ/m^3$, $M_S = 1.1MA/m$, $\xi = 0fJ/Vm$, $H_{app} = 0mT$, $\alpha = 0$

[11] Simulation parameters for Fig.2.12b: Diameter=30nm, $t_{SL} = 1nm$, $R_P = 5k\Omega$, $T = 0K$, $K_1 = 0.885MJ/m^3$, $K_2 = 0MJ/m^3$, $M_S = 1.1MA/m$, $\xi = 0fJ/Vm$, $H_{app} = 0mT$, $\alpha = 0$

can be seen, the overall width has a decreasing trend due to the enhancement of the anisotropy at low temperature. This means that a conventional memory which exhibits coherent/macrospin switching at room temperature might change to a reversal mediated by domain walls at lower temperature, requiring the fabrication of smaller devices that may be experimentally challenging. This is an unwanted property and must be accounted for when designing such devices, which is a constraint less critical for the case of low anisotropy because its critical diameter is larger $d_c^{20} > d_c^{80}$ and the presence of a $K_2$ term slightly favors coherent behavior for larger layers.

## 4 Macrospin numerical study of STT switching

To analyze the switching behavior of the reversal dynamics, a visually simple method is to calculate the pulse-phase diagrams, which gives us the boundary between zero and 100% probability of switching at 0K. They are generated by applying a single voltage pulse across the tunnel barrier with varying amplitude and duration / length, as shown in Fig.2.13a[12]. Fig. 2.13b) shows an example of this diagram at 0K, with the red region signifying full switching from the AP state to the P state (APP) with a clear switching boundary.

For the critical switching voltage, we can use the pMTJ critical switching current equation [109]:

$$I_C = \frac{4e}{\hbar}\frac{\alpha H_{Keff}}{\eta}M_S \tag{2.50}$$

Where $H_{Keff}$ is total effective anisotropy field and $\eta$ is the STT polarization given by [77]:

$$\eta = \sqrt{\frac{TMR}{2+TMR}} \tag{2.51}$$

The assumption of this model is that the current pulse has an infinite duration, which for our numerical approach could be approximated by microsecond timescales that would lead to an unreasonably long computational time. The magnetization reversal path is not trivial, and due to damping, a difficult task to calculate. As an example, we simulate a layer to modulate the switching voltage to be a few dozen milivolts in Fig.2.14a[13], with $\Delta_{300K} = 44$ and $V_C = 30mV$. The voltage pulse is applied at $t = 30ns$ and we can see that the z-component time-trace becomes stagnant at $\vec{m}_z \approx -0.5$ for 76mV, switching fully in 40ns. In Fig.2.14c, the magnetization's velocity on the z-axis decelerates in a region where the torque is almost compensated for by the effective field, and its precession around the in-plane direction decreases substantially. While, at higher voltages, the reversal is completed in only a few nanoseconds for 200 mV. This difference in switching time is more significant for voltage amplitudes closer to $V_C$.

Therefore, this section will focus on data analysis from simulation results, only using analytical solutions as a guide to set our material parameters and taking into account that our critical values are targeted for time scales below one microsecond. The macrospin model and the use of ideal values

---

[12] System parameters for Fig.2.13: $Diameter = 64nm$, $t_{SL} = 1nm$, $R_P = 5k\Omega$, $T = 0K$, $K_1 = 0.6MJ/m^3$, $K_2 = -0.0207MJ/m^3$, $M_S = 1MA/m$, $\xi = 0fJ/Vm$, $H_{app} = 0mT$, $\alpha = 0.015$

[13] System parameters for Fig.2.14: $Diameter = 30nm$, $t_{SL} = 1nm$, $R_P = 5k\Omega$, $T = 0K$, $K_1 = 0.7MJ/m^3$, $K_2 = -0.2MJ/m^3$, $M_S = 0.9MA/m$, $\xi = 0fJ/Vm$, $H_{app} = 0mT$, $\alpha = 0.015$

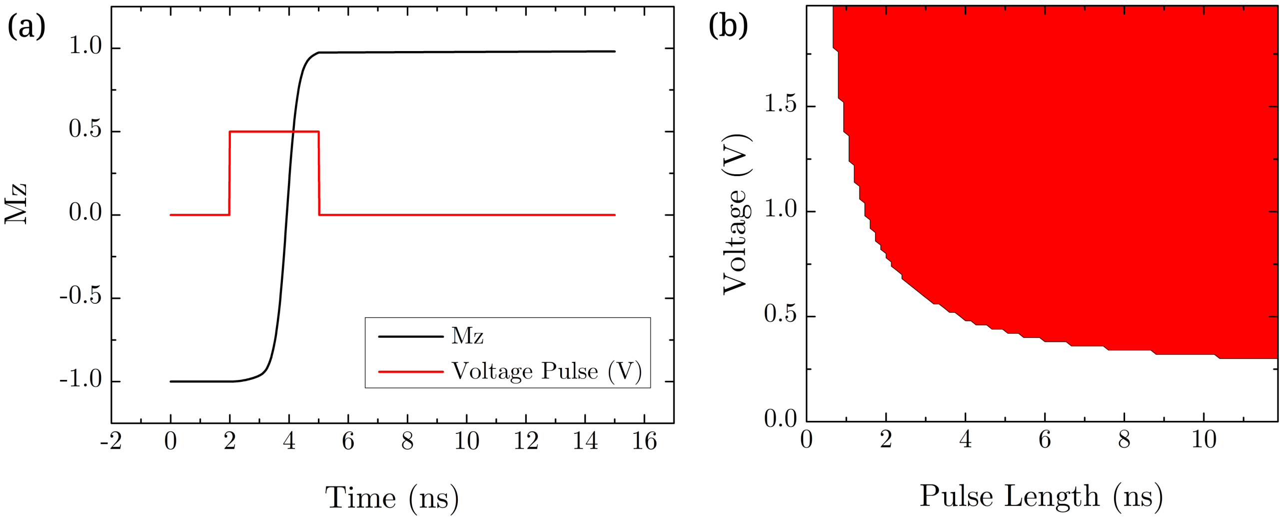

Figure 2.13: a) A time-trace of $\vec{m}_z$ (black) and an applied current pulse (red) leading to a reversal by STT. b) STT Pulse phase diagram at 0K. The APP switching probability has a sharp boundary from the absence of thermal noise, and the switching probability in the red region is 100%.

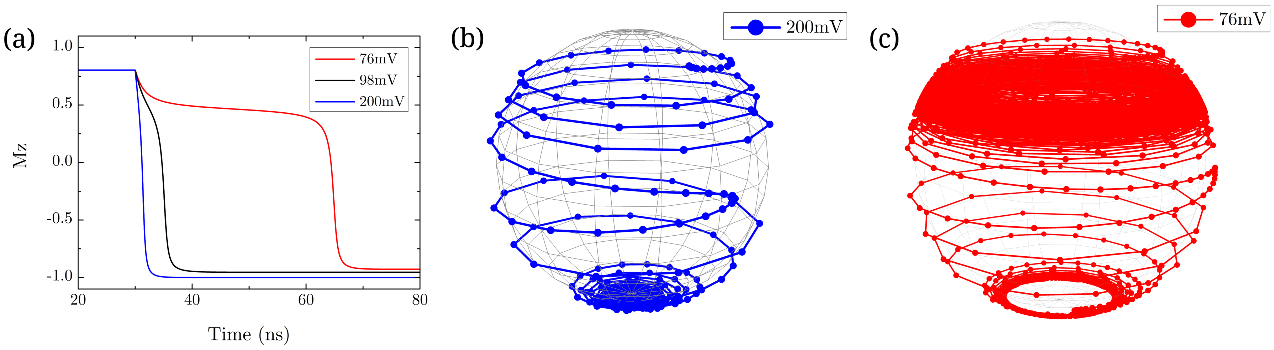

Figure 2.14: Magnetization time-trace of $\vec{m}$. a) $\vec{m}_z$ plotted against time for voltage pulses of 76mV, 96mV and 200mv, where reversal starts at $\tau = 30ns$; and a 3D representation of the magnetization path at b) 200mV and c)76mV, showing the increased switching delay for lower voltages close to the critical switching voltage.

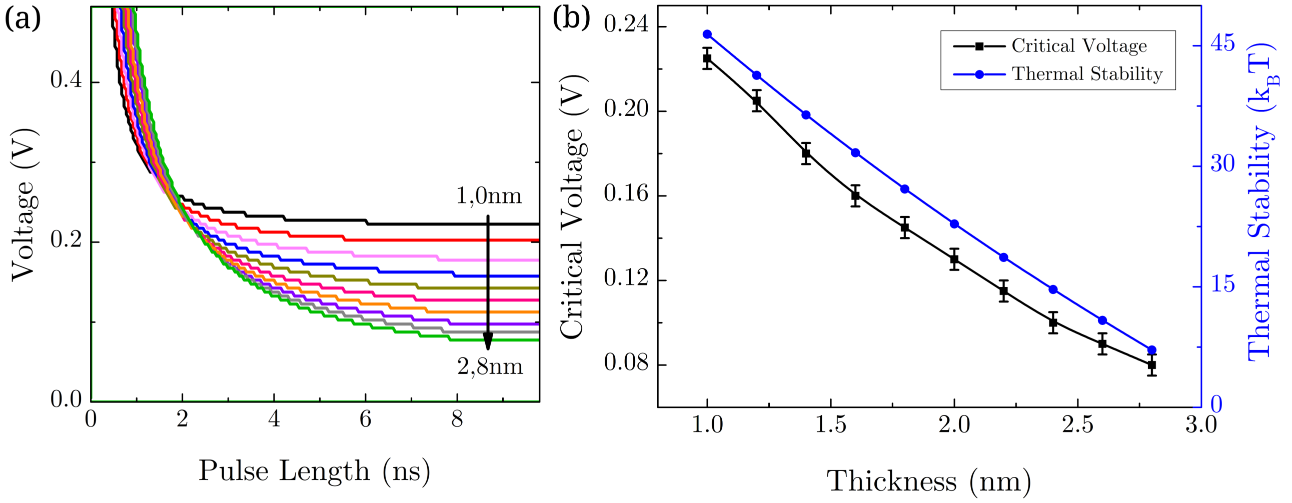

Figure 2.15: a) STT switching phase diagram boundary for $t_{SL}$ ranging from 1nm to 2.8nm. b) Critical STT switching voltage dependence with storage layer thickness.

for $K_1$, $K_2$ and $M_S$, will lead to conclusions that provide a qualitative insight and are not meant to be quantitatively accurate.

## 4.1 STT switching voltage dependence on storage layer thickness

The geometry of the storage layer plays an important role in the expression of $I_C$, as it defines the magnetic volume and sets the demagnetizing energy. The thickness in particular is a parameter that can be controlled with sub-nm precision, as will be discussed in the following chapters. This makes it interesting for our low-energy applications if we can modify the storage layer thickness to minimize $V_C$. Therefore, multiple switching limits are calculated for thicknesses ranging from 1nm to 2.8nm (the range of interest in our device fabrication) and are plotted in Fig.2.15a[14].

As we can see, $V_C$ has an almost linear relationship with $t_{SL}$. The critical voltage decreases for thicker layers since the demagnetizing energy will also increase, lowering the effective anisotropy and, thus, the thermal stability, as evidenced by Fig.2.15b. For even thicker layers $t_{SL} > 2.8nm$, the balance between $K_1$ and $M_S$ is such that the demagnetization energy becomes larger than the anisotropy, transitioning into an in-plane MTJ. For real devices using FeCoB storage layers, this threshold is typically lower around 1.8 nm for storage layers.

Another effect of higher thickness, albeit undesirable, is the crossover to the ballistic switching regime from the thermally activated reversal regime at longer pulse lengths and as the thickness of the storage layer is increased. This is visible by the way the boundary of $t = 2.8nm$ crosses the other curves at $\tau = 2ns$. This feature is expected, as a larger magnetic volume requires injection of more spins for the magnetization to reverse and, therefore, a longer current pulse duration.

---

[14] System parameters for Fig.2.15: $Diameter = 30nm$, $t_{SL} = 1.0 - 2.8nm$, $R_P = 5k\Omega$, $T = 0K$, $K_1 = 0.6MJ/m^3$, $K_2 = -0.0207MJ/m^3$, $M_S = 1MA/m$, $\xi = 0fJ/Vm$, $H_{app} = 0mT$, $\alpha = 0.015$

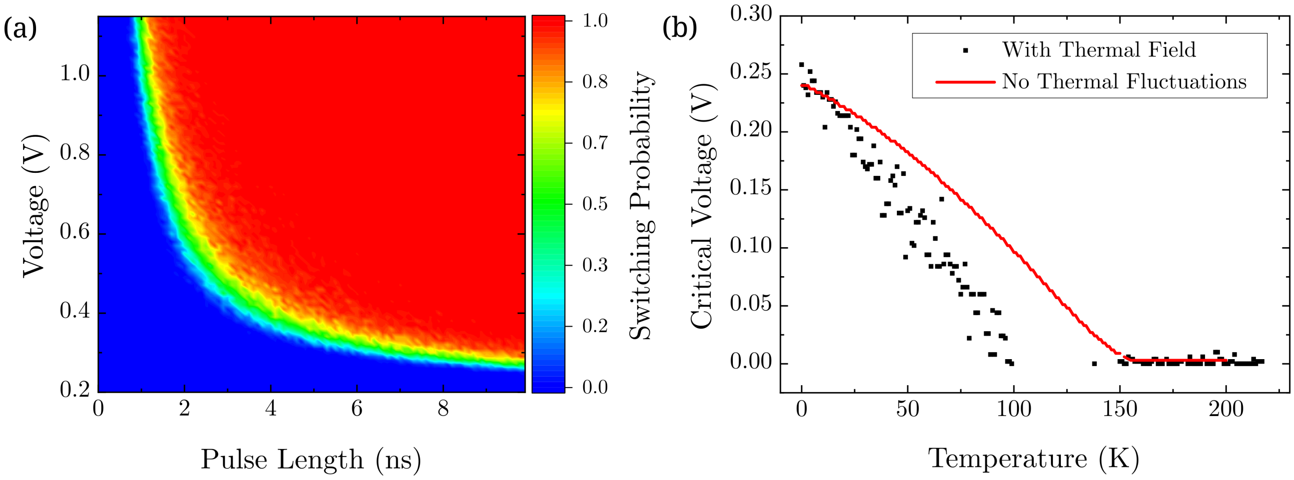

Figure 2.16: a) Pulse phase diagram at 10K for STT switching of a device with 30nm in diameter and 1nm thickness with a $K_2$ component. b) STT switching voltage dependence with temperature with (black) and without (red) the random thermal field.

## 4.2 STT switching voltage dependence with T

Evaluating the temperature dependence of the critical voltage is one of the most important aspects of this work, as it will function as an efficiency limiter and dictate the least amount of energy required for writing a device at a given temperature.

There are two ways in which we introduce the effect of temperature: by using the Callen-Callen law (eq. 2.21) and adding a thermal field. The first method is used to implement the temperature dependence of the material parameters of the system, modulating the energy landscape of the system and its equilibrium state. The random thermal noise in the system from the addition of the thermal field will act on the angle of the magnetization changing the total effective field at each time step.

The absence of thermal noise allows us to retrieve a smooth variation of the switching voltage, while in its presence we are required to accumulate multiple switching events to account for thermal-induced dispersion, such that an accurate average requires a larger number of iterations of the same event. By introducing stochasticity in the system, we can simulate the switching probability phase diagram and see that the switching boundary blurs with $T \neq 0K$ as shown in Fig.2.16a[15] for the 1 nm thick storage layer from Fig.2.15 at 10K. The diagram is calculated for 100 iterations of the simulations.

After acquiring the diagram for multiple temperature points, we can extract a plot $V_C$ vs. $T$ for pulse durations of 100ns, shown in Fig.2.16b with and without thermal fluctuations in red and black, respectively. Without thermal field, there is a smooth transition temperature at $T = 156K$ when the layer goes into the in-plane configuration due to the loss of PMA. If the thermal noise is taken into account, the transition temperature shifts to $T = 80K$ and the time retention of the memory becomes so small above this temperature that it becomes a stochastic superparamagnetic bit. At this point, $V_C$ can no longer be defined, since the magnetization of the storage layer spontaneously reverses during the duration of the pulse due to thermal fluctuations. As evident here, the thermal energy of

---

[15] System parameters for Fig.2.16: $Diameter = 64nm$, $t_{SL} = 1nm$, $R_P = 5k\Omega$, $T = 0 - 300K$, $K_1 = 0.6MJ/m^3$, $K_2 = -0.0207MJ/m^3$, $M_S = 1MA/m$, $\xi = 0fJ/Vm$, $H_{app} = 0mT$, $\alpha = 0.015$

the environment has a visible impact on the magnetization state, the loss of stability occurs at 80K with $\Delta_{80} = 5$, which means that a small amount of thermal energy in the environment is enough to completely destabilize the layer.

Therefore, caution is important when interpreting switching events and evaluating threshold values in this dependency using only analytical solutions or at 0K. A numerical approach is preferred for extracting these parameters, although it takes considerably more time to solve.

## 5 Numerical study of VCMA switching versus T

This section focuses on the dynamics of VCMA switching. There are significant differences between STT-switching and VCMA-switching, leading to different material stack requirements. VCMA devices require a much higher RA product, 100-1000 $\Omega.\mu m^2$ instead of single-digit values for STT. This leads to parallel resistance values of the order of $100k\Omega$ and higher, the damping-like $a_{\|}$ term is minimized and the STT contribution can be neglected. Second, a nonzero VCMA coefficient $\xi$ will modulate the anisotropy as the voltage pulse is applied. Third, an in-plane external magnetic field is applied and will be defined as a precessional axis for the magnetization.

### 5.1 VCMA switching dynamics at 300K

The precessional nature of the VCMA mechanism can be extracted by simulating a conventional MTJ layer at 300K. As an example, we plot the time-trace of $\vec{m_z}$ for both APP and PAP transitions and a phase diagram in Fig.2.17[16]. Here, the material parameters are set as $K_S = 1.2mJ/m^2$, $M_S = 1.0A/m$ and $\xi = 75fJ/Vm$ for a circular storage layer of 40nm in diameter and $\Delta_{300} = 65$. In the time trace, we can easily see the precessing of $\vec{m}$ for both events and the 'toggle-switch' property of VCMA. Independent of the initial state, the same pulse polarity can write the memory if the pulse width lasts a multiple of a half-precession. In the phase diagram, we can see opposite final states appear in succession creating precessional fringes characteristic of this reversal mechanism. Their frequency depends on the resulting effective field, but not on damping [110]. It can be seen the difficulty to achieve reliable VCMA switching, as the writing pulses have to be controlled to well-defined narrow pulse widths to maintain high switching reliability, the first fringe with the lowest pulse width being the one least affected by decoherence of the precession. As the magnetization precesses it becomes increasingly more likely for it to accumulate thermal agitation that increases stochasticity, seen by the reduction in width of the subsequent fringes. The figure shows that in this precessional switching regime, controlling the switching requires a very fine control of the voltage pulse duration and a read before write process, which limits its technological applicability in these working conditions.

---

[16] System parameters for Fig.2.17: $Diameter = 40nm$, $t_{SL} = 2nm$, $R_P = 300k\Omega$, $T = 0K$, $K_1 = 1.2MJ/m^3$, $K_2 = 0MJ/m^3$, $M_S = 1MA/m$, $\xi = 75fJ/Vm$, $H_{app} = 50mT$, $\alpha = 0.08$

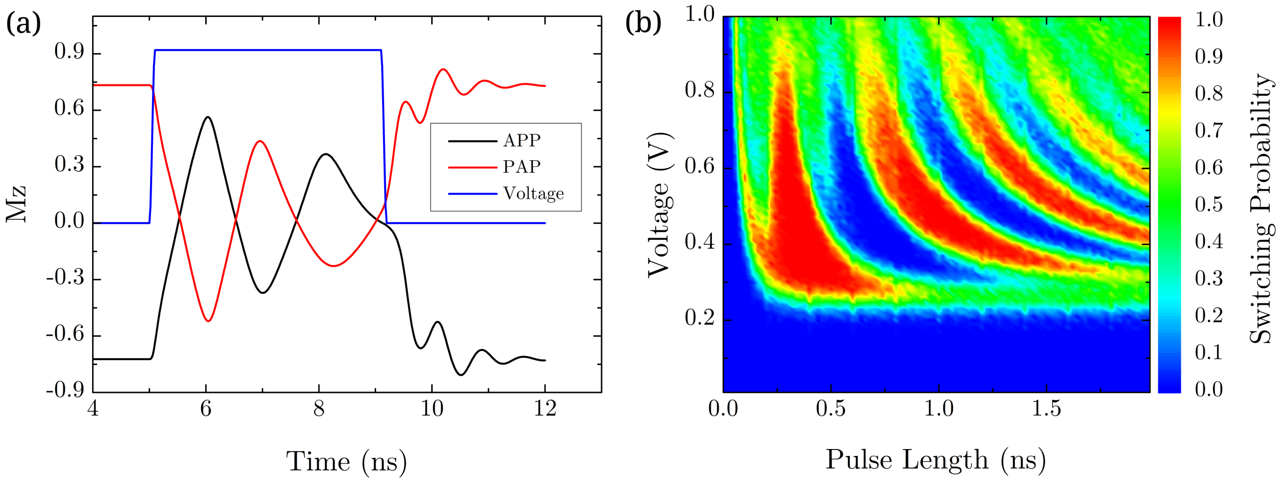

Figure 2.17: a) Time-trace of $\vec{m}_z$ for an initial P and AP state, in red and black respectively. The voltage amplitude is plotted in blue, showing that its application induces precession of $\vec{m}$ regardless of the equilibrium state. b) Pulse phase diagram at 300K for a pMTJ system with an applied 50mT field with visible precessional fringes.

## 5.2 Deterministic VCMA switching at low temperature

With these limitations of VCMA in mind, we look into the dynamics at low temperature in this section. Fig.2.18[17] shows the evolution of the phase diagram from 300K to 5K and how the fringes shift into a new switching regime defined by a deterministic switching band, between 0.55V and 0.75V, with an identifiable critical switching voltage. This is a very interesting property, as it avoids the main issues associated with precessional switching, that is, the very small pulse bandwidth for switching with high probability. This regime has been mentioned in a recent publication reporting simulation results [111], here we analyze this regime in more detail.

The deterministic switching band is the result of the energy landscape geometry of the system, given by Eq.2.26. At equilibrium and without applied voltage, two stable states, P and AP, are present and separated by a small energy barrier, as shown in Fig.2.9. With the modulation of the voltage of the energy, the separation between P and AP becomes smaller until the voltage bias reaches a threshold value $V_{IP}$ for which there is no more distinction between either state, with $\vec{m}$ relaxing to an in-plane state. If a voltage is applied with an amplitude larger than $V_C$ and smaller than $V_{IP}$, but not high enough so that the damping will dissipate energy preventing a double crossing of the energy barrier, we achieve a switching regime where it is not correlated with the pulse width.

We can use a 3D representation of the energy with the $\vec{m}$ time-trace to see the dynamics of this regime in Fig.2.19. Starting in the AP state, the magnetization is allowed to relax before a 1ns voltage pulse with 0.5V amplitude is applied at $t = t_0$. We see $\vec{m}$ following the isolines of the landscape as the damping dissipates energy and it crosses hemispheres, achieving a half-precession (i.e., a reversal). With the pulse still on, the damping further reduces the energy before the magnetization has time to complete a second half-precession, becoming lower than the energy barrier at 0.5V and forcing $\vec{m}$ to precess around the P stable state. When the pulse is turned off at $t = t_{off}$, the system then

---

[17] System parameters for Fig.2.18: $Diameter = 30nm$, $t_{SL} = 2nm$, $R_P = 300k\Omega$, $T = 0 - 200K$, $K_1 = 0.532MJ/m^3$, $K_2 = -0.0875MJ/m^3$, $M_S = 0.94MA/m$, $\xi = 50fJ/Vm$, $H_{app} = 9mT$, $\alpha = 0.1$

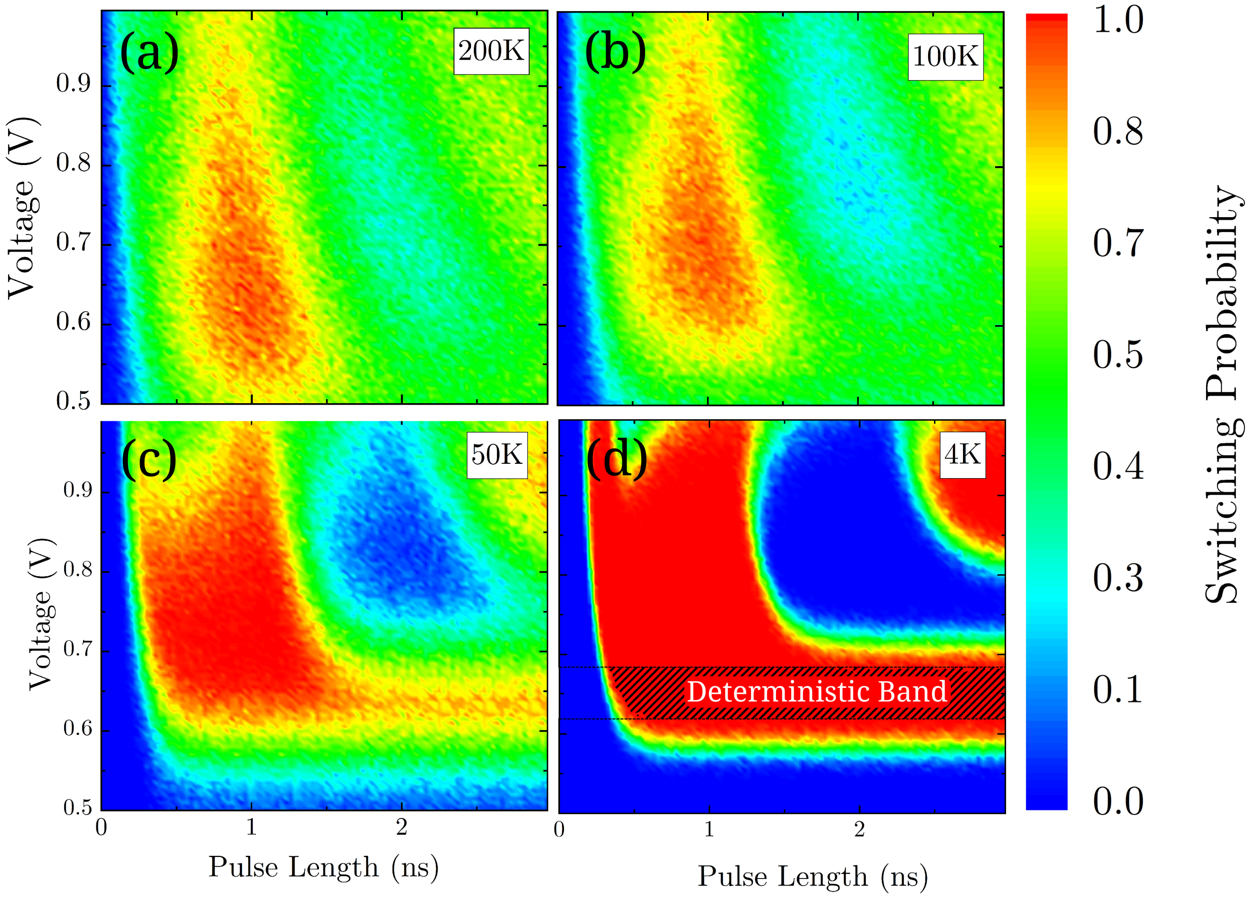

Figure 2.18: VCMA pulse phase diagram switching probability at a) 300K; b)200K; c)50K and d) 5K. For temperatures lower than 100K, the shape of the diagram changes and a deterministic switching band is visible at 5K.

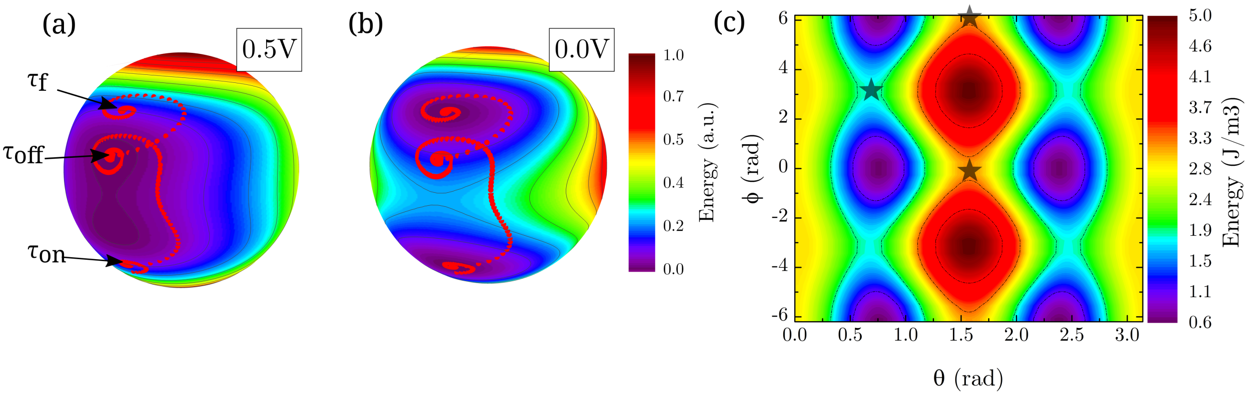

Figure 2.19: Representation of the energy density of the system for different applied voltages and the magnetization trace during switching in red for a pulse of 1ns. a) 3D Energy landscape at 0.5V, with $t_0$ being the time of pulse initialization, $t_{off}$ the time when the pulse is turned off, and $t_f$ the end of the simulation. b) 3D Energy landscape at 0V. c) 2D energy landscape at 0V with saddle points marked by black stars.

relaxes to the equilibrium P state at 0V. The voltage range for which this happens cannot be calculated analytically, requiring numerical simulations to study it because it depends on energy dissipation. The two parameters that will influence it more strongly are the Gilbert damping and the total effective anisotropy. The first dictates how fast the energy dissipation of the precession is and consequentially its frequency. The second will change the landscape of the system and the energy barriers that separate each state. With a larger anisotropy, the voltage range for this regime also increases.

From an application point of view, this regime brings the advantage over other writing mechanisms, such as STT or SOT, that the required write power is reduced because of the short time and small currents involved in the reversal. It also removes one main obstacle for the implementation of VCMA, since precessional switching is no longer present. The drawback then becomes the strict temperature requirement for it to be implemented. Since small thermal agitations are enough to induce decoherence of the deterministic switching, qbit and superconducting circuits that operate under 4K remain its most compatible technologies.

There are two other distinct features that appear when the switching phase diagram is visualized in the pulse voltage $V$ versus pulse length $\tau$ format at 0K. In Fig.2.20a[18] we see switching loops and a discontinuity at 0.7V. They are closely tied to the damping and energy of the system and occur when the applied voltage pulse is stopped when the magnetization is close to a saddle point in the energy landscape. In Fig.2.19c, there are two types of saddle points: the first is at $\theta = \pi/4$, which depends on $\theta_{EC}$ and $H_{IP}$; and the second is at the hemisphere crossing for $\theta = \pi/2$. The $\vec{m}$ relaxation in between these points is very sensitive to its position, and the damping determines how many precessions around the azimuthal axis will occur before equilibrium is reached. The number of precessions is what creates the fringe-like pattern of the diagram.

Of the three features discussed, only the switching band is relevant at non-zero temperatures.

---

[18] System parameters for Fig.2.20: $Diameter = 30nm$, $t_{SL} = 2nm$, $R_P = 300k\Omega$, $T = 0 - 4K$, $K_1 = 0.84MJ/m^3$, $K_2 = -0.04608MJ/m^3$, $M_S = 0.9MA/m$, $\xi = 75fJ/Vm$, $H_{app} = 10mT$, $\alpha = 0.1$

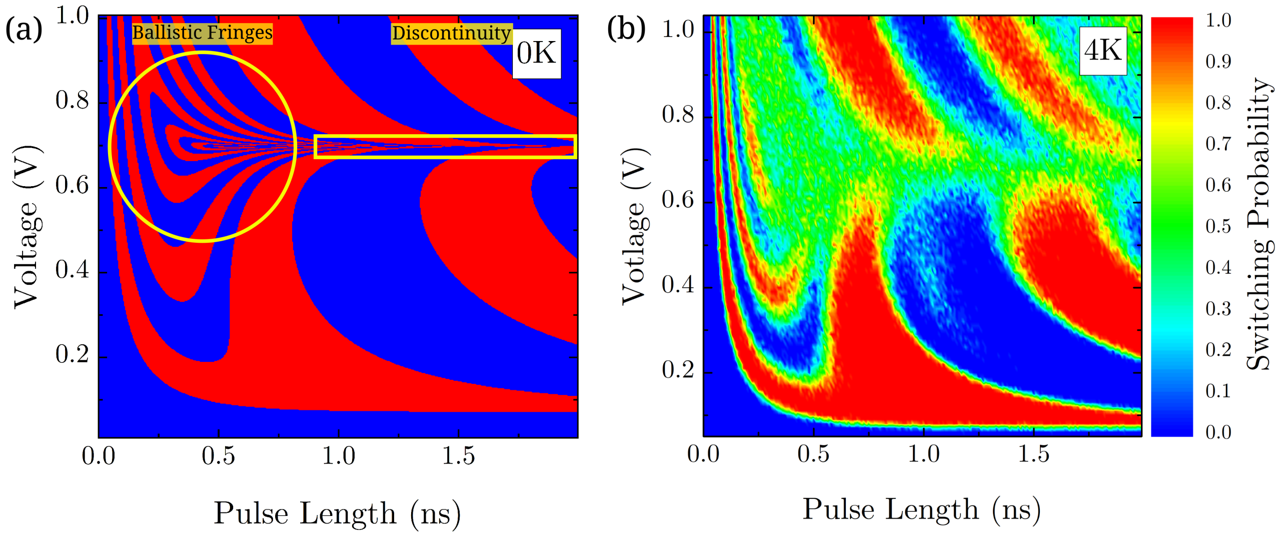

Figure 2.20: Pulse phase diagrams for VCMA switching. a) At 0K showing the three features of VCMA switching at low temperature: switching loops, a discontinuity at 0.7V and a critical switching voltage at 0.1V. b) The same diagram at 5K, with a visible degradation of the first two features, while it retains the threshold switching voltage.

Because the energy saddle points are metastable states, they are therefore highly sensitive to thermal fluctuations. In Fig.2.20b, there is an almost complete degradation of the switching loops and the discontinuity at only 5K, while the lowest switching band retains a high switching probability. Its deterministic nature is retained for higher temperatures up to 50K, at which point the writing probability quickly decreases.

## 5.3 Influence of damping on VCMA deterministic switching

The Gilbert damping used in the previous simulations is considerably large ($\alpha \geq 0.1$), when the literature work has measured it to be around 0.015 for a 1 nm thick layer of FeCoB [112]. The main reason for this choice is that it increases the range of voltages for which the deterministic switching regime exists due to the stronger energy dissipation due to a higher damping [110]. It will also reduce chaotic switching dynamics originating from small changes in the magnetization direction near the energy saddle points.

The effect is visible in Fig.2.21[19], where we have the same phase diagram plotted for a damping of $\alpha = 0.015$ and $\alpha = 0.1$ in (a) and (b), respectively. After pulse application, if the magnetization is close to the saddle point and does not lose energy quickly, the looping pattern in (a) in the diagram becomes more pronounced and repeats itself periodically, as seen for $\tau = 0.5, 1.5, 2.5ns$. In (b), this pattern completely disappears.

With higher damping, the main advantage is that the lowest switching band becomes wider, avoiding a very narrow range of switching voltage. Since the energy dissipation is stronger, once the magnetization flips state, it cannot switch back because it no longer has energy to overcome again the

---

[19] System parameters for Fig.2.21: $Diameter = 30nm$, $t_{SL} = 2nm$, $R_P = 300k\Omega$, $T = 0K$, $K_1 = 1.064MJ/m^3$, $K_2 = -0.175MJ/m^3$, $M_S = 0.94MA/m$, $\xi = 50fJ/Vm$, $H_{app} = 10mT$, $\alpha = 0.015 - 0.1$

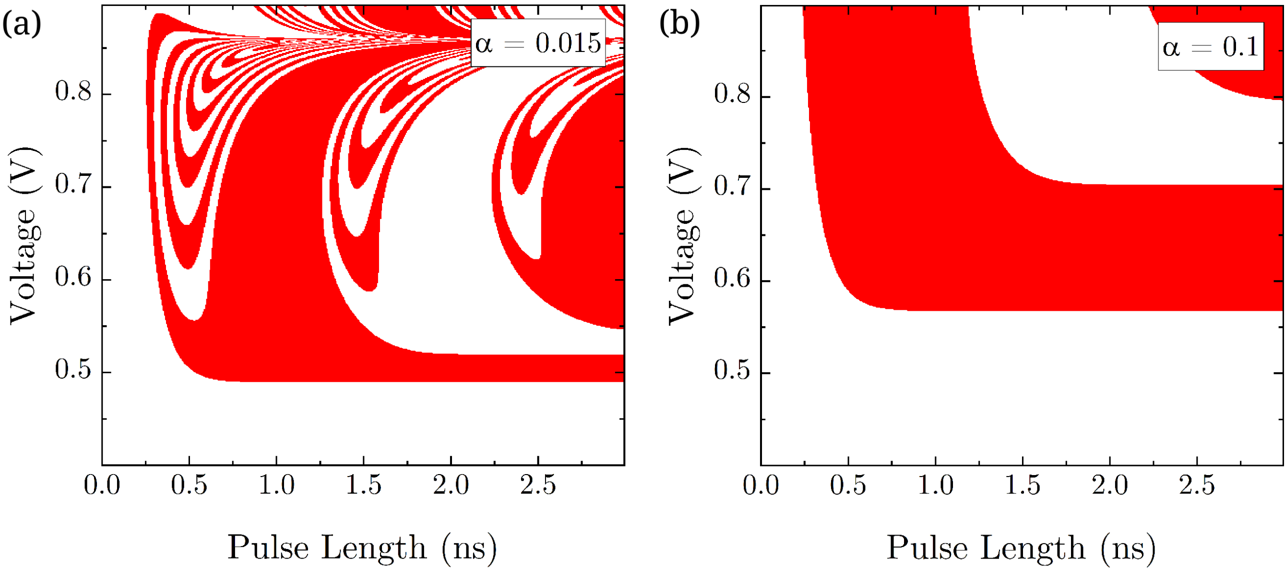

Figure 2.21: VCMA pulse phase diagram for Gilbert damping a) $\alpha = 0.015$ and b) $\alpha = 0.1$

energy barrier separating the two stable states. For the same reason, a higher voltage is needed to reach the switching threshold. A positive side effect is that higher damping reduces the time necessary to reach a stable state, also reducing the computational time required to stabilize $\vec{m}$.

## 5.4 Eliminating pre-read step in VCMA-MRAM.

For VCMA switching, its toggle-switch characteristic is not desirable for low-energy applications. Since the final state is not controlled by the pulse polarity, a small current needs to be applied to read its state before every write pulse, increasing power consumption and write access time. A way to circumvent this issue is by favoring one transition over the other, shifting the overlapping PAP and APP phase diagrams and breaking the degeneracy of the toggle-switch mechanic. To accomplish this, we can apply a vectorial magnetic field on the MTJ, as previously explored by IMEC [113].

A field with a small out-of-plane component can shift the critical switching voltage of one transition. It induces an asymmetry in the energy diagram and stability of the two states, as seen in Fig.2.9. With $\Delta_{PAP} > \Delta_{APP}$, we can switch an MTJ into a P state with an initial low voltage pulse that will only affect the magnetization if the start point is the AP state. Subsequently, we can write an AP state by applying a higher voltage pulse that switches the P state. This pulse sequence and magnetization reversal traces are shown in Fig.2.22a[20]. Phase diagram for both PAP and APP at 4K in Fig.2.22b. Depending on the amplitude of the OOP field, the window for which this writing sequence works can be tuned. However, applying a too large field will reduce the window of the low-temperature VCMA switching of the state not favored by the OOP field. The PAP diagram loses the switching band stability, so to maintain it, an MTJ with higher anisotropy is required to prevent the out-of-plane field from completely favoring only one transition.

In this configuration, we eliminate the necessity to read the device before writing, as each AP/P

---

[20] System parameters for Fig.2.22: $Diameter = 30nm$, $t_{SL} = 2nm$, $R_P = 300k\Omega$, $T = 0 - 4K$, $K_1 = 1.064MJ/m^3$, $K_2 = -0.175MJ/m^3$, $M_S = 0.94MA/m$, $\xi = 50fJ/Vm$, $H_{app} = 9mT$, $H_{OOP} = 2mT$ $\alpha = 0.1$

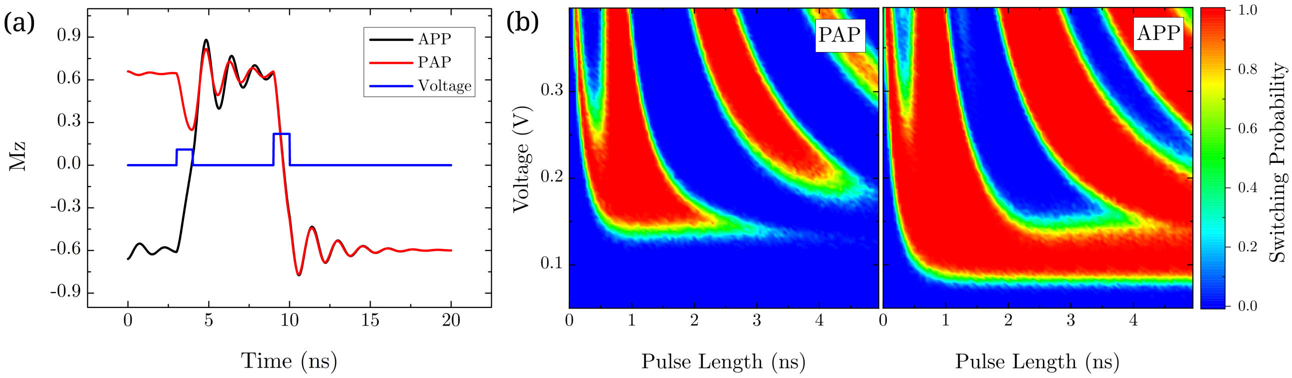

Figure 2.22: a) Time trace of $\vec{m_z}$ showing selective switching with a two-pulse sequence. A single weaker pulse writes the P state and then a second, stronger pulse, writes the AP state. b) Pulse phase diagram at 4K for PAP and APP transitions, respectively, under a 10mT in-plane and a 2mT out-of-plane field to break degeneracy of switching in VCMA.

state, corresponding to bits ’1’ and ’0’, can be written by a one-pulse or two-pulse sequence, respectively, independently of the initial bit state. Additionally, the requirement of a vectorial field can be fulfilled by in situ magnetic layers in the MTJ stack that have uncompensated stray fields on the storage layer.

## 6 Micromagnetic simulations

This section focuses on micromagnetic simulations using $MuMax^3$ [114]. It is an alternative way to describe magnetic systems allowing for a multi-spin configuration that is capable of replicating sub-micrometric structures such as domain walls. The tunnel junctions we fabricate have diameters of around 50nm, which may frequently bring the device into a non-macrospin state, where magnetic grains can form due to surface imperfections or due to the fact that the reversal occurs via domain wall nucleation and propagation. Therefore, to study the deviations to an ideal macrospin model as seen in the previous section, we analyze the behavior of VCMA and STT mechanisms in this context.

In this environment, due to how the computation is processed in the GPU, we usually define the number of cells and its dimensions in powers of 2. This parameter can considerably modify the end result, as shown in Fig.2.23a, where a 30nm diameter layer undergoing VCMA macrospin reversal in black serves as a guide to set the grid/cell size $N$ for different system initialization in $MuMax^3$. Here we see that the layers with 30 or 28 nm deviate strongly from macrospin behavior. Those with 32 or 34nm diameter work well when the grid size is 1nm (as in the red trace) or smaller (0.5nm for the blue trace). There is a limitation on how small we can make the grid, as sub-nanometric features start to go into the domain of atomistic calculations, which is not supported by $MuMax^3$.

Using then a 1nm grid, we simulate the relaxation of four different layers with diameters of 16, 32, 64 and 128nm and compare them to macrospin simulation results. In Fig.2.23b, we plot the average $\vec{m_z}$ and see that there is a clear impact of demagnetization and exchange interactions on the final equilibrium state. Knowing this, we create a 3D representation of a 64 nm layer in Fig.2.24a[21] and

---

[21] System parameters for Fig.2.24: $Diameter = 32nm$, $t_{SL} = 2nm$, $R_P = 300k\Omega$, $T = 0K$, $K_1 = 1.064MJ/m^3$,

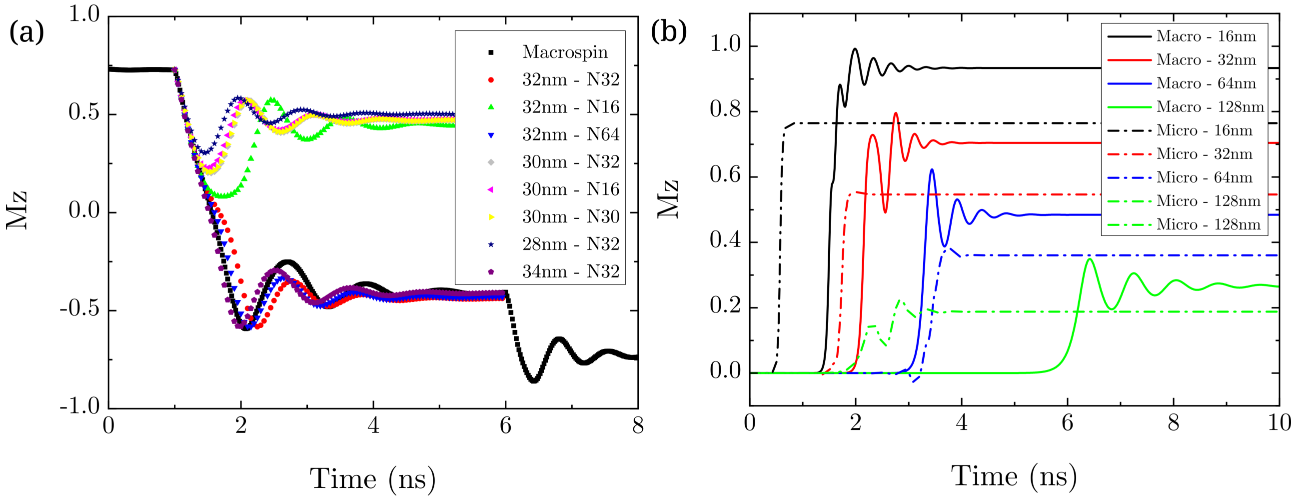

Figure 2.23: Time-trace of $\vec{m_z}$ a) For different diameter sizes and number of cells N, with the black line representing a macrospin reversal for reference. b) For diameters of 16, 32, 64 and 128nm using Macrospin model (continuous) and Mumax3 (dashed).

we see that the canted state, which comes from the presence of a term $K_2$ has a more pronounced component in the plane at its center, where $H_{demag}$ is strongest. Recreating a VCMA pulse phase diagram from this system, Fig.2.24b gives us a comparison between the macrospin model (light red) and the micromagnetic model (dark red), with an upward shift on the switching voltage and suppression of the loops at low pulse length.

This shows that although there is a deviation from macrospin, we can reliably study the dynamics of such systems and that the features present in the VCMA diagram are not an artifact of the macrospin model. The switching properties agree for diameters above 16nm. For smaller systems, the switching voltage increases above the breakdown voltage of MgO and therefore has no practical application.

## 6.1 Anisotropy Tessellation - Introduction of grain to grain anisotropy inhomogeneities

For a more realistic approach to the higher-order anisotropy $K_2$, we consider that the surface of our magnetic layer is not uniform. It is composed of magnetic grains randomly distributed considering only a first-order $K_1$ term that is randomly attributed to each grain with a 10% variance. The exchange interaction is also reduced to 90% between the grains to simulate the weaker interaction from their boundaries [?]. This configuration, called a tessellation, is used to mimic the $K_1$ variations in physical devices giving rise to $K_2$, as discussed in section 1.4. In Fig.2.25a, the micromagnetic environment is defined by arbitrarily distributed regions, which can be defined with different material parameters. In this case, each one has a slightly different $K_1$, creating a "tesellated" structure. The resulting circular ferromagnetic layer may then exhibit an inhomogeneous magnetization with an average $\vec{m_z}$ lower than 1, shown in Fig.2.25b.

To compare between a system with tessellation and one with $K_2$, Fig.2.26a[22] plots their hysteresis

---

$K_2 = -0.175MJ/m^3$, $M_S = 0.94MA/m$, $A_{ex} = 15pJ/m^2$, $\xi = 75fJ/Vm$, $H_{app} = 90mT$, $\alpha = 0.1$, $CellSize = 1nm$

[22] System parameters for Fig.2.26: $Diameter = 64nm$, $t_{SL} = 1nm$, $R_P = 5k\Omega$, $T = 1K$, $K_1 = 0.6MJ/m^3$, $K_2 =$

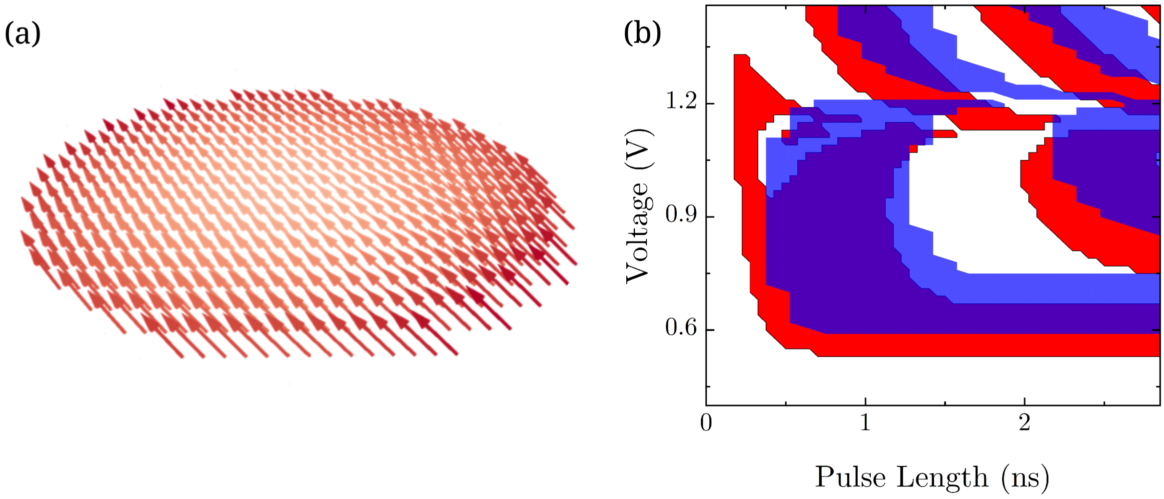

Figure 2.24: a) A 3D representation of a 64nm diameter layer with a $K_2$ component, where the magnetization changes slightly towards the in-plane state at the center. b) Comparison between a macrospin VCMA phase diagram (in red) and using $MuMax^3$ (in blue).

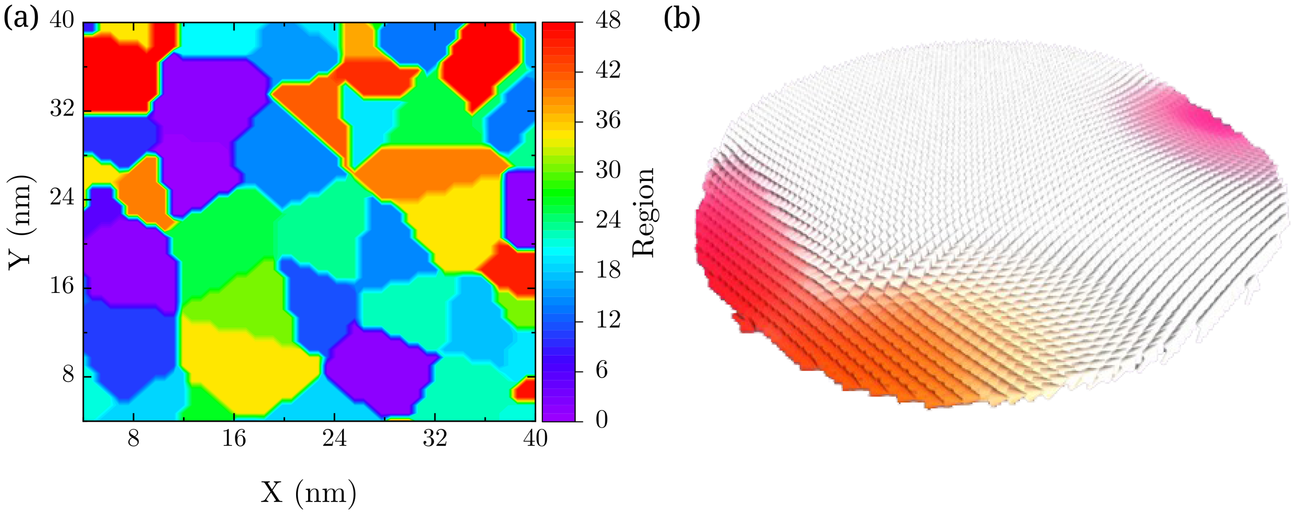

Figure 2.25: a)Region definition within MuMax3 environment in which each one has a $K_1$ that follows a normal distribution with a 10% variance. b)The magnetization state of a layer using a tessellated $K_1$ structure, with $\vec{m_z}$ lower than 1 without any external fields applied.

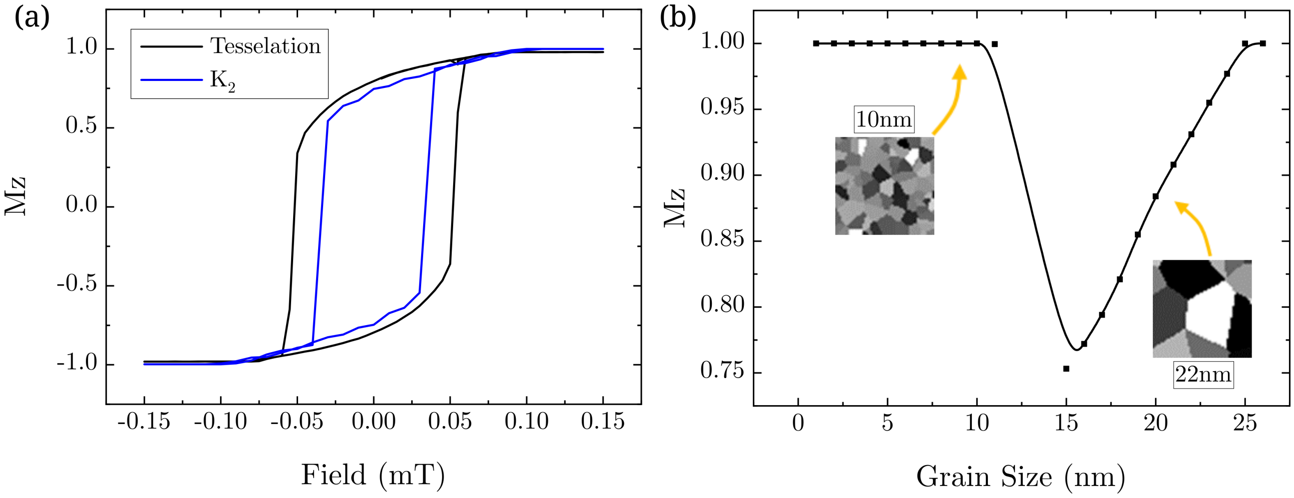

Figure 2.26: a) Comparison between a hysteresis loop for a 50nm layer using a tesselated anisotropy (in black) and a uniform layer with a $K_2$ component (in blue); b) The equilibrium state at zero field dependence for a tessellated layer with varying grain size. The inset images represent the grain distribution in the grid.

loops for a circular 50nm diameter layer. Their magnetic behavior is almost identical, differing only in coercivity, which depends on the amplitude of $K_2$ and the tessellation variance. This allows us to not use a higher-order anisotropy term and treat it as a virtual contribution within a tessellated structure. The stable state at zero field, which can change with the average grain size, is shown in Fig.2.26b[23], where we get a discontinuity at 15 nm for this specific set of parameters. When the grain size is small, they are composed of a single spin or very few individual spins that interact with neighboring grains with the same magnitude. As they grow in size, it will reach a threshold in which the intergrain interaction will be strong enough to create its own local magnetization due to the different $K_1$ of each grain, inducing a drop on average $m_z$. The $m_z$ component increases again with grain size until it returns to a fully saturated out-of-plane layer for very large grains as it fully envelopes the layer and approaches a single domain configuration. From the fabrication point of view, if processing induces non-uniformity on the layers, due to their thickness or diameter, we will see a transition from a square hysteresis loop into one showing a rotation of the stable state at the field compensation point, as shown in Fig.2.27a[24], for a 64nm diameter layer with 8-100nm average grain sizes. For 100nm size grains, the layer is close to a single crystal, exhibiting an almost entirely square loop while the rotation of the loop increases for smaller grains down to 8nm, which also increases the asymmetry in the resistance level.

To study the effects of temperature on simulations using tessellation, we look at the resistance hysteresis loop of a circular 64 nm diameter layer in Fig.2.27b[25]. A tessellated layer is used with a

---

$-0.05MJ/m^3$, $M_S = 0.97MA/m$, $A_{ex} = 15pJ/m^2$, $\xi = 0fJ/Vm$, $H_{app} = 0mT$, $\alpha = 0.1$, $CellSize = 4nm$

[23] System parameters for Fig.2.26: $Diameter = 50nm$, $t_{SL} = 1nm$, $R_P = 5k\Omega$, $T = 0K$, $K_1 = 0.532MJ/m^3$, $K_2 = 0MJ/m^3$, $M_S = 0.97MA/m$, $A_{ex} = 15pJ/m^2$, $\xi = 0fJ/Vm$, $H_{app} = 0mT$, $\alpha = 0.1$, $CellSize = 1nm$,

[24] System parameters for Fig.2.27: $Diameter = 64nm$, $t_{SL} = 1nm$, $R_P = 5k\Omega$, $T = 0K$, $K_1 = 0.6MJ/m^3$, $K_2 = 0MJ/m^3$, $M_S = 0.97MA/m$, $A_{ex} = 15pJ/m^2$, $\xi = 0fJ/Vm$, $H_{app} = 0mT$, $\alpha = 0.1$, $CellSize = 4nm$

[25] System parameters for Fig.2.27: $Diameter = 64nm$, $t_{SL} = 1nm$, $R_P = 5k\Omega$, $T = 0 - 300K$, $K_1 = 0.6MJ/m^3$, $K_2 = 0MJ/m^3$, $M_S = 1MA/m$, $A_{ex} = 15pJ/m^2$, $\xi = 0fJ/Vm$, $H_{app} = 0mT$, $\alpha = 0.01$, $CellSize = 2nm$, $GrainSize = 40nm$

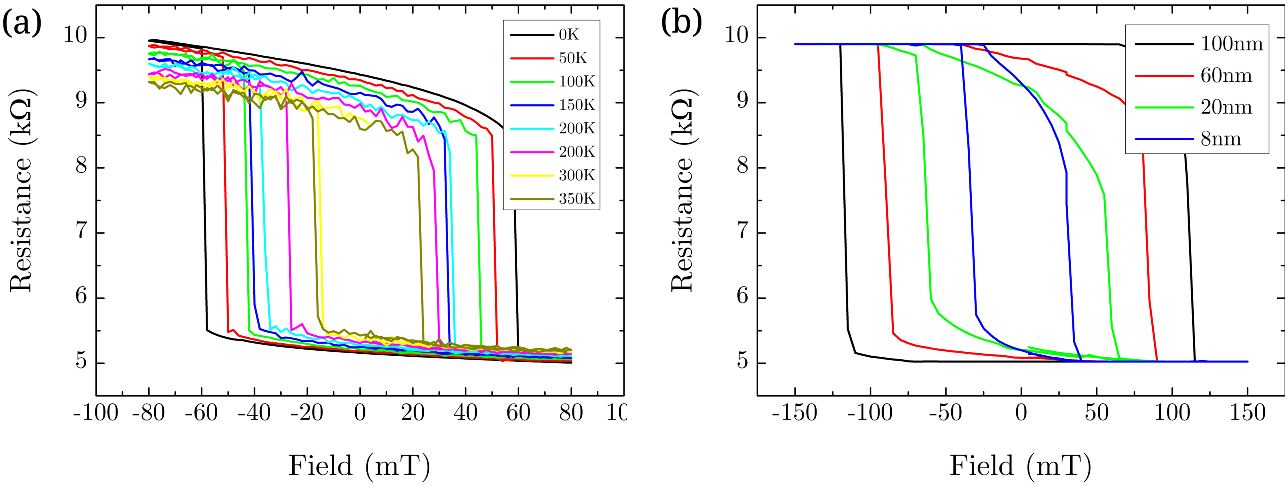

Figure 2.27: Dependence of hysteresis loop for a tessellated layer with 64nm diameter: a) For different average grain size and b) For different temperatures with 40nm grain size.

grain size of 40 nm. The increase in temperature does not change the resistance levels for the PAP and APP transitions, occurring at constant values, $5.5k\Omega$ and $8.5k\Omega$, respectively. The AP rotation profile does not change despite the coercivity and TMR increasing for lower temperatures. The rotation of the AP state is unchanged because it is the result of the grain-to-grain $K_1$ distribution, which remains constant, defined by the simulation parameters. In a real physical system, we know that a change in temperature will modulate both $K_1$ and $M_S$, consequentially varying the magnetic domain wall size. This may result in a reorganization of the magnetic substructures in the layer [115], changing the average grain size, which would result in some change of the rotation of the AP state, as seen in Fig.2.27a. In $MuMax^3$, it is not possible to compute the TMR dependence with temperature [116], so the increase in TMR at zero field is due to the first-order anisotropy enhancement at low T, which brings the magnetization closer to fully out-of-plane state, since at zero field the layer is in an intermediate state, equivalent to an easy cone.

## 6.2 STT Switching dependence with temperature on tessellated layer

Within the macrospin model, the switching voltage dependence follows the analytical solution of Eq.2.52, which was previously shown in Fig.2.16b. The critical voltage decreases monotonically with increasing temperature.

$$I_C = \frac{4e}{\hbar}\frac{\alpha}{\eta}\Delta\, k_B T \tag{2.52}$$

Its straightforward application to study the influence of the thermal stability $\Delta$ has the disadvantage that it does not take into account the properties of a real physical and finite system of an MTJ, such as the effects of the exchange and demagnetization energies on a micromagnetic system. Therefore, we looked at a conventional pMTJ layer with a single domain and $K_2 = 0$ to evaluate how the magnetization state and $V_C$ evolve with temperature. In Fig.2.28a[26], starting at 0K we see

---

[26] System parameters for Fig.2.28a: $Diameter = 64nm$, $t_{SL} = 1nm$, $R_P = 5k\Omega$, $T = 0 - 300K$, $K_1 = 0.6MJ/m^3$, $K_2 = 0MJ/m^3$, $M_S = 1.0MA/m$, $A_{ex} = 15pJ/m^2$, $\xi = 0fJ/Vm$, $H_{app} = 0mT$, $\alpha = 0.1$, $CellSize = 4nm$, $GrainSize =$

that the average component $m_z$ is stable, having a fully out-of-plane configuration (+1 direction) and quickly destabilizes above 160K to reach a fully in-plane state at 220K. The corresponding switching voltages steadily decrease until 160K, from which point any nonzero amount of current is enough to reverse the sign of the $m_z$ component. This reflects the drop-off of $m_z$ in the same temperature range. The inset image represents the layer in its stable state at 180K, where we can see that the central portion of the layer has lower effective anisotropy, which reduces the average $m_z$ value of the system. In Fig.2.28b[27], we introduce an average magnetic grain size of 40nm with a 10% dispersion of $K_1$ and $A_{ex}$. The behavior of $m_z$ is the same as expected from the macrospin model, as seen in Fig.2.3, where the transition to a fully in-plane layer with increasing temperature is smooth and starts at 0K for values of the Callen-Callen exponent calculated for $l$ lower than 1. The inset images show how portions of the layer lose effective anisotropy and go in-plane, while other sections remain partially out-of-plane, resulting in a reduction of the average $m_z$ component of the system. Its switching voltage, however, shows a large discrepancy with a conventional pMTJ in (a). There is now a stable plateau value $V_C$ between 100K and 160K, followed by a sharp drop above 160K. Between 100K and 180K, the changes in slope of the variation $V_C$ with temperature contrast with the continuous monotonic changes in $m_z$, up to the temperature when both approach zero.

This behavior / plateau appears only in micromagnetic simulations, strongly disagreeing with the macrospin model, as seen in Fig.2.16b. It results from considering a higher-order anisotropy $K_2$, as seen in Fig.2.28b. We could try to explain this by analyzing how the reversal affects the grains individually and how the boundary of the domain switching travels through the layer during the reversal, but the plateau is present whenever $K_2$ is considered. This is independent of the simulation approach, using a tessellated layer or a uniform layer with a $K_2$ term, which has coherent switching. Fig.2.29[28] shows a similar feature on a layer with $K_2 < 0$ and without magnetic grain structure. The change in the switching voltage dependence with temperature is that in this case it does not reach a constant plateau, but actually increases in a temperature range from 130K to 200K. This means that the plateau is not directly correlated to the grain structure of the system. This feature is important to understand, as will be shown in Chapter 4 (Fabrication and Characterization Methods), because it can be observed experimentally. Numerically, it would require a more in-depth investigation on the interplay between the higher-order anisotropy and the demagnetization energy of the system.

---

$0nm$

[27] System parameters for Fig.2.28b: $Diameter = 64nm$, $t_{SL} = 1nm$, $R_P = 5k\Omega$, $T = 0 - 300K$, $K_1 = 0.6MJ/m^3$, $K_2 = 0MJ/m^3$, $M_S = 1.0MA/m$, $A_{ex} = 15pJ/m^2$, $\xi = 0fJ/Vm$, $H_{app} = 0mT$, $\alpha = 0.1$, $CellSize = 4nm$, $GrainSize = 40nm$

[28] System parameters for Fig.2.29: $Diameter = 64nm$, $t_{SL} = 1nm$, $R_P = 5k\Omega$, $T = 0 - 300K$, $K_1 = 0.6MJ/m^3$, $K_2 = -0.0207MJ/m^3$, $M_S = 1.0MA/m$, $A_{ex} = 15pJ/m^2$, $\xi = 0fJ/Vm$, $H_{app} = 0mT$, $\alpha = 0.1$, $CellSize = 4nm$, $GrainSize = 0nm$

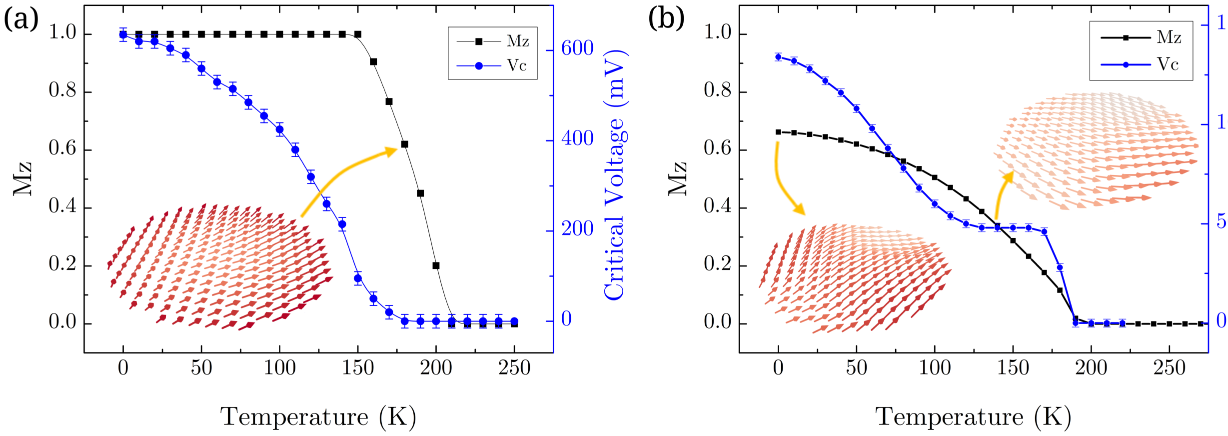

Figure 2.28: Micromagnetic temperature dependence of $\vec{m_z}$ in black and the critical switching voltage in blue for a circular 64nm layer in the following configurations: a) a conventional out-of-plane pMTJ and b) a tessellated layer with no $K_2$ term and average grain size of 40nm. The inset images represent the layer state at specific temperatures indicated by the arrows.

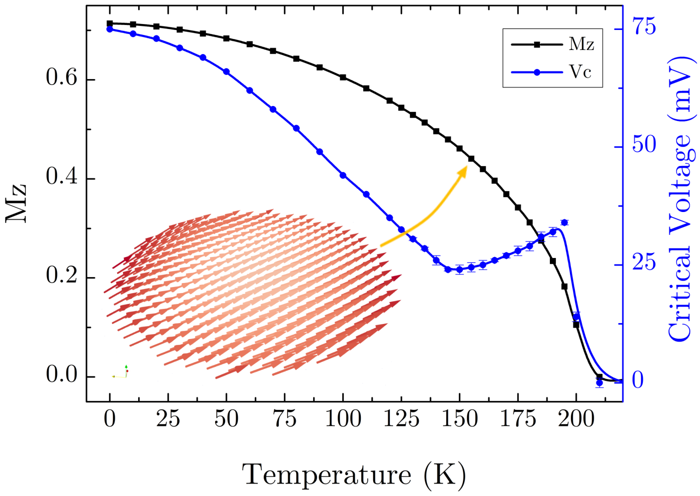

Figure 2.29: Micromagnetic temperature dependence of $\vec{m_z}$ in black and the critical switching voltage in blue for a circular 64nm layer with a finite $K_2$ term showing a $V_C$ plateau between 130K and 200K.

# 7 Conclusion

By using the results discussed so far, we can then guide our choice of parameters, interpretations, and conclusions for the phenomena we will be discussing when looking into experimental data and the magnetic/electrical characterization of fabricated devices in the following chapters. Thus, we have seen how with a relatively simple STT model we can deepen our understanding of systems such as the storage layer with the easy cone anisotropy and the advantages of using such a configuration, which is not easily accessible experimentally, as there is only a small window of stability available visible in Fig.2.6. It is interesting to pursue the easy cone anisotropy because it can reduce the writing energy per bit, as evidenced by the reduction of the switching voltage by the introduction of any amount of $K_2$ component into the system in Fig.2.5a. Additionally, the STT effect can potentially have much faster switching speeds, since the acting torque on the magnetization does not require thermal activation.

To better understand the origins of the easy cone, we assess the equivalence between a system with uniform $K_2$ and a system with a $K_1$ distribution, or tessellation. In Chapter 4 we will look for experimental evidence of the unusual behavior of the dependence of $V_C$ on temperature from Fig.2.29 in devices that show a similar rotation of the stable resistance states, as seen in Fig.2.27.

In the case of the VCMA mechanism, we have identified that a deterministic non-precessional switching is possible if the operating environment is limited to very low temperatures, below 50K, predicted by Fig.2.18. To maintain high switching reliability, deep cryogenics of 10K or less is an optimal condition for this regime. Its dynamics are analyzed and correlated to the energy barrier between the stable states P and AP of the system and how sensitive it is to material parameters.

Looking at the evolution of material parameters with temperature and how the magnetization behaves under different conditions allows us to form predictions and aid us in designing our devices from a material point of view and to identify the sizes and thicknesses we should aim for to reach the proper anisotropy and memory retention that we would like to obtain in the working cryogenic conditions.

# Chapter 3

# MTJ Material Optimization for Cryogenic Operation

Goals

For the stack design of both VCMA and STT systems aimed at cryogenic operation, some optimization steps are necessary to reach the desired properties of our devices. In this chapter we use MOKE analysis of thin films for preliminary magnetic characterization. For STT-MRAM, we focus on adjusting the perpendicular anisotropy of the storage layer to enable STT switching at low temperature. For VCMA-MRAM, tunnel barriers with resistance area products (RA) greater than 100 $\Omega\mu m^2$ are required for measurable VCMA effects, which effectively requires adjusting the tunnel barrier oxidation conditions.

## Contents

# 1 Magnetic tunnel junction structure

As mentioned previously, a magnetic tunnel junction essentially comprises three elements: a reference/hard layer, a tunnel barrier, and a storage/free layer. Although this defines the core of a magnetic memory, we must add other components that will enable the MTJ to function properly within a circuit. The stack structure of a perpendicular magnetic memory with each layer described with its intended purposes is listed as follows:

1. Seed Layer - also called "Bottom Electrode" or "buffer layer". It is the first layer deposited on the wafer and plays several roles, in particular, providing good adhesion of the stack on the substrate and to properly orient the texture of the layers subsequently deposited on it. The choice of the buffer layer is important to optimize the magnetic properties of the magnetic layers and minimize the roughness of the stack. Due to the importance of roughness, minimizing it at this step will reduce the accumulation of defects at later stages. Therefore, a simple Ta electrode can be modified into a compound structure, such as Ta(22) / FeCoB(0.8) / Ta(3) (thickness in nm). This sequence of layers reduces the root mean square (RMS) of the roughness from 0.44nm, for Ta 25nm, to an RMS roughness of 0.25nm[117] for the modified layer.

2. Texturizer - This layer, usually Pt, is added to the stack because the Synthetic Antiferromagnet that is going to be deposited on top of it requires an fcc (111) lattice structure to exhibit a strong perpendicular anisotropy [118][119]. The stability and coercivity of the structure is sensitive to its crystallographic configuration. The thickness of the texture promoter must minimize the roughness of the final stack, which increases for larger thicknesses, while maintaining its ability to induce the correct texture, which decreases for low thickness. Depending on the fabrication protocol implemented, Pt can be used as the seed layer, acting as a bottom electrode and promoting a (111) lattice structure. In nanofabrication process, the Ta layer is needed as our Reactive Ion Etching (RIE) step was optimized for Ta etching rather than Pt, which will be explored in Chapter 4. This also creates limitations on the design of devices that are "top-pinned", meaning that the SAF structure is deposited above the MgO tunnel barrier. In that case, the absence of a thicker seed layer will degrade the magnetic stability of the reference layer structure, although some success has been achieved in fabricating this type of stack[120].

3. Synthetic Anti-Ferromagnet (SAF) - Usually referred to as "SAF", it is a magnetically compensated hard layer, having a multilayer stack of (Co/Pt) repetitions with strong perpendicular magnetic anisotropy [121]. In our stacks, a $(Co/Pt)_6$ structure is exchange coupled through a thin layer of Ru by RKKY with $(Co/Pt)_3$. The first block has the strongest PMA in the stack. On top of it, a smaller block with lower PMA forms the complete antiferromagnet. The asymmetry of these blocks is necessary to minimize the stray field they create on the storage layer. Therefore, the magnetic block closest to the storage layer needs to have lower magnetic moment, but also large enough to cancel the stray field from the lower block with higher magnetic moment.

4. This boron absorption layer is of critical importance to induce PMA of the magnetic layers at the interface with the tunnel barrier if the chosen alloy is FeCoB, regardless of its stoichiometry. It is

also important to get a large TMR amplitude, since the spin filtering mechanism that yields the large TMR of MgO-based magnetic tunnel junctions requires bcc crystallization of the FeCoB alloy as well as of the MgO barrier. In our case, we can use either Ta or W, though the latter one yields better magnetic properties, as will be discussed in this chapter. The diffusion of boron out of the FeCoB layers is an important step for the magnetic layers and the tunnel barrier to crystallize correctly. In earlier iterations of MTJs, FeCo layers were deposited with a crystalline texture that prevented the formation of the preferred bcc (100) structure of the MgO layer. The current FeCoB layers deposited are initially amorphous and the subsequent MgO can crystallize in a (100) texture. After annealing at high temperatures (300C and above), boron diffuses out of the FeCoB alloy and the FeCoB / MgO / FeCoB structure of MTJ can crystallize with high PMA and TMR[122, 123, 124].

5. Reference Layer - Also called "hard layer", is the magnetic layer adjacent to the tunnel barrier, made from amorphous FeCoB, deposited on top of the B-getter. The B-getter used was a very thin W layer of 0.5nm or less, such that it can still couple ferromagnetically with the SAF below. Because of the high coercivity of the SAF, the reference layer is effectively pinned in the out-of-plane orientation.

6. Tunnel Barrier - The most common tunnel barrier for state-of-the-art MRAM is MgO, which has replaced alumina or alumina-based compounds due to its higher TMR and better interface quality, which enhances the PMA of the storage layer [125]. Our barrier is composed of naturally oxidized Mg, prepared by depositing a Mg metallic layer which can then be exposed to different oxygen pressures for a period of time. These parameters will modulate the amount of $O_2$ molecules that will adsorb on the surface of Mg and consequently the final oxidation state. In more conventional MgO RF-sputtered barriers, the tunnel barrier conductance decreases exponentially with MgO thickness. However, in Mg-oxidized barriers, increasing the thickness of Mg while maintaining the oxidation time will lead to a lower oxidation state and a lower resistance area product (RA) of the stack. On top of the naturally oxidized Mg, another layer of Mg (0.5nm) is deposited, acting as a cap the barrier to optimize the oxygen distribution within the MgO barrier during the annealing process.

7. Storage Layer - Also called "free layer", is the section of the stack that has the most flexibility for experimentation and change in its composition. FeCoB is commonly used due to its high perpendicular anisotropy. For our purposes, we modify it by adding insertion layers and varying its thickness to change the final electrical properties of the device. Since it is deposited on top of the MgO barrier, a B-getter is again necessary, with W being the material of choice. The total magnetic volume needed to achieve PMA in the storage layer is generally larger than in the reference layer. W is a heavy metal and can sputter off the lighter atoms in FeCoB during deposition. This will reduce the final amount of material in the layer. It also means that the dead layer will be higher for this top electrode, which must be taken into account when the stack structure is modified.

8. Capping - In our fabrication process, we have optimized the hardmask etching to work with a

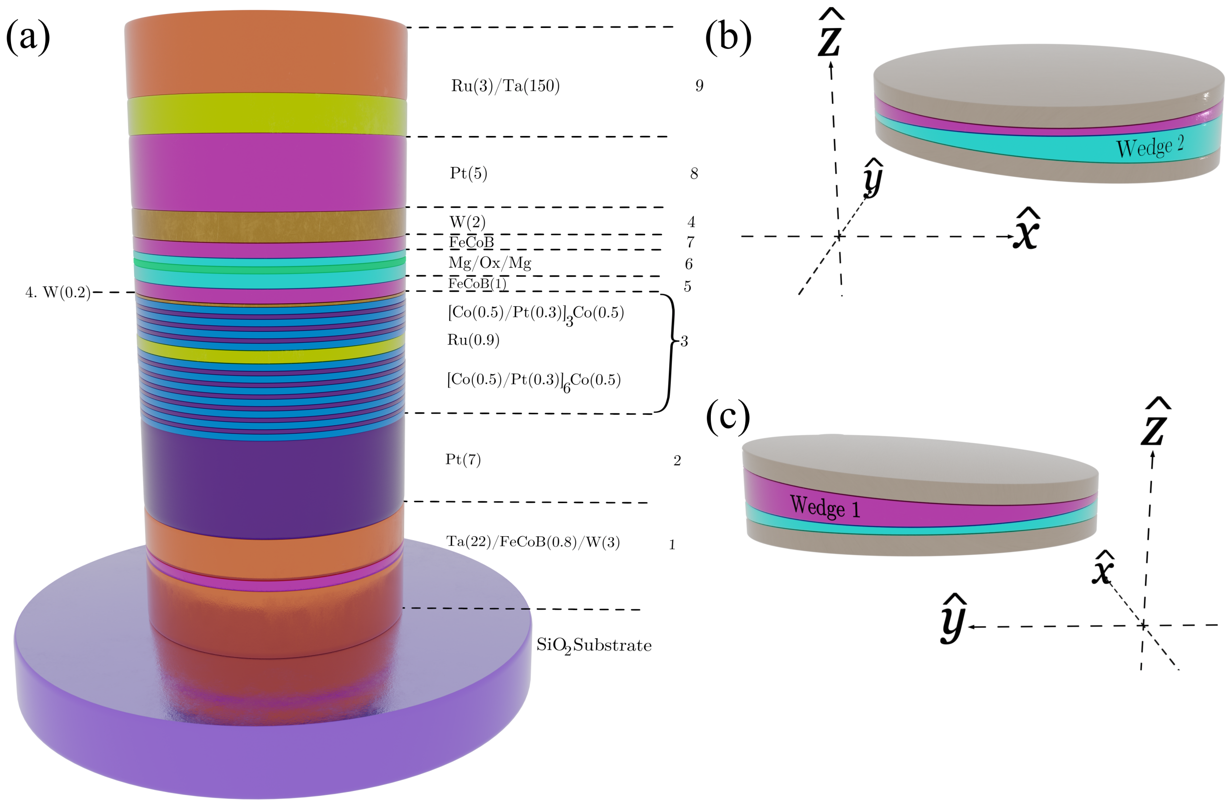

Figure 3.1: a) Schematic of a full stack with all its components enumerated with their respective thickness in *nm*. The layers are represented with their real scale in relation to each other with the exception of the substrate and Ta bottom and top electrodes. b) Cross wedge sample in YZ plane, showing the wedge thickness variation along the x-direction and c) Cross wedge in ZX plane, with wedge thickness variation along the y-direction.

non-annealed Ta. For that reason, we must anneal our stack before depositing it. We accomplish this by adding a capping layer of Pt, from 3nm to 5nm, on top of the stack to protect against oxidation. Additionally, with a thin capping we are able to analyze the wafer at thin-film level using MOKE before patterning the tunnel junctions, which helps understand and correlate magnetic properties before and after fabrication. In processes that skip the capping and deposit the hardmask directly, it is not possible to do MOKE analysis, as the laser penetration depth cannot reach the magnetic layers.

9. Hardmask - For the etching and definition of the magnetic pillar during fabrication, a dual layer of Ru(3) / Ta(150) is used. The etching of this hardmask is optimized for a non-annealed Ta and the quality of the pillar shape shape strongly depends on the definition of the Ta during fabrication. It acts as the top electrode of the device and has a much larger thickness compared to the MTJ itself, which is usually under 30nm in total for an STT-MRAM stack.

Fig.3.1a shows a schematic of a standard pMRAM stack fabricated with the enumeration indicating each section of the stack. The storage layer and the tunnel barrier do not have their thickness indicated because they are the main elements subject to change during the optimization process. Fig.3.1b shows the geometry of a cross-wedge sample, in which a layer is deposited with varying thickness in one direction and another layer is also deposited as a thickness wedge, but the second wedge thickness varies along an orthogonal direction, rotated by $90^o$. This creates a pattern with all possible combinations of thicknesses of the two layers.

## 1.1 Synthetic anti-ferromagnet optimization

As mentioned previously, measured devices can show a high stray field from the reference SAF layer structure. There are two straightforward issues that may be causing the large offset: either the (Co/Pt) repetitions from both SAF blocks are not canceling each other out; or it can also originate from the fabrication process during the ion beam etch (IBE) of the reference layer, such that the lateral dimensions of the two SAF blocks are not identical.

To solve the first issue, we sought to achieve better SAF compensation at the storage layer by fabricating a reference layer stack with a modified SAF structure using Co/Pt blocks of 6 and 2 repetitions instead of 6 and 3 repetitions, while also including a wedge on the reference layer FeCoB at the interface with the MgO barrier. In Fig.3.2a the two presented hysteresis curves have a different stray field $H_{stray}$ due to a better compensation of the 6x2 blocks, with the possibility of even further improvement by adjusting the thickness of the reference FeCoB layer. Therefore, Fig.3.2b shows a plot of the $H_{stray}$ as function of the FeCoB layer thickness, for devices of 20 nm nominal diameter after annealing at 300C for 10 min. The stray field $H_{stray}$ varies linearly with the thickness of the FeCoB layer, according to earlier calculations that establish the linear dependence with the magnetic moment ratio $m_2/m_1$, where $m_1$ and $m_2$ are the magnetic moments of the upper and lower SAF blocks [126], respectively. Considering that the only layer thickness variation on the SAF stack is the FeCoB layer thickness, the ratio of the moments is inversely proportional to the FeCoB layer thickness. A linear fit of the data provides the expected FeCoB ($\approx 1nm$) layer thickness required to achieve full compensation of the reference layer. A dispersion of $\pm 50Oe$ in stray field values is due to variability of cell diameter across the wafer, as the SAF compensation thickness depends on the actual cell diameter, the moment ratio increasing as the diameter decreases. This procedure provides a simple optimization of the SAF structure to ensure that at the expected operating temperature, the device will indeed be able to operate as a memory switching between 2 bi-stable states without requiring any additional stray field compensation. The additional requirement is that the device coercivity must be larger than the stray field variability $H_c > 50Oe$ in this case.

In the case of nanofabrication-related uncompensated SAF, it stems from the etch process starting with the Ta hardmask etch. Ideally the MTJ pillar is cylindrical, with each layer of the SAF producing a stray field that can be estimated from the number of Co/Pt repetitions. In practice, however, it is often the case that despite extensive optimization, the etching of the hardmask produces a shape that is not a proper cylinder. Most commonly, it will result in a conical shape. Since the magnetic pillar etching will inherit the form of the hardmask, each layer will have a slightly different field strength, resulting from the process variability. This creates a field offset in the devices and can render some stack designs unusable without a compensation offset field.

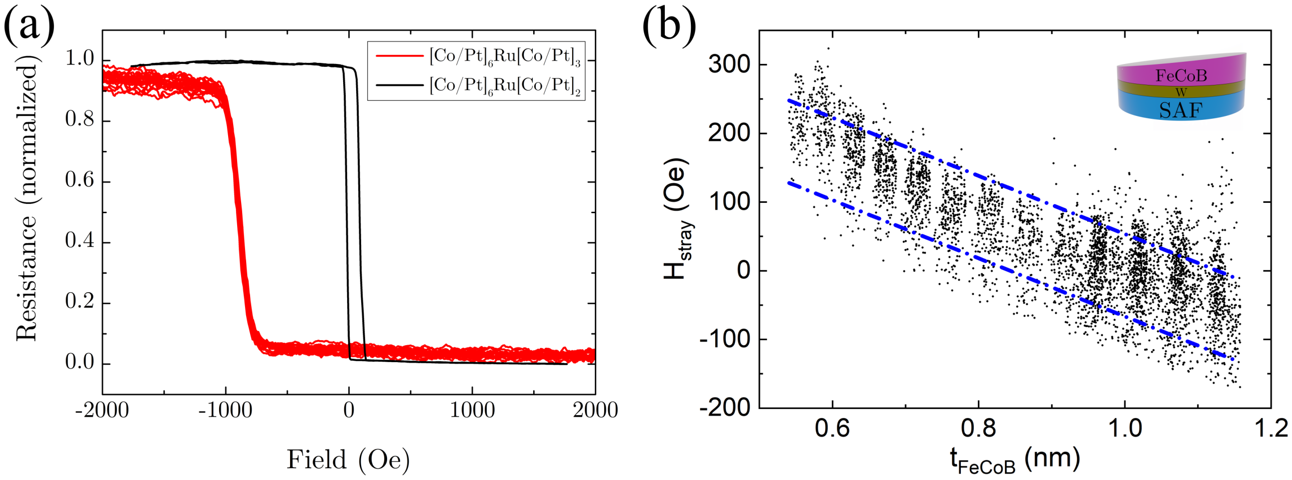

Figure 3.2: a) Field hysteresis loop of two devices from different samples, fabricated with a SAF using different Co/Pt repetitions in the top SAF block, $[Co/Pt]_6/Ru/[Co/Pt]_3$ in red and $[Co/Pt]_6/Ru/[Co/Pt]_2$ in black. b) Stray field dependence with the FeCoB reference layer thickness. The critical thickness of $\approx 1nm$ results in a mean zero offset with a dispersion of $\pm 50Oe$. The full stack of this sample is Ta(22) / FeCoB(0.8) / W(2) / Pt(7) / SAF / FeCoB(0.5-1.15) / MgO(2.3) / FeCoB(0.9-1.9) / W(2) / Pt(5) / Ru(3) / Ta(150)

## 2 Magnetic characterisation by MOKE

Most optimization work for our MTJs is done before the fabrication process. As nanofabrication is an expensive and time consuming step, we first characterize the magnetic properties of our stacks through the magneto-optic Kerr effect (MOKE) using a $NanoMOKE3$ tool from Durham Magneto Optics. It is a technique that measures how a linearly polarized light is rotated when interacting with a magnetized material [127]. The rotation in polarization is measured from the ellipticity of the reflected light in milli-degrees, exposed to a laser spot of $40\mu m$ in diameter. In our setup we utilize the polar Kerr effect, applying a sweeping out-of-plane field to capture the hysteresis loop associated with the rotation of the signal from what are mostly perpendicular anisotropy layers. The maximum magnetic field is about $3.5kOe$ due to the electromagnets amperage limitation. Although with this technique it is not possible to extract $M_S$ [128], it can give us information on the coercivity and amplitude of the Kerr signal [129]. Thus, it is a powerful tool to measure the evolution of magnetic properties across the surface of wafers of any size quickly and efficiently. Moreover, the penetration depth of the laser is on the order of tens of nanometers, allowing us to sense the properties of stacks, including the SAF layers.

For samples that will proceed to nanopatterning, we characterize them with the full MRAM stack with the exception of the hardmask. After MOKE mapping is done, the hardmask deposition and fabrication process is done. For investigation of different layer properties, we instead deposit "half-stack" junctions, without SAF, and the seed layer is replaced by a much thinner Ta, reducing the roughness. To study the storage layer, the reference layer FeCoB is replaced by a thin 0.4nm FeCoB that is magnetically dead, not contributing to the measured signal from the magnetic layer of interest. This facilitates the data analysis and interpretation of the PMA characteristics of our devices. As an example, the half-stack used to locate the thickness range where PMA exists for a storage layer would be: Ta(3) / FeCoB(0.4) / Mg(0.7) / Ox(30s) / Mg(0.5) / FeCoB(0.9-1.7) / W(3) / Pt(5). In the following discussion, when a half-stack structure is mentioned, the Ta(3) / FeCoB(0.4nm) seed layer and the Pt capping layer are omitted for simplicity. In addition, the tunnel barrier, deposited as Mg(0.7) / Ox(30s) / Mg(0.5nm), will be represented as MgO(1.3) when not explicitly modified in the stack.

## 2.1 Annealing optimization - W vs. Ta

The annealing step is an important part of the fabrication process. It is done using an AnnealSys oven using flash lamps to ramp the temperature to a setpoint under 10 minutes. During this process, the amorphous FeCoB and MgO will thermalize and settle into a crystalline structure, while also allowing for boron atoms to migrate towards the B-getter layers. For higher temperatures, the FeCoB/MgO interface will improve crystallinity and the spin filtering effect of the tunnel barrier will be enhanced [45]. Higher temperatures will also increase the diffusion of the B-getter layer, and generally the PMA of the Co/Pt multilayer system will degrade first, followed by a loss of PMA at the MgO/storage layer interface at even higher temperatures. In the context of CMOS integration, it is necessary that the stack material is compatible with the annealing temperatures used in the microelectronics industry, typically $400^oC$. Although we work with proof-of-concept devices, designing a stack that can maintain good magnetic properties at high temperatures is recommended, since its electrical characteristics will be improved, such as higher TMR levels.

Thus, the main modification to the stack that will have a direct impact on the heat endurance of the final device is the B-getter. We look into two different materials: Tungsten and Tantalum. So, we compare the following two stacks to quantify which one gives us the better properties in terms of endurance to high-temperature anneals: Seed / FeCoB (0.4) / MgO (1.75-3.5) / FeCoB (0.8-1.9) / Ta (3) / Pat (5) and Seed / W (3) / FeCoB (0.4) / MgO (1.75-3.5) / FeCoB (0.8-1.9) / W (2) / Ta (3) / Pat (5), the only difference being the addition of a Tungsten layer in the Ta/FeCoB interface. The seed layer is Ta(22) / FeCoB(0.8) /Ta(2). Their remanence of the Kerr signal is plotted in Fig.3.3 using MOKE analysis after being annealed at $250^o$ for 10 min. The red region in its center represents the area in which PMA exists for their respective combinations of MgO and FeCoB thicknesses. The W stack has an area 100% larger than the Ta stack and a maximum coercivity 66.5% stronger, going from 242Oe to 403Oe. At $300^oC$, with Ta, PMA is strongly degraded, losing its remanence across the wafer and its coercivity falling to 30Oe. For W the area increases 19% and the coercivity increases by 18.5%, with 480Oe. Then, at $350^oC$, Ta does not show a magnetic signal, and W starts to degrade, losing 7% of its area and coercivity, dropping to 450Oe.

Evidently, for the purpose of optimizing the crystallinity and diffusion of the materials in the stack, W is the best option. We use $300^oC$ as the standard temperature for annealing, as our samples cannot sustain setpoints higher than $350^oC$. To reach the industry standard of $400^oC$, extensive optimization in stack deposition conditions would be required to increase interface quality, notably the roughness of Mg and SAF magnetic stability.

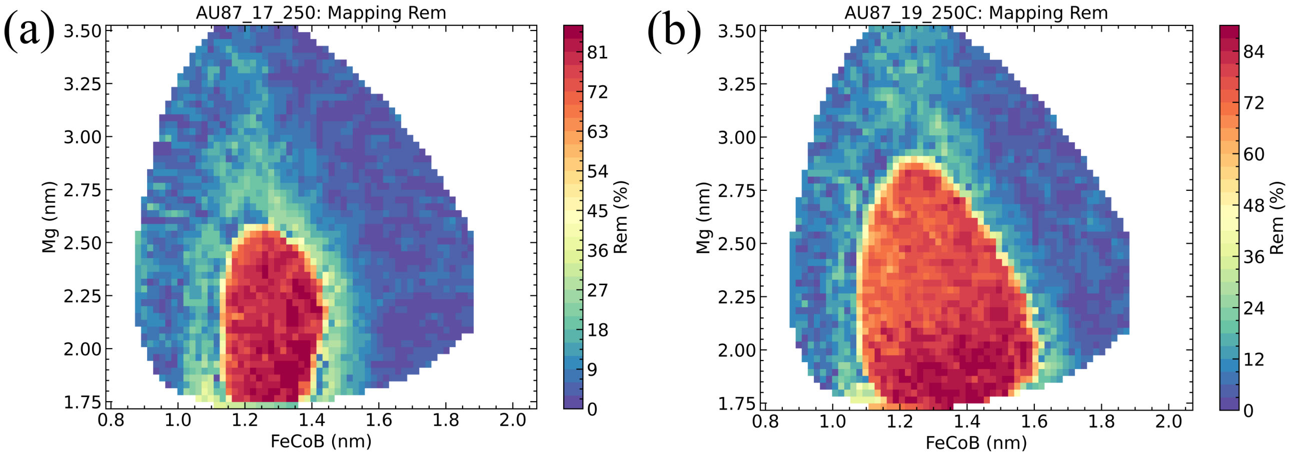

Figure 3.3: MOKE mapping of the remanence of two stacks annealed at 250$^o$. a)Using Ta as B-getter and b) Using W as a B-getter.

## 2.2 Determination of Magnetic Dead Layer thickness by MOKE

Another relevant impact that the choice of B-getter has on the stack design is the resulting magnetic dead layer thickness $t_d$ for our storage and reference layers. It is possible to use MOKE analysis to estimate the magnetic dead layer by looking at the saturation magnetic moment per unit area versus the thickness of the magnetic layer with the following equation [130]:

$$\frac{m_s}{A} = M_S(t - t_d) \tag{3.1}$$

Where $m_s$ is the magnetization, $A$ is the area of the sample, and $t$ is the total thickness of the layer. Most often used with VSM measurements, we can extrapolate the same concept to the MOKE. The Kerr signal is directly proportional to the magnetization of the sample, which gives us the slope $(t - t_d)$. This method is especially useful for ultrathin films such as ours due to their reduced magnetic signal, as it can be difficult to measure with VSM with precision. An additional advantage is the possibility to measure continuous thickness variation in wedge samples with higher resolution, since VSM requires measuring each thickness value separately.

To extract $t_d$, we must do a linear fitting on the Kerr signal amplitude in the range of thicknesses for which PMA exists, and there is no loss of $M_S$ due to layer discontinuities from very small thicknesses where we reach a super-paramagnetic state. Thus, we plot the remanence of the signal, and the plateau at $> 80\%$ will define the fit boundaries. In Fig.3.4a, we have the MOKE measurement using an out-of-plane field for a storage layer with Tungsten B-getter, with a high remanence state between 1 and 1.6nm. The Kerr signal shows a positive slope that changes abruptly outside the PMA region. For lower thicknesses, it is due to the transition between a continuous layer and one that becomes noncontinuous, affected by wetting of the FeCoB on the MgO surface. For higher thicknesses, the layer transitions into an in-plane state, causing a drop in the Kerr signal. In Fig.3.4b, the Kerr signal is plotted for four different stacks annealed at $300^oC$. For the reference layer, the stack is as follows: Ta(3) / FeCoB(1-1.6) / Mg(0.7) / Ox(30s) / Mg(0.5) / FeCoB(0.4) / Ta(3) / Pt(5) and for the storage layer: Ta(3) / FeCoB(0.4) / Mg(0.7) / Ox(30s) / Mg(0.5) / FeCoB(1-1.6) / Ta(3) / Pt(5),

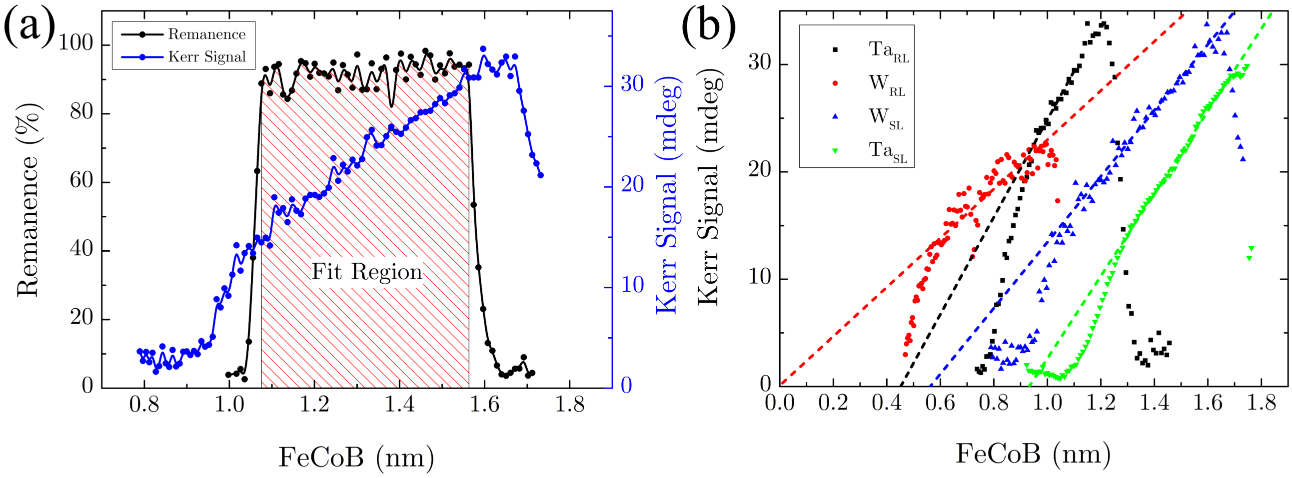

Figure 3.4: a) MOKE measurement of an FeCoB layer with 2nm of W as B-getter, showing in black the signal remanence and in blue the Kerr signal amplitude. The hashed red region is the fitting range for the magnetic dead layer extraction. b) Kerr signal measurement for 4 different stacks, with W and Ta as B-getters for either storage or reference layer wedges. The linear fitting of the signal crossing at 0 mdeg represents the dead layer.

Table 3.1: Measured maximum coercivity thicknesses and high remanence region for PMA with extracted dead layer thickness using either Ta or W as B-getters for the storage and reference FeCoB layers.

| | Layer | $H_C^{max}$ (nm) | $PMA$ (nm) | $t_{dead}$ (Å) |
|---|---|---|---|---|
| W | Storage | 1.2 | 1.0-1.6 | 5.6 |
| | Reference | 0.7 | 0.5-1.0 | 0.0 |
| Ta | Storage | 1.4 | 1.3-1.6 | 9.3 |
| | Reference | 1.0 | 0.8-1.2 | 4.5 |

with another pair of stacks having W 2nm at the FeCoB/Ta interface.

For the tungsten stacks, we get a wider range of available thicknesses for PMA, with a smaller magnetic dead layer for the storage layer and near zero for the reference layer. The coercivity peak is also shifted to smaller values for W by 0.2 or 0.3 nm. Thus, with these results, it is easy to conclude that tungsten is an optimal replacement for Ta, showing less diffusion than Tantalum and degrades the quality of the MTJ by diffusing to the MgO barrier, forming an interfacial Tantalum oxide [131]. The magnetic dead layer for the W and Ta storage layers could be attributed to sputtering of the FeCoB layer during their deposition. As heavy metals, tungsten and titanium have high momentum and can penetrate softer materials, creating defects at its surface. In the following chapter, we will discuss the impact Tungsten has on the electrical properties of devices.

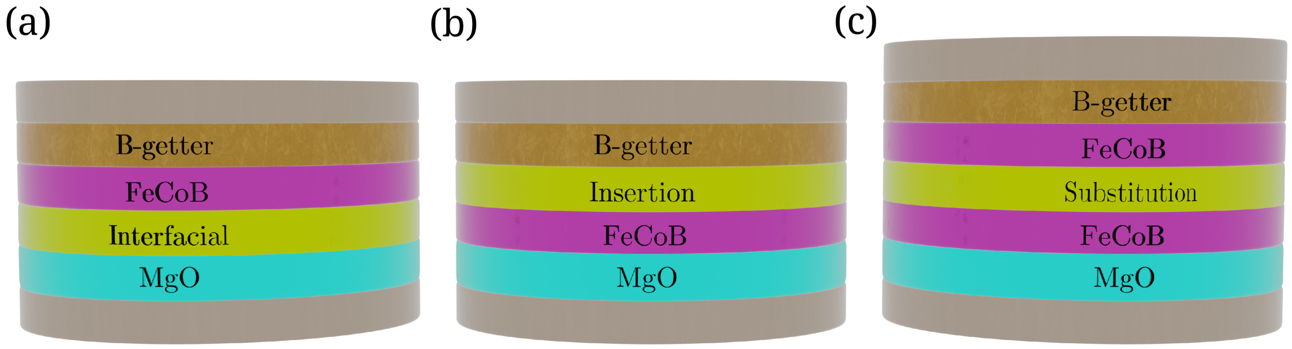

Figure 3.5: Structural modification to storage layer with an add-on layer (in yellow) at different positions in the stack. a) Interfacial layer, b) Insertion layer and c) Substitution layer.

# 3 STT-MRAM

## 3.1 Conventional stack design

A conventional MRAM bit refers to stack sequences that have been studied more widely and do not contain storage layer modification such as doping materials, substitute alloys for storage layers, or other layer insertions that increase the complexity of the design. For instance, Fig.3.1a is the simplest design of a functional STT-pMTJ and in the context of this work a conventional stack is any one that uses the storage layer MgO/FeCoB. It is not necessary to pattern our samples in order to analyze their magnetic characteristics, so the SAF and electrodes are not included in half-stack MTJs. In devices written with the STT mechanism, an important requirement is a low resistance-area product, optimally below $10\Omega.\mu m^2$, as it plays a role in modulating the critical switching voltage, which is minimized in optimized processes to avoid breakdown of the tunnel barrier. Although the limitations of fabricating ultrathin MgO layers makes it difficult, because the density of defects such as pinholes in the MgO will increase and reduce the magnitude of the TMR. RAs as low as $1\Omega.\mu m^2$ have been previously reported with significant TMR levels by optimization of the annealing step [132].

## 3.2 Low anisotropy tunnel junctions

In order to create a more efficient MRAM, or one with a lower effective anisotropy as in our case, it is necessary to explore alternative material stacks. We start by changing the storage layer structure from conventional FeCoB to those with an addition of thin magnetic layers at different positions in the stack, which will be referred to as "add-ons". Fig.3.5 shows a schematic representation of the three types of layer used, classified as Interfacial, if in the interface of MgO/FeCoB; Insertion, if located between FeCoB/B-getter; and Substitution, if added inside the FeCoB layer.

For the interfacial layers, the objective is to modify the hybridization of FeO on the MgO/FeCoB interface by either decreasing the density of the oxide or changing it into something with a different composition, such as CoO. In the case of an insertion layer, it can change the properties of the FeCoB by intermixing after annealing, modifying the stoichiometry of FeCo, or adding doping elements such as Ni with permalloy without affecting the interface with MgO. The substitution layer has a similar purpose as the insertion layer, with the difference being the split of FeCoB into two, creating two

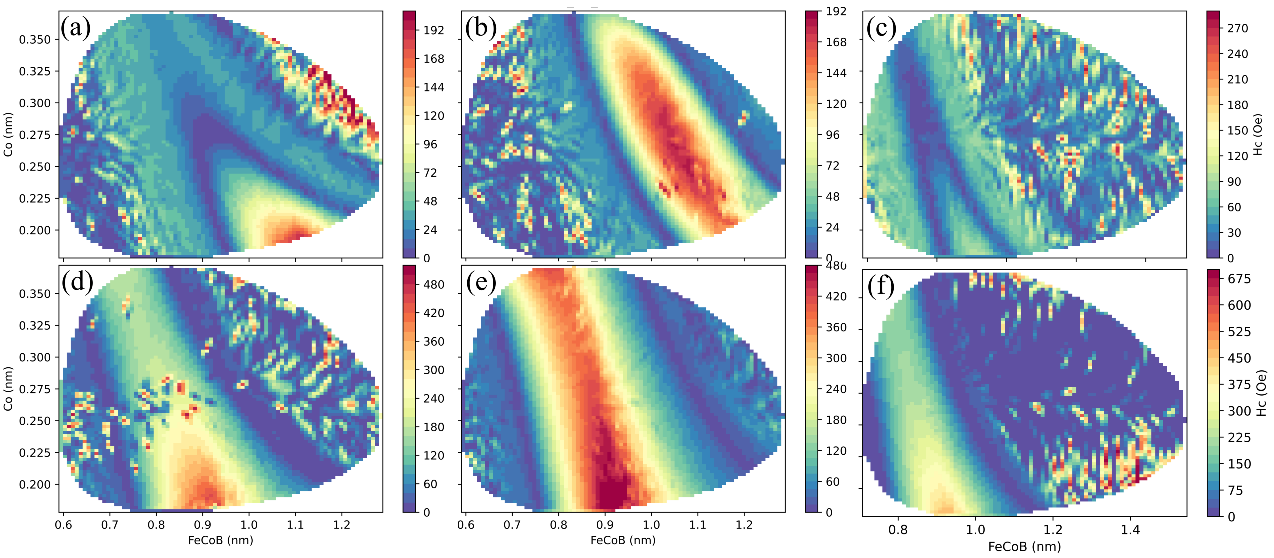

Figure 3.6: MOKE mapping of coercivity for an MgO/FeCoB/Ta structure with Co as an add-on layer on the interface (a) and (d); as an insertion (b) and (e); as a Substitution layer in (c) and (f). Ta is used as a B-getter layer in a, b and c, while W is used in d, e and f.

interfaces with the add-on layer replacing part of the FeCoB and leading to intermixing.

When these additional layers are introduced, they are deposited as a cross-wedge with FeCoB to find the optimal thicknesses for PMA and TMR. The total thickness of the resulting storage layer must take into account the PMA range of Table 3.1 based on the B-getter used. For example, if we use Ta, we know that our wedge combination should be such that it satisfies $1 < t_{FeCoB} + t_{add-on} < 1.6$. In Fig.3.6, we see the remanence MOKE mapping for the three types using either Ta or W. As discussed previously, we can see that using W improves the quality of the MTJ, giving us access to a larger range of thicknesses with PMA. For our purposes, we are searching for stacks with low coercivity, which would indicate that Ta is the appropriate choice, but the higher crystallinity of our layers using W will allow us to fabricate devices with better electrical properties.

Next, we looked at the effects of adding Ni to the storage layer. First, an interfacial stack MgO(1.3) / Ni(0.18-0.35) / FeCoB(0.6-1.3) / Ta(3) is deposited and its remanence map tells us the interface has no effective perpendicular anisotropy, in Fig.3.7a we can only see a small magnetic signal from the Kerr amplitude map. If we use Permalloy instead to limit the density of Ni atoms as an insertion rather than an interfacial layer, we get an unusual result in Fig.3.7b. Unlike pure FeCoB or using Co, the half-stack MgO(1.3) / FeCoB(0.32-0.68) / Py(0.35-0.95) / W(3) has no high remanence state for the storage layer, with a limited 64% for regions with a higher Py or FeCoB thickness. However, this does not mean that there is no PMA. By analyzing their hysteresis loops for $t_{Py} = 0.6$; 0.8 and $0.9nm$ at $t_{FeCoB} = 0.48nm$, we see a transition from fully hard-axis hysteresis to an intermediate state, with a rotation of the Kerr signal at high fields and with a sharp transition at low field. We assume that this state shows perpendicular anisotropy with an additional in-plane component, an indication of the easy-cone state discussed in Chapter 2. Therefore, Permalloy is a promising candidate for our device stack, with zero coercivity at room temperature (low anisotropy) and a transition state for a wide range of thicknesses. The latter point is an important distinction from a pure FeCoB layer, since

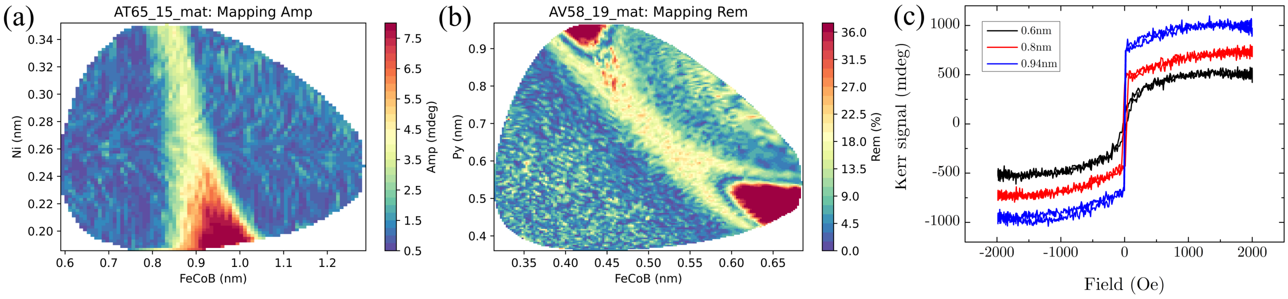

Figure 3.7: a)Kerr amplitude MOKE mapping of a Ni interfacial layer. b)Remanence MOKE mapping of a half-stack MTJ with a permalloy insertion layer: MgO(1.3) / FeCoB(0.32-0.68) / Py(0.35-0.95) / W(3). c) Kerr signal hysteresis of three different Py thicknesses for $t_{FeCoB} = 0.48nm$

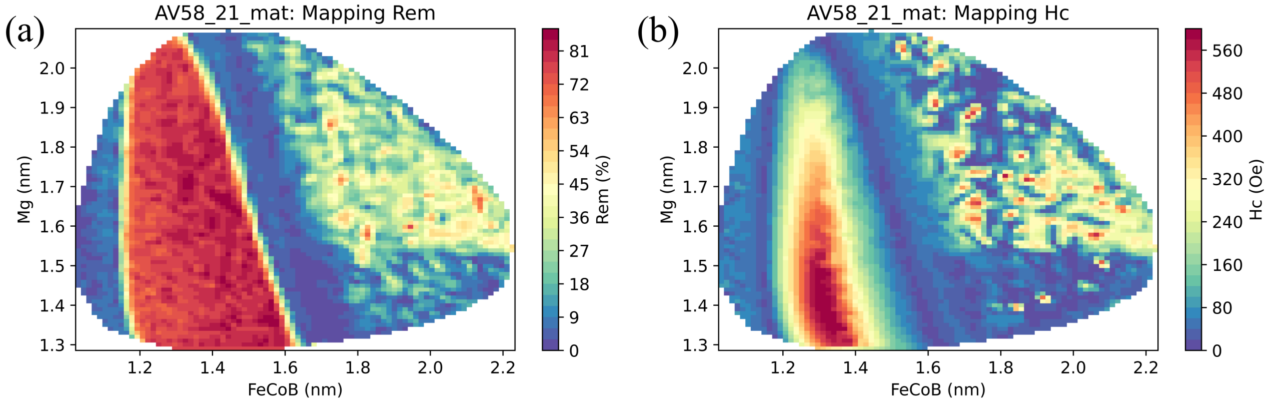

Figure 3.8: MOKE analysis of the half-stack MgO(0.7) / Ox(30s) / Mg(0.6-1.4) / FeCoB(1-2.2) / W(3). a)Remanence mapping and b)Coercivity mapping.

reaching an easy cone configuration is experimentally challenging [99].

Another approach used was to modify the Mg capping layer of our tunnel barrier. By changing its thickness, we can directly affect the density of FeO bonds formed at the interface and consequentially reduce its surface anisotropy. A half-stack with the following structure is shown in Fig.3.8[1]: MgO(0.75) / Ox(30s) / Mg(0.55-1.3) / FeCoB(1-2.2) / W(2). Its remanence remains at maximum for the entire range of Mg used between 1.2 and 1.6 nm of FeCoB. Although we can see a change in the anisotropy of the storage layer as the PMA range is reduced for higher Mg with its coercivity decreasing from 550 down to 100 Oe for $t_{Mg} = 2$, which is what we expected by changing the oxidation state of the interface. A thicker Mg capping could also have the additional benefit of limiting the formatiosn of boron oxides that degrades the tunneling efficiency of electrons [133]. Although at the thin film level it is unclear how this will affect the crystallinity of the barrier and its influence on TMR.

In the following chapter, we look at the fabrication of such structures. Focusing on the ones listed previously, we used either Co, Py, or Mg as add-on layers. And to finalize the MOKE study of the different materials available to reduce anisotropy, Fig.3.9 summarizes the results for a few different possibilities of insertion layers in the storage and reference layers using either Co or permalloy with W

---

[1] Stack structure of a half-stack Mg sample from Fig.3.8: Ta(3)/FeCoB(0.8)/W(2)/Pt(5)/FeCoB(0.4)/MgO(0.75)/Ox(30s)/Mg(0.55-1.3)/FeCoB(1-2.2)/W(2)/Pt(5)

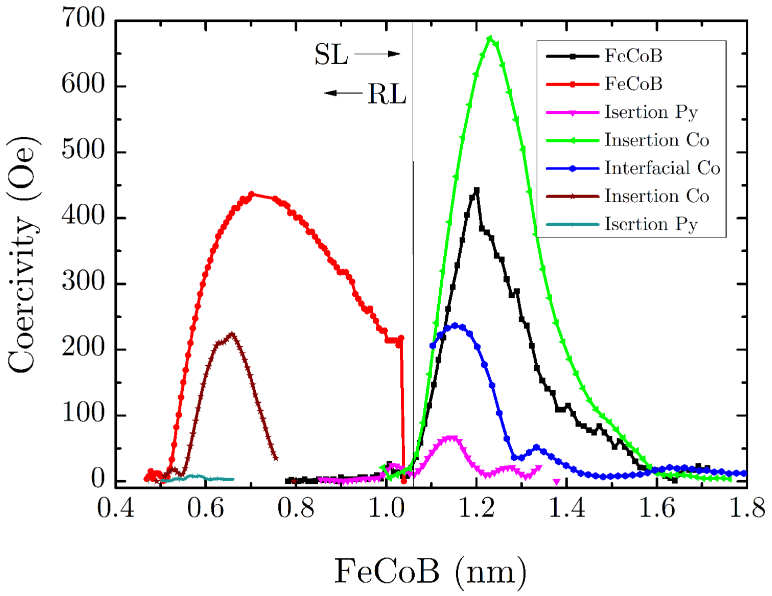

Figure 3.9: Coercivity dependence for different types of add-on layers with FeCoB thickness for the storage layer on the right and for the reference layer on the left.

as a B-getter. The unchanged FeCoB layers in black and red are from a conventional MTJ half-stack, which shows the same maximum coercivity. Because the storage layer has a higher roughness for being deposited on top of amorphous Mg, we can see how it degrades the profile compared to the reference layer. Moreover, the shift of maximum coercivity for the storage layer to higher thicknesses is due to its larger magnetic dead layer.

From the storage layer perspective, a 0.25 nm Co insertion increases the coercivity from 440 to 670 Oe, an enhancement of 52% that is not desirable for our purposes. However, by adding 0.29nm of Co as an interfacial layer, the maximum coercivity drops to 236Oe for a reduction of 46%. This difference is due to the higher CoO hybridization at the MgO interface, which leads to a lower anisotropy than FeO. The insertion layer will have an effect on the overall $M_S$ of the storage layer with a limited intermixing of Co into the MgO interface, having a smaller effect on $K_S$. And since $M_{S_{Co}} < M_{S_{Fe}}$, we will get a higher effective anisotropy that will increase coercivity. In the case of a 0.37 nm Permalloy insertion, we get a substantial decrease in coercivity of 85% with a maximum of 66Oe, with an even stronger effect for thicker layers. Unlike a Co insertion, the permalloy has a stronger effect on the anisotropy of the layer, which could come from a more prominent intermixing of Ni into FeCoB or a coupling of the storage layer with this magnetized insertion. If Py is used as an interfacial layer (not shown in Fig.3.9) there is no PMA present in the system, as it limits FeO from forming at the interface, and Ni provides a surface anisotropy much smaller than Fe at the MgO interface.

From the perspective of the reference layer, a 0.2 nm Co insertion reduces coercivity by 50% to 220Oe, differently from the storage layer configuration, which has shown an increase. This may be related to the 2Å of W that is not sufficient to absorb the boron of the reference layer through the Co insertion. For a permalloy insertion with 0.23nm thickness, the PMA is almost reduced to zero with only 10Oe of coercivity. In Tab.3.2, the results are summarized showing the maximum coercivity

Table 3.2: Summary of results of Fig.4.14, with the thicknesses of each "add-on" layer and the thickness $t_x^{max}$ for which they achieve maximum coercivity $H_C^{max}$.

| | Sample **x** | $H_C^{max}$ (Oe) | $t_x^{max}$ (nm) |
|---|---|---|---|
| Reference Layer | FeCoB/W | 430 | 0.72 |
| | FeCoB/W/**Py**(0.23) | 10 | 0.57 |
| | FeCoB/W/**Co**(0.2) | 223 | 0.66 |
| Storage Layer | FeCoB/W | 430 | 1.19 |
| | FeCoB/W/**Py**(0.37) | 66 | 1.14 |
| | FeCoB/W/**Co**(0.25) | 673 | 1.23 |
| | **Co**(0.29)/FeCoB/W | 236 | 1.15 |

$H_C^{max}$ reached and at which thickness $t_x^{max}$ of FeCoB it occurs.

Thus, we can conclude that modifying the structure of the MTJ has different results depending on the type of layer used and its location in the deposition sequence. Cobalt is more easily controllable because its effect on FeCoB is moderate in terms of coercivity changes. The fact that it has 100% remanence in all the trials made with it is evidence that we can expect very similar behavior from conventional stacks, which is an advantage if we want to fabricate devices that do not strongly deviate from the norm. On the other end of the spectrum, Permalloy exhibits a drastic influence on the properties of the storage layer with almost no coercivity for all the attempted structures, but with a bi-stable state at zero magnetic field. The expectation for these stacks is that Py devices will not be functional at room temperature, because its anisotropy is too weak for voltage switching, though it is a promising target for low-temperature operation. Its hysteresis characteristics will have to be studied further at device-level to understand what the storage layer switching mechanism is, either coherent or induced by domain walls.

# 4 VCMA-MRAM

One of the limitations discussed for the implementation of VCMA is the required presence of an in-plane field. This is because the effective field of the system must have a preferred direction; in other words, it needs a break of the azimuthal symmetry of a circular pMTJ. The easiest way to accomplish that is by having an IP field that affects the storage layer. There are different ways to integrate it into the system, such as using an external field source or an integrated field source. The latter is an interesting proposition, as it can act as a permanent magnet on the storage layer without associated energy consumption. An in-plane uncompensated SAF structure can have a sufficiently strong stray field to induce VCMA switching [134, 135]. If changing the stack composition of the device is not possible, elliptical magnetic pillars can be patterned instead. The non-symmetric demagnetization field will favor a directional effective field along the main axis of the ellipse that has an aspect ratio set by process-related techniques [71, 136]. However, optimizing the composition and shape of such a pillar will require extensive experimentation to mitigate the critical dimension variability induced by the clean-room process flow.

Alternatively, a system that avoids this issue is one that has a storage layer that has both PMA

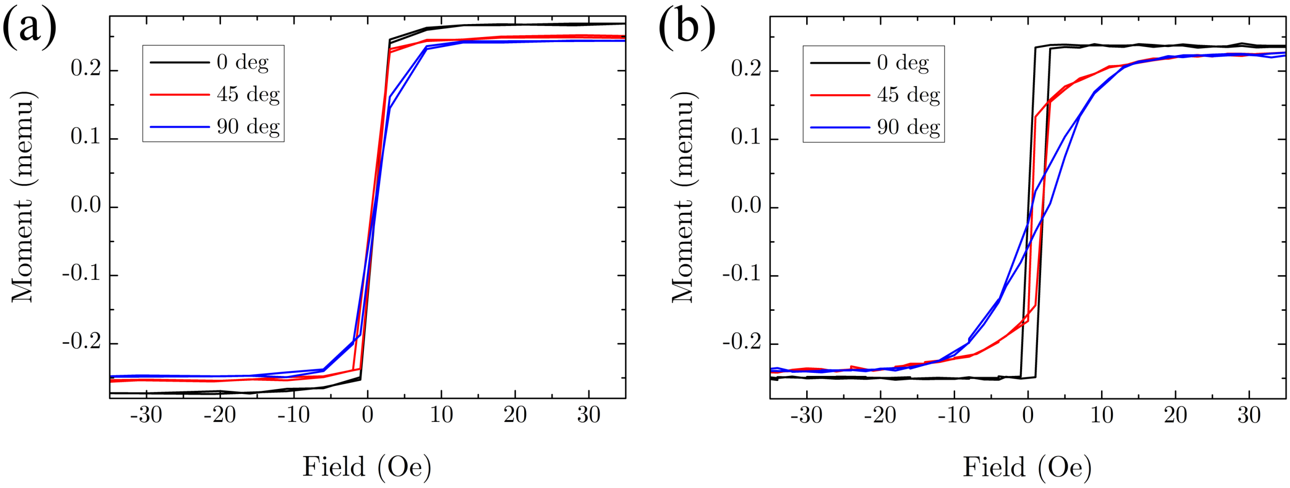

Figure 3.10: In-Plane VSM measurement at $0^o$, $45^o$ and $90^o$ of a standard MgO(1.3) / FeCoB(2.3) / Ta(3) half-stack. a)Annealed at $300^oC$ without any external fields. b)Annealed at $300^oC$ under an in-plane field.

and uniaxial IP anisotropy. With such a layer, there is no need for an external field and it is not sensitive to the shape of the magnetic pillar. To demonstrate this, we subjected an in-plane FeCoB storage layer of 2.3nm to magnetic annealing. As the layers are annealed under high temperatures, the in-plane applied field sets a favored direction of the exchange energy of the FeCo atoms and induces a small magnetocrystalline uniaxial anisotropy in the direction of the field. Fig.3.10 shows in-plane VSM hysteresis loops at angles $0^o$, $45^o$ and $90^o$ for two layers annealed at $300^oC$ for 1h: (a) was not subjected to the field, showing zero coercivity and IP anisotropy for all angles; however, in (b) the layer was annealed under a strong in-plane field at $0^o$, which correspond to the easy-axis loop that shows a small coercivity. As the sample is rotated we see that the loop changes to a hard-axis loop at $90^o$. It is not shown in the given figure, but the hysteresis behavior is symmetric in relation to the $90^o$ angle, with equivalent loop measurements between $0^o$ and $180^o$ and also $45^o$ and $135^o$. This tells us that the magnetization of the sample indeed has a uniaxial anisotropy.

For this work, we do not fully implement these strategies on fabricated devices to simplify its structure and facilitate its electrical analysis to investigate the proof-of-concept designs for VCMA-MRAM at low temperatures. The DC sputtered MgO of our tunnel barriers has not been properly addressed in literature and some aspects of how this system exhibits voltage-controlled anisotropy needs to be understood before more complex stacks are used for integration with other technologies.

## 4.1 High RA stack design

In any MTJ device that uses similar structures as the ones shown until this point, the storage layer magnetization will be subject to both STT and VCMA effects regardless of the main switching mechanism used to write it. Any tunnel barrier, being an insulator, will have dielectric properties that give rise to the VCMA effect. And at the same time, current will flow through it to allow reading of the memory bit. Therefore, in VCMA-oriented devices, this current must be reduced as much as possible to suppress or reduce the STT contribution of the system. The main goal is to minimize the energy

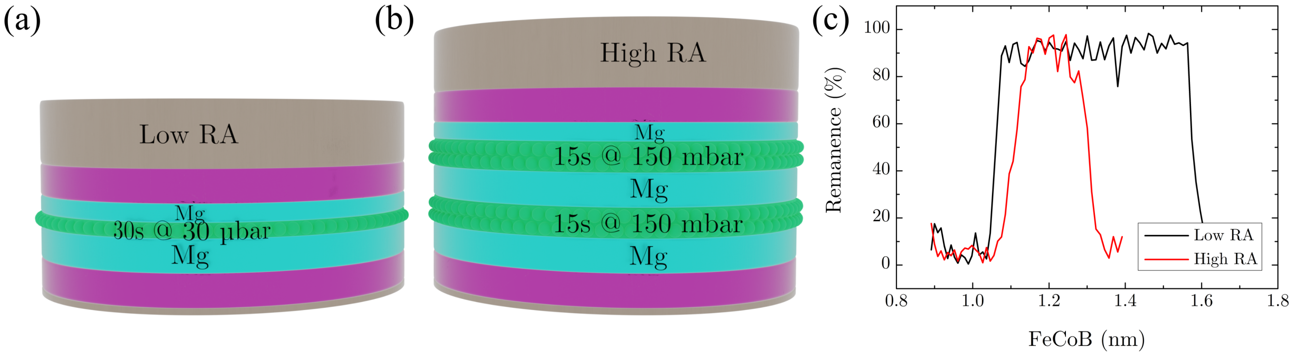

Figure 3.11: a)Low RA stack design with 30s oxidation time under $30\mu bar\ O_2$ partial pressure. b)High RA stack design with 10-15s oxidation time under $150 mbar\ O_2$ partial pressure. c)Remanence dependence with thickness of a half-stack FeCoB storage layer for the low and high RA barriers using a W B-getter. Samples are both annealed at 300°C after deposition.

consumption during writing. Because our MgO is the result of natural oxidation of metallic Mg, it is possible to increase its resistance by modifying the exposure parameters of the layer to a partial pressure of $0_2$. Figs.3.11 (a) and (b) show the schematics for a low and high RA MTJ, respectively. To achieve higher RA, barrier oxidation is done in two steps, with 10-15s of exposure to oxygen at 150 mbar, which is $10^4$ times higher than the low RA pressure of $30\mu bar$. Both are capped with an ultrathin Mg layer of 5Å. Depending on the oxidation time, the RA can go from $10\Omega.\mu m^2$ with low pressure and 30 s oxidation, to close to $1000\Omega.\mu m^2$ with 10 or 15 s oxydation at 150 mbar pressure. Fig.3.11c, shows the remanence plot for both barriers in a half-stack Ta(3) / W(2) / FeCoB(0.4) / MgO / FeCoB(0.8-1.7) / W(3). A decrease in the stable PMA range is observed for the high-RA stack. This may be due to the increased roughness of the Mg layer, as the capping is deposited on a layer stack having an accumulation of defects from the two oxidation steps that are not completely rectified after annealing.

Although the range of available thicknesses for PMA is reduced, the devices fabricated with this type of barrier still show high enough stability for room-temperature measurements.

## 4.2 Stack designs for VCMA coefficient extraction

When designing stacks that use VCMA writing, we must analyze the magnitude of its effect from its coefficient of magnitude $\xi$. There are a few possible ways to do that, but all of them require device patterning that can be done in either half- or full stacks. For the first one, we used a device in an orthogonal magnetization configuration. This means that the equilibrium state of the reference is rotated $90^0$ in relation to the storage layer, with them in an in-plane and out-of-plane state, respectively. Fig.3.12a shows a schematic, highlighting the magnetization vectors and the required IP magnetic field. Then, for full stacks in a conventional perpendicular configuration, the devices are normally fabricated with an out-of-plane reference and storage layer.

The methods of extraction discussed in this section are magnetic characterization techniques, precluding the necessity of executing VCMA switching, which can be experimentally difficult to achieve for novel designs, as the necessary conditions to write them with VCMA are initially unknown.

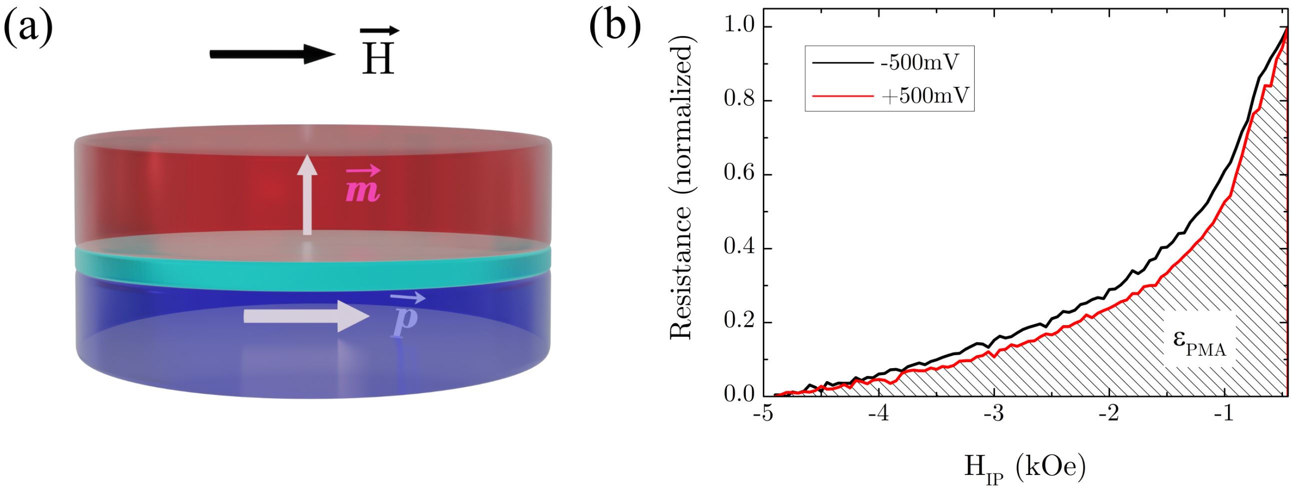

Figure 3.12: a) Schematic of an orthogonal MTJ with an applied in-plane field. b) Normalized resistance measurement for -500mV and +500mV, with the hashed region being used to calculate the PMA energy density for +500mV.

### 4.2.1 Orthogonal configuration

Using a structure similar to an in-plane MTJ's, the conventional SAF structure is replaced by an IP SAF: Cu (3) / MinIr (8) / Co (4) / Ru (0.9) / Co (0.6). And it uses an IP reference layer Ta(0.3)/FeCoB(2) that can be unpinned or pinned in the presence of the SAF. Then, by having the storage layer be a conventional FeCoB with 1.5nm, it forms an orthogonal MTJ configuration that allows us to use a method to extract the VCMA coefficient by measuring the TMR signal, seen in Fig.3.12a.

The TMR method used in the literature [137][138] is done by measuring the resistance state of an orthogonal device while an in-plane field is applied. By analyzing its profile and dependence with an applied voltage bias, it is possible to extract the normalized in-plane magnetization component $M_{norm}$ by using Eq.3.2 [139].

$$M_{norm} = \frac{G(H) - G_{90^o}}{G(0^o) - G_{90^o}} \tag{3.2}$$

Where $G(H)$, $G_{90^o}$ and $G_{0^o}$ are the field-dependent conductance measurement and the conductance at zero field and in parallel configurations, respectively. Fig.3.12b shows the resistance of a device from the following stack: Seed / W (2) / FeCoB (0.6-1.3) / MgO / FeCoB (5) / Ta (3) / Hardmask with tunnel barrier Mg (0.4-1.2) / Ox (10 s) / Mg (0.4-1.2) / Ox (10 s) / Mg (0.5) using 150 mbar of pressure $O_2$. By calculating the area under the normalized resistance curves, we can extract the PMA energy density for each applied voltage bias using Eq.3.4 [140]. Then, because $\varepsilon_{PMA} \propto K_{eff}$, we can then calculate the VCMA coefficient as follows.

$$\xi = \frac{\partial \varepsilon_{PMA}}{\partial V_b} \tag{3.3}$$

$$\varepsilon_{PMA} = \mu_0 M_S \int_0^1 H dM_{norm} \tag{3.4}$$

This setup has some advantages over conventional pMTJs, such as the absence of a pinning SAF and not having to rely on probabilistic/stochastic measurements, which is the case for perpendicular devices.

### 4.2.2 Perpendicular configuration

A first method to extract the VCMA coefficient in out-of-plane magnetized MTJ uses the relationship between the thermal stability of the MTJ and the effective anisotropy of $\Delta/V_{ol} = K_{eff}(V)/k_BT$. And using the assumption that $K_S = K_S(0) - \xi V_b/t_{MgO}$, we get [141, 138]:

$$\Delta(V) = \Delta_0 + \xi \frac{A}{t_{MgO}} \frac{V}{k_BT} \tag{3.5}$$

Here, $\Delta_0$ is the stability at zero bias and $A$ is the area of the MTJ. Then, by plotting it as a function of voltage bias, its slope will be proportional to $\xi$, requiring the physical parameters of the patterned pillar to accurately estimate it. With the same argumentation, one can also measure $K_{eff}$ and use its dependence on the bias to get $\xi$ from Eq.3.6.

$$\frac{\partial K_{eff}(V)}{\partial V_b} = \frac{\xi}{t_{MgO}} \tag{3.6}$$

In this work, to measure both the stability and effective anisotropy, we use a modified version of the Sharrock thermal activation model [142] by applying it to a system with magnetic field sweeping [143, 144] and fitting it to the switching probability distribution function in Eq.3.7.

$$P_{sw} = 1 - exp\left(-\left|\frac{H_K * f_0}{2R\sqrt{\Delta}}\right|\sqrt{\frac{\pi}{2}}erfc\left(\sqrt{\Delta}\left(1-\frac{H}{H_K}\right)\right)\right) \tag{3.7}$$

Here $f_0 \approx 1GHz$ is the attempt frequency, $R$ is the constant sweep rate, and $erfc$ is the complementary error function. The switching distribution is acquired by measuring field-resistance hysteresis loops over many iterations, as shown in Fig.3.13a for a high RA device with diameter of 75nm and $t_{MgO} = 2.2nm$ at 130K. The parameters are extracted using a 5Hz sweep rate, becoming more precise as the number of loops increases, but faces a drawback in regards to measurement time when going above 100 loops. It also increases the risk of tunnel barrier breakdown failure, especially for extracting $\xi$ that requires high DC voltage biases. In Fig.3.13b, the cumulative switching probability distribution is plotted for APP and PAP with their fitted $P_{sw}$ function.

Afterward, by fitting the data for multiple bias values, we can plot the dependence of the two extracted parameters ($\Delta$ and $H_k$) with voltage to get $\xi$. In Fig.3.15 we use a range of -1 to +0.5V, showing a linear slope for both (a) and (b) that are fitted using Eqs.3.5 and 3.6 and summarized in Table3.3. As we can see, there is a large discrepancy between the two values using $H_k$. We could try to extract the STT contribution for this asymmetry seen in the measurement, but these devices have an RA in the range of 100-500$\Omega\mu m^2$, which is high enough to minimize STT effects and prevent any writing from occurring using current pulses below the breakdown voltage of the junction. Similarly, we cannot attribute the asymmetry to Joule heating, as this effect is independent of polarity, and the dependencies of both $\Delta$ and $H_K$ with voltage bias are linear within the measured range, signifying limited heating in the stack. This can be seen in Fig.3.14a, where two devices with nominal diameters

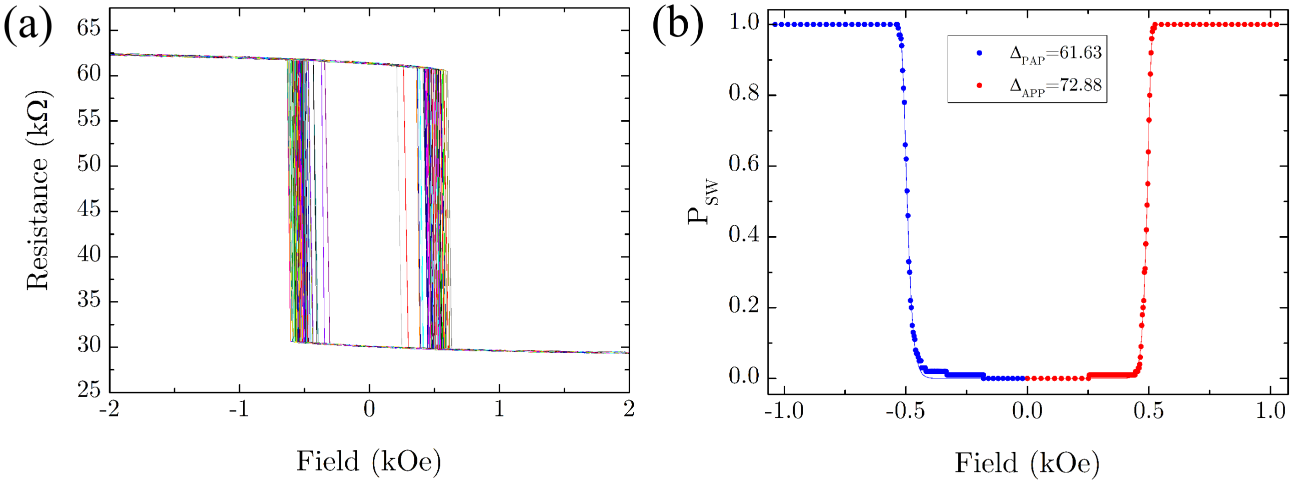

Figure 3.13: a)Field-resistance hysteresis loop for 100 iterations of a high RA device with diameter of 75nm and $t_{MgO} = 2.2nm$ at 130K. b)Probability switching distribution profile for APP and PAP branches with their respective fitting (continuous lines) using Eq.3.7.

Table 3.3: Calculated $\xi$ using $\Delta$ and $H_k$ dependence with voltage bias.

| $\xi_\Delta$ (fJ/Vm) | | $\xi_{H_k}$ (fJ/Vm) | |
|---|---|---|---|
| $\xi_{PAP}$ | $\xi_{APP}$ | $\xi_{PAP}$ | $\xi_{APP}$ |
| 11±2 | 11±2 | 9±2 | 12±1 |

of 100 nm and $t_{MgO} = 1.9nm$ (in black) and $t_{MgO} = 2.45nm$ (in blue) show resistances that differ by an order of magnitude and the same dependence of coercivity with voltage bias.

The same behavior is present for other devices, though as seen in Fig.3.14b there is a change in the dependence of the coercivity with the voltage from device to device of the same wafer or even the same die, which excludes effects from different compositions due to our wedge deposition. Device #1 shows a parabolic dependence that could be attributed to only Joule heating, while #2 has a mixture of heating and VCMA from the saturation that is only seen for positive bias, and #3 exhibits a dependence solely attributed to the linear effect of VCMA. This suggests that the asymmetry of $\xi$ could be caused by processing defects or that our barrier has fundamentally different properties from RF sputtered MgO. Another issue that this method has is the significant dispersion of the data even when accumulating over 100 iterations per voltage point, which may be artificially manifesting the discrepancy between the $\Delta$ and $H_k$ results. As an example, the prober setup used for these measurements has a standard deviation of $\sigma_{50} = 2.4$ using 200 data points and 50 loops per point on a device with a mean $\overline{\Delta} = 33.5$. The difference between the maximum and minimum stability measured for this particular device is of $15k_BT$ within the voltage range used, which is comparable to $3\sigma_{50} = 7.2$. Therefore, this particular method is not reliable for quantitative or qualitative analysis of devices with low $\xi$, as the effect on stability may be too small to be measured without significant uncertainty.

The second method to extract $\xi$ is the one described in [145]. A resistance phase diagram is measured by applying a sweeping out-of-plane magnetic field under different DC bias, giving us the

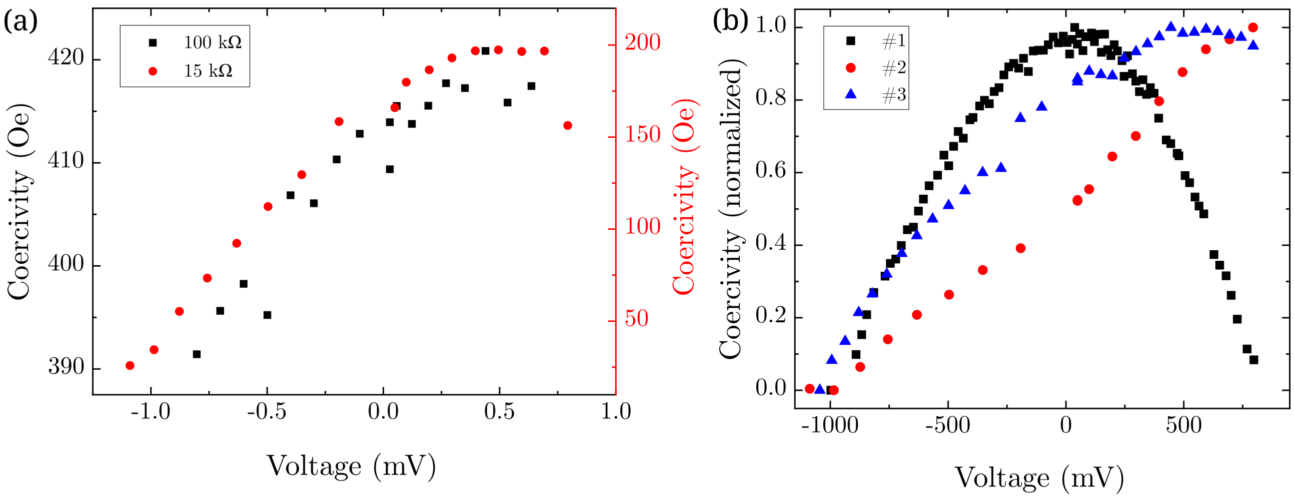

Figure 3.14: Measurement of coercivity dependence with voltage bias of devices in a high RA sample with naturally oxidized MgO tunnel barrier. a)Comparison between two devices with same diameter and different MgO composition, exhibiting the same dependence with $V_b$. b)Normalized coercivity of three random devices with $R_P \approx 15k\Omega$ and diameter of 80nm.

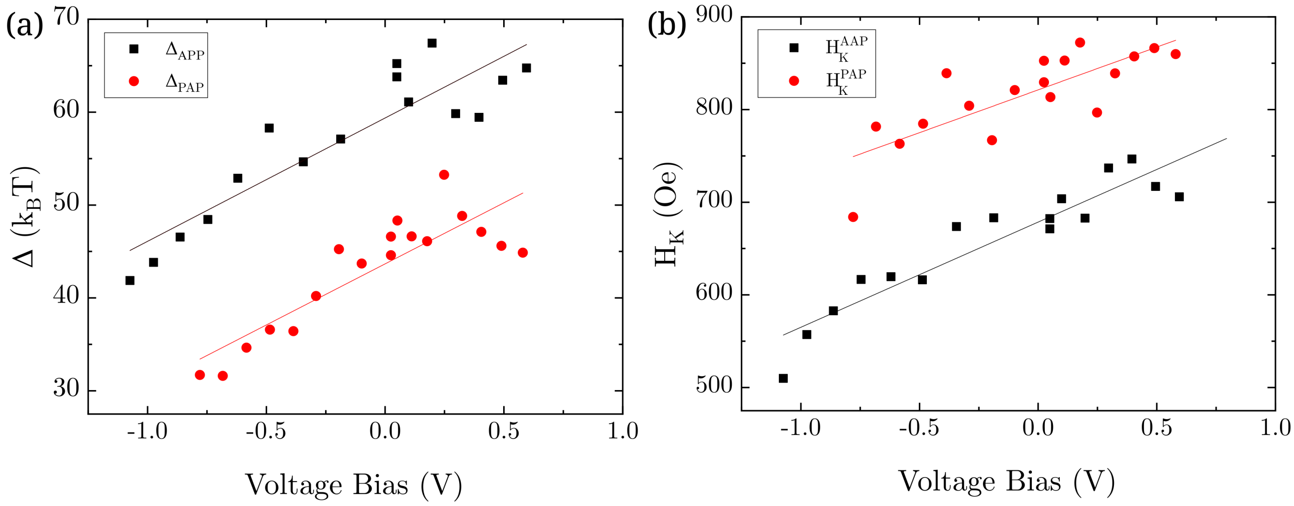

Figure 3.15: Dependence with DC bias voltage for a device with diameter of 75nm and $t_{MgO} = 2.2nm$ and their linear fit measured at 300K for a)Median thermal stability $\Delta$ and b)Anisotropy field $Hk$ for APP and PAP separately.

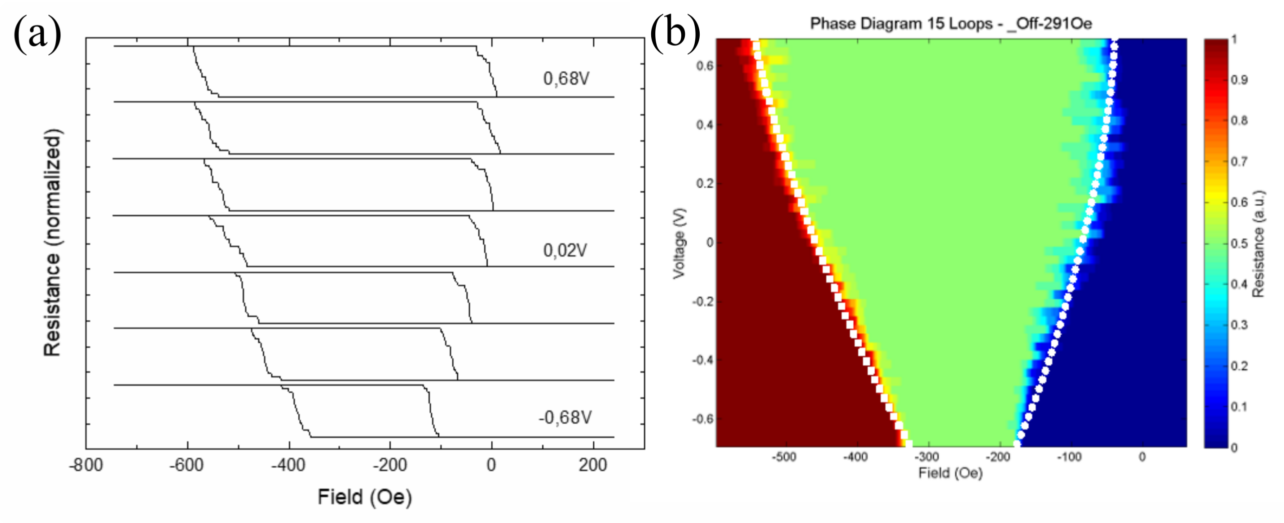

Figure 3.16: a)Normalized field-resistance hysteresis loops for different applied voltages, from -0.68V to +0.68V. b)DC phase diagram at 300K showing the boundaries of the field switching for PAP and APP transitions, with normalized resistance.

switching field dependence on the applied voltage. The range used is limited to 0.8V, lower than the writing breakdown voltage of our devices (1.6V) at pulse widths close to 1ns. Fig.3.16a shows the cumulative distribution field-resistance loops at different applied voltages and Fig.3.16b the full phase diagram, with a trend of increased/decreased coercivity for positive/negative bias. In the absence of parasitic effects and Joule heating, we should retrieve a perfectly triangular shape, as is characteristic of VCMA with limited STT due to low current levels at high RA ($> 100\Omega.\mu m^2$).

Then, by fitting the parallel-to-antiparallel (PAP) and the antiparallel-to-parallel (APP) transitions simultaneously with the switching field equation from Eq.3.8, we can obtain the contributions from STT, VCMA and self-heating [145].

$$H_{sw}^{\pm} = \pm H_C + H_{RL} + \frac{\tau}{\alpha}\frac{V_b}{RA} \pm \epsilon V_b \mp \zeta \frac{V_b^2}{RA_V} \tag{3.8}$$

Here $H_{sw}^{+}$ refers to the PAP and $H_{sw}^{-}$ to the APP branch. $H_C$ is the coercivity, $H_{RL}$ is the stray field from the reference layer, and $RA_V = RA(1 + TMR|_{V_b=0})(1 - 0.5|V_b|)$ is the voltage-dependent resistance of the AP state. The coefficient $\epsilon$ extracted for this particular device is 155 Oe/V, with its STT factor $\tau/(\alpha RA)$ showing a smaller contribution of 41.8 Oe/V and a heating effect of $\zeta/RA_V = 16.8$ Oe/V. To further reduce this term, devices with RA of the order of $1k\Omega.\mu m^2$ are necessary. The most relevant contribution will come from the VCMA term $\epsilon$. It is equivalent to coercivity modulation with voltage $dH_C/dV_b$, which gives us the triangular shape of the diagram.

Using the thermally assisted barrier crossing model to estimate the anisotropy field from the extracted coercivity [146], we can calculate $\xi$ by measuring the thermal stability of each device [147]:

$$\frac{\partial H_K}{\partial V_b} = \epsilon \left( 1 - \frac{1}{2}\sqrt{\frac{\ln(\frac{\tau}{\tau_0})}{\Delta}} \right)^{-1} \tag{3.9}$$

$$\xi = \frac{M_S \; t_{FeCoB} \; t_{MgO}}{2} \frac{\partial H_K}{\partial V_b} \tag{3.10}$$

The stability is extracted from the field switching probability distribution at zero bias, $\tau_0$ is the attempt frequency $\approx 10^{-9}s$ and $\tau = 100ns$ is the measurement time. The main advantages of this method are that it is a more precise technique compared to the previous ones and it returns information on more than just VCMA for potentially thousands of devices. Because a complete MTJ structure is being used, additional electrical characterization is possible to assess other qualities that we would not see if an orthogonal configuration was adopted.

# 5 Conclusions

When a project involves research and development of new MTJ structures that will exhibit properties for specific applications, studying all of its component layers is important to understand their role in the final set of electrical and magnetic characteristics. It also allows us to optimized said layers, such as the Synthetic Antiferromagnet of Sect.1.1, in which we altered the number of Co/Pt repetitions from a 6x3 sequence to 6x2, which gave us the thickness value of 1.0nm for our reference layer that minimized the stray field on the storage layer.

The study of the stack's magnetic behavior is of particular interest in the initial stages of the investigation as it can be assessed to some degree before the device patterning process begins. To do so, we turn to one of the most valuable tools available: the MOKE technique, as it enables the characterization of thin films in a fast and reliable manner.

We were able to extract information on the magnetic dead layer for two different B-getter layers: Tungsten and Tantalum. The first one had a larger PMA region on the annealed wafers, with a dead layer of 5.6Å compared to the 9.3Å using Ta from Tab.3.1. This means that W diffuses less into the storage layer, giving us better crystallinity of the MTJ.

In this work, multiple stack designs were tested for engineering low-anisotropy devices by modifying the composition of its storage layer. It was modified from a conventional FeCoB to a structure with "add-on" layers, using different positions on the stack coined as interfacial, insertion and substitution layers. Fig.4.14 gives us the coercivity dependence of each of the approaches used, with a very drastic reduction of maximum $H_C^{max} =$ for Permalloy insertion layers, both in the reference and storage layers.

To deposit samples for VCMA measurements, we increase the oxidation conditions of the tunnel barrier to increase its resistance and reduce the STT contributions. The usual sputtering sequence is Mg(0.8) / Ox(30s) / Mg(0.5), in which the 30s exposure at $30\mu bar$ of oxygen pressure is used to oxidize the metallic Mg layer. The VCMA barrier, however, is Mg(0.8) / Ox(10s) / Mg(0.8) / Ox(10s) / Mg(0.5), with a partial pressure of $150mbar$ of oxygen. This brings the resistance-area product of the fabricated devices from $5 - 10\Omega\mu m^2$ to $100 - 1000\Omega\mu m^2$.

With the composition of the storage layer chosen and barrier conditions optimized, we can then decide in which MTJ configuration the devices will be patterned in to extract the VCMA coefficient $\xi$. Different approaches can be used to do this, by patterning orthogonal or perpendicular MTJs. In the perpendicular case, the dependence of the thermal stability $\Delta$ and anisotropy field $H_K$ with voltage bias $V_b$ were used to extract $\xi_\Delta = 11 \pm 2$ and $\xi_{H_K} = 9 \pm 2$. A third method, using phase diagrams, has presented more advantages for this type of measurement, as we will see in the following chapter the data analysis of such a method.

# Chapter 4

# Fabrication and Characterization Methods

Goals

In this chapter we will delve into the nanofabrication process for patterning our devices in the clean-room and how we proceed with their magnetic and electrical characterization. Some of the tools are explained in more detail and the results of the measurements are discussed for both STT and VCMA samples.

## Contents

## 1 Clean-room nanofabrication process

All of the aforementioned samples and the ones described in this chapter are fabricated using the facilities of the Plateforme Technologique Amont at the CEA Grenoble site. The process has been established to accommodate a wide range of device sizes and in its totality, has 30 steps. Its main steps are illustrated in Fig.4.1. They are as follows:

(a)The substrate of choice is a 100mm diameter polished $SiO_2$ wafer;

(b)Using a physical vapor deposition technique with a magnetron sputtering tool, we deposit the magnetic stack up to the Pt(5) capping layer as described in Chapter 3, then after annealing at $300^oC$, the full material stack is completed with the hardmask Ru(3)/Ta(150);

(c)A solution of 2% PMMA is spin-coated on the wafer and exposed to an electron beam cannon that defines the patterning mask for the device pillars;

(d)The e-beam mask is developed using an MIBK solution and subsequently exposed to a Cr deposition using an evaporation tool;

(e) A PMMA/Cr lift-off is performed using an acetone bath with ultrasound for 5min to remove the PMMA layer and define the Cr mask, it is cleaned with an IPA bath with ultrasound for 2min and blow-dried with $N_2$;

(f)The hardmask is etched using Reactive Ion Etching (RIE) with a gas mixture of $SF_6$ and $CH_2F_2$;

g)Magnetic stack is etched using Ion-Beam Etching (IBE) at $55^o$ incidence angle, defining the pillars, and subsequently trimmed at $10^o$ incidence angle;

h)Spin-coating of AZ resist at 4000 deg/s with an acceleration of 2000 deg/s$^2$ for 60s and baked at $100^oC$ for 1min30s.

(i)A UV lithography step is performed to define the mask for the Ta bottom electrode using an AZ resist and subsequently developed;

(j)The bottom electrode is etched using the same procedure as the hardmask step. Since the same chemistry of the RIE using $SF_6$ acts on both the Ta and the $SiO_2$ substrate below, this step should be timed to limit its etching to a maximum of 30nm to avoid wetting issues with the resist in the following steps due to the large aspect ratio of the features on the wafer;

k)Lift-off of the resist in acetone bath with ultrasound for 5min and IPA for 2min, then dried with $N_2$ gun;

(l)An insulating polymer called "Accuflo" is spin-coated onto the wafer to encapsulate the pillars and isolate the two electrodes. Differently from the AZ resist, a "promoter" is initially spin-coated before the polymer proper. The settings for both are 4000 deg/s with an acceleration of 200 deg/s$^2$ for 120s. The baking is done in 3 steps: 2min at $120^oC$, 2min at $180^oC$ and 13min at $250^oC$.

(m)A second AZ resist UV lithography is done on the Accuflo, which is etched using RIE. Subsequently, with a profilometer, the height of the total polymer and bottom electrode thicknesses are measured for the following step;

(n)A third UV lithography is done to open a small window in the polymer to provide access to the top contact of the pillar and prevent electrical shorts between the top contact lead and the bottom electrode lead.

(o)An additional RIE etching is done to accomplish this. We implement a careful approach to calculate the correct thickness to be removed, thinning the polymer down to expose only the Ta hardmask;

(p)Repeat of step (k): Lift-off of the resist in acetone bath with ultrasound for 5min and IPA for 2min, dried with $N_2$ gun;

(q)A final lithography step defines the mask for the deposition of the top and bottom metallic contacts using Cr(20)/Al(300) with an Ar pre-etch step to remove oxidation and impurities on the surface of the exposed pillars;

(r)After the resist lift-off, we finish the fabrication process with a wafer containing a total of 27400 devices.

The critical steps that correlate strongly with the device's final electrical properties are the electron beam mask definition of the PMMA layer, the hardmask etching by RIE and magnetic pillar definition by IBE. The first one defines the patterning mold from which the pillars are created, with a minimum diameter of 20nm, which is a typical limit of the Cr lift-off step to create perfectly circular MTJs. The quality of the subsequent Cr deposition can affect the final shape of the pillar, but it is inconsequential if the hardmask etching is not optimized. Our process flow uses the ICP-RIE plasma etcher SI 500 from SENTECH [148], in which a gas mix of $\mathrm{SF_6}$ and $\mathrm{CH_2F_2}$ must be controlled. The isotropic etching of $\mathrm{SF_6}$ [149] is mediated by a passivating $\mathrm{CH_2F_2}$, which coats the newly exposed surface and induces an anisotropic etching of vertical walls. The ratio of the two gases will give us three possible outcomes for the pillar shape, shown in Fig.4.2: in (a) there is an "undercut" of the Ta which constricts the base and makes the pillars susceptible to tilting or breaking, decreasing the sample yield substantially. The rate of etch is larger than that of the passivation. In (b) we have the optimal conditions, with a mostly circular base and perpendicular walls. In (c) we have weaker etching and strong passivation of the sidewalls, resulting in a conical MTJ. Although the latter is not ideal, the final device's electrical properties are not degraded; however, it can induce an offset to its magnetic hysteresis because the SAF structure will not be compensated as a result of the different diameters of the top and bottom Co/Pt blocks.

The initial chromium deposition acts as a mask on the hardmask itself and is the initial limiting factor of the final pillar's shape quality. In Fig.4.3a we see the holes created by the development of the PMMA, which is already not perfectly circular. The cracks formed on the surface could be the result of the heating caused by the electron gun on the polymer. Then in (b) we get the Cr mask on top of the Ta hardmask. The lift-off process used is a bath of acetone under ultrasound for 5 minutes, which is known to be an aggressive method for patterning, though for sizes larger than 30 nm in diameter there is enough precision for the pillar bases to be circular with little defects and durability to withstand the ultrasound cleaning of the resists for the photolithography steps.

Then, when etching the magnetic stack with IBE, the adopted protocol is to angle the plasma gun at $35^o$ incidence with the vertical direction until the bottom Ta(22) electrode is exposed. The angle has been chosen due to the smaller re-deposition rate of the material onto the pillar and a better consistency in achieving perpendicular walls. Subsequently, a short trimming at $80^o$ incidence will reduce the diameter size of the growing pillars, counteracting most of the re-deposition. This step is crucial for certain types of target devices, as it is a direct method to minimize lateral MTJ size if the e-beam mask has precision limitations, making it possible to fabricate devices with macrospin behavior.

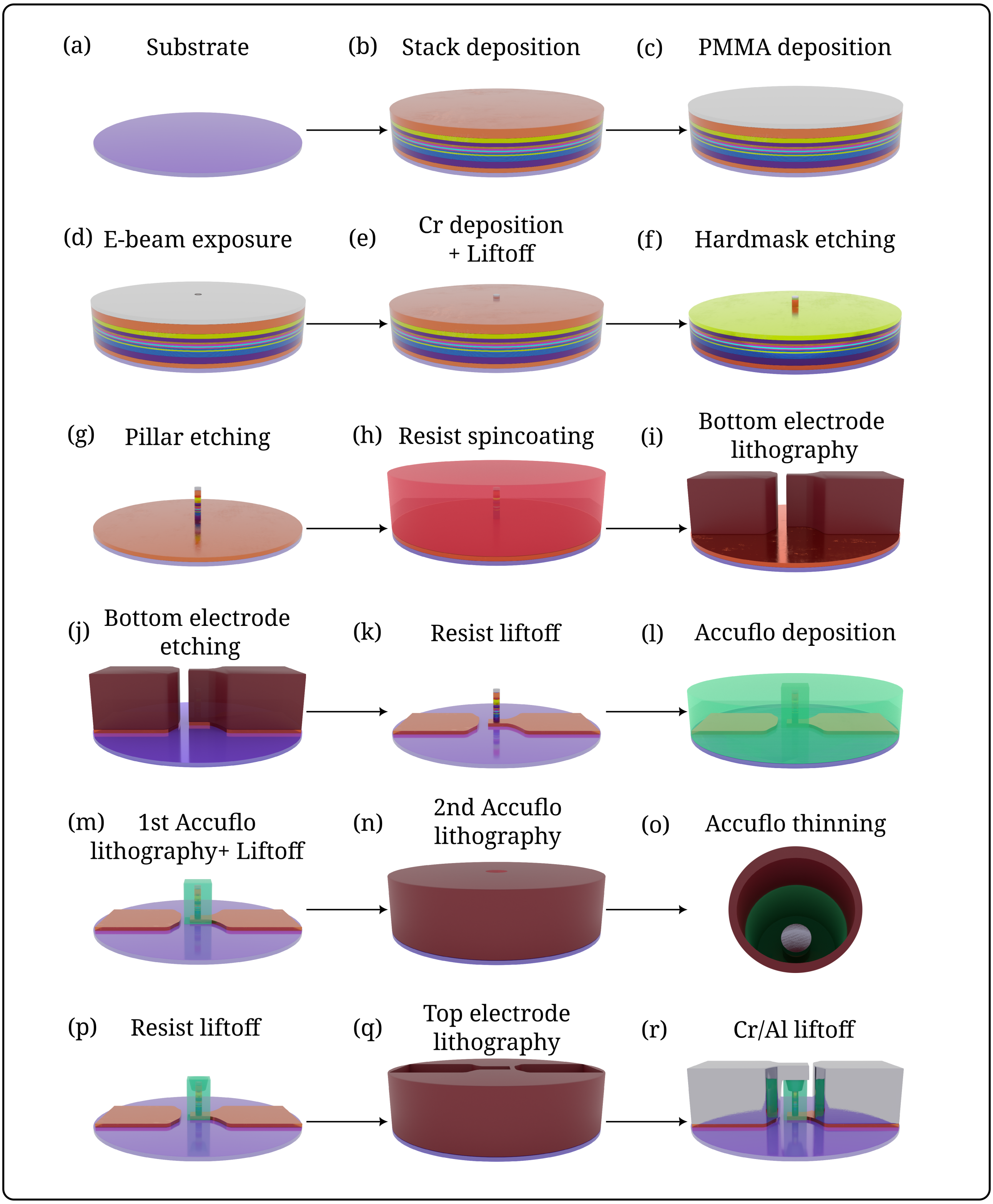

Figure 4.1: Nanofabrication main steps for device patterning: a)Virgin polished silicon wafer; b)Material deposition of MRAM and a hardmask; c)Spin-coating of PMMA layer; d)E-beam exposure for pillar definition; e)Cr deposition and lift-off; f)Ta hardmask RIE etching; g)Magnetic pillar IBE etching; h)Resist spin-coating; i)Bottom electrode lithography; j)Bottom electrode etching; k)Resist liftoff; l)Accuflo deposition; m)Accuflo resist lithography and etching; n)Resist spin-coating and lithography; o)Accuflo thinning; p)Resist liftoff; q)Top electrode lithography; r)Cr/Al deposition and resist lift-off.

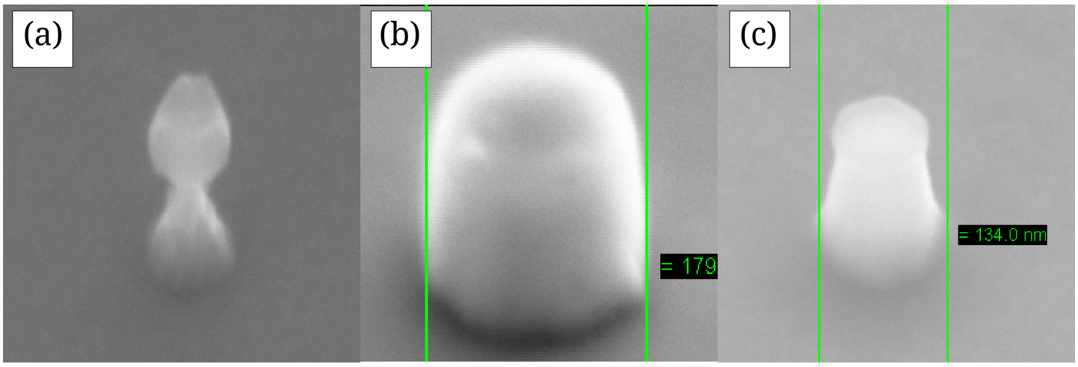

Figure 4.2: Scanning electron microscopy of the reactive-ion-etching of the hardmask in three conditions: a)The "undercut" with stronger etching and little passivation, b)Balanced mix of $SF_6$ and $CH_2F_2$ gases and c)The overgrowth, with stronger passivation and weaker etching.

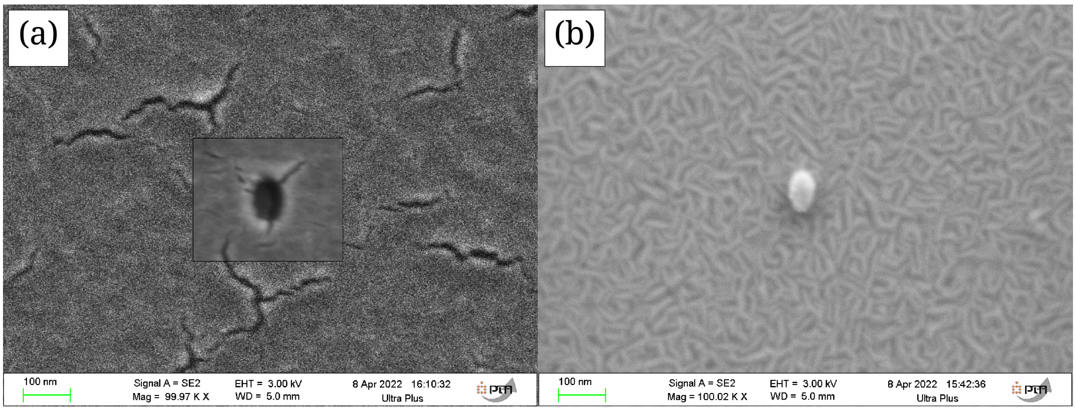

Figure 4.3: Scanning electron microscopy of: a)Development of the PMMA layer after exposure to the e-beam mask and b)The wafer after the lift-off of the Cr deposition, showing the Ta under-layer.

By performing a preliminary trimming step for a variable amount of time (it will depend on the total thickness of the stack and etch power) and verifying in SEM imaging the etch rate, we can reach the final pillar diameter with a second trimming step. With the vertical $35^o$ IBE typically works at an etching rate of 5nm/min, requiring around 4min to reach the bottom Ta electrode, while trimming is higher at 10nm/min. It is important to note that excessive trimming can etch the hardmask into a conical shape, creating contact resistance issues at the final stages. Therefore, to achieve diameters smaller than 20nm, a starting point between 30 nm and 50 nm maximum should be used.

## 2 Characterization Tools

In this work, two main tools are used for electrical characterization. The prober stage and the Physical Properties Measurement System (PPMS). The former allows us to quickly measure 100mm wafers and the latter will allow us to go to very low temperatures and perform temperature dependence studies with it.

Furthermore, an Hprobe station [150] was also used for VCMA switching measurements at room temperature, and two other cryostats are used less extensively, which will be briefly discussed.

### 2.1 Prober Stage

The first step to verify the quality of the sample after fabrication is performing a full wafer characterization using an automated probe station. By measuring magnetoresistance hysteresis loops for each device, we can extract the sample's properties in terms of yield, resistance, TMR, coercivity, remanence, stability, stray-field, etc. This is done by applying a sweeping perpendicular magnetic field controlled by a wave generator capable of creating fields up to 3kOe using a Kepco DC power supply. A two-point contact microprobe closes the circuit of the measuring apparatus with the top and bottom electrodes of the devices. Then a low bias of 20 mV is applied to acquire the voltage drop related to the switch of the tunnel junction with the field using a digital multimeter.

Depending on the acquisition precision with the number of loops and, most importantly, the yield, the process of mapping the entire wafer can take from a couple of hours to upwards of 40h. Therefore, we use the yield value as a first quality factor, which will give us a measure of statistical data from our sample, as seen in Fig.4.4a for a yield of 93%. It is calculated by sorting out all shorted and open devices that have threshold resistance values set at appropriate values. Any device with a maximum resistance below $1k\Omega$ is usually defined as a Short due to the bottom and top electrodes series resistance in the circuit. And any device with a minimum resistance above $1M\Omega$ is considered an Open, though this value may change to accommodate the much higher RAs of devices engineered for VCMA switching. They are a result of fabrication variability through the surface of the wafer, with nonuniform pillar definitions during the magnetic stack etching and random defects (i.e. fallen pillars) occurring throughout the multiple lithography steps and exposure to ultrasound for lift-offs and cleaning. With a good fabrication process, we can map the magnetic properties of the sample, such as TMR, shown in Fig.4.4b, and interpret these results based on the wedge deposition made for the stack. Fig.4.4c represents an easier way to assess this type of data, plotting the dependence of TMR with the thickness of the FeCoB storage layer, where we can see a maximum TMR value at $t_{FeCoB} = 1.55nm$, while the reference layer FeCoB thickness shown in the color code has a steep drop-off at very low thicknesses as shown in Fig.4.4e. The shift of the two profiles in relation to each other means that the thickness of the dead layer of the storage layer is higher by at least 4Å, possibly due to the larger roughness from the texture breaking of the SAF by the deposition of the amorphous FeCoB reference layer and the oxidation of the Mg layer.

An extra level of modulation of physical properties is achieved in the wafer by defining different pillar diameters inside the same die. Fig.4.4d is the lithography mask for every die, containing two distinct sections: an upper section of 4 rows designed for 4-point contact transmission RF measurements and a lower section with 5 rows for DC measurements. Additionally, there are 6 columns of 2 devices for RF and 4 devices for DC, representing a different junction diameter previously defined by the PMMA e-beam exposure. With this type of pillar patterning we can obtain data for both small and large devices, giving us information on the influence of magnetic volume for stability, switching dynamics and more. Due to this, throughout this work the diameters of characterized devices may vary considerably, from 15nm to 180nm, depending on the e-beam mask used and the amount of lateral trimming done during nanofabrication. Then, in Fig.4.4e, we have the TMR dependence with thickness for a fixed reference and a fixed storage layer, showing the shift to higher thicknesses for the storage, since its dead layer is higher due to the larger roughness from the break in texture of the Mg oxidation of the stack and amorphous FeCoB depositions, as measured in Tab.3.1.

## 2.2 Physical Properties Measurement System (PPMS)

In this work, the most used tool for the cryogenic characterization of memory bits is the Physical Properties Measurement System (PPMS) [151]. It uses a closed He circuit to cool a small 12-pin sample board, with operating temperature between 2K and 400K and fields between 0T and 16T. The processed wafers need to be diced, however, as the holder board only has space for a single die. Therefore, by fixing it onto the PCB material of the holder with cryo or silver paste, each device is wire-bonded with aluminum to the gold pads of the board. This is a very delicate process for MRAM devices, as they have been shown to be sensitive to electrostatic discharges (ESDs) that may occur at any point of the step and especially when transferring them into the PPMS chamber. With the sample inside the tool, it is possible to measure the magnetic properties of the device in many different ways by using a rotating holder and applying a current to reach a reading bias of 20 mV to the MTJ, which is calculated by injecting a $1\mu A$ current to read the resistance state at zero field.

When STT devices are the focus, experiments that involve switching can be conducted with some restrictions. Since the applied writing voltage pulses are usually in the range of 1ns to $1\mu s$ for this type of measurement, ideally an RF connection must be used for their larger bandwidth. But the tool does not allow for pulses that are shorter than 100 ns due to the long connection made within it to reach the cooling chamber, even though it uses a twisted cable to reduce noise. Below this threshold, the pulse shape becomes heavily distorted and we cannot claim to know how much energy we are injecting into the device and, consequentially, what its switching voltage is.

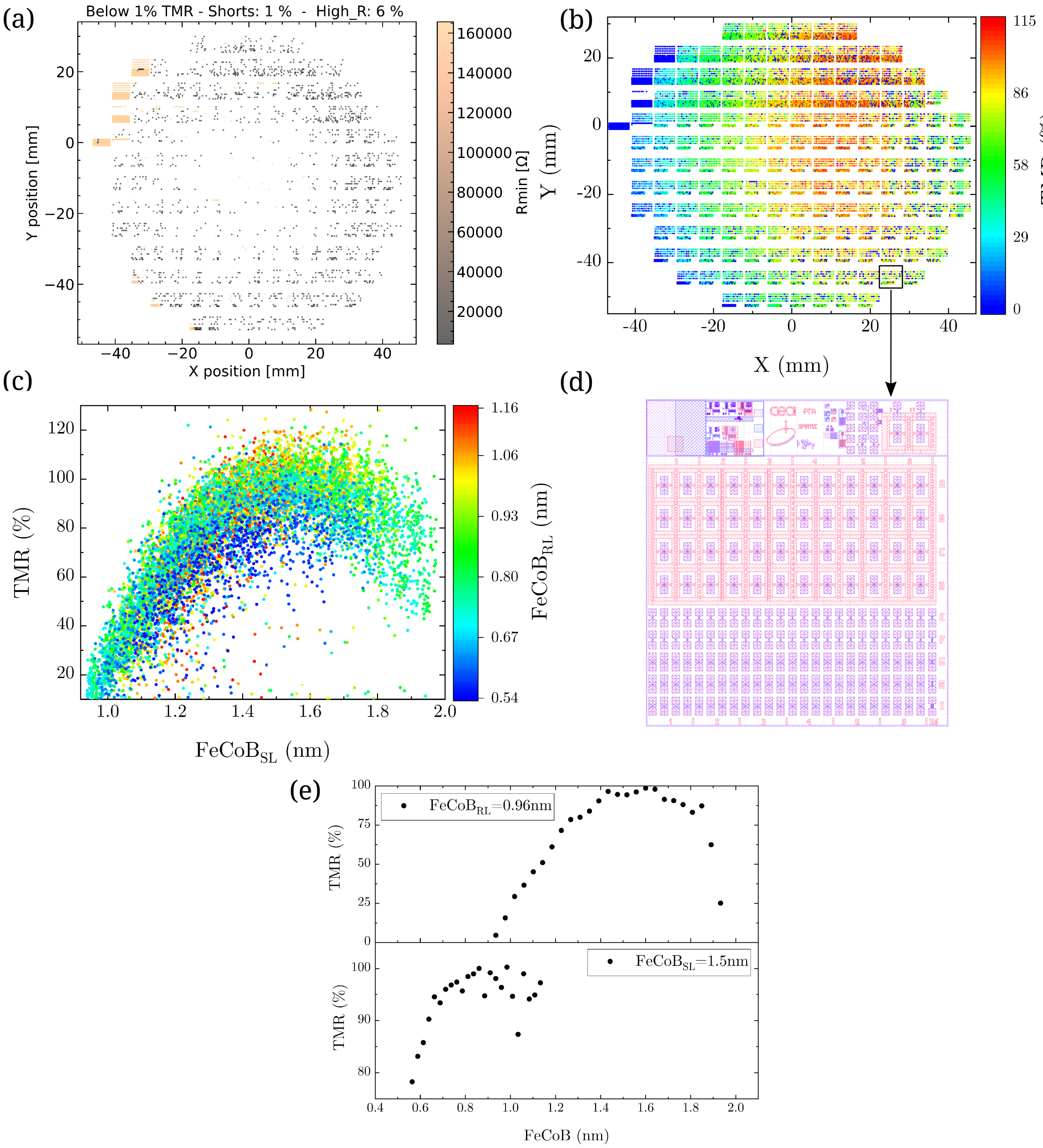

Figure 4.4: Electrical characterization of TMR in a 100mm wafer used for SAF optimization, measured in the prober setup. a) Short and Open device count on the wafer with a total yield of 91%. c) TMR dependence on storage layer FeCoB thickness, with FeCoB reference layer thickness shown as color code. d) Die structure of the lithography mask, with an upper section dedicated to devices for RF measurements and a bottom section for DC measurements. e)TMR dependence with FeCoB thickness with a fixed $t_{RL} = 0.96nm$ (upper) and a fixed $t_{SL} = 1.5nm$ (lower).

## 2.3 Electrostatic discharge protection

Measurement of devices with instruments such as the PPMS requires us to wire-bond its bottom and top electrodes to a circuit line of the sample holder. This technique uses ultrasound to locally melt the ends of a thin aluminum or gold wire that connects the pads of the holder to the electrodes. Unlike the prober, which contacts the electrodes using a grounded closed circuit, wire bonding exposes the tunnel barrier to charges from the environment and parasitic voltages from the instrumentation. Device breakdown often occurs when the connections to the board are made, creating current spikes due to electrostatic discharge. It is important to make sure that any metal line in the room is properly grounded and that users have discharged themselves before manipulating the sample by wearing a grounding bracelet or touching ground lines.

An effective way to avoid this is to insert schottky diodes in parallel into the connection line of the device and the PPMS holder, preventing the MTJ from being exposed to high voltages. In Fig.4.5 we see the characteristics of a single 6pin diode 30V 0.2A SOT363, where we can see that at room temperature it acts as "open" with $500k\Omega$, effectively invisible to our electrical measurements if our device has a resistance at least one order of magnitude lower. The current flowing through the diode and tunnel junction can be calculated from the parallel circuit to correct for the measured tunnel junction resistance. At 0.15V or higher bias, the diode is shorted, bypassing any other components of the line, such as an MTJ. We also have that at lower temperatures the diode properties change to our advantage, with an increased drop-off voltage and zero bias resistance, which allows us to apply higher voltage pulses to the device for switching experiments, since the STT critical switching voltage VC also increases at lower temperatures.

It is worth noting that the "open" state of the diode has a low cutoff at 150mV, but by adding several of them in series we can increase this threshold by 100% for each added diode, though at temperatures above 270K we must calculate the error in our MTJ's resistance measurements due to the zero bias value of the diode. When the diode resistance saturates below 250K, the error becomes negligible for devices exhibiting low resistance levels, which is the case for samples fabricated for STT switching. For junctions targeting VCMA the introduction of diodes can induce a large error in the measurement because their resistance can be comparable, if not higher, than the maximum diode resistance of $900k\Omega$. Though for this case, since their RA is considerably larger than for STT, its tolerance to ESD is similarly higher, not requiring protection mechanisms to have good survivability in experiments that involve wire-bonding the device electrodes to a circuit line.

## 2.4 Alternative characterization tools

An alternative prober stage from Hprobe, called the IBEX-WAT MRAM Parametric Test [152], is also used to perform switching experiments at room temperature with GHz current pulses. With its vectorial field application, with independent X,Y,Z magnets, it is possible to characterize VCMA switching. Full wafers or single pieces can be loaded into its chamber, and an automated system will map out the available dies and use a calibration file for its specific lithography mask. The electrical contact is done similarly to the previous probe, using a 2-point contact probe. The field application is done by three sets of electromagnets sitting atop the probe, with amplitude limitation on X, Y due

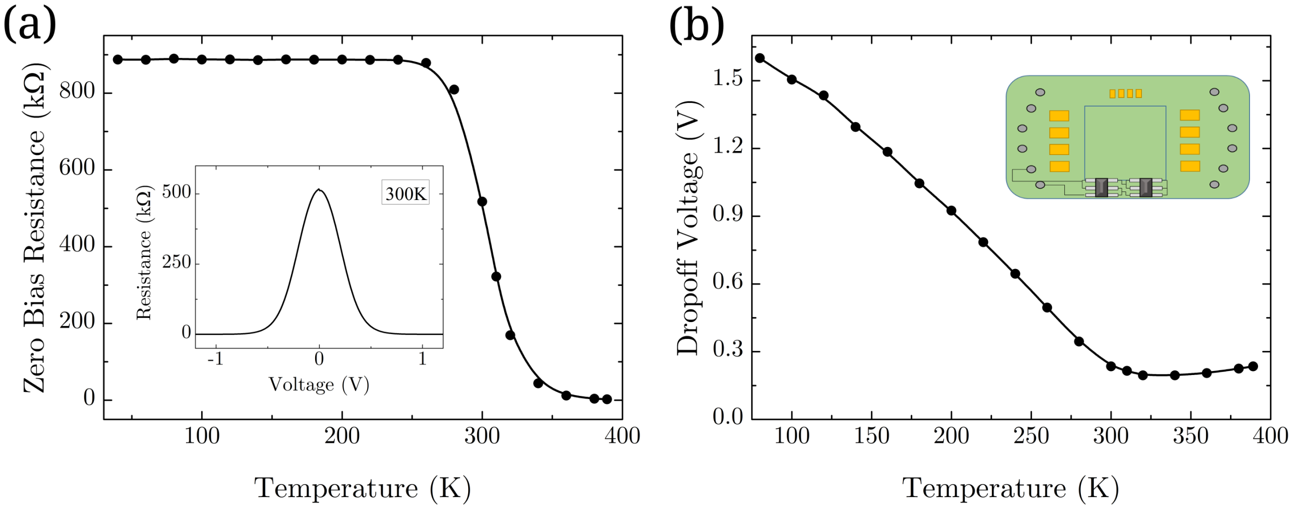

Figure 4.5: a)Diode resistance measurement dependence with temperature down to 40K at 20mV read voltage. The inset image is the diode measured at different applied biases up to 1.1V. b)The voltage drop-off dependence with temperature for a single diode with a schematic representation of its integration to the PPMS holder.

to heating of the coils and calibration. The maximum perpendicular field applied can be 2000 Oe in steps of 50Oe, while for the in-plane directions it goes up to 800 Oe in steps of 200 Oe.

A LakeShore cryostat was also used. The same electrical instrumentation used on the PPMS to send pulses and measure the resistance of the devices is mounted on an EMPX-HF cryogenic probe station [153]. It has an open cooling system that relies on a PID-controlled heating plate to stabilize the temperature at values between the coolant bath (77K or 4K, if nitrogen or helium is used) and 300K. An advantage of this system is that it can measure multiple devices in sequence using a probe tip without wire-bonding, which avoids any junction breakdown before the measurement. This tool has three inner temperature stages, two of them acting as shields with an additional prober arm shield to isolate the system. However, using He as our coolant, the sample stage can reach 4K, while the probe tip sits at a minimum of 15K. This poses a problem, as the act of measuring itself can induce local heating of the device and create artifacts in the results. Also, the stage and sample must have a very good thermal contact to ensure they are at the same temperature. This creates another issue, as we cannot measure at temperatures different from the set point of the coolant. Because the heating plate and cooling system are not capable of stabilizing the system quickly enough, there is a delay in establishing a temperature equilibrium between the surface of the cooled chamber and the sample.

## 3 Electrical characterization of STT devices

In the context of low-energy devices, our memories are engineered to have very low or even zero coercivity at room temperature. Because of this, our electrical characterization must be conducted almost exclusively using a cryostat such as the PPMS. In the figures of the following sections, the data points for temperatures close to 300K for $V_C$, $H_C$ and TMR may be seemingly missing because the device has very low stability, does not show any switching, or is in an in-plane state at those

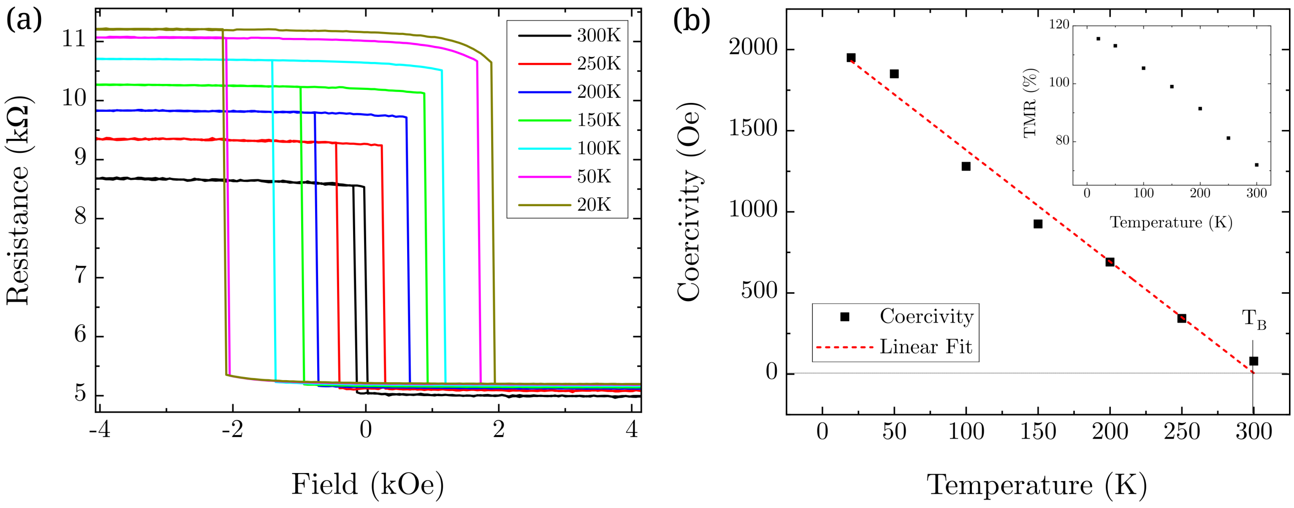

Figure 4.6: a)Hysteresis field loop for multiple temperature points for a device with 50nm in diameter and $t_{FeCoB} = 1.28nm$ and an interfacial Co of $t_{Co} = 0.13nm$. b)Coercivity with temperature with a linear fit to extract the blocking temperature $T_B = 300K$. Inset)TMR dependence with temperature.

temperatures.

### 3.1 Properties dependence with T

The initial characterization for each device is done by collecting field-resistance hysteresis for a large range of temperatures, between 10K and 300K. Since the field sweep rate is slower than the prober station (around 5-15mHz instead of 5Hz), only one loop is measured without any averaging. At these speeds, sweeping the field between -2000 and +2000 Oe, each loop takes on average 1-2 minutes to measure. To obtain information of coercive field distributions as the prober measurement, each resistance loop would take 100-200 minutes. Therefore, statistical information on this type of data is limited so that the total time taken for each data point is manageable within our time constraints.

In Fig.4.6a[1] we have an example of a device with an interfacial Co layer with thicknesses $t_{FeCoB} = 1.28nm$ and $t_{Co} = 0.13nm$ with 50nm in nominal diameter, measured at different temperatures showing the increase in coercivity and $R_{AP}$, which increases TMR as $R_P$ is mostly independent of temperature. The lower precision measurement in $H_C$ can be visualized by comparing the loops at 20K and 50K, where the PAP transition for both occurs almost at the same field, while the APP transition is slightly larger at 20K, as expected. The dependence will behave very close to a first-order polynomial, seen in Fig.4.6b. These measurements serve as a starting point for the electrical characterization of the device in the next section, so that we can qualitatively assess the anisotropy of our layers by looking at their blocking temperature $T_B$, defined by the point in which coercivity decreases to zero, taken from the dependence $H_C$ with temperature and fitting it with the expression [154, 155]:

$$H_C(T) = H_K(0)\left(1 - \left(\frac{T}{T_B}\right)^{1/\lambda}\right) \tag{4.1}$$

---

[1] Stack structure of the interfacial Co sample from Fig.4.6: Ta(22) / FeCoB(0.8) / W(2) / Pt(5) / SAF$_{6/3}$ / W(0.2) / FeCoB(0.9) / MgO(0.7) / Ox(30s) / Mg(0.5) / Co(0.1-0.2) / FeCoB(0.9-1.5) / W(2) / Ru(3) / Ta(150)

where $H_K(0)$ is the anisotropy field at absolute zero and $\lambda$ is an exponent such that $\lambda \in [1, 2]$, which for our purposes has been set to $\lambda = 1$. By fitting the dependence of Fig.4.6b, we can extract a blocking temperature of $T_B = 300K$.

An interesting phenomenon that occurs with this device is the gradual change in the squareness of the resistance loops as the temperature decreases. At 300K, we have 100% remanence at zero field, differently from the loops at lower temperatures where there is a slight rotation or angle appearing in transitions between the P and AP states as the field increases in magnitude. This effect is more pronounced at the edges of the switching transitions, seen at $\pm 2kOe$ at 20K. Because of this, a clarification must be made for the definition of the TMR. Normally, it is calculated from $R_{AP}/R_P$, but with a rotation present, these two values vary with applied field. Therefore, the full TMR, or the TMR extracted from field switching, is defined as $R_{AP}(H_{min})/R_P(H_{max})$ where $H_{max}$ and $H_{min}$ are the maximum and minimum fields applied during measurement, respectively.

This is shown in Fig.4.7a[2], a device with a diameter of 90 nm and $t_{FeCoB} = 1.53nm$ and an interfacial Mg layer of $t_{Mg} = 0.88nm$. A distinction must also be made between the TMR measured while switching the devices with field (Field TMR) or current/voltage (Voltage TMR). The Field TMR is measured at a specific applied offset field, seen in Fig.4.7b, while the Voltage TMR is extracted by switching the device with STT at a constant applied offset field, shown in Fig.4.7b. Fig.4.7c compares the two TMR values extracted at different fields at 5K, within the bi-stability region. Notice that the data range for Voltage TMR is smaller than for Field TMR. For applied fields close to $H_C$, it is no longer possible to write the bit with voltage as a single state is strongly favored, P or AP, depending on the orientation of the field. STT is not sufficient to flip the state before reaching barrier breakdown.

The curvature of both TMRs seen in (c) can be explained by the relative change of rotation between the P and AP states, which for this device is more pronounced than the previous one from Fig.4.6a. The slightly lower Voltage TMR in (c), compared to Field TMR, may be due to series resistances in the different instrumentation used to measure the field loops and to perform STT writing that do not share the same circuit line. The difference in TMR signals seen in (d) can be accounted for by the definition of full TMR, which is taken from the saturation of the rotation of $R_{AP}$ seen in (a). The increase in TMR with decreasing temperature in all measured devices, with a saturation value approaching 0K, has been reported to be related to the dependence of the inelastic electron tunneling with temperature [156].

## 3.2 Engineering low anisotropy devices

To achieve a low switching energy, as discussed previously, $T_B$ can be used to compare the magnitude of $K_{eff}$ of each device in an initial stage. With very low $T_B$ one can assume a very low effective anisotropy, therefore the first step is to analyze the dependence of coercivity with temperature, shown in Fig.4.8a. A sample with a thicker Mg capping, known to have a lower $K_{eff}$ from the MOKE studies of the previous chapter, is shown in Fig.4.2. For a device with 50nm in nominal diameter, $t_{FeCoB} = 1.43nm$ and an Mg of total thickness $t_{MgO} = 1.76nm$, we have $T_B = 186K$, fitted with Eq.4.1, which is smaller than the previous devices mentioned that had a blocking around 300K.

---

[2] Stack structure of the interfacial Mg sample from Fig.4.7: Ta(22) / FeCoB(0.8) / W(2) / Pt(7) / SAF$_{7/3}$ / W(0.2) / FeCoB(0.9) / MgO(0.8) / Ox(30s) / Mg(0.75-1.6) / FeCoB(0.95-1.9) / W(2) / Ru(3) / Ta(150)

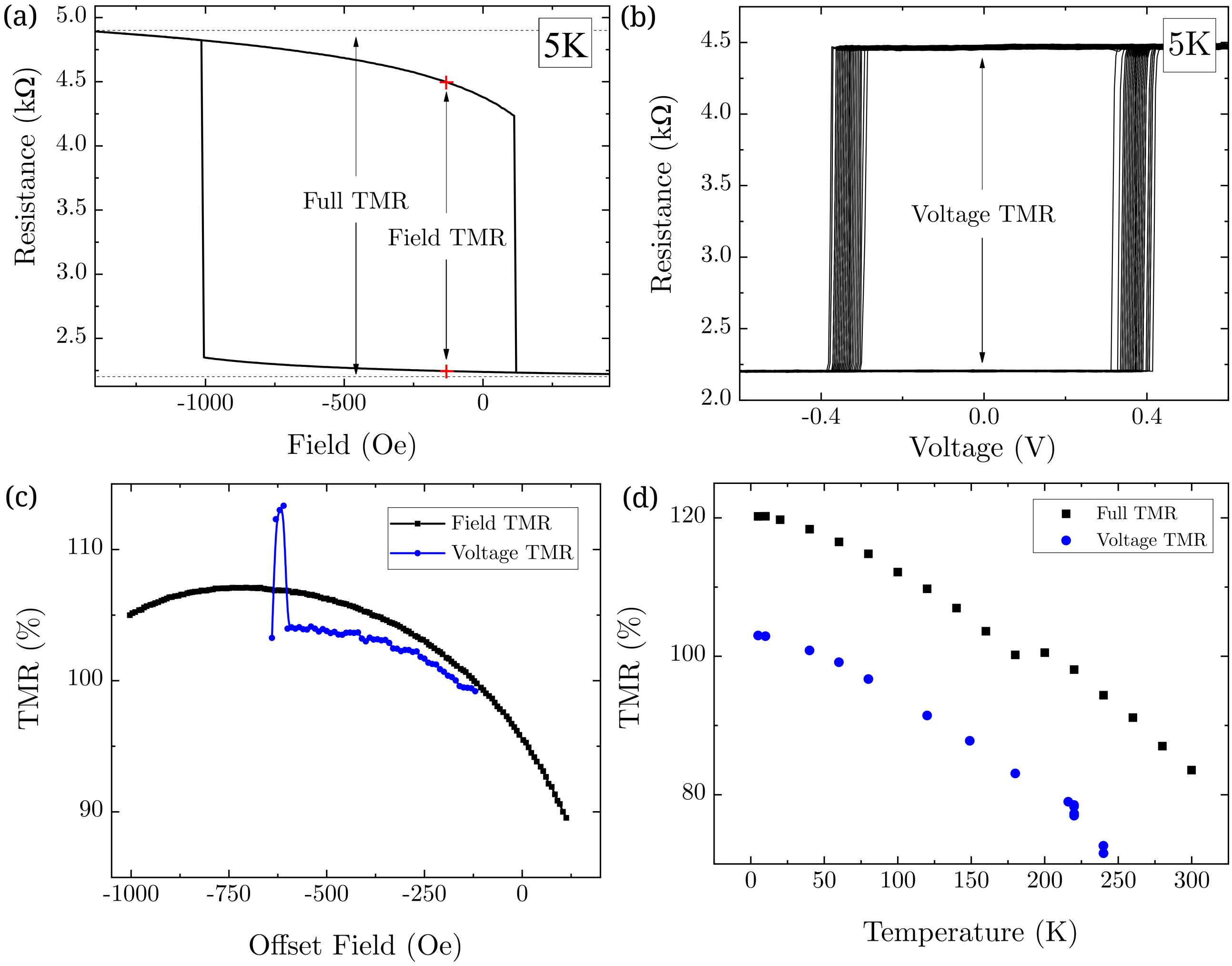

Figure 4.7: TMR dependence measurements for a device with 90nm diameter and $t_{FeCoB} = 1.53nm$ and $t_{Mg} = 0.89nm$. a)Field hysteresis loop showing the definition of a Full TMR measurement and Field TMR at 5K. b)STT switching voltage loops at 5K showing the definition of Voltage TMR. c)Field and Voltage TMR dependence with offset field at 5K. d)Full and Voltage TMR dependence with temperature.

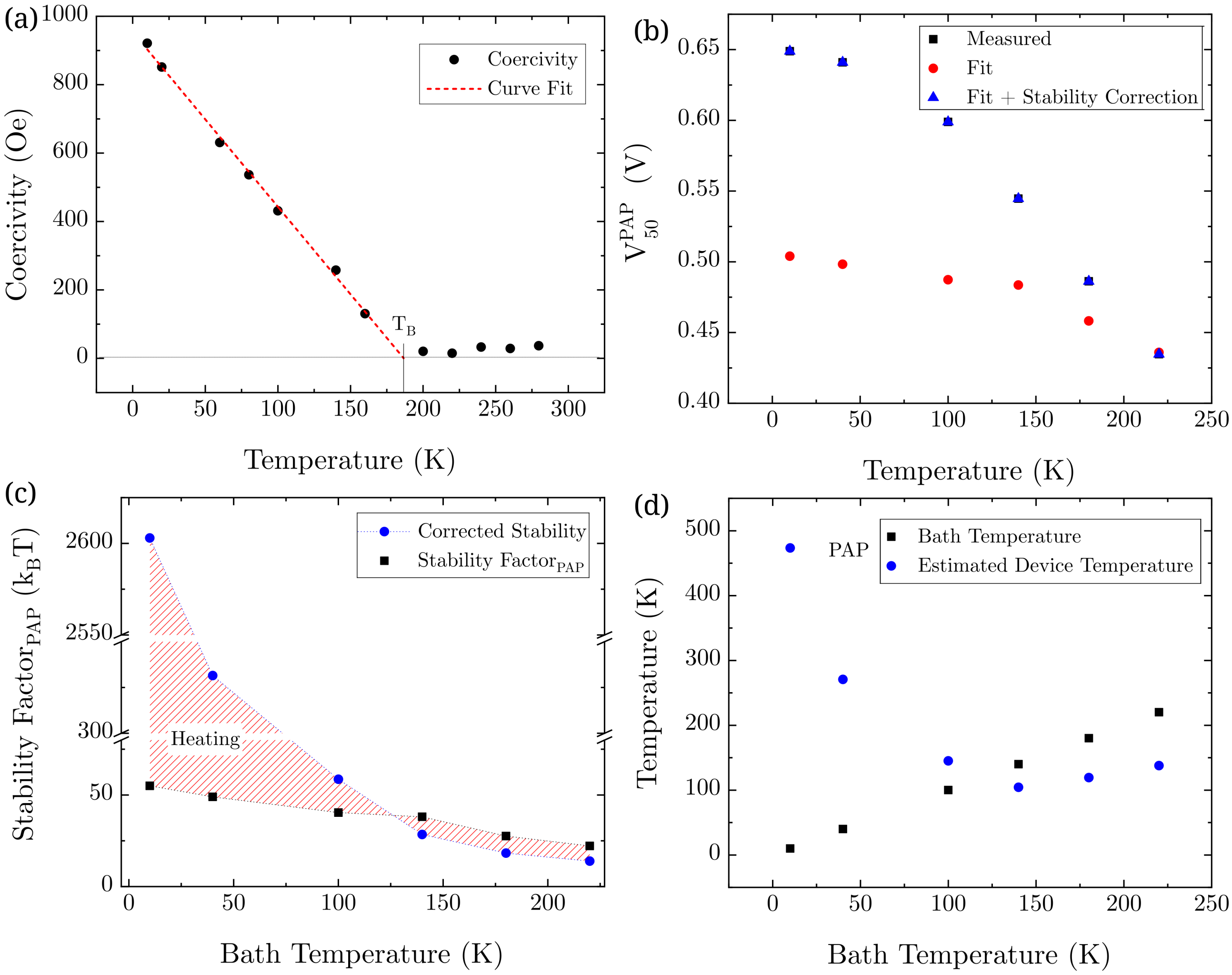

Figure 4.8: Measurement of a device with 50nm in nominal diameter, $t_{FeCoB} = 1.43nm$ and $t_{MgO} = 1.76nm$. a)Coercivity dependence with temperature, with blocking temperature $T_B = 186K$ and $H_K = 954Oe$. b)Switching voltage $V_{50}$ dependence with temperature for PAP transition from 10K to 220K showing the fit using Eq.4.2 in red and the same fit with a $\Delta$ correction in blue. c)Stability factor dependence with temperature for extracted value in black and the corrected value in blue. d)Estimated device temperature extracted from the corrected stability at a given bath temperature.

Just below the blocking temperature, the device exhibits a bi-stable state at its compensation field, becoming writable through STT by applying 100ns pulses with sweeping voltage from -0.8V to +0.8V. The quantity $V_{50}^{PAP}$ is plotted in Fig.4.8b, which correspond to the threshold of 50% switching for either the PAP transition. We have then at 220K that $V_{50}^{APP} = 0.34V$ and $V_{50}^{PAP} = -0.44$, while at the lowest point measured of 10K they are $V_{50}^{APP} = 0.62V$ and $V_{50}^{PAP} = -0.65V$, representing an increase of 82% for APP and 47% for PAP.

The observed dependence with temperature should follow the thermally activated regime of Eq.4.2 [157], where it depends on the thermal stability and the pulse width $\tau$. It will have a saturation value at 0K given by $V_C(0)$.

$$V_C(T) = V_C(0)\left[1 - \frac{1}{\Delta} ln\left(\frac{\tau}{\tau_0}\right)\right] \tag{4.2}$$

If the $V_C$ profile is fitted with this function, there is a large discrepancy between the measured and expected values, as seen in Fig.4.8b. This suggests that stability extraction is not qualitatively accurate, which is unlikely due to existing work supporting its method of extraction [34], or that these devices are undergoing Joule heating during writing, which decreases its stability. By correcting the measured $\Delta_{PAP}$ so that the model is equivalent to the experiment, we can see the discrepancy of the two stabilities in Fig.4.8c. The $\Delta_{PAP}$ varies linearly with temperature due to heating, while the corrected value has a behavior $1/T$, as expected from the definition of $\Delta = E_B V_{ol}/k_B T$. Assuming that the energy barrier $E_B$ is the same, we can then plot the estimated effective device temperature by doing $T_{Dev} = T_{Bath}\Delta_C/\Delta_{PAP}$, where $T_{Bath}$ is the bath/chamber temperature and $\Delta_C$ is the corrected stability. In Fig.4.8d, there is a significant increase in heating that can be seen for values below 100K, with a maximum model predicted temperature of 480K at a bath of 10K. This is an unrealistic estimation of the heating based on the fitting of $\Delta$ from Eq.4.2, which overestimates the stability for very low temperatures, since the model predicts infinite retention at 0K. In this range, a large difference in stability will have only a small effect on the expected value of $V_C$, because device temperature during writing is dominated by the pulse generated temperature increase and not the bath temperature. For temperatures above 100K, estimation of the device temperature based on $\Delta_C$ may also not be accurate since model predicted temperature values are colder than the bath temperature. One possible explanation would be an error associated with the $\Delta_C$ value obtained from fitting, creating the observed difference between model predicted temperature and bath temperature.

Another deviation present in the measurements of the thermally activated model is that $V_C$ does not decrease monotonically with higher temperatures indefinitely. The minimum switching voltage observed is $V_{50}^{APP}(220K) = 0.34V$, just before when the device completely loses its PMA and is no longer write-able at any higher temperature due to the transition into an in-plane state. Because of this, optimization of the switching voltage becomes more difficult to engineer, as the dependence with temperature and $V_C(T_B)$ varies from device to device from its composition to the diameter of the pillar. It is also important to note that, for these devices, their magnetic hysteresis shows the aforementioned rotation of both P and AP states, indicating a nontrivial configuration of the magnetization in the storage layer.

Now, focusing on a sample with a Permalloy insertion layer, we look at three different types

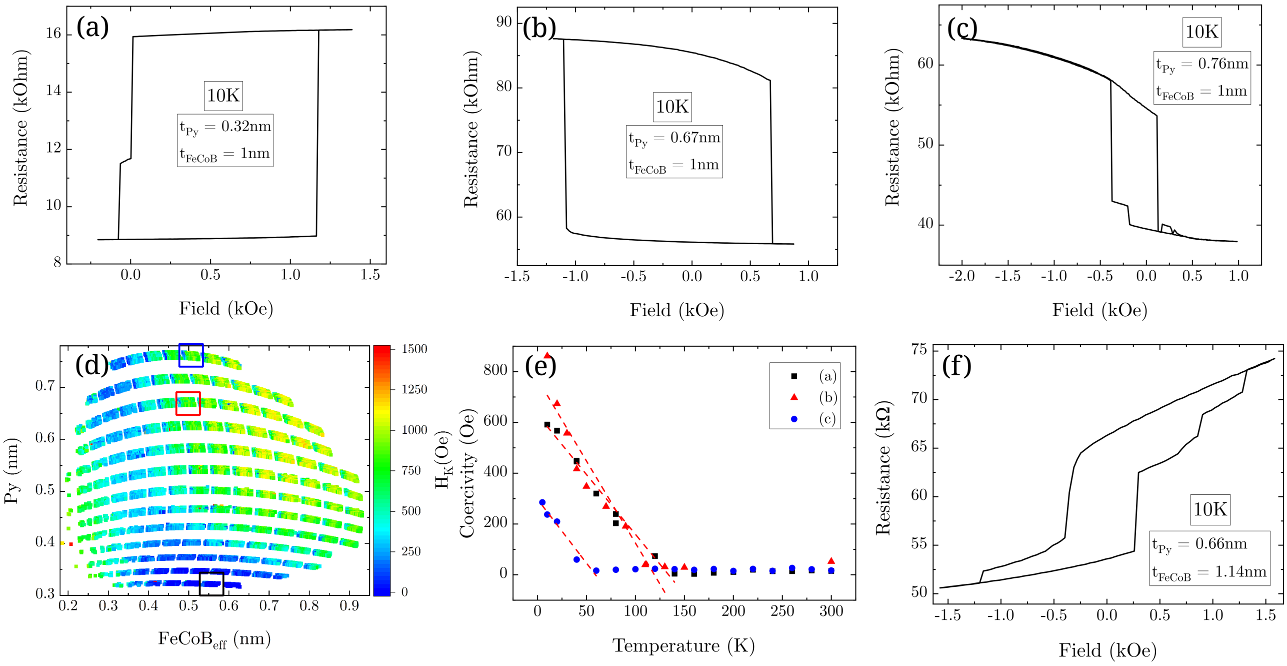

Figure 4.9: Magnetic hysteresis loops at 10K for devices with $t_{FeCoB} = 1nm$ and different permalloy thicknesses: a)$t_{Py} = 0.32nm$, b)$t_{Py} = 0.67nm$ and c)$t_{Py} = 0.76nm$. d)Anisotropy field mapping of the wafer identifying the dies in which the devices are located, color-coded as in e)Coercivity dependence with temperature with blocking temperatures at 59.2K, 119.3K and 134K for (a), (b) and (c), respectively. f)Hysteresis loop of a device with $t_{FeCoB} = 1.14nm$ and $t_{Py} = 0.66nm$ and 50nm in nominal diameter.

of devices in Fig.4.9[3]. All have the same FeCoB thickness of around 1nm and different permalloy thicknesses of $t_{Py} = 0.32nm$, $t_{Py} = 0.67nm$ and $t_{Py} = 0.76nm$. We see that with increasing Py content, the squareness and remanence of the hysteresis loop drastically changes, with a pronounced rotation of the AP state for $t_{Py} = 0.76nm$. The devices are identified in the effective anisotropy map of the wafer in Fig.4.9d to help visualizing how the Py wedge is deposited and their coercivity is measured in (e). For the thicker permalloy, the blocking temperature drops to 70K, while for the thinner layer it was measured to be 140K. This composition of materials a priori seems like a promising candidate for low switching energy, as the total $H_C$ at 10K becomes limited with very low $T_B$. Here, we have for (a) $H_C(10K) = 590Oe$, while for (b) it is $H_C(10K) = 860Oe$ and for (c) it is $H_C(10K) = 285Oe$.

The drawback of using this particular stack is the reduced TMR, as the difference between the Voltage TMR and the Field TMR increases for higher permalloy content. It could still be optimized at the tunnel barrier level with optimal oxidation conditions, which could also improve the electrical qualities of these devices. Another precaution that must be taken is to limit the total thickness $t_{FeCoB} + t_{Py}$, as values larger than 1.8nm start showing a predominant domain switching hysteresis, which must be avoided due to reliability issues as its granular structure is not reproducible and STT efficiency is compromised from non-coherent switching, shown as an example in Fig.4.9f.

---

[3] Stack structure of the insertion Py sample from Fig.4.9: Ta(22) / FeCoB(0.8) / W(2) / Pt(5) / SAF$_{6/3}$ / W(0.2) / FeCoB(1) / MgO(0.8) / Ox(30s) / Mg(0.5) / FeCoB(0.75-1.45) / W(0.2) / Py(0.3-0.8) / W(2) / Ru(5) / Ta(150)

## 3.3 Extraction of surface anisotropy

The next type of sample characterization to be performed is the estimation of the material properties of some of the discussed samples, namely the surface anisotropy $K_S$. This can be done following different methods based on magnetic measurements. In this section we discuss two of them: the first relies on the measurement of the anisotropy field $H_K$ of single devices and the second is on MOKE measurements of thin-film samples.

### 3.3.1 Anisotropy field method

Previous work has shown that by using a different formulation of Eq.2.28 to express the effective anisotropy, $K_S$ can be estimated if $M_S$ is known [158, 159, 160, 161]. Multiplying it by the effective storage layer thickness we get:

$$K_{eff}t_{eff} = (K_V - 2\pi M_S^2)t_{eff} + K_S \tag{4.3}$$

To fit this linear function, we assume a constant value of the saturation magnetization at room temperature $M_S^{FeCoB}(300K) = 1240$ emu/cm$^3$ [158] and calculate the $K_{eff}$ from the anisotropy field with the following expression:

$$K_{eff} = \frac{H_K M_S}{2} \tag{4.4}$$

$H_K$ is measured from the magnetic response of a ferromagnetic layer in its hard-axis direction, defined as the field for which the measured magnetic moment saturates to a maximum value. It can be measured from vibrating sample magnetometry or from resistance hysteresis loops. The latter is used for the Prober measurement of the previous Py sample of Fig.4.9d.

In Fig.4.10[4] (a) the quantity $K_{eff}t_{eff}$ is plotted for the Py sample with the permalloy thickness plotted in color code and in (b) the color code identifies the different nominal diameters for each of the six columns of the wafer die mask, as seen in Fig.4.4d. To extract the surface anisotropy, the data must be filtered by device size and Py thickness, which it can then be fitted with Eq.4.3, shown in Fig.4.10c. The $K_S$ will be the intercept with the y-axis, plotted for three different diameters in Fig.4.10d. As a note, devices close to the out-of-plane region and beyond cannot be taken into account in the fit since their $H_K$ cannot be calculated accurately with the change of its easy-axis.

Within the full Py thickness range of 0.3nm to 0.75nm of the sample, the anisotropy fluctuates around a mean value of 0.36 erg/cm$^2$, meaning that the "add-on" layer does not have a noticeable influence on the interfacial anisotropy, as expected. The layer sequence FeCoB / W / Py limits the permalloy diffusion into the storage layer proper and doesn't modify the hybridization of the MgO interface. Then, the intercept with the x-axis defines a critical thickness $t_C$, the thickness in which the storage layer transitions from an in-plane configuration to out-of-plane. Its dependence with $t_{Py}$ is shown in Fig.4.10e. With it, we can calculate the effective $M_S$ of the layer by also extracting the slope from the linear fit. Its dependence with $t_{Py}$ in Fig.4.10f is as we could expect, increasing as the

---

[4] Stack structure of the insertion Py sample from Fig.4.10: Ta(22) / FeCoB(0.8) / W(2) / Pt(5) / SAF$_{6/3}$ / W(0.2) / FeCoB(1) / MgO(0.8) / Ox(30s) / Mg(0.5) / FeCoB(0.75-1.45) / W(0.2) / Py(0.3-0.8) / W(2) / Ru(5) / Ta(150)

permalloy content increases, due to the decrease in blocking temperatures of Fig.4.9e. The saturation of permalloy, however, is $M_S^{Py}(300K) = 835emu/cm^3$ [162], which is counter-intuitive since we observe an overall increase of $M_S$. To explain this, one can assume that the inclusion of more magnetic material will add magnetic moment that does not contribute with its uniaxial anisotropy to the storage layer, since it has no interface with MgO. Therefore, we see an increase of $M_S$ without change in the $K_S$ of the storage layer.

This characterization method is useful for the Py sample because it has been designed to show no coercivity levels for all compositions, meaning that the operating temperatures for it are below 300K. Thus, analyzing $H_K$ is possible using our standard out-of-plane configuration setup for the Prober stage.

### 3.3.2 MOKE method

An alternative, but similar, method can be done at thin-film level. Before patterning and fabrication, we can analyze the Kerr signal amplitude of MOKE measurements to estimate $t_C$ directly and acquire $K_S$. As previously explored in Sect.2, using the polar MOKE effect with the application of a perpendicular field to the plane of the thin-film, the magnetization of the layer under the polarized light will be proportional to the Kerr rotation [163, 164]. With it, we can directly probe the transition between the in-plane and out-of-plane regions of a ferromagnetic wedge.

We mapped the Kerr signal amplitude for two thin-film interfacial Mg samples: the half-stack structure from Fig.3.8[5], mapped in amplitude in Fig.4.11a and for comparison a full-stack version of the same MTJ, shown in Fig.4.11[6]b. A noticeable difference between the two is the lower Kerr rotation from the full stack, which is around a maximum of 3 mdeg, while for the half-stack it reaches 28 mdeg. This is due to the small penetration depth of the MOKE laser and the higher roughness from the larger stack contribute to a degrading of the measurement signal compared to the half-stack mapping. This roughness of the full stack is originated by the addition of the much thicker Tantalum seed layer and the Co/Pt multilayers that compose the SAF.

Now, similarly to Sect.2.2, we look into the Kerr signal dependence with the storage layer thickness for a fixed Mg composition. Fig.4.11c defines the critical thickness $t_C$ from the sharp increase in the magnetization signal and shows the remanence profile in black. Though the PMA region is considered to be restricted to the plateau of the remanence, the transition to out-of-plane occurs at its edges, as indicated in the figure. Then, with $t_C$ extracted for multiple MgO thicknesses and assuming a fixed value for $M_S^{FeCoB}(300K) = 1240$ emu/cm$^3$, deriving the surface anisotropy is straightforward, while neglecting any contribution from volume anisotropy:

$$K_S = t_C * 2\pi M_S^2 \tag{4.5}$$

In Fig.4.11d we have the $K_S$ dependence with Mg thickness for the full-stack sample, in which there is a striking linear behavior. Fig.4.11 (e) and (f) compare the $t_C$ and $K_S$ dependencies for both samples

---

[5] Stack structure of a half-stack Mg sample from Fig.4.11a: Ta(3) / FeCoB(0.8) / W(2) / Pt(5) / FeCoB(0.4) / MgO(0.75) / Ox(30s) / Mg(0.55-1.3) / FeCoB(1-2.2) / W(2) / Pt(5)

[6] Stack structure of the interfacial Mg sample from Fig.4.11b: Ta(22) / FeCoB(0.8) / W(2) / Pt(7) / SAF$_{7/3}$ / W(0.2) / FeCoB(0.9) / MgO(0.8) / Ox(30s) / Mg(0.75-1.6) / FeCoB(0.95-1.9) / W(2) / Ru(3) / Ta(150)

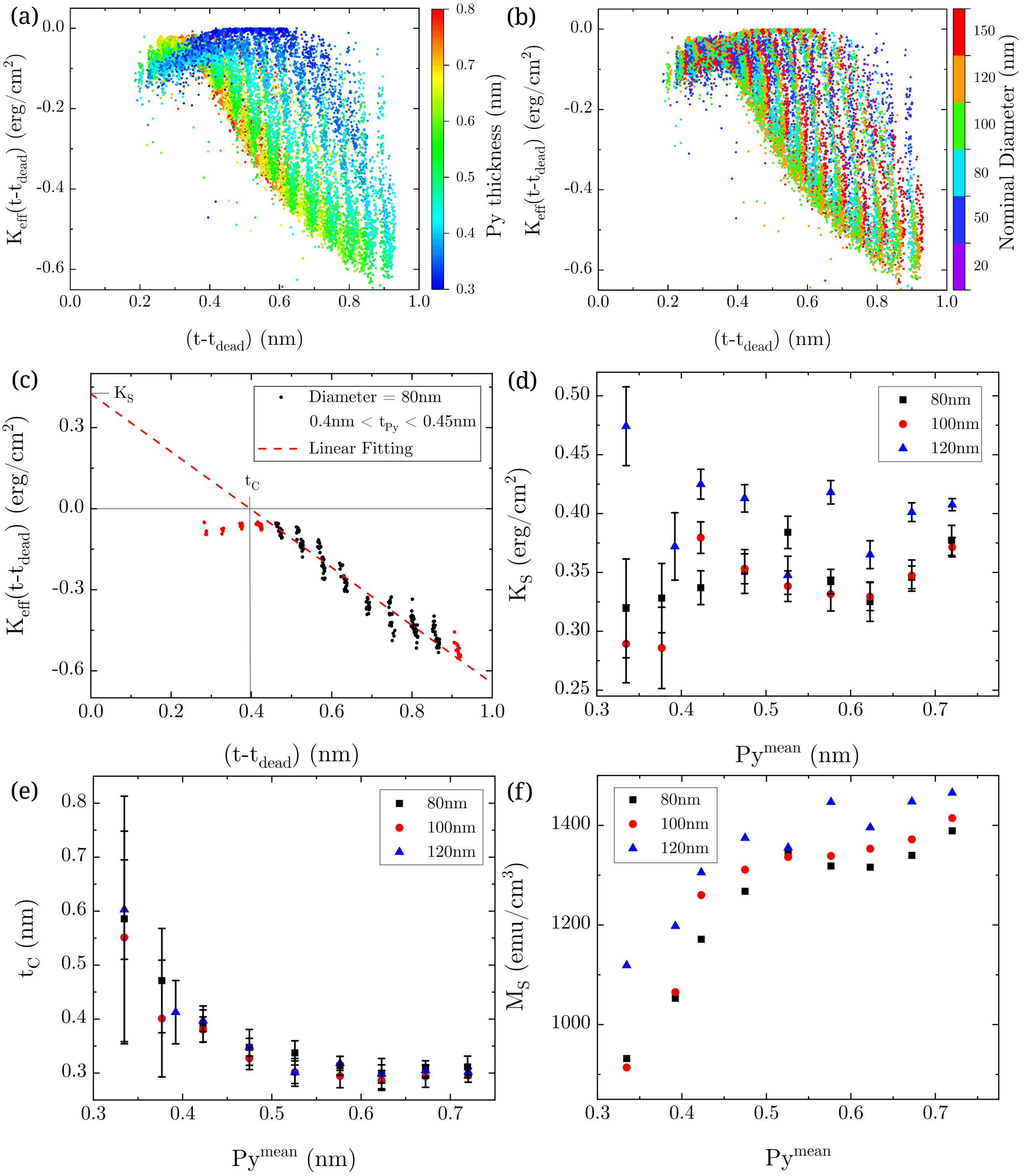

Figure 4.10: a) Dependence of $K_{eff} * t_{eff}$ with effective FeCoB thickness $t_{eff}$, with total permalloy thickness in color code. b)Same dependence as in (a), but differentiating all the 6 different nominal diameters of the wafer in color code. c)Linear fit of the dependence in (a) by selecting only the 80nm nominal diameter and with permalloy thicknesses between 0.4nm and 0.45nm. The red data points are devices not accounted for in the fitting. d)Extracted $K_S$ by repeating fit of (c) for 3 different nominal diameters and permalloy thicknesses from 0.3nm to 0.75nm. e)Extracted critical thickness dependence with permalloy thickness. f)$M_S$ dependence with permalloy thickness, taken from the slope of the linear fitting of (c)

.

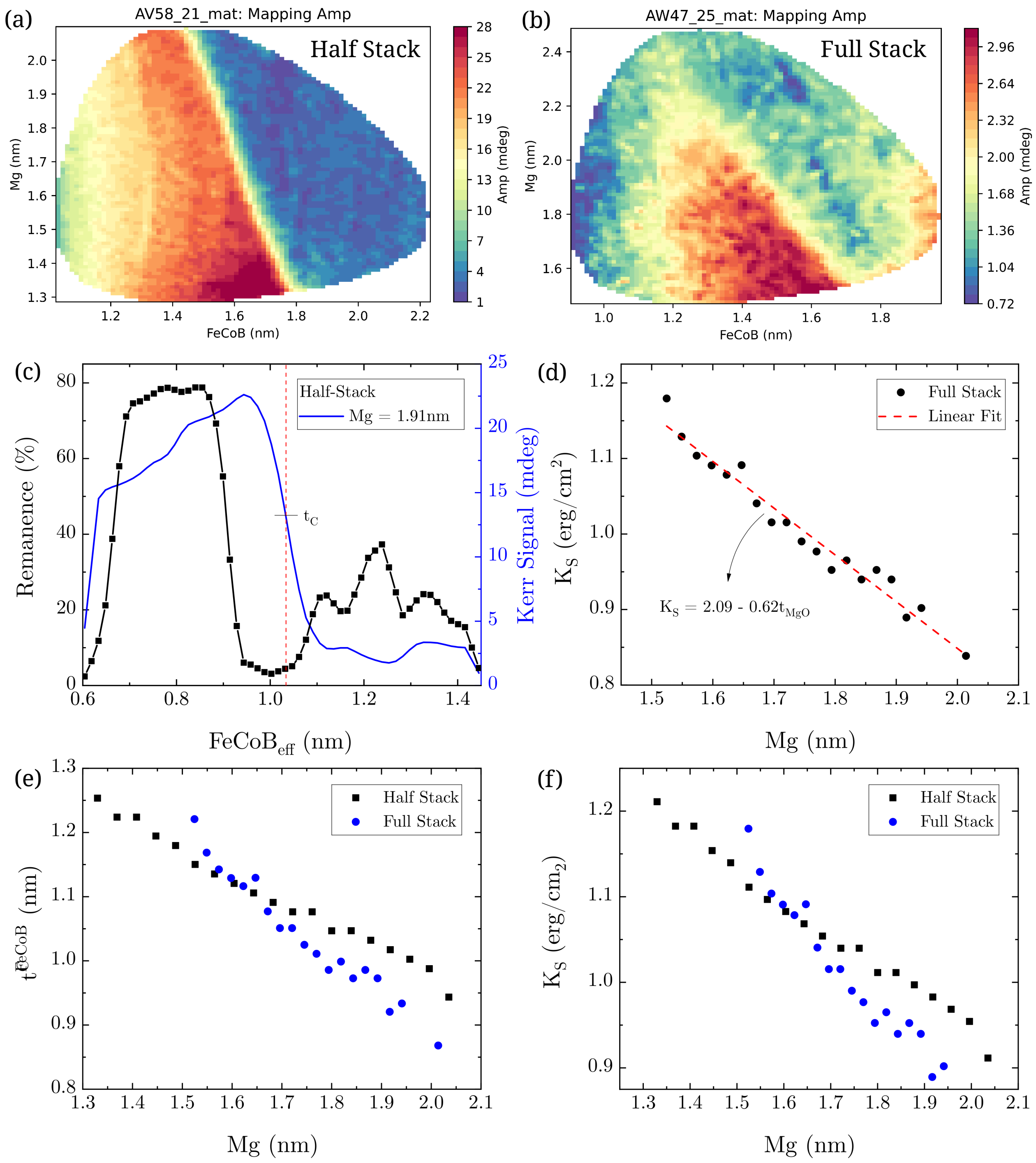

Figure 4.11: a)Kerr signal amplitude mapping of an interfacial Mg half-stack; b)Kerr signal amplitude mapping of an interfacial Mg full-stack. c)Remanence and Kerr amplitude plot in black and blue, respectively. Measured for a composition of 1.91nm of Mg in the half-stack sample. The dotted vertical line indicates the critical thickness $t_C$, the transition between in-plane and out-of-plane states for the layer. d)Extraction of the surface anisotropy dependence with MgO thickness for the full-stack sample, fitted with a linear function. e)Critical thickness dependence with MgO thickness for both samples. f)Surface anisotropy dependence with MgO thickness for both samples.

measured, which show this linear property with Mg. The difference in the observed slopes may be due to the larger roughness of the full stack sample that is aggravated for higher Mg content, since it is deposited as an amorphous layer.

The decrease of the anisotropy with thickness can be understood from the stoichiometry of the oxidation at the interface. With more Mg, it becomes more under-oxidized and the PMA drops steadily. If the thickness range for the Mg wedge was shifted to a thinner wedge, we can assume we would observe a maximum of $K_S$ for the optimal composition of the interface and a decrease for even thinner values when the layer becomes over-oxidized.

The MOKE method of extracting $K_S$ is very useful for thin-films and especially for half-stacks, since the signal has much less noise. In some instances, however, it can be large enough to make it impossible for certain stacks to be analysed with this method. As an example, a half-stack variant of a Py insertion layer in Fig.4.12a[7], with storage layer MgO / FeCoB / Py / W, has a clear signal and enables the extraction of $t_C$ using the same procedure as discussed above. For comparison, the MOKE mapping, before fabrication, of the sample of Fig.4.10 is shown in Fig.4.12b[8], with storage layer MgO / FeCoB / W / Py. Its signal is unusable due to the low amplitude and noisy background compared to the half-stack, as it can be observed. Here, the Kerr signal cannot be used to measure $t_C$ with reliability.

To analyse this particular half-stack, a slightly different approach must be used. We assume that, due to the diffusion of permalloy into the FeCoB, that the saturation magnetization is dependent on the thickness of permalloy. Therefore, to calculate the slope $2\pi M_S^2$, a weighted average is used for $M_S$ as:

$$M_S^{avg} = \frac{M_S^{Py} t_{Py} + M_S^{FeCoB}(t_{FeCoB} - t_{dead}^{FeCoB})}{t_{Py} + (t_{FeCoB} - t_{dead}^{FeCoB})} \tag{4.6}$$

Where the FeCoB dead layer is remeasured to be $t_{dead}^{FeCoB} = 0.38nm$, since the storage layer structure is not the same as the one used until this point. The permalloy is assumed to have no dead layer for simplification purposes, as we define our single storage layer as FeCoB+Py.

In Fig.4.12c we see the comparison between the previous measurements of Fig.4.10e, for the three measured device diameters, superimposed with the MOKE data in green. The profile of all four are very similar, with the half-stack $t_C$ being slightly shifted to thicker Py values. The bigger difference comes in the calculation of the $K_S$ in Fig.4.12d, where the $M_S$ scales with Py thickness and therefore will return us a similar drop in anisotropy, proportional to the Py composition. The $t_C$ dependence results show that both methods of using either $H_K$ of patterned devices or the Kerr signal of thin-films are equivalent. Additionally, swapping the layer sequence of FeCoB/W/Py to FeCoB/Py/W can have major changes in the properties of the storage layer. The added magnetic Permalloy into the FeCoB composition can have a direct influence or not on the MgO interface depending on the presence of a heavy metal spacer, such as Tungsten.

---

[7] Stack structure of a half-stack alternative Py insertion sample from Fig.4.12a: Ta(3) / FeCoB(0.8) / W(2) / Pt(5) / FeCoB(0.4) / MgO(0.75) / Ox(30s) / Mg(0.5) / FeCoB(0.5-1.0) / Py(0.3-0.8) / W(2) / Pt(5)

[8] Stack structure of the insertion Py sample from Fig.4.12b: Ta(22) / FeCoB(0.8) / W(2) / Pt(5) / SAF$_{6/3}$ / W(0.2) / FeCoB(1) / MgO(0.8) / Ox(30s) / Mg(0.5) / FeCoB(0.75-1.45) / W(0.2) / Py(0.3-0.8) / W(2) / Ru(5) / Ta(150)

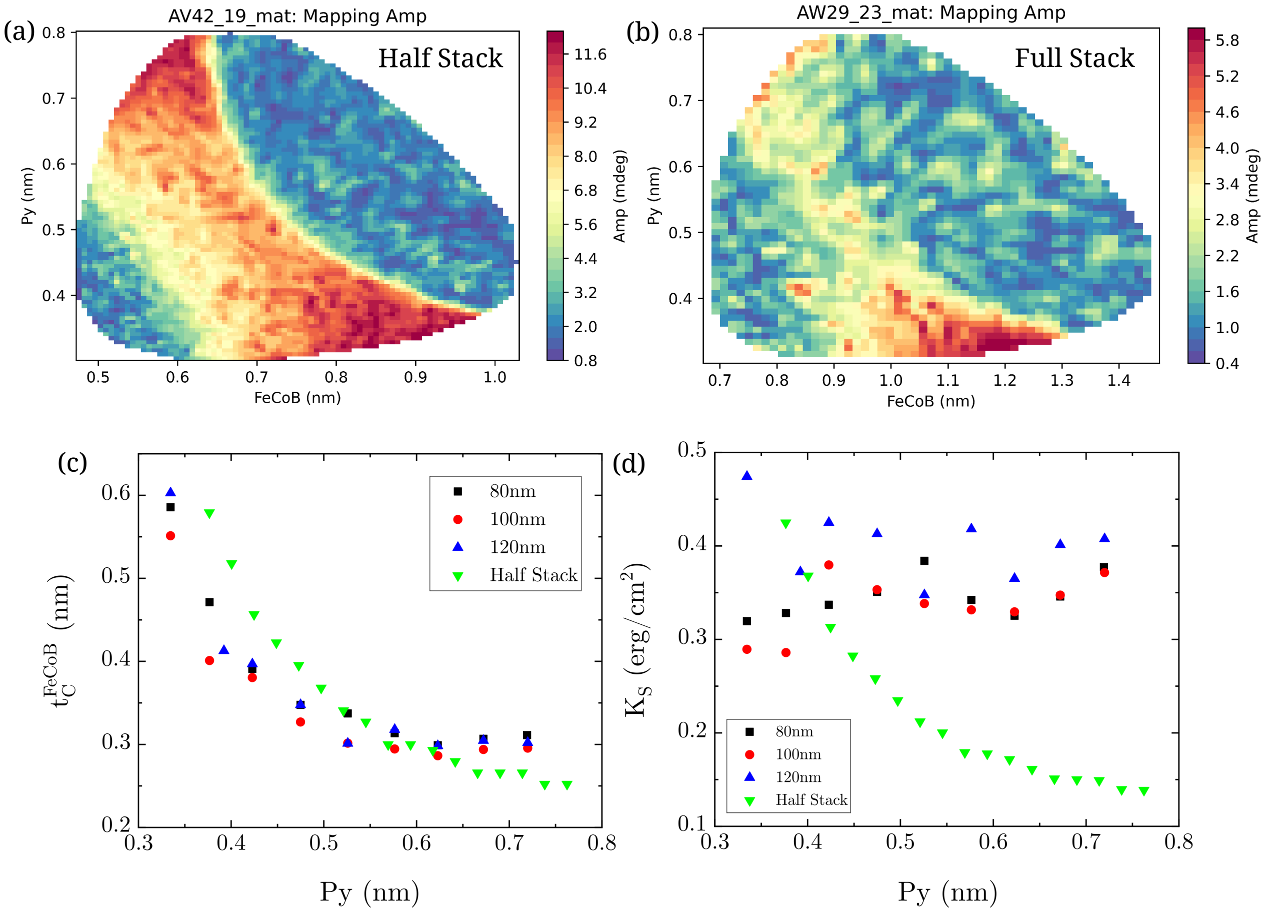

Figure 4.12: a)Kerr signal amplitude of a half-stack alternative Py insertion sample. b)Kerr signal amplitude of a full-stack Py insertion sample. c)Critical thickness dependence with Py thickness. b)Surface anisotropy dependence with Py thickness. The 80, 100 and 120nm diameter data points are from the fabricated full-stack structure of Fig.4.10, while the green data represents the thin-film half-stack sample.

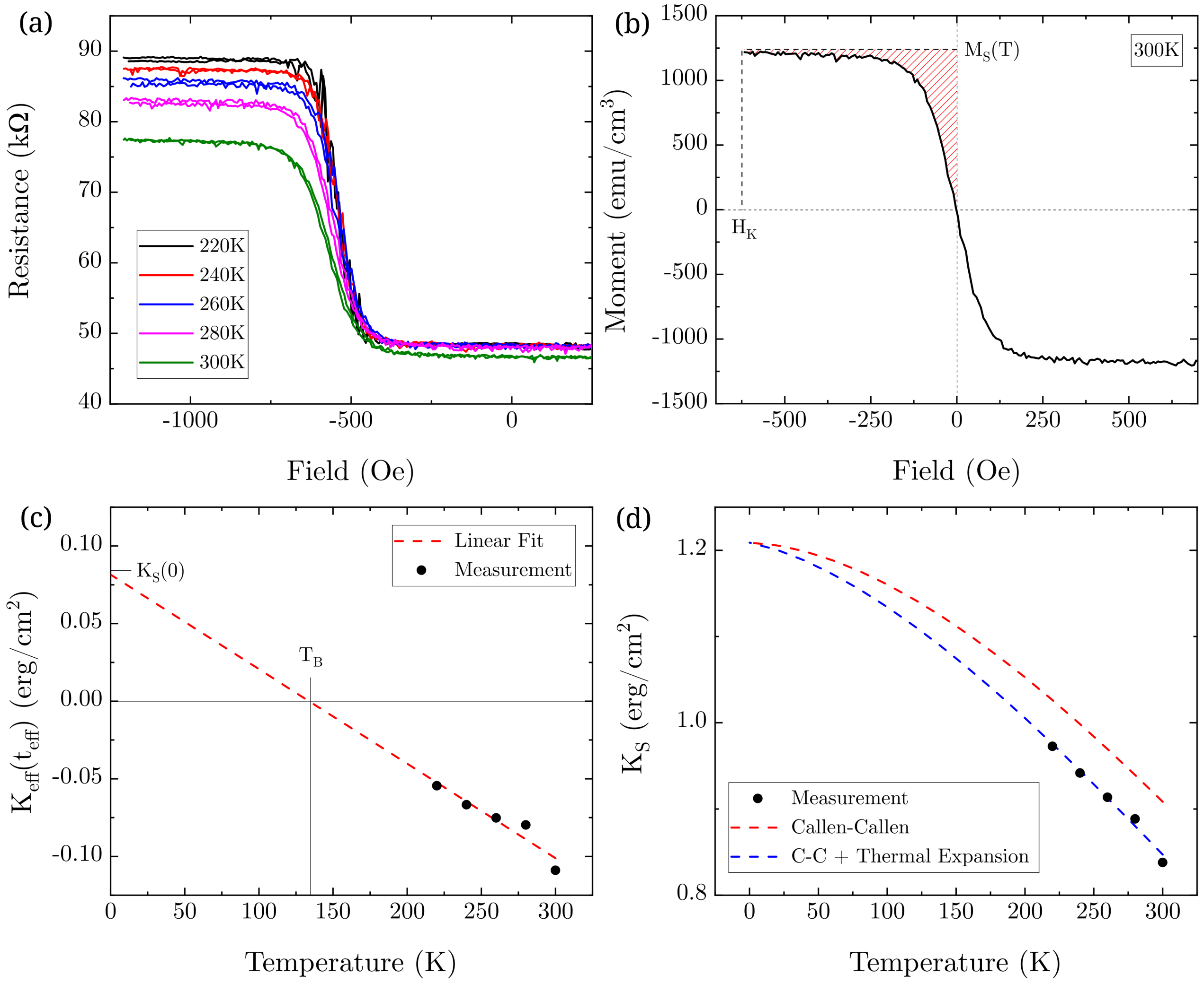

Figure 4.13: $K_S$ extraction of a device with nominal diameter of 25nm. a)Magnetic hysteresis loops for temperatures between 220K and 300K with dashed lines indicating the saturated resistance levels. b)$K_S$ dependence with temperature, showing a linear fit in red, the Callen-Callen law in green and the same law fitted with a thermal expansion factor in blue.

### 3.3.3 Surface anisotropy dependence with temperature

The $H_K$ method can also be used to acquire the surface anisotropy dependence with temperature. The anisotropy field $H_K$ and saturation $M_S$ are taken from magnetic hysteresis measurements of a device with interfacial Mg and 25nm nominal diameter in Fig.4.13a[9]. The hysteresis loops are shown down to 220K, with a blocking temperature of $T_B = 145.3K$, taken from the linear fit of the coercivity dependence with temperature. Therefore, in this particular case, the range between 300K and 145K can be used in the PPMS tool to extract the needed parameters.

As shown in Fig.4.13b, we utilize a more rigorous approach to defining the $K_{eff}$ with Eq.4.7, where the effective anisotropy is given by the area enclosed by the hysteresis loop and the saturation signal:

---

[9] Stack structure of the interfacial Mg sample from Fig.4.13: Ta(22) / FeCoB(0.8) / W(2) / Pt(7) / SAF$_{7/3}$ / W(0.2) / FeCoB(0.9) / MgO(0.8) / Ox(30s) / Mg(0.9) / FeCoB(1.48) / W(2) / Ru(3) / Ta(150)

$$K_{eff} = H_K * M_S - \int_0^{H_K} MdH \tag{4.7}$$

Here, the moment is extrapolated from the assumption that the layer has the same room temperature magnetization saturation for FeCoB of $M_S(300K) = 1240$ emu/cm$^3$. By application of the power law from Sect.2.2, we have $M_S(0) = 1364$ emu/cm$^3$ and we can estimate the magnetic moment for each temperature point in between. Then, by plotting the effective anisotropy in Fig.4.13c and fitting a linear function, we can extract the surface anisotropy at 0K of $K_S(0) = 1.21$ erg/cm$^2$ and the blocking temperature $T_B = 133.7K$, which is similar to the value acquired from the coercivity measurement.

In Fig.4.13d we fit the dependence of $K_S$ in red by initially using the Callen-Callen law, with an exponent of 3. The deviation seen can be explained by taking into account the strain in the material due to thermal expansion as it is heated to room temperature, which can affect the intrinsic surface anisotropy $K_S(0)$ [97]. The modified Callen-Callen formulation of Eq.2.21 that includes a linear thermal expansion term is used [165]:

$$K_S(T) = K_S(0)\left(1 - b\frac{T}{T_C}\right)\left[\frac{M_S(T)}{M_S(0)}\right]^3 \tag{4.8}$$

The thermal coefficient is fit with a value of $b = 0.27$ and shows that indeed a contribution from a crystalline rearrangement has to be accounted for to match the observed dependence of $K_S$ for this material.

### 3.4 Analysis of the figure of merit

In this section, we summarize the magnetic and electrical characterization of 4 different samples in Fig.4.14. They are samples deposited with an Mg interfacial layer[10], a Permalloy insertion[11], a reference stack with no add-on layers[12] and a Ru insertion layer[13]. In (a), we see its dependence on coercivity with temperature and the difference in $T_B$, though as we have seen, this can change with the composition of each insertion. Even then, the Py sample was the only one to achieve blocking temperature values below 100K. However, the maximum coercivity of HC is similar across the samples with the exception of the reference stack. Blocking temperature may differ, but coercivity evolution shows different slopes depending on composition of the stack, even within the same sample. For the four devices chosen, we have $H_C^{Mg}(10K) = 580Oe$, $H_C^{Py}(10K) = 460Oe$, $H_C^{Ref}(10K) = 970Oe$ and $H_C^{Ru}(10K) = 260Oe$. A more thorough investigation is needed to assess whether this is an effect of the stack composition itself or properties such as the diameter have an important role in modulating this dependence.

---

[10] Stack structure of the interfacial Mg sample from Fig.4.7: Ta(22) / FeCoB(0.8) / W(2) / Pt(7) / SAF$_{7/3}$ / W(0.2) / FeCoB(0.9) / MgO(0.8) / Ox(30s) / Mg(0.75-1.6) / FeCoB(0.95-1.9) / W(2) / Ru(3) / Ta(150)

[11] Stack structure of the insertion Py sample from Fig.4.9: Ta(22) / FeCoB(0.8) / W(2) / Pt(5) / SAF$_{6/3}$ / W(0.2) / FeCoB(1) / MgO(0.8) / Ox(30s) / Mg(0.5) / FeCoB(0.75-1.45) / W(0.2) / Py(0.3-0.8) / W(2) / Ru(5) / Ta(150)

[12] Stack structure of a reference / conventional MTJ: Ta(22) / FeCoB(0.8) / Ta(3) / Pt(5) / SAF$_{6/3}$ / W(0.3) / FeCoB(1) / MgO(0.3-0.8) / Ox(30s) / Mg(0.5) / FeCoB(0.5) / FeCoB(0.8-1.3) / W(2) / Ta(1) / Pt(2) / Ru(8) / Ta(150)

[13] Stack structure of a Ru insertion sample: Ta(14) / FeCoB(0.8) / Pt(8) / SAF$_{6/2}$ / W(0.2) / FeCoB(1) / MgO(0.75) / Ox(20s) / Mg(0.5) / FeCoB(0.9) / FeCoB(0.4-0.65) / Ru(0.11-0.23) / W(2) / Ta(3) / Ru(8) / Ta(150)

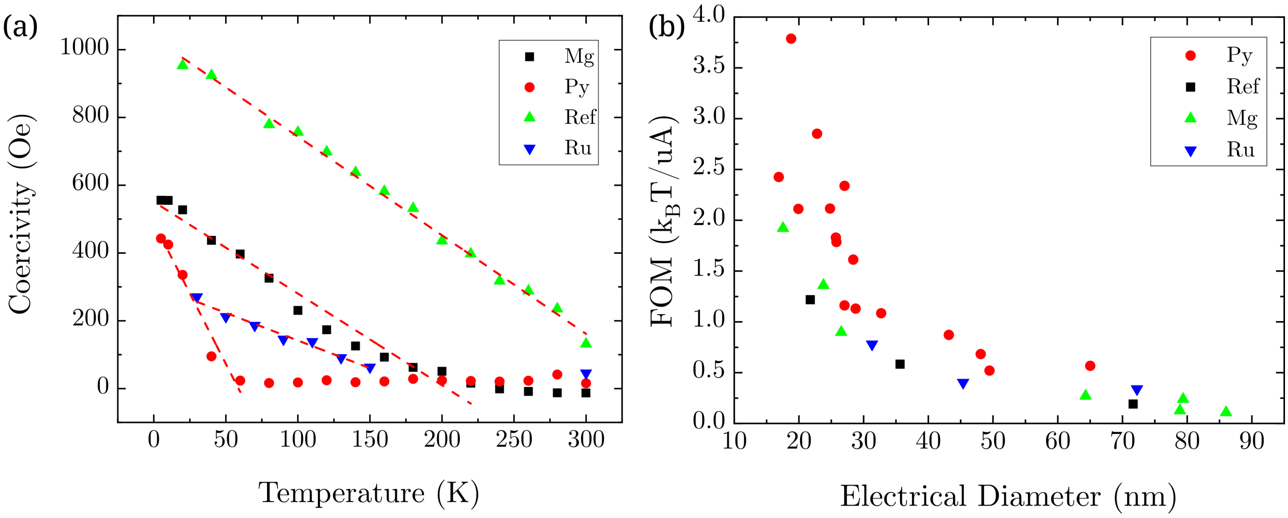

Figure 4.14: Comparison of different insertion devices on: a)Coercivity dependence with temperature with extracted blocking temperatures $T_B^{Mg} = 204K$, $T_B = 58.75$, $T_B^{Ref} = 355.4K$ and $T_B^{Ru} = 187K$. b)Figure of merit dependence with electrical diameter.

In Fig.4.14b, we summarize the electrical properties by plotting multiple devices with respect to their electrical diameter and figure of merit (FOM). The FOM parameter is defined by the ratio $\Delta/I_{sw}$ and quantifies the amount of current required to switch a memory cell with respect to its thermal stability. The electrical diameter is calculated using the average RA of the sample and the measured resistance of each device from the respective hysteresis loops. It can be shown to be the dominant parameter for the FOM, since junctions require switching currents scaling with $D^2$, assuming a constant STT switching critical current density. In the literature, this value is usually around $1k_BT/\mu A$ [166][167], which is reached by our devices with $D \approx 30nm$. For the Py insertion sample, we see a sharp increase in the FOM up to $3.79k_BT/\mu A$ for devices with sizes smaller than 30nm. This difference could be attributed to their smaller diameter. However, FOM values are consistently higher than for the other pursued strategy samples in the measured cell diameter range from 15nm to 90nm, which means that their $V_{50}$ is reduced compared to other insertions and the reference stack.

The extraction of the figure of merit depends on the accurate estimation of the thermal stability, which can be done by the method described in the previous chapter by sweeping the magnetic field. In the context of current/voltage switching of the devices, an alternative method can be used by fitting the switching voltage distribution to Eq.3.7. From this we define two types of stability: field stability $\Delta^H$ and voltage stability $\Delta^V$. The first is the conventional usage of $\Delta$, calculated for the devices up to this section. The second one provides a measurement of the energy barrier, i.e. retention, of the memory dot during the writing process, with possible impacts from secondary effects such as Joule heating. This is an important distinction to make because as the temperature decreases in the system and $V_C$ increases, the contribution and impact of heat dissipation will also become larger. The most notable impact on the tunnel junction is the heating generated as the electrons tunnel through the oxide barrier. This electrical power is dissipated in the pillar, creating a finite temperature increase, above the bath temperature as discussed previously. That in turn will limit $\Delta$ to a smaller value instead

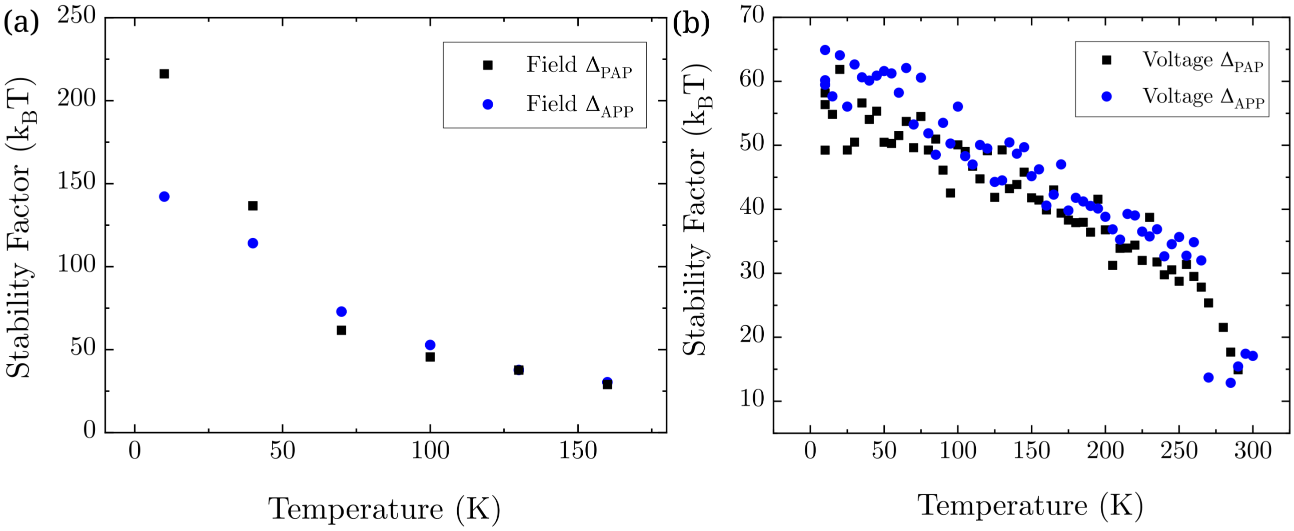

Figure 4.15: Stability factor extraction of a device with 70nm diameter and $t_{FeCoB} = 1.5nm$ and $t_{MgO} = 1.68nm$. a)Field Δ using a field-sweep method, with no Joule heating, sample measured at 20mV DC. b)Voltage Δ using current-pulse writing with junction heating, induced by the locally dissipated power.

of increasing indefinitely as the temperature gets closer to 0K [34]. This effect can be seen in Fig.4.15, as thermal stabilities based on field $\Delta^H$ and voltage $\Delta^V$ are plotted in (a) and (b), respectively.

Both stabilities are extracted by fitting 100 loops per temperature point. The $\Delta^H$ for both PAP and APP transitions rapidly increases, reaching values as high as $216 k_B T$ at 10K. The energy barrier $E_B$ is also temperature dependent, but scales with the effective anisotropy, which evolves according to a power law of Sect.2.2. Therefore, $E_B$ will converge to a finite value at 0K, while the term $k_B T$ will make Δ diverge, dominating proportionality at low temperatures.

However, for voltage loops extracted thermal stability $\Delta^V$, it has a distinct linear dependence with temperature with a maximum of $\approx 60 k_B T$ at 10K. At 250K, it rapidly drops from $30 k_B T$ to $10 k_B T$ at 300K, at which point the device is no longer stable. The measurement of the resistance state at the end of the switching pulse is done after the junctions have had time to cool down to bath temperature, as the characteristic cooling time is 3-5 nanoseconds such that complete cooling is achieved within 15-25ns [154]. This means that the measured $R_P$ and $R_{AP}$ are at their equilibrium temperature, and the resistance values will not reflect the temperature conditions during the actual voltage switching process. The estimation of the heating can be seen in Fig.4.16 , much like what was discussed for Fig.4.2d. Here, however, the calculation of the effective device temperature is done from the measured field stability $\Delta^H$ instead of fitting Eq.4.2, which gives us a more reasonable maximum heating of 80K for a bath temperature of 40K. The stability $\Delta^H$ at 10K seems to have been underestimated, such that the predicted device temperature is lower.

To evaluate how much the tunnel barrier is heating at each temperature point with precision, the field stability needs to be acquired with more accuracy, and the heat dissipation needs to be taken into account by considering the composition and dimensions of the MTJ. The complexity of the effective heat capacity of the stack prevents us from easily estimating the temperatures reached within the pillar, although estimations have been made in previous work [34, 168].

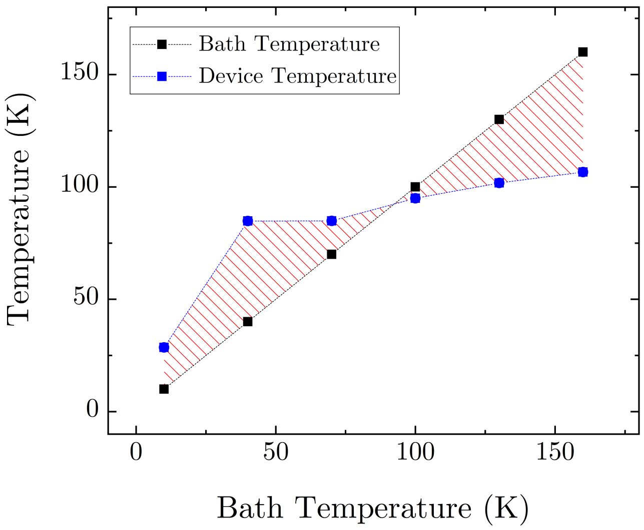

Figure 4.16: Estimated device temperature from heating extracted from the difference between the measured field $\Delta^H$ and voltage $\Delta^V$.

Table 4.1: Electrical properties for the best devices of each of the 4 samples analyzed in Fig.4.14, as measured at 10K.

| Sample | FOM ($k_BT/\mu A$) | Diameter (nm) | Volt. TMR (%) | $T_B$ (K) | $H_C^{max}$ (Oe) | $V_{50}$ (V) | $R_P$ (kΩ) | $I_C^{APP}$ ($\mu A$) | Volt. $\Delta_{PAP}$ ($k_BT$) |
|---|---|---|---|---|---|---|---|---|---|
| Mg | 1.8 | 21.8 | 119 | 192 | 777 | 0.88 | 29.4 | 30 | 57 |
| Py | 3.78 | 18.8 | 32.2 | 65 | 450 | 0.75 | 71 | 9.5 | 38 |
| Ref | 1.21 | 21.8 | 69.6 | 190 | 637 | 0.9 | 26.8 | 20 | 49 |
| Ru | 0.41 | 53.9 | 48.9 | 310 | 576 | 0.8 | 7.5 | 70 | 59 |
| Ref.[33] | - | 40 | 200 | - | 2830 | 0.42 | 3 | 130 | - |
| Ref.[34] | 1.18 | 40 | 220 | - | - | 0.34 | 2.5 | 136 | 152 |
| Ref.[169] | - | 64 | 176 | >300 | >530 | 0.26 | 3 | 80 | - |

In Tab.4.1, we have the summary of the results from the figure of merit measurements of Fig.4.14. The best of each of the 4 samples is given with a reference value from literature, also indicating the critical switching current and their thermal stabilities when available.

## 3.5 Pulse (H,I) phase diagrams under pulse current

In this section, we discuss a more complete method of device characterization, the pulse current phase diagram. It is plotted by extracting the voltage, or RV, loops for a large range of applied out-of-plane fields. An average of 50 loops is taken to account for stochasticity of the switching and measured under a 20mV DC bias voltage after a sequence of 100ns pulses is applied for the writing process. The diagram has three distinct regions: the high-resistance state AP in red, the low-resistance state in blue, and the bistable region in yellow. An example is shown in Fig.4.17[14] (a) and (b) for 220K and 40K, respectively, for a device with 26nm in diameter and $t_{FeCoB} = 1.43nm$ and $t_{Mg} = 1.76nm$. We

---

[14] Stack structure of the interfacial Mg sample from Fig.4.17: Ta(22) / FeCoB(0.8) / W(2) / Pt(7) / SAF$_{7/3}$ / W(0.2) / FeCoB(0.9) / MgO(0.8) / Ox(30s) / Mg(0.75-1.6) / FeCoB(0.95-1.9) / W(2) / Ru(3) / Ta(150)

have measured a blocking temperature $T_B = 220K$, which results in a vertical switching boundary in (a). At lower temperatures, the coercivity increases, and we obtain a writable device that exhibits macrospin characteristic behavior, as seen by the linear slopes of the diagram boundaries in (b). At the edges of the diagram, where $V_b$ is the highest, there is no coercivity and the boundaries merge, meaning that STT renders one state unstable and there is no more bi-stability. The increase in $V_C$ and the decrease in the stochasticity of the writing is shown in Fig.4.17c, where the RV loops for 10K and 180K with $H_Z = -500Oe$ are plotted. The larger dispersion of the switching loops at 180K is indicative of a lower stability, and we can see an increase in the TMR of the junction at 10K.

From the LLGS equation, one can numerically solve the diagram's switching boundaries using a macrospin approximation to predict the values of the STT efficiency term $dH/dV_b = a_{\|}/\alpha$ [77]. In Fig.4.17d the slopes of the diagram are fitted using a first-order polynomial at 10K, with an asymmetry for both transitions as we have $a_{\|}^{APP} = 4974Oe/V$ and $a_{\|}^{PAP} = 2575Oe/V$, which differ by a factor of 2. The full expression of the efficiency term is given by:

$$\frac{a_{\|}}{\alpha} = \frac{2e}{\hbar} \frac{\eta}{\alpha t_{FeCoB} M_S R_P A} \tag{4.9}$$

With $\eta$ being the STT spin polarization. Then in Fig.4.17e we have the temperature dependence of $a_{\|}/\alpha$, with an increase of 180% for APP and only an increase of 20% for PAP. By analyzing the efficiency equation, we only have three parameters that could contribute to this dependence: the polarization, the damping, and the saturation magnetization $M_S$. We know from the power law that the magnetization will increase at lower temperatures, so it only leaves us with the first two. The variation in damping with temperature has been studied in length in other works that indicate that it is not the driving factor for a higher efficiency [170, 171, 172]. At the device level, there has been reported to be no discernible variation, with a constant value for a wide range of temperatures (9K to 350K) [173]. Therefore, only the polarization may be the parameter of interest, as it scales with $\eta \propto (1 - \beta T^{3/2})$ according to the literature [174]. As a rough approximation, we consider $M_S$ as a constant in the range of 10K to 200K, but the theoretical exponent 3/2, however, does not fit our experimental data, with a fitting exponent of $2.3 \pm 0.1$ for APP and $3.0 \pm 0.3$ for PAP in Fig.4.17e. These results also suggest that for these devices there is a large asymmetry in the tunneling properties of the electrons through the MgO, which may be correlated with the rotation of the states seen in the hysteresis loops of Fig.4.17f. The P state has only a small change in its rotation with decreasing temperature, while the AP state has a shift from a high-remanence loop at 200K to one with lower at 10K as it is progressively cooled down.

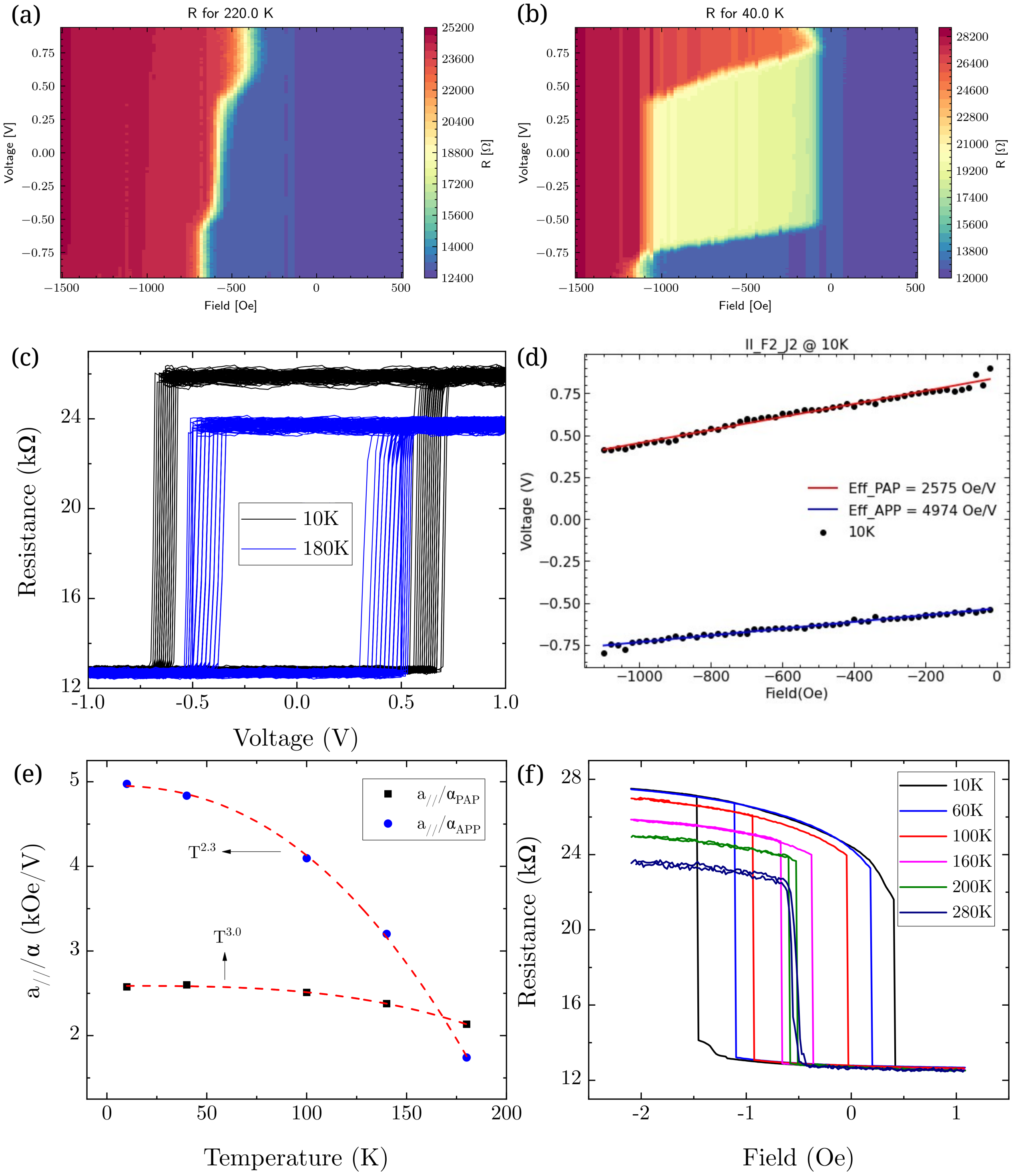

Figure 4.17: Pulsed phase diagram for a device with 26nm in diameter and $t_{FeCoB} = 1.43nm$ and $t_{Mg} = 1.76nm$. a)At 40K with a coercivity of 920Oe. b)At the blocking temperature 220K. c)Voltage RV loops at 10K in black and 180K in blue for 50 loops and $H_Z = -500Oe$. d)Linear fit of the diagram's boundaries at 10K for STT efficiency extraction. e)Temperature dependence of the STT efficiency for APP and PAP transitions. f)Hysteresis loops from 10K to 280K, with increasing rotation of the AP state for lower temperatures.

# 4 Electrical characterization of VCMA devices

For this section, we focus on the characterization of a high RA sample with a cross-wedge on the storage layer and the MgO tunnel barrier with MgO deposition of Mg(0.5-1.2) / Ox(10s) / Mg(0.5-1.2) / Ox(10s) / Mg(0.5). Its SAF structure is $[Co(0.5) / Pt(0.25)]_6$ / Ru(0.9) / $[Co(0.5) / Pt(0.25)]_3$. It has a variable RA from $100\Omega\mu m^2$ to $1500\Omega\mu m^2$ along the Mg wedge, with higher resistance states for thinner Mg composition, since the Mg layer is oxidized naturally for the two first Mg layers deposited for 10s at 150mbar oxygen pressure.

## 4.1 VCMA coefficient versus T

Using the method described in Sect. 4.2, we can extract the VCMA coefficient $\xi$ from single devices at different temperatures. Fig.4.18a[15] plots three DC phase diagram boundaries at 280K, 80K and 10K for a device with 100 nm diameter and $t_{FeCoB} = 1.54nm$ and $t_{Mg} = 2.72nm$. They are obtained by measuring wire-bonded devices in the PPMS tool without the use of any diodes, waiving any need to correct the resistance measurement that we take for this sample.

The dependence of $\xi$ on temperature in Fig.4.18b shows us one of the limitations of the method used to extract it. Two devices are plotted and their error propagated to the fitting by only doing single-loop measurements on the PPMS will induce a high dispersion of the calculated values at higher temperatures. Multiple loops are necessary to access the switching field and its dispersion to accurately calculate the thermal stability and correctly fit any temperature dependence using existing models [175], as shown in Sect.4.2.2. However, an increase in $\xi$ with temperature is observed, similar to other reports, ranging from $\xi(280K) = -20\pm1fJ/Vm$ to $\xi(10K) = -32\pm3fJ/Vm$ representing an increase in 60%. Similarly to what was previously reported [176], $\xi$ was calculated assuming $M_S(0K) = 1.45$ MA/m with the application of the Callen-Callen law to correct for $M_S$ with decreasing temperature.

Another change in the diagram we must take into account is that the symmetric term given by the heating coefficient $\zeta$, which accounts for the Joule heating of the device, becomes more dominant, impacting the measured coercivity and switching fields in (a). We can observe this in Fig.4.18c, where $\zeta$ is plotted and shows a value of $40 \pm 30kOe.\mu m^2/W$ at higher temperatures. It could be taken as a negligible contribution considering the large uncertainty, which quickly rises below 100K, reaching $\zeta = 655 \pm 50kOe.\mu m^2/W$ at 5K. The explanation for this phenomenon may be directly related to the thermal properties of the tunnel barrier; as we see in the inset of Fig.4.18c, the heat capacity of a crystalline MgO material will decrease sharply below 100K by multiple orders of magnitude. This will lead to much higher heat dissipation within the tunnel junction that may degrade the writing properties of the device, as the effective temperature during switching will not be the same as the thermal bath in which it is located in the cryostat.

This effect is an obstacle for the implementation of VCMA switching at cryogenic temperatures. The deterministic writing discussed in Chapter 2 is highly sensitive to thermal fluctuations; therefore, a more extensive study of the heating dissipation on the storage layer is necessary.As we utilize the DC current to extract the phase diagrams, there is no cooling of the junction during the measurement, so

---

[15] Stack structure of the high RA sample from Fig.4.18: Ta (22) / FeCoB (0.8) / Ta (2) / SAF / Co (0.5) / W (0.3) / FeCoB (0.9) / MgO (1-1.6) / W (2) / Pat (5) / Ru (30) / Ta (150)

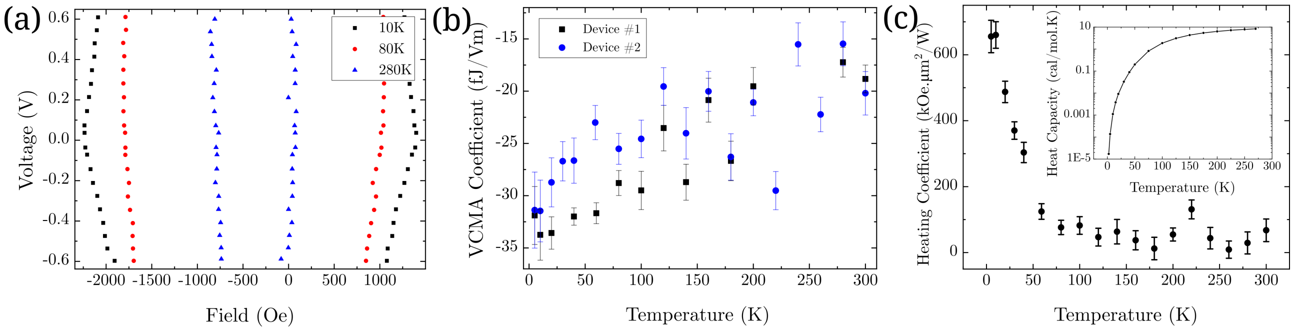

Figure 4.18: a)Switching field boundaries for a device with 100nm in diameter and $t_{FeCoB} = 1.54nm$ and $t_{Mg} = 2.72nm$ for 10K, 80K and 280K. b)$\xi$ dependence with temperature for two devices with similar physical and magnetic properties. c)Heating coefficient dependence with temperature. The inset image is the crystalline MgO's heat capacity dependence with temperature [2].

the maximum temperature reached by the device will not be the same in pulsed switching experiments. It is essential to determine if the short-duration writing pulses of approximately 1 ns are within the range of ballistic switching in order to guarantee its practicality.

## 4.2 Variation of the VCMA coefficient with thickness

This high RA sample being studied has a wedge thickness on the FeCoB storage layer that varies from 0.5nm to 1.1nm by taking into account a dead layer of 0.5nm. This will give us a variation of magnetic/electric properties from a superparamagnetic state, when the layer is not fully continuous at its low thickness value, to a high anisotropy state at higher FeCoB thickness. The presence of the MgO wedge will then ensure that we achieve an optimal thickness for the oxidation of the tunnel barrier for TMR optimization. It also creates a variation of the RA in the sample to see its influence on the measured values.

The target devices for VCMA extraction cannot be chosen at random, requiring a minimum magnetic hysteresis signal and a coercivity greater than zero for the VCMA effect to be visible. Because of this, we plot the value of $\xi$ for only 1450 (yield of 9.6%) of the working devices that have a nonzero VCMA coefficient. Fig.4.19a shows a monotonic increase of $\xi$ with an effective FeCoB thickness at 300K with a maximum value of -22.9 fJ/Vm at 1.1nm. The maximum TMR measured at room temperature in these devices is 115%, which corresponds to a thicker FeCoB layer with 1.1nm. Therefore, the dependence we see does not cover the full range of thicknesses for which PMA exists in this sample, and it deviates from the expected trend of $\xi \propto 1/t_{eff}$ [177, 178] or no dependence observed with $t_{FeCoB}$ [86, 179]. A broader analysis is needed to verify whether the linear proportionality of $\xi$ with effective FeCoB thickness extends to thicker layers or if there is a deviation in this dependence when the demagnetization energy decreases even further the effective perpendicular anisotropy approaching the transition to an in-plane state.

We then investigated the dependence of the VCMA effect on the magnetic properties of the device, since the dependence of MgO suggests the highest VCMA coefficient for the thickness of 2.2 nm Mg for the oxidation conditions used, corresponding to the observed peak in the TMR values. In Fig.4.19b, the dependence of $\xi$ on coercivity shows that there is no clear coercivity/anisotropy dependence, apart

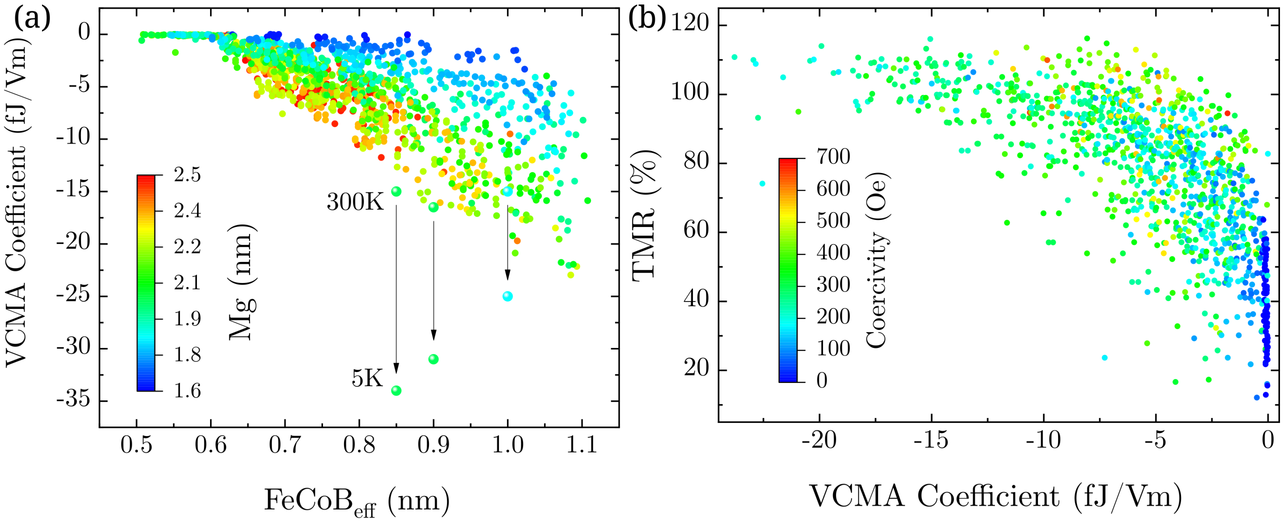

Figure 4.19: a)VCMA coefficient $\xi$ dependence with effective FeCoB thickness and Mg thickness in color-map. The arrows indicate the increase of $\xi$ measured at 5K for three different devices. b)The relationship between TMR and $\xi$, with a coercivity color-map.

Table 4.2: Comparison of the VCMA extracted from this work and other known literature values.

| | Sample | Tunnel Barrier | $\xi$ (fJ/Vm) | TMR (%) | RA ($\Omega.\mu m^2$) | $\Delta$ |
|---|---|---|---|---|---|---|
| This Work | FeCoB | Natural Oxidation | 22.9 | 95 | 210 | 35 |
| Ref.[141] | FeCoB | RF MgO | 30.5 | 49 | 650 | 35 |
| Ref.[138] | $Co_2FeAl/W/Co_2FeAl$ | RF MgO | 64.8 | 78 | - | - |
| | CoFeB/W/CoFeB | | 19.6 | 36 | - | - |
| Ref.[147] | FeCoB | RF MgO | 15 | 110 | 5000 | 38 |

from low-coercivity devices that do not show any measurable VCMA. However, the dependence of TMR shows an increase in $\xi$ for larger TMR values, suggesting that VCMA may also be dependent on the same factors that influence TMR and less dependent on the anisotropy of the storage layer, since $\xi$ seems to be uncorrelated with coercivity. These statements are based on expected proportionality between coercivity and effective anisotropy of the storage layer, and TMR is an indicator of the FeCoB/MgO interface quality and tunnel barrier crystallinity. The modest values achieved for both TMR and VCMA also indicate that the MgO barrier used, with natural oxidation of the deposited metallic Mg and a 0.5 nm Mg capping, might induce high levels of roughness at the interface with the storage layer, limiting the magnitude of both effects, as seen in the extraction of the dead layer in Sect.2.2. As a reference, some values for $\xi$ at room temperature are shown in Tab.4.2 with a comparison of the storage layer used and device properties.

## 4.3 VCMA Preliminary Switching Measurements

With $\xi$ extracted for our tunnel junctions, we then used the Hprobe measurement system to perform VCMA switching experiments. As discussed previously, this writing mechanism is very sensitive to the pulse width, which needs to be in the sub-ns range to observe any switching by VCMA. Conducting this experiment requires us to set the correct parameters for the device being measured, which can

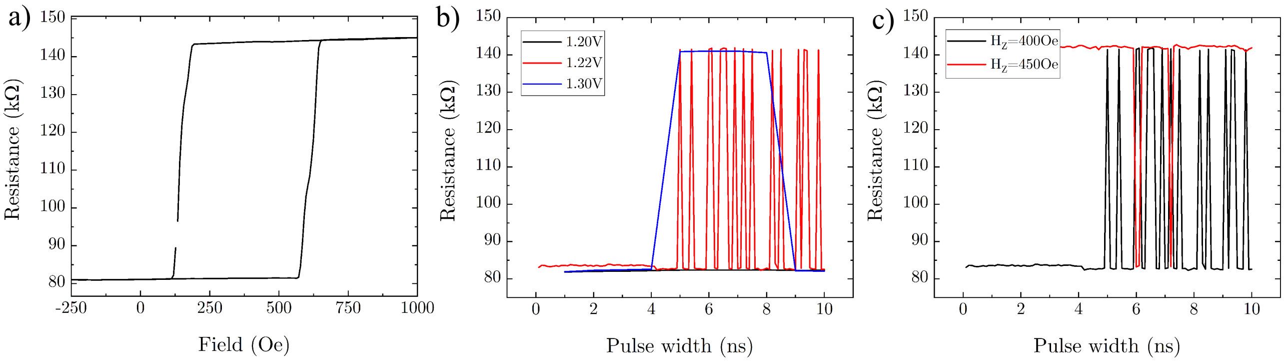

Figure 4.20: a)Resistance hysteresis loop of a device with $RA = 407\Omega\mu m^2$, 80nm in diameter, $t_{FeCoB} = 1.25nm$, $t_{MgO} = 1.57nm$, $R_P = 81k\Omega$ and a stray field of $H_{stray} = 380Oe$. b)VCMA switching measurement after voltage pulses with varying pulse lengths are applied for 1.2V, 1.22V and 1.3V under $H_Z = 400Oe$ and $H_{IP} = 600Oe$. c)Resistance measurement after a 1.22V pulse application for different pulse lengths under $H_Z = 400Oe$ and $H_Z = 450Oe$.

be a very delicate matter of optimization. Due to the precessional nature of VCMA, the switching probability is very sensitive to the conditions of the device, and only a narrow window of pulses is capable of writing them with low error rates. Therefore, for each set of in-plane field, $\xi$ and $\Delta$, the writing pulse will have a different voltage threshold. Therefore, only a preliminary study is performed for this section of the work. Setting up the measurement required initially pursuing a trial and error method that was not possible to fully complete during this thesis.

The VCMA effect of our samples is small in magnitude, which would normally mean that we may need to use higher in-plane fields $H_{IP}$ and voltages than those reported in the literature of $1.5kOe$ and 1.9V pulses [180]. However, our lower coercivity values (less than $1kOe$ for all devices at room temperature), which translates to lower effective anisotropy, do not require such high values. Due to the presence of a stray field from the reference layer on the storage layer, an out-of-plane field $H_Z$ is necessary to compensate for it and center the hysteresis loop so that both transitions PAP and APP have equal probability of switching and not to favor a single-state outcome. In Fig.4.20a, a hysteresis loop is shown for a device 80nm in nominal diameter with an RA of $407\Omega\mu m^2$ and thicknesses of $t_{FeCoB} = 1.25nm$ and $t_{MgO} = 1.57nm$ with resistance of $R_P = 81k\Omega$. Preliminary measurements performed on the Prober stage showed an offset of $H_{stray} = 380Oe$. In the Hprobe setup, we must take into account that the field calibration of both instruments may not be identical. The additional difficulty was that the tool has only been calibrated for Z fields in multiples of 50Oe steps; therefore we use $H_Z = 400Oe$ for the measurement in Fig.4.20b. Here, we see the resistance signal at three different pulse voltages: 1.2, 1.22 and 1.3V, with a $V_C \approx 1.21V$ using $H_{IP} = 600Oe$, since at 1.2V (in black) there is no switching, and with 1.22V we see writing occur.

Then, in Fig.4.20c we have two measurements at 1.22V for two values of the Z field of 400Oe in black and 450Oe in red. There is a reduction in switching events for the higher $H_Z$, meaning that our choice of 400Oe for stray field compensation was better, in agreement with the field offset measured in the initial Prober setup in (a). These results indicate that there may be VCMA switching in these devices, although partially conclusive, as the acquisition of a full phase diagram is necessary to ensure the writing we observe is from precession and not random due to the applied field and instability from the voltage pulses. Additionally, the pulse lengths between 0ns and 4ns do not show any switching, which has no evident cause in the VCMA framework. Due to time constraints and setup limitations, statistics on the switching probability were not acquired. To rectify that, the Hprobe setup requires a field calibration capable of applying a large range of values instead of the 50Oe step of the last measurement. The pulse generator and analysis script should also be optimized to send a fast sequence of pulses as in the Prober stage, in which over 100 data points can be captured per voltage/field values. With these improvements a phase diagram can be constructed and low temperature measurements in the PMMS tool will allow us to assess the viability of VCMA at temperatures below 10K.

## 5 Experimental investigation of the easy-cone

Up to now, in many of the HR loops from measured devices or thin-film samples, the low remanence state and the tilt/rotation of the stable states have not been well described. In this section we investigate one possible explanation for this distinct behavior experimentally, which has already been described in a micromagnetic framework in Chapter 2.

The presence of an easy cone state in the storage layer, as seen in Fig.2.26, can create a magnetization configuration with a symmetrical rotation of both the P and the AP states. By analyzing a half-stack thin film sample using a permalloy insertion with $t_{FeCoB} = 0.66nm$ and $t_{Py} = 0.48nm$, we see the same "S"-shaped curve in Fig.4.21[16], albeit with zero coercivity due to the very weak effective anisotropy of Permalloy at room temperature. Thus, this initial evidence leads us to believe that the easy-cone could be achieved with this alternate method of layer insertions as opposed to fine-tuning the thickness of the FeCoB layer, which has a very small working range for it.

To assess the magnetization state of the sample with more accuracy, we start by conducting micromagnetic simulations on 4 different types of layer using the magnetic force microscopy (MFM) mode in Mumax3. We calculate in Fig.4.22[17] the resulting force image for circular 100nm in diameter layers of a pMTJ with out-of-plane magnetization, an MTJ with a K2 component, a tessellated MTJ, and a thin-film layer with 400nm in lateral size. We have $M_S = 1MA/m$, $K_1 = 0.6MJ/m^3$ and in (d) a $K_2 = -207kJ/m^3$, with the grains of the tessellations in (c) and (d) having an average size of 40nm. This tessellation structure can be visualized in Chapter 2:Fig.2.25, where the region discretization is evident.

For the fully out-of-plane MTJ in Fig.4.22a, with no $K_2$, the MFM signal shows a uniform distribution across the surface of the layer with a small dip in the signal at its center. In this 500nm diameter layer, the demagnetization energy is nonuniform and starts overcoming the uniaxial anisotropy in this region. By adding a $K_2$ component to the layer in Fig.4.22b, we see a drastic difference in force signal behavior, with a contrast between opposite edges of the layer. Here, we achieve a uniform magnetization, tilted to a $45^o$ angle relative to the vertical axis. In Fig.4.22c, a thin-film layer of 1x1 micron is simulated to give us an indication of the grain structure across its surface. The $K_1$ normal

---

[16] Stack structure of the permalloy thin-film sample from Fig.4.21: Ta(3) / FeCoB(0.8) / W(2) / Pt(5) / FeCoB(0.4) / MgO(1.3) / FeCoB(0.5-1.0) / Py(0.3-0.8) / W(2) / Pt(5)

[17] System parameters for Fig.4.22: $Diameter = 100nm$, $t_{SL} = 1nm$, $R_P = 5k\Omega$, $T = 0K$, $K_1 = 0.6MJ/m^3$, $K_2 = -0.0207MJ/m^3$, $M_S = 1.0MA/m$, $A_{ex} = 15pJ/m^2$, $\xi = 0fJ/Vm$, $H_{app} = 0mT$, $\alpha = 0.1$, $CellSize = 2nm$, In (c) and (d): $GrainSize = 40nm$

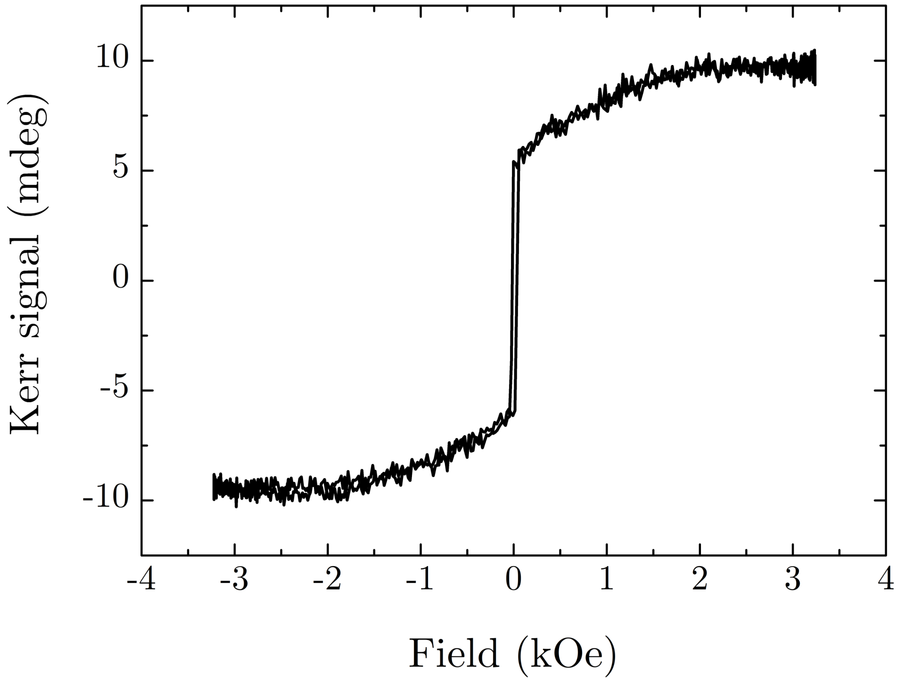

Figure 4.21: MOKE measurement of a thin-film half-stack MTJ FeCoB(0.66)/Py(0.48)/W(2) with out-of-plane field.

distribution gives rise to a random domain formation, with no discernible patterns. The size of these domains are directly related to the grain size choice and to the temperature conditions. The change in ratio of $K_1/M_S$ will enlarge these domains as the anisotropy is reduced for higher temperatures. Then, for Fig.4.22d, a tessellated layer is simulated, showing us magnetic domain boundaries as in (c). As discussed in Chapter 2 and seen experimentally in Chapter 4, the presence of this type of layer is a strong contender to explain the magnetic behavior measured in devices and thin-film samples, such as Fig.4.21. Therefore, to validate these simulation results, we conduct MFM imaging on a Permalloy half-stack structure, as it has been systematically showing the "S"-shaped hysteresis in both MOKE and device electrical measurements.

In Fig.4.23a[18], we have an optical microscope image of a patterned sample. The markings "X" and "XI" represent the rows of pillars with 500nm and 400nm diameter junctions, respectively. A similar Permalloy thin film sample is diced in a 1cm square piece for MFM imaging on two different regions. One with lower permalloy content $t_{Py}^{LOW} = 0.4nm$ and another with higher $t_{Py}^{HIGH} = 0.65nm$, but both with the same FeCoB thickness of $t_{FeCoB} = 0.85nm$. The low and high regions are scanned in a $10\mu m^2$ area in Fig.4.23b and Fig.4.23c, respectively. In the first we cannot identify any type of magnetic structure, with a phase shift of 60mdeg, while the second region has a diagonal striation with a slightly higher phase shift of 70mdeg. Upon zooming in on the central section of the region in a $1\mu m^2$ area, in Fig.4.23d we can identify more clearly a faint structure of the magnetization that could indicate a variation of the anisotropy on the layer.

To conduct the same measurement on a device, we deposited the same sample composition of the

---

[18] Half-stack structure of a Permalloy insertion sample from Fig.4.23: Ta(3) / FeCoB(0.8) / W(2) / Pt(5) / FeCoB(0.4) / MgO(1.3) / FeCoB(0.5-1.0) / Py(0.35-0.8) / W(2) / Pt(5)

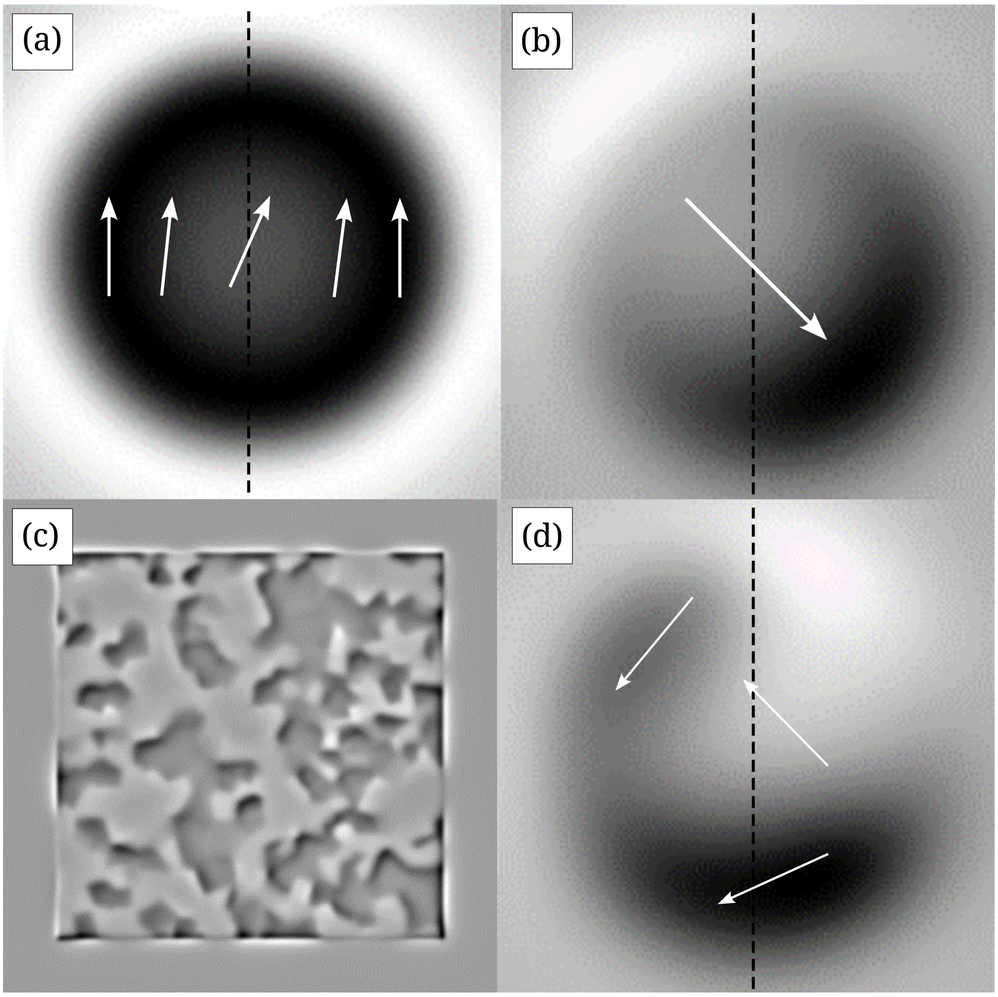

Figure 4.22: MuMax3 simulations of MFM measurements on: a)A standard FeCoB layer with 100nm in diameter exhibiting PMA and a uniform force distribution across its surface. b)The same layer with a $K_2$ component to the anisotropy, with a break in the force symmetry. c)A 400nm area with a tessellated $K_1$. d)A 100nm circular section of a tessellated layer. The domain sizes of the tessellations have 40nm in average. The vertical dashed lines represent the out-of-plane direction and the white arrows are the local magnetization vectors of each layer.

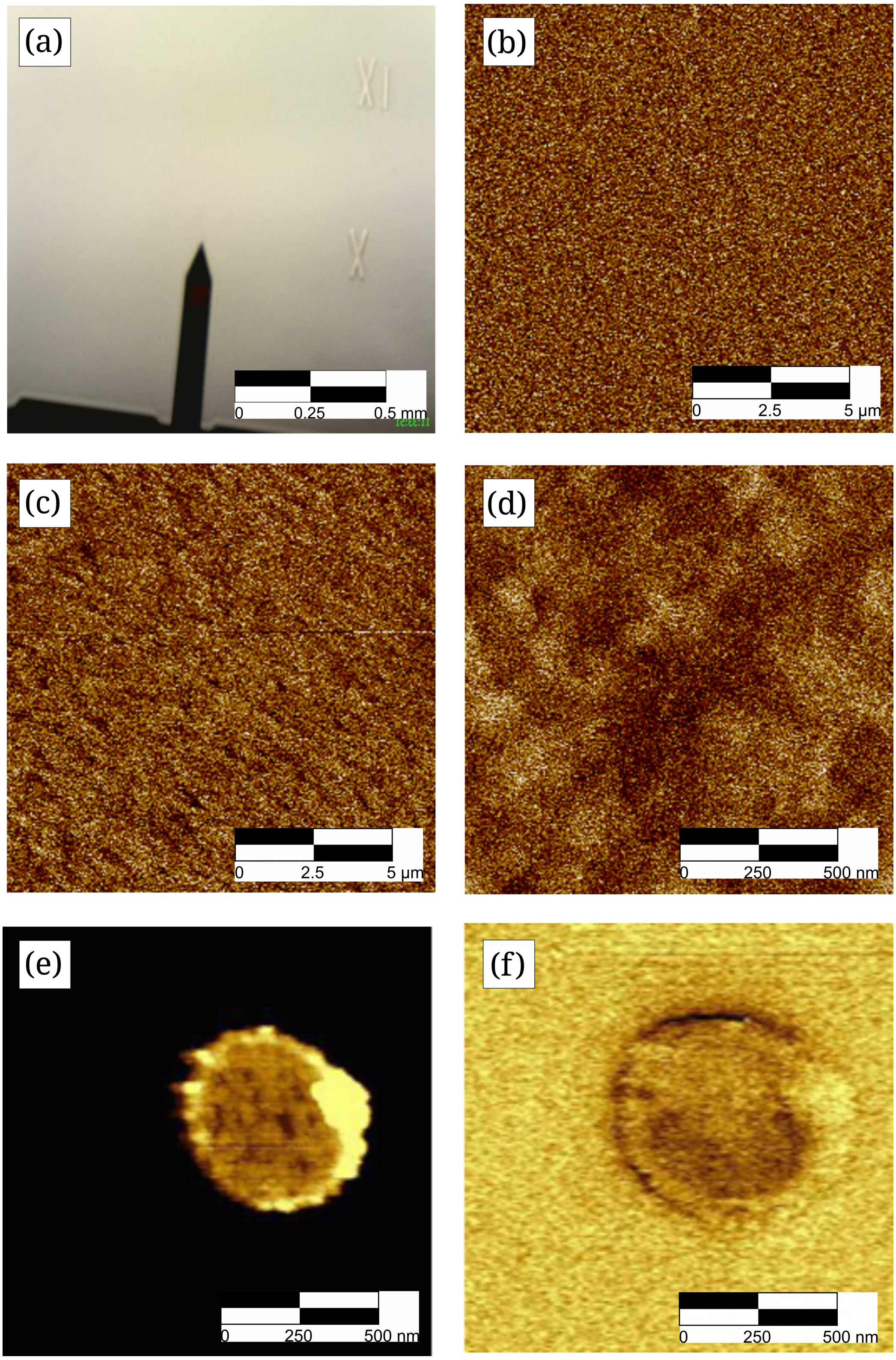

Figure 4.23: MFM measurements of a half-stack MTJ with a Py insertion layer with a storage layer as FeCoB(0.5-1.0)/Py(0.3-0.8)/W(2). a)Optical microscopy of the wafer, showing the row markings "X" and "XI" for MFM imaging. b)Phase AFM signal from a thin film with $t_{FeCoB} = 0.85nm$ and $t_{Py} = 0.4nm$. c)The phase signal with $t_{Py} = 0.65nm$ in a $10\mu m^2$ area. d)Same signal of (c) in a $1\mu m^2$ area. e)AFM signal of a patterned 500nm diameter pillar of the same stack and thicknesses. f)The MFM phase signal of the pillar, with contrast between the upper and bottom halves of the layer.

thin film on a separate wafer with a custom mask to pattern multiple arrays of pillars of varying diameter sizes between 100nm and 500nm. The top electrode was reduced to Ru(3)/Ta(30) instead of the usual Ru(3)/Ta(150) and after the magnetic pillar etching step the fabrication process was terminated, as we only required the pillar definition for the MFM. The sizes were chosen because of the limitation in resolution for the scanning and because we do not know the exact size range for any potential magnetic grains on the layer. The result from Fig.4.23d indicates that the texture is greater than 100nm. So any pillar below that size may not show enough contrast for us to identify any structure. In Fig.4.23e we do an AFM height scan of a 500nm circular pillar without SAF or reference layer. So that in (f) we have the phase shift with a discernible variation of the signal across the surface of the pillar, which is uncorrelated with its physical structure from (e). All of these samples were prepared without any demagnetization protocol, since they were in their relaxed state.

The results are promising in identifying the structures that give rise to the magnetic behavior of these layers, but some difficulties for collecting concrete evidence still remain. The weak anisotropy of permalloy with small remanence and no coercivity may lead to artifacts in the MFM due to the capping of the magnetic stack. On top of the weak layer, we have Ru(3)/Ta(30)/Cr(20) and an additional 10nm to 50nm from the distance between the tip and the sample during scanning. The tip itself may also induce artifacts in the images. We utilize a "low-moment" tip to be able to see any contrast on the phase signal, and if we swap it to a standard or "high-moment" tip, we can only observe noise. This may be explained if the tip is simply dragging the layer magnetization along and destroying any pre-existing domains. Moreover, not every tip is in perfect working conditions to make these structures appear, which also requires us to test different parameters in the scanning settings to obtain contrast. Another limitation is that other samples that show some stable-state tilt/rotation and larger coercivity, such as the interfacial Mg insertion sample, exhibit it only at lower temperatures, requiring a specialized MFM tool capable of cryogenic cooling for direct imaging.

Finally, for electrical characterization, we chose to work with the Mg interfacial sample, as the reduction of the blocking temperature by permalloy limits the temperature range that can be used for temperature-dependent measurements. A device with 18nm electrical diameter and $t_{FeCoB} = 1.53nm$ and $t_{Mg} = 0.89nm$ is measured in Fig.4.24[19], with its hysteresis loops at 10K and 160K in (a) taken with 100 sweeps on the PPMS. There is, as seen for previous junctions, a transition of the hysteresis from a fully remanent loop into one showing strong rotation of the AP state with a weaker one for the P state, with the dispersion of the switching field decreasing for 10K, as expected. From the micromagnetic numerical simulations on tessellated layers from section 6, we get this same transition when the magnetic domain sizes change, as seen in Fig.2.27a. Due to the effects on temperature with a fixed domain size of Fig.2.27b, which does not influence the remanence, we can assume that there is a modification of the magnetization structure of the layer when temperature is decreased [115]. This is further corroborated using the macrospin approximation and the results of Fig.2.12 that indicate that the domain wall width should decrease and, therefore, increase the disorder of the layer with more domain structures. Then, by performing STT writing on this device from 10K to 300K, we obtain the dependence plotted in Fig.4.24b for PAP and APP under an offset field of $-500Oe$. The inset of

---

[19] Stack structure of the interfacial Mg sample from Fig.4.24: Ta(22) / FeCoB(0.8) / W(2) / Pt(7) / SAF$_{7/3}$ / W(0.2) / FeCoB(0.9) / MgO(0.8) / Ox(30s) / Mg(0.75-1.6) / FeCoB(0.95-1.9) / W(2) / Ru(3) / Ta(150)

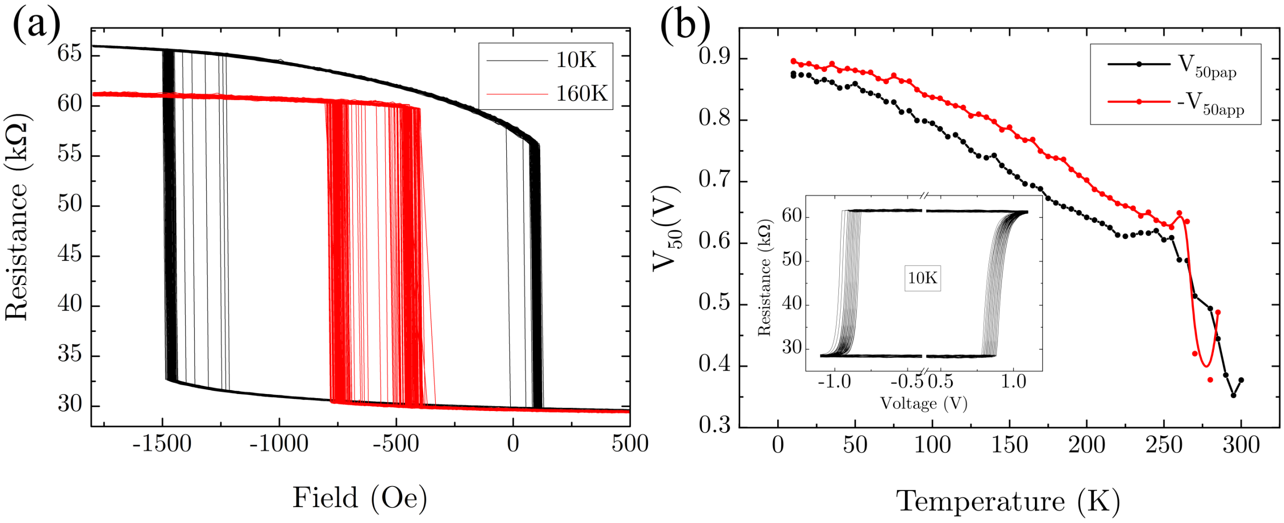

Figure 4.24: a)A 100-loops hysteresis at 10K in black and 160K in red for a device with 18nm in diameter and $t_{FeCoB} = 1.53nm$ and $t_{Mg} = 0.89nm$. b)The 50% switching voltage dependence with temperature. the inset image shows a square voltage hysteresis for STT switching at 10K.

the figure represents the 50 loops acquired for the extraction of $V_C$ at 10K. An interesting feature is present in the range of 200K to 275K for both transitions: there is a small plateau of the voltage, with a slight increase before it quickly vanishes as the device loses stability at the measured temperature. This effect is similar to what was observed in Fig.2.28b and Fig.2.29, which is a behavior that only arises within the framework of micromagnetism with the presence of the second order anisotropy $K_2$.

Thus, our accumulated evidence points to the presence of an "easy-cone-like" state of our samples. With the MFM imaging, a tessellated layer seems to be the better approximation for the behavior we observe. And through temperature studies and magnetic hysteresis changes we can correlate it with the granularity of the layer and the formation of magnetic domains. Further investigation is needed, however, to prove this statement by acquiring higher-resolution images and its temperature dependence.

## 6 Conclusions

We have fabricated magnetic nanopillars using a nanofabrication clean-room protocol illustrated in Fig.4.1. Achieving high-quality samples is critical for the study of the magnetic/electrical properties of our devices, with yield being the most sensitive parameter to defects, artifacts, and process issues.

We investigated different samples with an unconventional storage layer to modify its effective anisotropy and potentially engineer devices with targeted STT switching voltages for cryogenic operation. The use of insertion layers proved successful in changing the blocking temperature of the bits, as observed in Fig.4.9, in which the lowest measured was $T_B = 59.2K$ with an insertion of 0.76nm of Permalloy, while the highest in the same sample had $T_B = 134K$ with 0.32nm of Permalloy. With this approach, it is possible to target specific applications operating in different low-temperature ranges, such as high-performance computing below 10K or in "shallow cryoelectronics" around 77K.

Within the trial samples, the Permalloy insertion showed to have better electrical properties, with a maximum figure of merit of $3.79k_BT/\mu A$, compared to the second best $1.8k_BT/\mu A$ of the interfacial Mg sample. Most of these devices also showed an unusual property in which the stable states rotate with the field, suggesting we do not have a fully out-of-plane layer. From correlating our magnetic and electrical characterization of Fig.4.24 with the MFM imaging of Fig.4.23, and the micromagnetic simulations of Chapter 2 in Sect.6, there is a strong case to be made that the addition of the "add-on" layers modifies its domain structure such that it gives rise to an easy-cone-like state, in which a random distribution of $K_1$ can give rise to a "virtual $K_2$" term.

We also investigated high resistance-area samples larger than $100\Omega\mu m^2$ to study the influence of the storage layer and tunnel barrier thicknesses on the VCMA effect. The highest VCMA coefficient of -22.9 fJ/Vm was extracted at the thickest FeCoB of 1.1nm and close to the optimal oxidation of the MgO barrier, correlated with the highest TMR values in Fig.4.19. This is likely due to an improved tunnel barrier quality that also plays a role in the VCMA effect.

Preliminary VCMA switching experiments showed some evidence of switching at 1.22V voltage pulses between 1-10ns and an applied in-plane field of 600Oe, but the results are not conclusive, requiring the acquisition of full phase diagrams to assess their behavior at 300K and at temperatures below 10K. By doing so, we can attempt to measure the deterministic switching regime discussed in Chapter 2.

# Chapter 5

# Conclusion and future prospects

Goals

In this chapter, final remarks are made on the results and the lesson we can take from the presented data. Furthermore, ideas for future measurements are given to continue the proposed line of investigation and to discuss how we could best move forward with some of the experimental evidence that has not been fully developed.

**Contents**

# 1 Conclusion

The work carried out in this thesis was aimed at engineering MRAMs capable of operating in a cryogenic environment and characterizing them for a wide range of temperatures from 300K to as low as 5K. Within this objective, we investigated two types of devices: STT-MRAM and VCMA-MRAM.

In Chapter 2, we introduced the concept of numerical simulations using a macrospin approach based on the LLGS equation. The two writing mechanisms that we investigated are used to compare their properties and search for their optimal conditions for cryogenic memory operation. Part of the work was done under the assumption that a VCMA effect is present in the layer, while the other part assumed only STT is present. The macrospin basis for the calculation allowed us to easily extract the dependencies of the critical switching voltage $V_C$ with pulse width, thickness, material parameters and temperature that help us to qualitatively interpret the measurement data for real devices. We then discussed the effects that a higher order anisotropy has on the storage layer in regards to its magnetic and electrical characteristics. We see that by adding a $K_2$ term, we reach the easy-cone state, in which the magnetization is not fully out-of-plane, and that it can add beneficial traits to the energy consumption associated with the writing of the bit. An analytical expression for $V_C$ was derived for the VCMA system and the stability factor was reworked to include the new term. The hysteresis loop was calculated for this type of storage layer, which manifests a low remanence state at zero field, with a rotation of the stable states and an asymmetry that arises from the AP conductance definition when plotting the resistance state. Subsequently, a pulse phase diagram was calculated for both STT and VCMA between 0K and 50K, with the first one showing the conventional switching boundaries of literature work, while for the latter we identified new features that are correlated to the energy landscape of the system. This gives rise to a novel deterministic switching regime for VCMA writing that outperforms the precessional nature of its conventional operation, thus circumventing a major obstacle for the application of such technology. However this new regime is limited to temperatures below 50K as a result of its sensitivity to thermal fluctuations. In the micromagnetic section, we showed that the VCMA deterministic switching was still present and that the effects of $K_2$ on the layer can be reliably reproduced by using a tessellated layer. This is done by subjecting $K_1$ to a spatial variation that can be modulated through the average magnetic grain size and the magnitude of the variations. These results helped us to interpret the experimental data in Chapter 5, where we correlate our simulations with physical evidence of the existence of an "easy-cone-like" state.

In Chapter 3, we discussed the composition of an MRAM in greater detail, explaining the role of each of the layers in its structure and how they interact with each other. Part of the work in this section was done by focusing on the optimization of some of the layers with direct influence on the device's magnetic/electrical properties. The SAF was highlighted as a key component of a functioning MTJ and was shown to be the cause of an offset field in the hysteresis of the devices. This was remediated by changing the Co/Pt repetitions of its structure. Additionally, an annealing study on the usage of either W or Ta layers as the B-getter was carried out to enhance the quality of the interface between the storage layer and the tunnel barrier, with W being the best of the two. Next, we explored the storage layer and how we can modify its composition to deposit a low effective anisotropy layer for low energy STT writing. There are multiple ways to realize a storage layer with low anisotropy energy: by reducing the diameter of the MTJ pillar to reduce its volume, by changing its annealing temperature, by doping it, etc. The method we chose was to introduce an "add-on" layer, an additional material to interact with the main storage layer and modulate its material parameters. It can be deposited in three different configurations: as an interfacial layer (MgO/A/FeCoB), an insertion layer (MgO/FeCoB/A), or as a replacement layer (FeCoB/A/FeCoB), with "A" being the add-on. An advantage of this method is that it is the most straightforward way to change the properties of the stack, since it does not depend on the device fabrication process, annealing, etc. The three materials tested for these modified structures were permalloy, cobalt, and magnesium, showing a range of different effects compared to the conventional stack that only has a FeCoB storage layer. For the development of VCMA samples, we used a conventional MRAM design to assess the magnitude of its effect on our stacks and how we can optimize the VCMA coefficient $\xi$. The first modification done was the substantial increase of the resistance state of the tunnel barrier, by using thicker Mg layers and exposing them to higher oxygen pressures to increase the oxidation of the final MgO layer. Doing so increases the resistance-area product of the final devices by at least one order of magnitude, which will decrease the STT contribution to the switching and facilitate the study of the VCMA. To extract the magnitude of $\xi$, four methods are discussed that each have their own advantages and drawbacks related to the fabrication of the samples and the type of measurement involved. The switching field method proved to be the most reliable, being capable of collecting data from large arrays of devices with more reliability than the other three, since it is used on functional devices and does not rely so heavily on parameters such as the stability factor, which can be difficult to extract with a high degree of quantitative accuracy.

In Chapter 4, the nanofabrication process was described in greater detail, focusing on the most important steps of the procedure to achieve high yield and good device quality. The hardmask etching steps were given special attention due to their critical influence on the final magnetic pillar shape. It dictates the overall performance of the device in a physical way independent of its composition, which can only be evaluated at the end of the fabrication. The device properties were finally characterized by a few different characterization tools. The prober stage, being capable of full wafer measurements, was our ideal tool to quickly extract the yield and general state of the new samples, allowing us to select promising candidates for our low-temperature setups. Thus, after an initial assessment, the PPMS tool was used for single devices, which requires a wire bonding step to connect it to the sample holder. This, however, may provoke breakdown of the junctions due to the risk of exposure of the tunnel barrier to electrostatic discharges from the environment, circuit lines, and instrumentation that affect mostly low-RA samples such as the ones for STT writing. To avoid this issue, multiple Schottky diodes can be connected head to tail in parallel with the device, increasing their resistance to spikes in the voltage.

For the investigation of fabricated samples for STT, we based our choices on the studies of the previous chapter, selecting the ones showing lower coercivity at the thin-film level because it correlates with the effective anisotropy. The temperature dependence of the main magnetic and electrical properties were measured for different samples embedding insertion/interfacial layers of Mg, Co or Py. The change in coercivity was analyzed to extract the blocking temperature of a particular storage layer composition, giving us insight into its $H_K$ field and aiding us in characterizing the behavior of their $V_C$. An interesting observation for many of these samples was the increase of rotation of the stable states at their compensation field, much like the one calculated in Chapter 2 for systems using a $K_2$ term. This was further investigated by MFM imaging of a Py insertion sample, since it showed the largest rotation states. What was observed is a faint change in the force signal across the sample surface at both thin film level and patterned devices 500 nm in diameter. Following these results with micromagnetic simulations on tessellated surfaces, we have independent confirmation of the existence of an intermediate state between out-of-plane pMTJs and in-plane MTJs, which exhibits properties similar to those of an easy cone.

The conventional MTJ fabricated for VCMA applications was mainly characterized by using the prober stage, extracting $\xi$ with the method of Chapter 3 for 1450 devices that gives us a deeper understanding of the relationship between the coefficient and the thicknesses of the storage layer and tunnel barrier. At lower temperatures, only a few devices were measured, showing not only an enhancement of the VCMA effect, but also a rapid increase of the heating inside the junction below 100K, which can be an obstacle to integrate them within cryogenic circuitry that has limited cooling powers.

## 2 Future work

### 2.1 Stochastic memories

Throughout the fabrication of multiple samples and the analysis of different combinations of storage layers and stack structures, we came across devices with interesting characteristics that we did not investigate fully because they do not show our target properties. However, they can still be useful for other applications. This was the case for a Py insertion layer using the following stack: a seed Ta(22)/FeCoB(0.8)/W(2)/Pt(5), a SAF using a 6x3 Co / Pt repetition, and a tunnel junction FeCoB(1)/MgO(1.3)/FeCoB(0.5-1.0)/Py(0.3-0.7)/W(2). After annealing at $250^oC$, all compositions of this sample had a stochastic behavior at room temperature, as seen in Fig.5.1a. At 300K and at the compensation field, there is no stable state, with the resistance stochastically switching at no applied currents. The observed field offset of -200Oe comes from the earliest iteration of the SAF, which was not optimized. The softer annealing process crystallized the MTJs in such a way that their blocking temperature was almost exactly 300K, with coveted properties for areas such as neuromorphic or stochastic computing.

Subsequently, we measured one of these devices with a real-time setup that is capable of registering the resistance state of the device with very high precision. In Fig.5.1b, we have a time-trace signal under a 20mV reading bias and a corrected offset field, showing the presence of two stable states and random crossings between them as time passes. Unfortunately, no further studies were conducted for this type of device, although this opens up the possibility of manipulating the blocking temperature to fabricate p-bits for different ranges of operating temperatures.

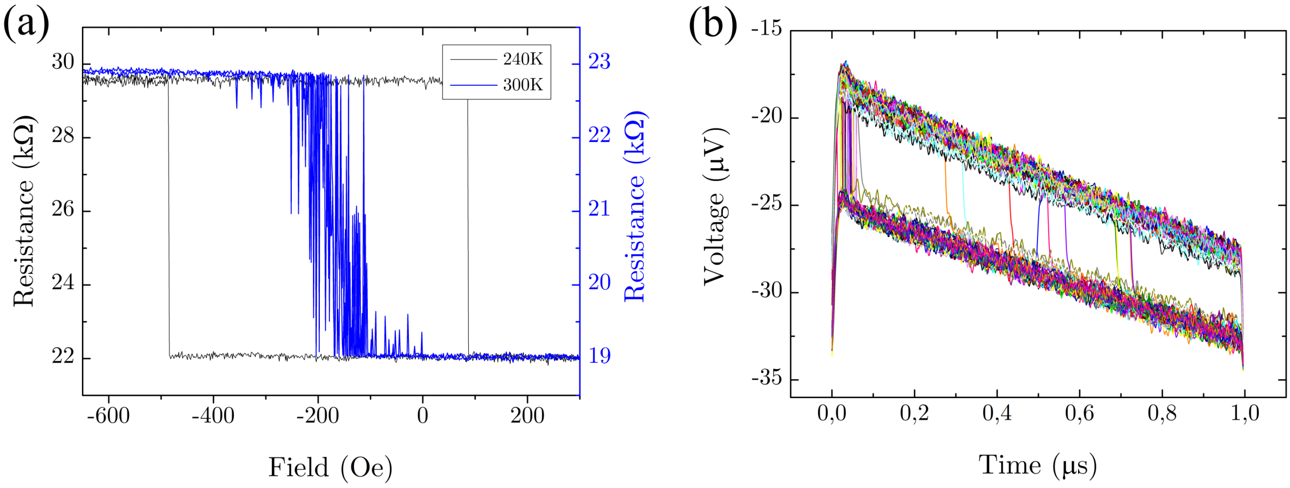

Figure 5.1: A permalloy insertion sample with 50nm in nominal diameter, $t_{FeCoB} = 0.9nm$ and $t_{Py} = 0.4$. a)HR loops at 300K and 240K. b)Real-time measurement of the device under reading bias of 20mV.

## 2.2 Ultra-fast STT switching

The next step on the investigation of the STT samples is to perform high-speed switching experiments in the GHz range. These are important to further consolidate the hypothesis of anisotropy tessellation on our storage layer from the experimental results and MFM imaging in the previous chapter. The type of information we can collect with writing operations under 1ns pulses is the increase in switching voltage compared to the 100ns pulses that have been used, alongside the transition of the thermal activation regime to the ballistic switching regime, which occurs at a critical pulse length. Studying the evolution of the write voltage versus voltage pulse width at cryogenic temperatures is important to know whether we have reached ballistic writing or not on these new devices. Another important aspect of this experiment is to make a comparison between the switching times of a conventional MTJ embedding an easy-cone storage layer. By the nature of STT, its kick-start relies on thermal fluctuations. Knowing this, we can expect the STT writing to start instantaneously on layers with this easy cone anisotropy.

In Fig.5.2 we show an initial measurement of an interfacial Mg sample with $t_{FeCoB} = 1.48nm$ and $t_{Mg} = 1.02nm$ and 80nm nominal diameter. In (a) we have $V_{50}^{PAP}$ plotted for 10K, 50K, 100K, 150K and 200K using pulses of 20 to 1000ns, which shows the increase in the voltage with both decreasing temperature and pulse width, as expected. Though certain instrumentation limitations prevented the measurement to be reliable, the data points all shift to slightly higher voltages for pulses shorter than 40ns. In the phase diagram of (b), we can see more clearly the dependence of the critical switching voltage at 50K for both PAP and APP and how it quickly increases for shorter pulses. Identifying where the ballistic regime starts and how it evolves with temperature can provide us with information on the different properties of these layers possess and how or if they are more suitable for cryogenic implementation.

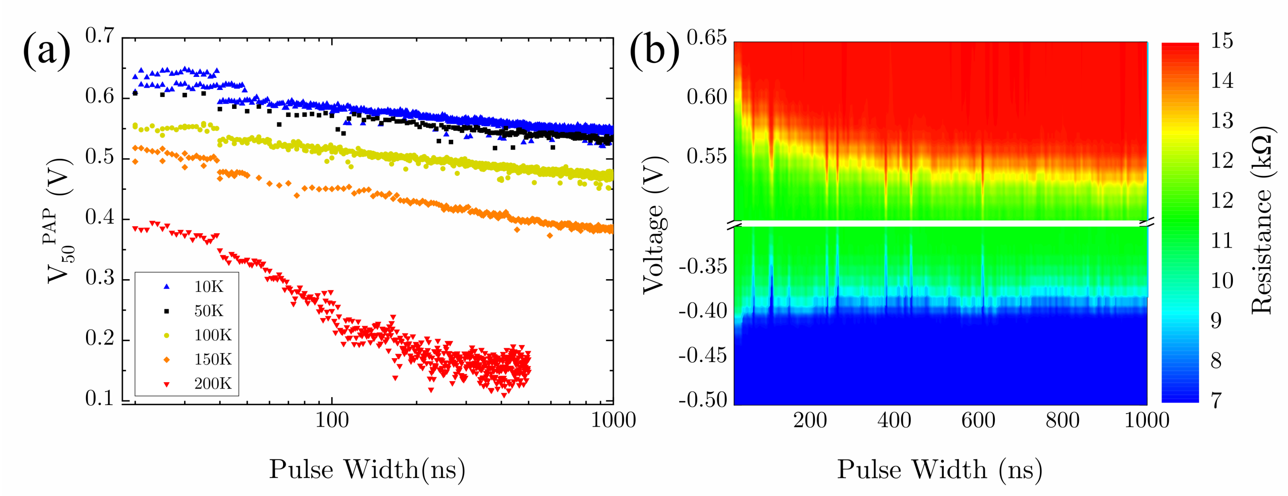

Figure 5.2: Pulse switching dependence measurement of an interfacial Mg sample with $t_{FeCoB} = 1.48nm$ and $t_{Mg} = 1.02nm$ and 80nm in nominal diameter. a)PAP switching voltage dependence for 10K, 50K, 100K, 150K and 200K. b)Pulse phase diagram at 50K for PAP and APP switching voltages.

## 2.3 Deterministic VCMA switching

The experimental work on VCMA devices of this thesis was not concluded due to time constraints. A last measurement was done in the writing experiments and the fabricated sample proved to be a viable candidate for further testing as it showed switching under the correct set of system parameters. Knowing that the VCMA effect becomes stronger with reduced temperature, we can have a strong argument to attempt the same experiment at lower temperatures. However, further improvement on $\xi$ may be necessary, because the $V_C$ of the tested device was only a few decimal points below its breakdown voltage. Therefore, we must ensure that the junctions become more robust and less sensitive to breakdown for the target temperatures.

This is an important step to reach cryogenic operation, since our predictions with macrospin and micromagnetic simulations indicate that a novel deterministic switching regime is present below 50K. And finding experimental evidence for it will be a step towards making VCMA-MRAM, not only viable, but preferable when compared to other writing mechanisms such as STT or SOT. Therefore, this is the most promising point for future work to develop a new type of device and drastically reduce the energy consumption of MRAM bits for very low temperatures.

# Bibliography

[1] Tetsuo Endoh. Nonvolatile logic and memory devices based on spintronics. In *2015 IEEE International Symposium on Circuits and Systems, ISCAS 2015*, Proceedings - IEEE International Symposium on Circuits and Systems, pages 13–16. Institute of Electrical and Electronics Engineers Inc., July 2015. IEEE International Symposium on Circuits and Systems, ISCAS 2015 ; Conference date: 24-05-2015 Through 27-05-2015.

[2] T. H. K. Barron, W. T. Berg, J. A. Morrison, and Edgar William Richard Steacie. On the heat capacity of crystalline magnesium oxide. *Proceedings of the Royal Society of London. Series A. Mathematical and Physical Sciences*, 250(1260):70–83, 1959.

[3] Néel, Louis. Anisotropie magnétique superficielle et surstructures d'orientation. *J. Phys. Radium*, 15(4):225–239, 1954.

[4] M. N. Baibich, J. M. Broto, A. Fert, F. Nguyen Van Dau, F. Petroff, P. Etienne, G. Creuzet, A. Friederich, and J. Chazelas. Giant magnetoresistance of (001)fe/(001)cr magnetic superlattices. *Phys. Rev. Lett.*, 61:2472–2475, Nov 1988.

[5] P. F. Carcia, A. D. Meinhaldt, and A. Suna. Perpendicular magnetic anisotropy in Pd/Co thin film layered structures. *Applied Physics Letters*, 47(2):178–180, 07 1985.

[6] M. Julliere. Tunneling between ferromagnetic films. *Physics Letters A*, 54(3):225–226, 1975.

[7] L. Berger. Emission of spin waves by a magnetic multilayer traversed by a current. *Phys. Rev. B*, 54:9353–9358, Oct 1996.

[8] T. Miyazaki and N. Tezuka. Giant magnetic tunneling effect in fe/al2o3/fe junction. *Journal of Magnetism and Magnetic Materials*, 139(3):L231–L234, 1995.

[9] D. A. Thompson and J. S. Best. The future of magnetic data storage techology. *IBM Journal of Research and Development*, 44(3):311–322, 2000.

[10] Yiming Huai. Spin-transfer torque mram (stt-mram): Challenges and prospects. *AAPPS Bulletin*, 18, 01 2008.

[11] Candid Reig, Susana Cardoso, and S.C. Mukhopadhyay. *Giant Magnetoresistance (GMR) Sensors From Basis to State-of-the-Art Applications.* 05 2013.

[12] Ando. Koji. Nonvolatile magnetic memory. *Journal of FED*, vol. 12, no. 4, pp. 89-95, 2001.

[13] Dmytro Apalkov, Bernard Dieny, and J. M Slaughter. Magnetoresistive Random Access Memory. *Proceedings of the IEEE*, 104:1796 – 1830, August 2016.

[14] I L Prejbeanu, M Kerekes, R C Sousa, H Sibuet, O Redon, B Dieny, and J P Nozières. Thermally assisted mram. *Journal of Physics: Condensed Matter*, 19(16):165218, apr 2007.

[15] J. A. Katine, F. J. Albert, R. A. Buhrman, E. B. Myers, and D. C. Ralph. Current-driven magnetization reversal and spin-wave excitations in co /cu /co pillars. *Phys. Rev. Lett.*, 84:3149–3152, Apr 2000.

[16] W. Zhao, E. Belhaire, Q. Mistral, C. Chappert, V. Javerliac, B. Dieny, and E. Nicolle. Macro-model of spin-transfer torque based magnetic tunnel junction device for hybrid magnetic-cmos design. In *2006 IEEE International Behavioral Modeling and Simulation Workshop*, pages 40–43, 2006.

[17] Luís Vitório Cargnini, Lionel Torres, Raphael Martins Brum, Sophiane Senni, and Gilles Sassatelli. Embedded memory hierarchy exploration based on magnetic random access memory. *Journal of Low Power Electronics and Applications*, 4(3):214–230, 2014.

[18] Li. Zheng Hu. Jia-Mian. High-density magnetoresistive random access memory operating at ultralow voltage at room temperature. *Nature Communications*, 2(1):2041–1723, 2011.

[19] S. Ikeda. A perpendicular-anisotropy cofeb–mgo magnetic tunnel junction. *Nature Materials*, 9(9):1476–4660, 2010.

[20] B. Dieny and A. Vedyayev. Crossover from easy-plane to perpendicular anisotropy in magnetic thin films: Canted anisotropy due to partial coverage or interfacial roughness. *Europhysics Letters*, 25(9):723, mar 1994.

[21] Gordon E. Moore. Cramming more components onto integrated circuits, reprinted from electronics, volume 38, number 8, april 19, 1965, pp.114 ff. *IEEE Solid-State Circuits Society Newsletter*, 11(3):33–35, 2006.

[22] H. Lee, L.-E. Yu, S.-W. Ryu, J.-W. Han, K. Jeon, D.-Y. Jang, K.-H. Kim, J. Lee, J.-H. Kim, S. Jeon, G. Lee, J. Oh, Y. Park, W. Bae, H. Lee, J. Yang, J. Yoo, S. Kim, and Y.-K. Choi. Sub-5nm all-around gate finfet for ultimate scaling. In *2006 Symposium on VLSI Technology, 2006. Digest of Technical Papers.*, pages 58–59, 2006.

[23] V.V. Zhirnov, R.K. III, James Hutchby, and George Bourianoff. Limits to binary logic switch scaling - a gedanken model. *Proceedings of the IEEE*, 91:1934 – 1939, 12 2003.

[24] Nicola Jones. How to stop data centres from gobbling up the world's electricity. *Nature*, 561:163–166, 2018.

[25] W. Chen, A.V. Rylyakov, V. Patel, J.E. Lukens, and K.K. Likharev. Rapid single flux quantum t-flip flop operating up to 770 ghz. *IEEE Transactions on Applied Superconductivity*, 9(2):3212–3215, 1999.

[26] J. Bulzacchelli W. Gallagher and M. Ketchen. Hybrid superconductingmagnetic memory cell and array. U.S. Patent 8 208 288, Jun. 26, 2012.

[27] A. Herr and Q. Herr. Josephson magnetic random access memory system and method. U.S. Patent 8 270 209 B2, Sep. 18, 2012.

[28] O. Mukhanov A. Kadin I. Nevirkovets and I. Vernik. Superconducting devices with ferromagnetic barrier junctions. U.S. Patent Appl. 2012/0 184 445 A1, Jan. 13, 2012.

[29] Shuichi Nagasawa, Kenji Hinode, Tetsuro Satoh, Yoshihiro Kitagawa, and Mutsuo Hidaka. Design of all-dc-powered high-speed single flux quantum random access memory based on a pipeline structure for memory cell arrays. *Superconductor Science and Technology*, 19(5):S325, mar 2006.

[30] Butsurin Jinnai, Kyota Watanabe, Shunsuke Fukami, and Hideo Ohno. Scaling magnetic tunnel junction down to single-digit nanometers—challenges and prospects. *Applied Physics Letters*, 116(16):160501, 2020.

[31] L. Berger. Emission of spin waves by a magnetic multilayer traversed by a current. *Phys. Rev. B*, 54:9353–9358, Oct 1996.

[32] D. Scott Holmes, Andrew L. Ripple, and Marc A. Manheimer. Energy-efficient superconducting computing—power budgets and requirements. *IEEE Transactions on Applied Superconductivity*, 23(3):1701610–1701610, 2013.

[33] L. Rehm, G. Wolf, B. Kardasz, M. Pinarbasi, and A. D. Kent. Sub-nanosecond spin-torque switching of perpendicular magnetic tunnel junction nanopillars at cryogenic temperatures. *Applied Physics Letters*, 115(18):182404, 2019.

[34] L. Rehm, G. Wolf, B. Kardasz, E. Cogulu, Y. Chen, M. Pinarbasi, and A.D. Kent. Thermal effects in spin-torque switching of perpendicular magnetic tunnel junctions at cryogenic temperatures. *Phys. Rev. Applied*, 15:034088, Mar 2021.

[35] Lili Lang, Yujie Jiang, Fei Lu, Cailu Wang, Yizhang Chen, Andrew D. Kent, and Li Ye. A low temperature functioning cofeb/mgo-based perpendicular magnetic tunnel junction for cryogenic nonvolatile random access memory. *Applied Physics Letters*, 116(2):022409, 2020.

[36] Kaihua Cao, Huisong Li, Wenlong Cai, Jiaqi Wei, Lezhi Wang, Yanpeng Hu, Qifeng Jiang, Hushan Cui, Chao Zhao, and Weisheng Zhao. Low-temperature performance of nanoscale perpendicular magnetic tunnel junctions with double mgo-interface free layer. *IEEE Transactions on Magnetics*, 55(3):1–4, 2019.

[37] Sabpreet Bhatti, Rachid Sbiaa, Atsufumi Hirohata, Hideo Ohno, Shunsuke Fukami, and S.N. Piramanayagam. Spintronics based random access memory: a review. *Materials Today*, 20(9):530–548, Nov 2017.

[38] E. Girgis, J. Schelten, J. Shi, J. Janesky, S. Tehrani, and H. Goronkin. Switching characteristics and magnetization vortices of thin-film cobalt in nanometer-scale patterned arrays. *Applied Physics Letters*, 76(25):3780–3782, 06 2000.

[39] Shun ichi IWASAKI. Perpendicular magnetic recording mdash;its development and realization-mdash;. *Proceedings of the Japan Academy, Series B*, 85(2):37–54, 2009.

[40] Miura K. Yamamoto H. et al Ikeda, S. A perpendicular-anisotropy cofeb–mgo magnetic tunnel junction. *Nature Mater*, 9:721–724, 2010.

[41] B. Dieny and M. Chshiev. Perpendicular magnetic anisotropy at transition metal/oxide interfaces and applications. *Reviews of Modern Physics*, 89(2):025008, Jun 2017.

[42] J. S. Moodera, Lisa R. Kinder, Terrilyn M. Wong, and R. Meservey. Large magnetoresistance at room temperature in ferromagnetic thin film tunnel junctions. *Phys. Rev. Lett.*, 74:3273–3276, Apr 1995.

[43] Stuart S. P. Parkin. Giant tunnelling magnetoresistance at room temperature with mgo (100) tunnel barriers. *Nature Materials*, 3, Dec 2004.

[44] J. Mathon and A. Umerski. Theory of tunneling magnetoresistance of an epitaxial fe/mgo/fe(001) junction. *Phys. Rev. B*, 63:220403, May 2001.

[45] W. H. Butler, X.-G. Zhang, T. C. Schulthess, and J. M. MacLaren. Spin-dependent tunneling conductance of Fe|MgO|Fe sandwiches. *Phys. Rev. B*, 63:054416, Jan 2001.

[46] H. X. Wei, Q. H. Qin, M. Ma, R. Sharif, and X. F. Han. 80
*Journal of Applied Physics*, 101(9):09B501, 04 2007.

[47] S. Ikeda, J. Hayakawa, Y. Ashizawa, Y. M. Lee, K. Miura, H. Hasegawa, M. Tsunoda, F. Matsukura, and H. Ohno. Tunnel magnetoresistance of 604
*Applied Physics Letters*, 93(8):082508, 08 2008.

[48] Thomas Scheike, Zhenchao Wen, Hiroaki Sukegawa, and Seiji Mitani. 631
*Applied Physics Letters*, 122(11):112404, 03 2023.

[49] Louis Néel. Théorie du traînage magnétique des ferromagnétiques en grains fins avec application aux terres cuites. *Annales de géophysique*, 5:99–136, 1949.

[50] W. T. Coffey, P. J. Cregg, and Y. U. P. Kalmykov. *On the Theory of Debye and Néel Relaxation of Single Domain Ferromagnetic Particles*, pages 263–464. John Wiley Sons, Ltd, 1992.

[51] O. Chubykalo-Fesenko and R.W. Chantrell. Modeling of long-time thermal magnetization decay in interacting granular magnetic materials. *IEEE Transactions on Magnetics*, 41(10):3103–3105, 2005.

[52] A V Khvalkovskiy, D Apalkov, S Watts, R Chepulskii, R S Beach, A Ong, X Tang, A Driskill-Smith, W H Butler, P B Visscher, D Lottis, E Chen, V Nikitin, and M Krounbi. Basic principles of stt-mram cell operation in memory arrays. *Journal of Physics D: Applied Physics*, 46(7):074001, jan 2013.

[53] J.C. Slonczewski. Current-driven excitation of magnetic multilayers. *Journal of Magnetism and Magnetic Materials*, 159(1-2):L1–L7, June 1996.

[54] A. A. Timopheev, R. Sousa, M. Chshiev, L. D. Buda-Prejbeanu, and B. Dieny. Respective influence of in-plane and out-of-plane spin-transfer torques in magnetization switching of perpendicular magnetic tunnel junctions. *Physical Review B*, 92(10):104430, Sep 2015.

[55] William Fuller Brown. Thermal fluctuations of a single-domain particle. *Phys. Rev.*, 130:1677–1686, Jun 1963.

[56] J. Z. Sun. Spin-current interaction with a monodomain magnetic body: A model study. *Phys. Rev. B*, 62:570–578, Jul 2000.

[57] D. Bedau, H. Liu, J.-J. Bouzaglou, A. D. Kent, J. Z. Sun, J. A. Katine, E. E. Fullerton, and S. Mangin. Ultrafast spin-transfer switching in spin valve nanopillars with perpendicular anisotropy. *Applied Physics Letters*, 96(2):022514, 01 2010.

[58] Ioan Mihai Miron, K. Garello, and G. Gaudin. Perpendicular switching of a single ferromagnetic layer induced by in-plane current injection. *Nature*, 476(7359), 2011.

[59] A. Manchon, J. Železný, I.M. Miron, T. Jungwirth, J. Sinova, A. Thiaville, K. Garello, and P. Gambardella. Current-induced spin-orbit torques in ferromagnetic and antiferromagnetic systems. *Reviews of Modern Physics*, 91(3):035004, Sep 2019.

[60] K. Garello, F. Yasin, S. Couet, L. Souriau, J. Swerts, S. Rao, S. Van Beek, W. Kim, E. Liu, S. Kundu, D. Tsvetanova, K. Croes, N. Jossart, E. Grimaldi, M. Baumgartner, D. Crotti, A. Fumémont, P. Gambardella, and G.S. Kar. Sot-mram 300mm integration for low power and ultrafast embedded memories. In *2018 IEEE Symposium on VLSI Circuits*, pages 81–82, 2018.

[61] Shy-Jay Lin, Yen-Lin Huang, MingYaun Song, Chien-Ming Lee, Fen Xue, Guan-Long Chen, Shan-Yi Yang, Yao-Jen Chang, I-Jung Wang, Yu-Chen Hsin, Yi-Hui Su, Jeng-Hua Wei, Chi-Feng Pai, Shan X. Wang, and Carlos H. Diaz. Challenges toward low-power sot-mram. In *2021 IEEE International Reliability Physics Symposium (IRPS)*, pages 1–7, 2021.

[62] K. Cai, G. Talmelli, K. Fan, S. Van Beek, V. Kateel, M. Gupta, M.G. Monteiro, M. Ben Chroud, G. Jayakumar, A. Trovato, S. Rao, G.S. Kar, and S. Couet. First demonstration of field-free perpendicular sot-mram for ultrafast and high-density embedded memories. In *2022 International Electron Devices Meeting (IEDM)*, pages 36.2.1–36.2.4, 2022.

[63] Behzad Zeinali, Jens K. Madsen, Praveen Raghavan, and Farshad Moradi. Ultra-fast sot-mram cell with stt current for deterministic switching. In *2017 IEEE International Conference on Computer Design (ICCD)*, pages 463–468, 2017.

[64] Rajesh Saha, Yogendra Pratap Pundir, and Pankaj Kumar Pal. Comparative analysis of stt and sot based mrams for last level caches. *Journal of Magnetism and Magnetic Materials*, 551:169161, 2022.

[65] Atsushi Okada, Shun Kanai, Shunsuke Fukami, Hideo Sato, and Hideo Ohno. Electric-field effect on the easy cone angle of the easy-cone state in CoFeB/MgO investigated by ferromagnetic resonance. *Applied Physics Letters*, 112(17):172402, April 2018.

[66] Chun-Gang Duan, Julian P. Velev, R. F. Sabirianov, Ziqiang Zhu, Junhao Chu, S. S. Jaswal, and E. Y. Tsymbal. Surface magnetoelectric effect in ferromagnetic metal films. *Phys. Rev. Lett.*, 101:137201, Sep 2008.

[67] Kohji Nakamura, Riki Shimabukuro, Yuji Fujiwara, Toru Akiyama, Tomonori Ito, and A. J. Freeman. Giant modification of the magnetocrystalline anisotropy in transition-metal monolayers by an external electric field. *Phys. Rev. Lett.*, 102:187201, May 2009.

[68] Stewart E. Barnes, Jun'ichi Ieda, and Sadamichi Maekawa. Rashba spin-orbit anisotropy and the electric field control of magnetism. *Scientific Reports*, 4, 2014.

[69] Wang Kang, Yi Ran, Youguang Zhang, Weifeng Lv, and Weisheng Zhao. Modeling and exploration of the voltage-controlled magnetic anisotropy effect for the next-generation low-power and high-speed mram applications. *IEEE Transactions on Nanotechnology*, 16(3):387–395, 2017.

[70] V. Novosad, Y. Otani, A. Ohsawa, S. G. Kim, K. Fukamichi, J. Koike, K. Maruyama, O. Kitakami, and Y. Shimada. Novel magnetostrictive memory device. *Journal of Applied Physics*, 87(9):6400–6402, 05 2000.

[71] Jian Zhu, J. A. Katine, Graham E. Rowlands, Yu-Jin Chen, Zheng Duan, Juan G. Alzate, Pramey Upadhyaya, Juergen Langer, Pedram Khalili Amiri, Kang L. Wang, and Ilya N. Krivorotov. Voltage-induced ferromagnetic resonance in magnetic tunnel junctions. *Phys. Rev. Lett.*, 108:197203, May 2012.

[72] Takayuki Nozaki, Tatsuya Yamamoto, Shinji Miwa, Masahito Tsujikawa, Masafumi Shirai, Shinji Yuasa, and Yoshishige Suzuki. Recent progress in the voltage-controlled magnetic anisotropy effect and the challenges faced in developing voltage-torque mram. *Micromachines*, 10(5):327, May 2019.

[73] Leiden Cryogenics. Dilution refrigeration available power. `http://www.leidencryogenics.nl/`. Accessed: 2022-09-25.

[74] Bluefors Cryogenics. Dilution refrigeration available power. `http://www.bluefors.com/`. Accessed: 2022-09-25.

[75] Linde Kryotechnik AG. High power refrigeration plants. https://www.linde-kryotechnik.ch/en/products/helium-refrigeration-plants/lr-series/. Accessed: 2023-08-03.

[76] Martin Nurizzo, Baptiste Jadot, Pierre-André Mortemousque, Vivien Thiney, Emmanuel Chanrion, David Niegemann, Matthieu Dartiailh, Arne Ludwig, Andreas D. Wieck, Christopher Bäuerle, Matias Urdampilleta, and Tristan Meunier. Complete readout of two-electron spin states in a double quantum dot. *PRX Quantum*, 4:010329, Mar 2023.

[77] A. A. Timopheev, R. Sousa, M. Chshiev, L. D. Buda-Prejbeanu, and B. Dieny. Respective influence of in-plane and out-of-plane spin-transfer torques in magnetization switching of perpendicular magnetic tunnel junctions. *Physical Review B*, 92(10):104430, September 2015.

[78] W. Heisenberg. Mehrkörperproblem und resonanz in der quantenmechanik. *Zeitschrift f¨ur Physik*, 38:411–426, 1926.

[79] Dr. P. Zeeman. Vii. doublets and triplets in the spectrum produced by external magnetic forces. *The London, Edinburgh, and Dublin Philosophical Magazine and Journal of Science*, 44(266):55–60, 1897.

[80] B. Dieny, B. Barbara, G. Fillion, M. Maeder, and B. Michelutti. Hysteresis loop and torque experiments on a random anisotropy system. *Journal de Physique*, 48(10):1741–1749, 1987.

[81] B. Dieny and A. Vedyayev. Crossover from easy-plane to perpendicular anisotropy in magnetic thin films: Canted anisotropy due to partial coverage or interfacial roughness. *Europhysics Letters*, 25(9):723, mar 1994.

[82] Justine L. Drobitch, Md Ahsanul Abeed, and Supriyo Bandyopadhyay. Precessional switching of a perpendicular anisotropy magneto-tunneling junction without a magnetic field. *Japanese Journal of Applied Physics*, 56(10):100309, sep 2017.

[83] Ren-Ci Peng, Jia-Mian Hu, Kasra Momeni, Jian-Jun Wang, Long-Qing Chen, and Ce-Wen Nan. Fast 180° magnetization switching in a strain-mediated multiferroic heterostructure driven by a voltage. *Scientific reports*, 6:27561, June 2016.

[84] Kuntal Roy, Supriyo Bandyopadhyay, and Jayasimha Atulasimha. Energy dissipation and switching delay in stress-induced switching of multiferroic nanomagnets in the presence of thermal fluctuations. *Journal of Applied Physics*, 112(2):023914, 2012.

[85] Stewart E. Barnes, Jun'Ichi Ieda, and Sadamichi Maekawa. Rashba spin-orbit anisotropy and the electric field control of magnetism. *Scientific Reports*, 4:1–5, February 2014. Funding Information: This work is partly supported by KAKENHI (No. 24740247) from MEXT, Japan.

[86] A. Okada, S. Kanai, M. Yamanouchi, S. Ikeda, F. Matsukura, and H. Ohno. Electric-field effects on magnetic anisotropy and damping constant in ta/cofeb/mgo investigated by ferromagnetic resonance. *Applied Physics Letters*, 105(5):052415, 2014.

[87] William Fuller Brown. Thermal Fluctuations of a Single-Domain Particle. *Physical Review*, 130(5):1677–1686, June 1963.

[88] José Luis García-Palacios and Francisco J. Lázaro. Langevin-dynamics study of the dynamical properties of small magnetic particles. *Phys. Rev. B*, 58:14937–14958, Dec 1998.

[89] N. D. Mermin N. W. Ashcroft. Solid state physics, 1976.

[90] R. F. L. Evans, U. Atxitia, and R. W. Chantrell. Quantitative simulation of temperature-dependent magnetization dynamics and equilibrium properties of elemental ferromagnets. *Phys. Rev. B*, 91:144425, Apr 2015.

[91] B. E. Argyle, S. H. Charap, and E. W. Pugh. Deviations from $T^{\frac{3}{2}}$ law for magnetization of ferrometals: Ni, fe, and fe+3% si. *Phys. Rev.*, 132:2051–2062, Dec 1963.

[92] Jodi M. Iwata-Harms. High-temperature thermal stability driven by magnetization dilution in cofeb free layers for spin-transfer-torque magnetic random access memory. *Scientific Reports*, 8:14409, Sep 2018.

[93] Kyoung-Min Lee, Jun Woo Choi, Junghyun Sok, and Byoung-Chul Min. Temperature dependence of the interfacial magnetic anisotropy in w/cofeb/mgo. *AIP Advances*, 7(6):065107, 2017.

[94] H Ohno, D Chiba, F Matsukura, T Omiya, E Abe, T Dietl, Y Ohno, and K Ohtani. Electric-field control of ferromagnetism. *Nature*, 408(6815):944—946, 2000.

[95] H. B. Callen and E. Callen. The present status of the temperature dependence of magnetocrystalline anisotropy, and the l(l+1)2 power law. *Journal of Physics and Chemistry of Solids*, 27(8):1271–1285, 1966.

[96] C. Zener. Classical theory of the temperature dependence of magnetic anisotropy energy. *Phys. Rev.*, 96:1335–1337, Dec 1954.

[97] Kyoung-Min Lee, Jun Woo Choi, Junghyun Sok, and Byoung-Chul Min. Temperature dependence of the interfacial magnetic anisotropy in w/cofeb/mgo. *AIP Advances*, 7(6):065107, 2017.

[98] Fatima Ibrahim, Ali Hallal, Alan Kalitsov, Derek Stewart, Bernard Dieny, and Mairbek Chshiev. Unveiling Temperature-Dependence Mechanisms of Perpendicular Magnetic Anisotropy at Fe / Mg O Interfaces. *Physical Review Applied*, 17(5):054041, May 2022.

[99] B. M. S. Teixeira, A. A. Timopheev, N. Caçoilo, S. Auffret, R. C. Sousa, B. Dieny, and N. A. Sobolev. Stabilization of the easy-cone magnetic state in free layers of magnetic tunnel junctions. *Phys. Rev. B*, 100:184405, Nov 2019.

[100] R. Moreno, R. F. L. Evans, S. Khmelevskyi, M. C. Muñoz, R. W. Chantrell, and O. Chubykalo-Fesenko. Temperature-dependent exchange stiffness and domain wall width in co. *Phys. Rev. B*, 94:104433, Sep 2016.

[101] M. Mulazzi, A. Chainani, Y. Takata, Y. Tanaka, Y. Nishino, K. Tamasaku, T. Ishikawa, T. Takeuchi, Y. Ishida, Y. Senba, H. Ohashi, and S. Shin. Temperature dependence of the exchange stiffness in fepd(001) thin films: Deviation from the empirical law $a(t) \propto M_S^2$ at intermediate temperatures. *Phys. Rev. B*, 77:224425, Jun 2008.

[102] N. Strelkov, A. Chavent, A. Timopheev, R. C. Sousa, I. L. Prejbeanu, L. D. Buda-Prejbeanu, and B. Dieny. Impact of joule heating on the stability phase diagrams of perpendicular magnetic tunnel junctions. *Phys. Rev. B*, 98:214410, Dec 2018.

[103] Jan Winter, Jürgen Sotrop, Stephan Borek, Heinz P. Huber, and Jan Minár. Temperature-dependent determination of electron heat capacity and electron-phonon coupling factor for $\mathrm{fe}_{0.72}\mathrm{cr}_{0.18}\mathrm{ni}_{0.1}$. *Phys. Rev. B*, 93:165119, Apr 2016.

[104] E. Gapihan, J. Hérault, R. C. Sousa, Y. Dahmane, B. Dieny, L. Vila, I. L. Prejbeanu, C. Ducruet, C. Portemont, K. Mackay, and J. P. Nozières. Heating asymmetry induced by tunneling current flow in magnetic tunnel junctions. *Applied Physics Letters*, 100(20):202410, May 2012.

[105] Wolfram Research, Inc. Mathematica, Version 13.2. Champaign, IL, 2022.

[106] J. C. Slonczewski. Conductance and exchange coupling of two ferromagnets separated by a tunneling barrier. *Phys. Rev. B*, 39:6995–7002, Apr 1989.

[107] Gabriel D. Chaves-O'Flynn, Georg Wolf, Jonathan Z. Sun, and Andrew D. Kent. Thermal stability of magnetic states in circular thin-film nanomagnets with large perpendicular magnetic anisotropy. *Phys. Rev. Appl.*, 4:024010, Aug 2015.

[108] Alex Hubert and Rudolf Schäfer. *Magnetic domains: the analysis of magnetic microstructures.* Springer, Berlin ; New York, 1998.

[109] S. Mangin, D. Ravelosona, J. A. Katine, M. J. Carey, B. D. Terris, and Eric E. Fullerton. Current-induced magnetization reversal in nanopillars with perpendicular anisotropy. *Nature Materials*, 5(3):210–215, March 2006.

[110] Shun Kanai, Michihiko Yamanouchi, Shoji Ikeda, Yoshinobu Nakatani, Fumihiro Matsukura, and Hideo Ohno. Electric field-induced magnetization switching in cofeb-mgo—static magnetic field angle dependence. *IEEE Transactions on Magnetics*, 50(1):1–3, Jan 2014.

[111] Roxana-Alina One, Hélène Béa, Sever Mican, Marius Joldos, Pedro Brandão Veiga, Bernard Dieny, Liliana D. Buda-Prejbeanu, and Coriolan Tiusan. Route towards efficient magnetization reversal driven by voltage control of magnetic anisotropy. *Scientific Reports*, 11(1):8801, December 2021.

[112] T. Devolder, P.-H. Ducrot, J.-P. Adam, I. Barisic, N. Vernier, Joo-Von Kim, B. Ockert, and D. Ravelosona. Damping of Co $_{\mathrm{x}}$ Fe $_{80\mathrm{x}}$ B $_{20}$ ultrathin films with perpendicular magnetic anisotropy. *Applied Physics Letters*, 102(2):022407, January 2013.

[113] Y. C. Wu, W. Kim, K. Garello, F. Yasin, G. Jayakumar, S. Couet, R. Carpenter, S. Kundu, S. Rao, D. Crotti, J. Van Houdt, G. Groeseneken, and G. S. Kar. Deterministic and field-free voltage-controlled mram for high performance and low power applications. In *2020 IEEE Symposium on VLSI Technology*, pages 1–2, 2020.

[114] Arne Vansteenkiste, Jonathan Leliaert, Mykola Dvornik, Mathias Helsen, Felipe Garcia-Sanchez, and Bartel Van Waeyenberge. The design and verification of Mumax3. *AIP Advances*, 4(10):107133, 2014.

[115] Akira Sugawara, T. Akashi, P. D. Brown, R. P. Campion, T. Yoshida, B. L. Gallagher, and A. Tonomura. High-resolution observations of temperature-dependent magnetic domain structures within Ga x Mn 1  x As by Lorentz microscopy. *Physical Review B*, 75(24):241306, June 2007.

[116] V. Drewello, J. Schmalhorst, A. Thomas, and G. Reiss. Evidence for strong magnon contribution to the tmr temperature dependence in mgo based tunnel junctions. *Phys. Rev. B*, 77:014440, Jan 2008.

[117] Alvaro Palomino. *Scalable spintronics devices with reduced Pt and Ru content.* Theses, Université Grenoble Alpes [2020-....], June 2022.

[118] F. Garcia, G. Casali, S. Auffret, B. Rodmacq, and B. Dieny. Exchange bias in (pt/co0.9fe0.1)n/femn multilayers with perpendicular magnetic anisotropy. *Journal of Applied Physics*, 91(10):6905–6907, 2002.

[119] Hideo Sato, Shoji Ikeda, Shunsuke Fukami, Hiroaki Honjo, Shinya Ishikawa, Michihiko Yamanouchi, Kotaro Mizunuma, Fumihiro Matsukura, and Hideo Ohno. Co/pt multilayer based reference layers in magnetic tunnel junctions for nonvolatile spintronics vlsis. *Japanese Journal of Applied Physics*, 53(4S):04EM02, feb 2014.

[120] Jyotirmoy Chatterjee. *Engineering of magnetic tunnel junction stacks for improved STT-MRAM performance and development of novel and cost-effective nano-patterning techniques.* Theses, Université Grenoble Alpes, March 2018.

[121] Hideo Sato, Shoji Ikeda, Shunsuke Fukami, Hiroaki Honjo, Shinya Ishikawa, Michihiko Yamanouchi, Kotaro Mizunuma, Fumihiro Matsukura, and Hideo Ohno. Co/pt multilayer based reference layers in magnetic tunnel junctions for nonvolatile spintronics vlsis. *Japanese Journal of Applied Physics*, 53(4S):04EM02, feb 2014.

[122] Chando Park, Lena Miloslavsky, Ira Lim, Sangmun Oh, Christian Kaiser, Qunwen Leng, and Mahendra Pakala. Influence of boron diffusion on transport and magnetic properties in cofeb/mgo/cofeb magnetic tunnel junction. *IEEE Transactions on Magnetics*, 45(10):3457–3459, 2009.

[123] H. Honjo, S. Ikeda, H. Sato, K. Nishioka, T. Watanabe, S. Miura, T. Nasuno, Y. Noguchi, M. Yasuhira, T. Tanigawa, H. Koike, H. Inoue, M. Muraguchi, M. Niwa, H. Ohno, and T. Endoh.

Impact of tungsten sputtering condition on magnetic and transport properties of double-mgo magnetic tunneling junction with cofeb/w/cofeb free layer. *IEEE Transactions on Magnetics*, 53(11):1–4, 2017.

[124] Henning Schuhmann, Michael Seibt, Volker Drewello, Andy Thomas, Vladyslav Zbarsky, Marvin Walter, and Markus Münzenberg. Controlling boron redistribution in CoFeB/MgO magnetic tunnel junctions during annealing by variation of cap layer materials and MgO deposition methods. Technical Report arXiv:1405.1907, arXiv, May 2014. arXiv:1405.1907 [cond-mat].

[125] Shoji Ikeda, Jun Hayakawa, Young Min Lee, Fumihiro Matsukura, Yuzo Ohno, Takahiro Hanyu, and Hideo Ohno. Magnetic tunnel junctions for spintronic memories and beyond. *IEEE Transactions on Electron Devices*, 54(5):991–1002, 2007.

[126] S. Bandiera, Ricardo Sousa, Y. Dahmane, Clarisse Ducruet, Celine Portemont, Vincent Baltz, Stephane Auffret, Ioan Prejbeanu, and Bernard Dieny. Comparison of synthetic antiferromagnets and hard ferromagnets as reference layer in magnetic tunnel junctions with perpendicular magnetic anisotropy. *Magnetics Letters, IEEE*, 1:3000204 – 3000204, 02 2010.

[127] M. R. Parker. The Kerr magneto-optic effect (1876–1976). *Physica B+C*, 86-88:1171–1176, 1977.

[128] J. C. Suits. Magneto-optical rotation and ellipticity measurements with a spinning analyzer. *Review of Scientific Instruments*, 42(1):19–22, 1971.

[129] J. L. Erskine and E. A. Stern. Magneto-optic kerr effect in ni, co, and fe. *Phys. Rev. Lett.*, 30:1329–1332, Jun 1973.

[130] Der-Sheng Lee, Hao-Ting Chang, Chih-Wei Cheng, and Gung Chern. Perpendicular magnetic anisotropy in mgo/cofeb/nb and a comparison of the cap layer effect. *IEEE Transactions on Magnetics*, 50(7):1–4, 2014.

[131] Bruno Teixeira. *Ferromagnetic multilayers with programmable magnetic anisotropy.* PhD thesis.

[132] Hiroki Maehara, Kazumasa Nishimura, Yoshinori Nagamine, Koji Tsunekawa, Takayuki Seki, Hitoshi Kubota, Akio Fukushima, Kay Yakushiji, Koji Ando, and Shinji Yuasa. Tunnel magnetoresistance above 170% and resistance–area product of 1 Ω (µm)2 attained by in situ annealing of ultra-thin mgo tunnel barrier. *Applied Physics Express*, 4(3):033002, mar 2011.

[133] Hyunsoo Yang, See-Hun Yang, and Stuart Parkin. The role of mg interface layer in mgo magnetic tunnel junctions with cofe and cofeb electrodes. *AIP Advances*, 2(1):012150, 2012.

[134] Y. C. Wu, W. Kim, K. Garello, F. Yasin, G. Jayakumar, S. Couet, R. Carpenter, S. Kundu, S. Rao, D. Crotti, J. Van Houdt, G. Groeseneken, and G. S. Kar. Deterministic and field-free voltage-controlled mram for high performance and low power applications. In *2020 IEEE Symposium on VLSI Technology*, pages 1–2, 2020.

[135] Liang G. Deng J. and Gupta G. Ultrafast and low-energy switching in voltage-controlled elliptical pmtj. *Sci Rep*, 7(16562), 2017.

[136] Venkata Pavan Kumar Miriyala, Xuanyao Fong, and Gengchiau Liang. Influence of size and shape on the performance of vcma-based mtjs. *IEEE Transactions on Electron Devices*, 66(2):944–949, 2019.

[137] Yushi Kato, Hiroaki Yoda, Yoshiaki Saito, Soichi Oikawa, Keiko Fujii, Masahiko Yoshiki, Katsuhiko Koi, Hideyuki Sugiyama, Mizue Ishikawa, Tomoaki Inokuchi, Naoharu Shimomura, Mariko Shimizu, Satoshi Shirotori, Buyandalai Altansargai, Yuichi Ohsawa, Kazutaka Ikegami, Ajay Tiwari, and Atsushi Kurobe. Giant voltage-controlled magnetic anisotropy effect in a crystallographically strained cofe system. *Applied Physics Express*, 11(5):053007, apr 2018.

[138] Cecile Grezes, Xiang Li, Kin L Wong, Farbod Ebrahimi, Pedram Khalili Amiri, and Kang L Wang. Voltage-controlled magnetic tunnel junctions with synthetic ferromagnet free layer sandwiched by asymmetric double mgo barriers. *Journal of Physics D: Applied Physics*, 53(1):014006, oct 2019.

[139] Yoichi Shiota, Shinichi Murakami, Frédéric Bonell, Takayuki Nozaki, Teruya Shinjo, and Yoshishige Suzuki. Quantitative evaluation of voltage-induced magnetic anisotropy change by magnetoresistance measurement. *Applied Physics Express*, 4(4):043005, mar 2011.

[140] Yoichi Shiota, Frédéric Bonell, Shinji Miwa, Norikazu Mizuochi, Teruya Shinjo, and Yoshishige Suzuki. Opposite signs of voltage-induced perpendicular magnetic anisotropy change in cofeb|mgo junctions with different underlayers. *Applied Physics Letters*, 103(8):082410, 2013.

[141] C. Grezes, A. Rojas Rozas, F. Ebrahimi, J. G. Alzate, X. Cai, J. A. Katine, J. Langer, B. Ocker, P. Khalili Amiri, and K. L. Wang. In-plane magnetic field effect on switching voltage and thermal stability in electric-field-controlled perpendicular magnetic tunnel junctions. *AIP Advances*, 6(7):075014, 2016.

[142] P. J. Flanders and M. P. Sharrock. An analysis of time-dependent magnetization and coercivity and of their relationship to print-through in recording tapes. *Journal of Applied Physics*, 62(7):2918–2928, 1987.

[143] Xuebing Feng and P. B. Visscher. Sweep-rate-dependent coercivity simulation of FePt particle arrays. *Journal of Applied Physics*, 95(11):7043–7045, June 2004.

[144] Luc Thomas, Guenole Jan, Jian Zhu, Huanlong Liu, Yuan-Jen Lee, Son Le, Ru-Ying Tong, Keyu Pi, Yu-Jen Wang, Dongna Shen, Renren He, Jesmin Haq, Jeffrey Teng, Vinh Lam, Kenlin Huang, Tom Zhong, Terry Torng, and Po-Kang Wang. Perpendicular spin transfer torque magnetic random access memories with high spin torque efficiency and thermal stability for embedded applications (invited). *Journal of Applied Physics*, 115(17):172615, May 2014.

[145] G. Mihajlovic, N. Smith, T. Santos, J. Li, M. Tran, M. Carey, B.D. Terris, and J.A. Katine. Origin of the resistance-area-product dependence of spin-transfer-torque switching in perpendicular magnetic random-access memory cells. *Phys. Rev. Appl.*, 13:024004, Feb 2020.

[146] Michael P. Sharrock. Time dependence of switching fields in magnetic recording media (invited). *Journal of Applied Physics*, 76:6413–6418, 1994.

[147] Y.C. Wu, K. Garello, W. Kim, M. Gupta, M. Perumkunnil, V. Kateel, S. Couet, R. Carpenter, S. Rao, S. Van Beek, K.K. Vudya Sethu, F. Yasin, D. Crotti, and G.S. Kar. Voltage-gate-assisted spin-orbit-torque magnetic random-access memory for high-density and low-power embedded applications. *Phys. Rev. Appl.*, 15:064015, Jun 2021.

[148] Icp-rie plasma etcher si 500. https://www.sentech.com/en/ICP-RIE-SI-500$_{262/}$.

[149] Rob Legtenberg, Henri Jansen, Meint de Boer, and Miko Elwenspoek. Anisotropic reactive ion etching of silicon using sf6/o2/chf3 gas mixtures. *Journal of The Electrochemical Society*, 142(6):2020, jun 1995.

[150] Hprobe. https://www.hprobe.com/. Accessed: 25-08-2023.

[151] Physical property measurement system. `https://qd-europe.com/it/en/product/physical-property-measurement-system-ppms/`. Accessed: 06-07-2023.

[152] Ibex-wat mram parametric test. `https://www.hprobe.com/products/`. Accessed: 06-07-2023.

[153] Empx-hf cryogenic probe station. `https://www.lakeshore.com/products/categories/overview/discontinued-products/discontinued-products/model-empx-hf-cryogenic-probe-station`. Accessed: 06-07-2023.

[154] Ricardo Sousa. *Spintronics memory function : materials and device concepts.* Habilitation à diriger des recherches, Universite Grenoble Alpes, May 2017.

[155] Wei Zhang, Zihan Tong, Yuzan Xiong, Weigang Wang, and Qiming Shao. On the temperature-dependent characteristics of perpendicular shape anisotropy-spin transfer torque-magnetic random access memories. *Journal of Applied Physics*, 129(22):223903, Jun 2021.

[156] Dongyan Zhao, Yubo Wang, Jin Shao, Yanning Chen, Zhen Fu, Qingtao Xia, Shuaipeng Wang, Xiuwei Li, Guangzhi Dong, Min Zhou, and Dapeng Zhu. Temperature dependence of tunnel magnetoresistance in serial magnetic tunnel junctions. *AIP Advances*, 12(5), 05 2022. 055114.

[157] R. H. Koch, J. A. Katine, and J. Z. Sun. Time-resolved reversal of spin-transfer switching in a nanomagnet. *Phys. Rev. Lett.*, 92:088302, Feb 2004.

[158] Léa Cuchet. *Magnetic and transport properties of single and double perpendicular magnetic tunnel junctions.* Theses, Université Grenoble Alpes, November 2015.

[159] Sébastien Bandiera. *Jonctions tunnel magnétiques à anisotropie perpendiculaire et écriture assistée thermiquement.* Theses, Université de Grenoble, October 2011.

[160] Jyotirmoy Chatterjee. *Engineering of magnetic tunnel junction stacks for improved STT-MRAM performance and development of novel and cost-effective nano-patterning techniques.* Theses, Université Grenoble Alpes, March 2018.

[161] Lavinia Nistor. *Jonctions tunnel magnétiques à aimantation perpendiculaire : anisotropie, magnétorésistance, couplages magnétiques et renversement par couple de transfert de spin.* Theses, Université de Grenoble, October 2011.

[162] Kevin Coffey Katayun Barmak. *Metallic Films for Electronic, Optical and Magnetic Applications. Structure, Processing and Properties.* Woodhead Publishing, December 13, 2013.

[163] M. Freiser. A survey of magnetooptic effects. *IEEE Transactions on Magnetics*, 4(2):152–161, 1968.

[164] J. Suits. Faraday and kerr effects in magnetic compounds. *IEEE Transactions on Magnetics*, 8(1):95–105, 1972.

[165] Jr. Carr, W. J. Temperature Dependence of Ferromagnetic Anisotropy. *Journal of Applied Physics*, 29(3):436–437, 06 2004.

[166] I L Prejbeanu, S Bandiera, J Alvarez-Hérault, R C Sousa, B Dieny, and J-P Nozières. Thermally assisted mrams: ultimate scalability and logic functionalities. *Journal of Physics D: Applied Physics*, 46(7):074002, jan 2013.

[167] Jonathan Z. Sun. Spin-transfer torque switched magnetic tunnel junction for memory technologies. *Journal of Magnetism and Magnetic Materials*, 559:169479, 2022.

[168] R. C. Sousa, I. L. Prejbeanu, D. Stanescu, B. Rodmacq, O. Redon, B. Dieny, Jianguo Wang, and P. P. Freitas. Tunneling hot spots and heating in magnetic tunnel junctions. *Journal of Applied Physics*, 95(11):6783–6785, 05 2004.

[169] Kaihua Cao, Huisong Li, Wenlong Cai, Jiaqi Wei, Lezhi Wang, Yanpeng Hu, Qifeng Jiang, Hushan Cui, Chao Zhao, and Weisheng Zhao. Low-temperature performance of nanoscale perpendicular magnetic tunnel junctions with double mgo-interface free layer. *IEEE Transactions on Magnetics*, 55(3):1–4, Mar 2019.

[170] T. Usami, M. Itoh, and T. Taniyama. Temperature dependence of the effective Gilbert damping constant of FeRh thin films. *AIP Advances*, 11(4):045302, 04 2021.

[171] et al Zhao, Yuelei. Experimental Investigation of Temperature-Dependent Gilbert Damping in Permalloy Thin Films. *Scientific Reports*, 6:22890, 2016.

[172] Guangduo Lu, Xiufeng Huang, Shuaiwei Fan, Weiwei Ling, Min Liu, Jie Li, Lichuan Jin, and Liqing Pan. Temperature-and thickness -dependent dynamic magnetic properties of sputtered cofeb/ta bilayer films. *Journal of Alloys and Compounds*, 753:475–482, 2018.

[173] Lili Lang, Yujie Jiang, Fei Lu, Cailu Wang, Yizhang Chen, Andrew D. Kent, and Li Ye. A low temperature functioning cofeb/mgo-based perpendicular magnetic tunnel junction for cryogenic nonvolatile random access memory. *Applied Physics Letters*, 116(2):022409, Jan 2020.

[174] Chang He Shang, Janusz Nowak, Ronnie Jansen, and Jagadeesh S. Moodera. Temperature dependence of magnetoresistance and surface magnetization in ferromagnetic tunnel junctions. *Phys. Rev. B*, 58:R2917–R2920, Aug 1998.

[175] Y. C. Wu, W. Kim, S. Van Beek, S. Couet, R. Carpenter, S. Rao, S. Kundu, J. Van Houdt, G. Groeseneken, D. Crotti, and G. S. Kar. Impact of ambient temperature on the switching of voltage-controlled perpendicular magnetic tunnel junction. *Applied Physics Letters*, 118(12):122404, 03 2021.

[176] Juan G. Alzate, Pedram Khalili Amiri, Guoqiang Yu, Pramey Upadhyaya, Jordan A. Katine, Juergen Langer, Berthold Ocker, Ilya N. Krivorotov, and Kang L. Wang. Temperature dependence of the voltage-controlled perpendicular anisotropy in nanoscale mgo/cofeb/ta magnetic tunnel junctions. *Applied Physics Letters*, 104(11):112410, 2014.

[177] Yong-Chang Lau, Peng Sheng, Seiji Mitani, Daichi Chiba, and Masamitsu Hayashi. Electric field modulation of the non-linear areal magnetic anisotropy energy. *Applied Physics Letters*, 110(2):022405, 2017.

[178] James Lourembam, Jiancheng Huang, Sze Ter Lim, and Ernult Franck Gerard. Role of cofeb thickness in electric field controlled sub-100 nm sized magnetic tunnel junctions. *AIP Advances*, 8(5):055915, 2018.

[179] Xiang Li, Guoqiang Yu, Hao Wu, P. V. Ong, Kin Wong, Qi Hu, Farbod Ebrahimi, Pramey Upadhyaya, Mustafa Akyol, Nicholas Kioussis, Xiufeng Han, Pedram Khalili Amiri, and Kang L. Wang. Thermally stable voltage-controlled perpendicular magnetic anisotropy in Mo|CoFeB|MgO structures. *Applied Physics Letters*, 107(14):142403, 10 2015.

[180] C. Grezes, A. Rojas Rozas, F. Ebrahimi, J. G. Alzate, X. Cai, J. A. Katine, J. Langer, B. Ocker, P. Khalili Amiri, and K. L. Wang. In-plane magnetic field effect on switching voltage and thermal stability in electric-field-controlled perpendicular magnetic tunnel junctions. *AIP Advances*, 6(7):075014, 07 2016.